Algorithms for 5G physical layer

ScuDo
Scuola di Dottorato ~ Doctoral School
WHAT YOU ARE, TAKES YOU FAR

Doctoral Dissertation
Doctoral Program in Electronics Engineering (29^{th}cycle)

Algorithms for 5G Physical Layer

By

Pawan Dhakal

******

Supervisor(s):
Prof. Roberto Garello, Supervisor

Doctoral Examination Committee:
Prof. Paola Pierleoni, University of Marche,
Prof. Fulvio Babich, University of Trieste,
Prof. Francesca Vatta, University of Trieste,
Prof. Stefano Mangione, University of Palermo

Politecnico di Torino
2017

Declaration

I hereby declare that, the contents and organization of this dissertation constitute my own original work and does not compromise in any way the rights of third parties, including those relating to the security of personal data.

Pawan Dhakal
2017

* This dissertation is presented in partial fulfillment of the requirements for **Ph.D. degree** in the Graduate School of Politecnico di Torino (ScuDo).

I would like to dedicate this thesis to my loving parents, my wife and my son.

Acknowledgements

I take immense pleasure in thanking Department of Electronics and Telecommunication Engineering, Politecnico di Torino, Italy, for providing me an opportunity to carry out this PhD Research during the years 2014/2016.

My deepest gratitude to my advisor, Prof. Roberto Garello, for the able guidance and for his invaluable professional and human support in all possible ways ever since.

Then, I am grateful to Prof. Anand Gachhadar for hosting me at Kathmandu University, Nepal. Special thanks to all my former colleagues at Department of Electrical and Electronics Engineering of Kathmandu University for the friendly and welcoming atmosphere that really made me feel at home. Furthermore, I want to sincerely thank my friend and colleague Dr. Daniel Riviello for our fruitful and lasting collaboration, Mr. Research Dawadi for his help in the reviewing process. Special thanks to Adriana Scavello and Franco Mantione for their moral support and deepest concern, and last but not least, my family and everyone who supported me during these years.

Abstract

There is a great activity in the research community towards the investigations of the various aspects of 5G at different protocol layers and parts of the network. Among all, physical layer design plays a very important role to satisfy high demands in terms of data rates, latency, reliability and number of connected devices for 5G deployment. This thesis addresses the latest developments in the physical layer algorithms regarding the channel coding, signal detection, frame synchronization and multiple access technique in the light of 5G use cases. These developments are governed by the requirements of the different use case scenarios that are envisioned to be the driving force in 5G.

All chapters from chapter 2 to 5 are developed around the need of physical layer algorithms dedicated to 5G use cases. In brief, this thesis focuses on design, analysis, simulation and the advancement of physical layer aspects such as 1. Reliability based decoding of short length Linear Block Codes (LBCs) with very good properties in terms of minimum hamming distance for very small latency requiring applications. In this context, we enlarge the grid of possible candidates by considering, in particular, short length LBCs (especially extended BCH codes) with soft-decision decoding; 2. Efficient synchronization of preamble/postamble in a short bursty frame using modified Massey correlator; 3. Detection of Primary User activity using semi-blind spectrum sensing algorithms and analysis of such algorithms under practical imperfections; 4. Design of optimal spreading matrix for a Low Density Spreading (LDS) technique in the context of non-orthogonal multiple access. In such spreading matrix, small number of elements in a spreading sequences are non zero allowing each user to spread its data over small number of chips (tones), thus simplifying the decoding procedure using Message Passing Algorithm (MPA).

Publicationss

Some of the contents of this thesis have previously appeared or will appear in the following publications:

Book Chapter

1. [49] Pawan Dhakal, Shree K. Sharma, Symeon Chatzinotas, Björn Ottersten and Daniel Riviello, "Effect of Primary User Traffic on Largest Eigenvalue Based Spectrum Sensing Technique", in *Cognitive Radio Oriented Wireless Networks, 11th International Conference, CROWNCOM 2016, Grenoble, France, May 30 - June 1, 2016, Proceedings*, Springer International Publishing, pp. 67-78, 2016. ISBN: 978-3-319-40351-9, http://dx.doi.org/10.1007/978-3-319-40352-6_6.

Journal

1. [22] M. Baldi and M. Bertinelli and F. Chiaraluce and P. Dhakal and R. Garello and N. Maturo and E. Paolini, "A Study on State-of-the-Art Space Mission Telecommand Receivers", In *IEEE Aerospace and Electronic Systems Magazine*, 2017. In Press.

Conference Proceedings

1. [48] Pawan Dhakal, Roberto Garello, Shree Krishna Sharma, Symeon Chatzinotas and Bjorn Ottersten, "On the Error Performance Bound of Ordered Statis-

tics Decoding of Linear Block Codes", *IEEE Intl. Conf. on Commun*. 2016, Jun 2016, http://dx.doi.org/10.1109/ICC.2016.7510798.

2. [44] Pawan Dhakal, Daniel Riviello, "Multi-Antenna Energy Detector Under Unknown Primary User Traffic", *COCORA 2016, The Fourth Intl. Conf. on Advances in Cognitive Radio*, Feb. 2016. http://www.thinkmind.org/download.php?articleid=cocora_2016_1_40_80032.

3. [146] Daniel Riviello, Pawan Dhakal, Roberto Garello, "Performance Analysis of Multi-Antenna Hybrid Detectors and Optimization with Noise Variance Estimation", *International Conference on Advances in Cognitive Radio (COCORA)*, April 2015, http://www.thinkmind.org/download.php?articleid=cocora_2015_1_30_80029.

4. [147] Daniel Riviello, Pawan Dhakal, Roberto Garello, "On the Use of Eigenvectors in Multi-Antenna Spectrum Sensing with Noise Variance Estimation", 2^{nd} *Intel. Conf. in Signal Processing and Integrated Networks*, Feb. 2015, http://dx.doi.org/10.1109/SPIN.2015.7095339.

5. [45] Pawan Dhakal, Daniel Riviello, Roberto Garello, "SNR Wall Analysis of Multi-Sensor Energy Detection with Noise Variance Estimation", *11th IEEE Intl. Symp. on Wireless Commun. Systems (ISWCS)*, Aug. 2014, http://dx.doi.org/10.1109/ISWCS.2014.6933440.

6. [46] Pawan Dhakal, Roberto Garello, Federico Penna and Daniel Riviello, "Impact of Noise Estimation on Energy Detection and Eigenvalue Based Spectrum Sensing Algorithms", *IEEE Intl. Conf. on Commun. 2014*, Jun 2014, http://dx.doi.org/10.1109/ICC.2014.6883512.

7. [47] Pawan Dhakal, Daniel Riviello, Roberto Garello and Federico Penna, "Hybrid Approach Analysis of Energy Detection and Eigenvalue Based Spectrum Sensing Algorithms with Noise Power Estimation", *COCORA 2014, The Fourth Intl. Conf. on Advances in Cognitive Radio*, Feb. 2014, http://www.thinkmind.org/download.php?articleid=cocora_2014_1_40_80029.

Contents

List of Figures

List of Tables

Acronyms

Acronyms / Abbreviations

3*GPP* 3rd Generation Partnership Project

5*GNOW* 5th Generation Non-Orthogonal Waveforms for Asynchronous Signalling

AWGN Additive White Gaussian Noise

BCH Bose, Chaudhuri, and Hocquenghem

BER Bit Error Rate

BP Belief Propagation

BPSK Bipolar Shift Keying

CCSDS Consultative Committee for Space Data Systems

cdf Cumulative Distribution Function

CDMA Code Division Multiple Access

CDR Constant Detection Rate

CFAR Constant False Alarm Rate

CP Cyclic Prefix

CRSC Circular Recursive Systematic Constituent

DVB−RCS Digital Video Broadcasting - Return Channel via Satellite

DVB−T Digital Video Broadcasting - Terrestrial

DySPAN Dynamic Spectrum Access Networks

eBCH Extended BCH

EBD Eigenvalue Based Detection

ED Energy Detection

ENP Estimated Noise Power

EOF End of Frame

ERD Eigenvalue Ratio Detection

ESA European Space Agency

EU European Union

FBMC Filter Bank Multi-Carrier

FDMA Frequency Division Multiple Access

FFT Fast Fourier Transform

GF Galois Field

GFDM Generalized Frequency Division Multiple Access

GLRT Generalized Root Test

GSM Global System for Mobile Communications

ICT Information and Communication Technologies

IFFT Inverse Fast Fourier Transform

IID Independent and Identically Distributed

IMT − A International Mobile Telecommunication - advanced

IOT Internet of Things

ISM Industrial Scientific and Medical

ITU − R International Telecommunication Union - Radio Communication Sector

LBC Linear Block Codes

LDPC Low Density Parity Check Codes

LDPC − CC LDPC-Convolution Code

LDS Low Density Spreading

LRT Likelihood Ratio Test

LTE − A Long Term Evolution - Advanced

M2M Machine to Machine

MAI Multiple Access Interference

MAP Maximum a Posteriori

MAS Moving Average System

MDL Minimum Description Length

METIS Mobile and Wireless Communications Enablers for Twenty-twenty Information Society

MIMO Multiple Input Multiple Output

ML Maximum Likelihood

MLD Maximum Likelihood Decoding

mMTC Massive Machine Type Communication

MPA Message Passing Algorithm

MPEG Moving Picture Experts Group

MRI Most Reliable Independent

MSE Mean Square Error

MUD Multi-User Detection

NGMN Next Generation Mobile Networks

NOMA Non-Orthogonal Multiple Access

NP Neyman Pearson

NTA Nepal Telecom Authority

OFCOM Office of communications

OFDM Orthogonal Frequency Division Multiple Access

OoB Out of Band

OSA Opportunistic Spectrum Access

OSD Ordered Statistics Decoding

pdf Probability Density Function

pmf Probability Mass Function

RAT Radio Access Technology

RLRT Roy's Largest Root Test

RMT Random Matrix Theory

ROC Receiver Operating Characteristics

ROF Rank Order Filtering

RS Reed Solomon

RSMA Resource Spread Multiple Access

SC − LDPC Spatially Coupled LDPC

SCMA Sparse Code Multiple Access

SINR Signal to Interference Plus Noise Ratio

SNR Signal to Noise Ratio

SOF Start of Frame

SW Synchronization Word

TDMA Time division Multiple Access

TEP Test Error Pattern

TTI Transmission Time Interval

UE User Equipment

UFMC Universal Filtered Multi-Carrier

UHF Ultra High Frequency

UMP Uniformly Most Powerful

UMTS Universal Mobile Telecommunications System

VNI Visual Network Index

WiMaX Worldwide Interoperability for Microwave Access

WLAN Wireless Local Area Network

WPAN Wireless Personal Area Network

WRAN Wireless Regional Area Network

WRC World Radio Conference

WSN Wireless Sensor Network

xMBB Extreme Mobile Broadband

Chapter 1

Introduction

1.1 Motivation

Wireless communication networks are perhaps one of the most important element in the global Information and Communication Technologies (ICT) strategy, underpinning many other industries. It is one of the fastest growing and most dynamic sectors in the world. The phenomenal success of wireless mobile communications is mirrored by a rapid pace of technology innovation. From first generation (1G) analog FM cellular systems in 1981 to fourth generations (4G) Long Term Evolution - Advanced in 2011, the wireless mobile network has transformed from a pure telephony system to a network that can transport rich multimedia contents [27, 62]. Long Term Evolution (LTE) and its extension have now been deployed around the globe to deliver high quality, low latency video and multimedia applications for wireless devices. Table 1.1 illustrates the main features of the 3rd Generation Partnership Project (3GPP) standards now in the market, highlighting the trend towards widespread use of spectrum, higher bandwidth, higher spreading efficiency and lower latency.

In 4G systems, an advanced radio interface is used with orthogonal frequency-division multiplexing (OFDM), Multiple-Input Multiple-Output (MIMO), and link adaptation technologies. 4G wireless networks can support data rates of up to 1 Gb/s for low mobility, such as nomadic/local wireless access, and up to 100 Mb/s for high mobility, such as mobile access. However, it is widely agreed that similar to previous technologies, the current technologies also follow a similar technology maturity

Table 1.1 Features of 3GPP standards up to now

Properties	GSM	UMTS	HSPA	LTE
Band (MHz)	450, 800 900, 1800 1900	850, 900 1700, 1900 2100	850, 900 1700, 1900 2100	700, 800, 850, 900 1700, 1800, 1900, 2100 2500, 2600, 3500
Max. Band (MHz)	0.20	5	10	20
Peak Data Rate	9.6 Kbps	384 Kbps	42Mbps	326 Mbps
Round Trip Time	600 ms	75 ms	41 ms	20 ms

where only incremental improvements and small amounts of new spectrum can be expected; where a mere evolution of the status quo cannot achieve the extreme higher aggregate data rates and much lower latency required by next generation technology.

The development of wireless technologies has greatly improved people's ability to communicate and live in both business operations and social functions. Essential services such as e-banking, e-learning, and e-health will continue to proliferate and become more mobile. On-demand information and entertainment (e.g., in the form of augmented reality) will progressively be delivered over mobile and wireless communication systems. More and more people crave faster internet access on the move, trendier mobile phones, and, in general, instant communication with others or access to information. Every year, the demand in mobile broadband communications is increasing dramatically as more and more users subscribe to mobile broadband packages. In addition, smart phones, super-phones, tablets and laptops with powerful multimedia capabilities and applications are becoming increasingly popular and are creating new demands on mobile broadband. The possible evolution of Mobile Broad-band (MBB) from IMT-2000 and IMT-Advanced towards 2020 and beyond is as shown in Figure 1.1 [66], based on the assumption that the traffic requirements would be increased by a thousand times over the next decade.

New data services and applications, for example pervasive 3D multimedia, are making the experience of using mobile broadband better and more exciting. Furthermore, it is generally predicted that today's dominating scenarios of human-centric communication will, in the future, be complemented by a tremendous increase in the numbers of communicating machines. This so-called Internet of Things will make our everyday life more efficient, comfortable, and safe. These trends, shown in Figure 1.2, are expected to maintain their momentum over the next decade and will be complemented by the arrival of billions of machine devices and related machine-

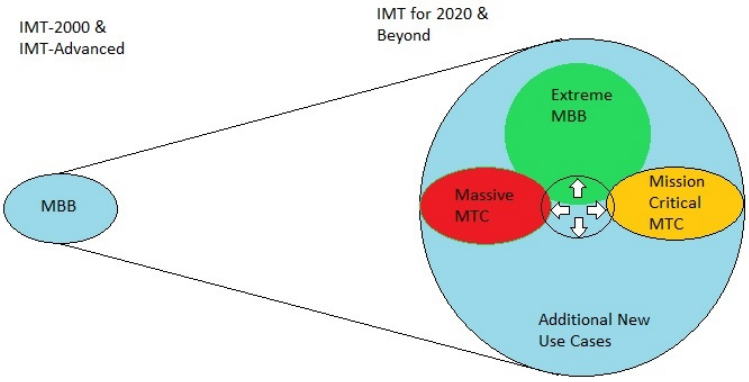

Fig. 1.1 Evolution of current MBB services towards beyond-2020. [66]

to-machine (M2M) applications [135]. These developments will lead to an avalanche of mobile and wireless traffic volume, predicted to increase a thousand-fold over the next decade [60].

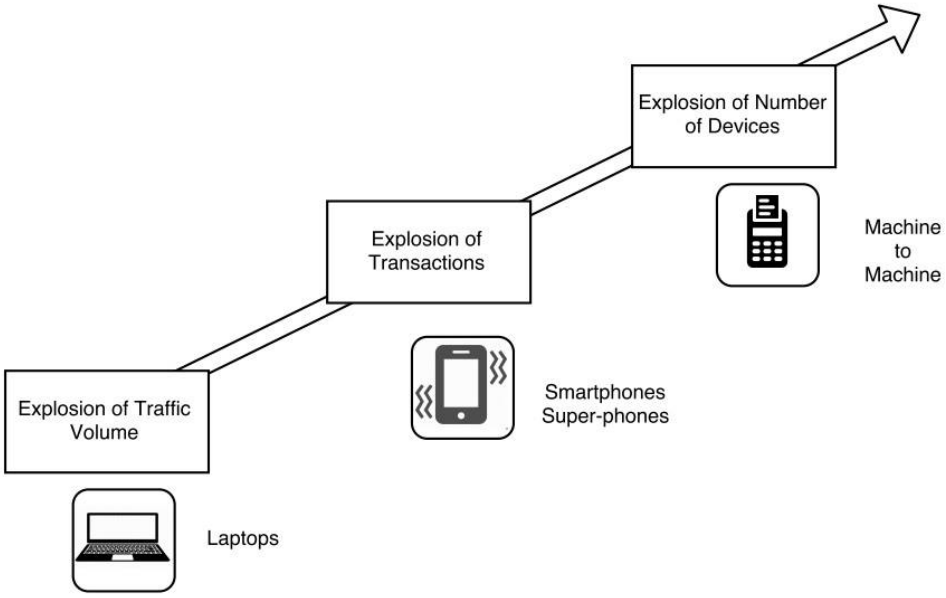

Fig. 1.2 Enhancement of key capabilities from LTE-Advanced to IMT-2020. [135]

Thanks largely to the annual visual network index (VNI) reports released by Cisco, we have quantitative evidence that the wireless data explosion is real and will continue. Driven largely by smartphones, tablets, and video streaming, the most recent (Feb. 2016) VNI report [39] shows, just in a decade, the amount of mobile

data has increased by well over a factor of 4000-fold and almost 400-million fold over the past 15 years. Mobile networks carried fewer than 10 gigabytes per month in 2000, and less than 1 petabyte per month in 2005. In 2015, it was 3.7 exabytes per month. Similarly, although 4G connections represented only 14 percent of mobile connections in 2015, they already account for 47% of the mobile data traffic and for the first time in 2015, 4G traffic exceeded 3G traffic. This deluge of data has been driven chiefly by video thus far, but new unforeseen applications can reasonably be expected to materialize by 2020. In addition to the sheer volume of data, the number of devices and the data rates will continue to grow exponentially. Smart-phones accounted for most of that growth. Global mobile devices and connections in 2015 grew to 7.9 billion, up from 7.3 billion in 2014.

Further, machine-type applications are becoming important in addition to the human centric communications that have been dominating the cellular scene so far. In fact, the number of communicating machine was some point forecasted to be trending towards the number 50 billion by 2020. The expected uptake of machine-type and human-type wireless communications in many economic sectors and vertical industries will lead to a large and wide diversity of communication characteristics imposing different requirements on mobile and wireless communication systems, e.g., in terms of cost, complexity, energy dissipation, data rate, mobility, latency, and reliability. On the other hand, 4G networks have just about reached the theoretical limit on the data rate with current technologies and therefore are not sufficient to accommodate the above challenges.

All the above issues are putting more pressure on cellular service providers, who are facing continuously increasing demand for higher data rates, larger network capacity, higher spectral efficiency, higher energy efficiency, and higher mobility required by new wireless applications. In this sense, we need ground breaking wireless technologies to solve the above problems caused by trillions of wireless devices.

Foreseeing all these future requirements to meet, the International Mobile Telecommunication (IMT) - 2020 was established in 2013, which is dedicated to investigate beyond 4G (B4G) or 5G wireless techniques. The aim is to connect the entire world, and achieve seamless and ubiquitous communications between anybody (people to people), anything (people to machine, machine to machine), wherever they are (anywhere), whenever they need (anytime), by whatever electronic

devices/services/networks they wish (anyhow). This means that 5G networks should also be able to support communications for some special scenarios not supported by 4G networks (e.g., for high-speed train users). 5G is considered to be the enabler of fully connected network society. It is enabler of the world where there is unlimited access to information and sharing of data any-time and anywhere to anyone and anything. So it is not only about mobile broadband and mobile telephony, it is about connectivity for any kind of application. It is not only for any kind of devices and connectivity for people. It is about connectivity for any kind of devices and connectivity should be available truly at any time and anywhere [177].

Amount of traffic carried by communication systems will increase tremendously. In the future, we may see 1000 times more traffic than we see today. And we have to ensure that wireless communication systems can really handle such enormous traffic. In addition to this, number of devices will also increase tremendously. In the future, we will probably see 100's of billions of devices which will be very different from small phones and tablets that we see today. Finally, our wireless communication system have to handle a very large range of requirements for the future [59]. It will not only be about high data rates; some applications may require small latency, some applications may require ultra high reliability of the system, some applications may require extremely low device cost and extremely low device energy consumption.

5G is the overall wireless access solution of the future and that will of-course include revolution of currently existing Radio Access Technologies (RAT) including LTE-A, WiFi, WiMax etc. But it will also include new complementary RAT that will address use cases and scenarios that cannot be properly handled by current RAT. And all these together, existing RAT in combination with complementary new technologies that we refer to as 5G [59].

Let us look at the future wireless communication scenario. In the future, the cellular technologies such as LTE, LTE-A will continue to be very important and will provide mobile telephony and mobile broadband with wide area coverage. But they will be extended by lots of new applications and lots of new use cases and new scenarios. Some of which can be revolution of existing technologies but some of which will need new technologies. Let us take a few examples: To provide extreme data rates or extreme traffic capacities, for instance in indoor office environments of in outdoor hot spot scenarios, ultra dense deployment may be needed.

Machine type communications, will be more and more important in the future. This will include communications for electronics and home appliances, communications for transports, communications for medical equipments and many more. A lot of dense communications will probably be carried out by our currently existing wireless access technologies but some of these use cases will have so high requirements that they will require new wireless access technologies.

Ultra reliable communications may be needed, for example, for critical infrastructure, or for industrial processes. And once again this may very well require new radio access technologies. Car-to-car or car-to roadside communication will be introduced for traffic safety and traffic control. There may be completely new ways to communicate for example, communicating directly between devices. It is all those together, the revolution of currently existing RAT and new complementary RAT that is referred to as 5G.

The following spider diagram shown in Figure 1.3 is the best way to illustrate a wide range and expansion of the 5G requirements in comparison to prior cellular generations such as LTE-Advanced. Some of these applications can be supported by today's mobile broadband networks and their future evolution. However, some other applications will impose additional and very diverse requirements on mobile and wireless communication systems that the next generation (Fifth Generation 5G) will have to support:

- Far more stringent latency and reliability requirements are expected to be necessary to support applications related to healthcare, security, logistics, automotive applications, and mission-critical control.
- A wide range of data rates has to be supported, up to multiple gigabits per second, and tens of megabits per second need to be guaranteed with very high availability and reliability.
- Network scalability and flexibility are required to support a large number of devices with very low complexity and requirements for very long battery lifetimes.

5G research has been quite active in the past years. Thus, several funded projects and standardization bodies like Mobile and Wireless Communications Enablers for Twenty-twenty Information Society -II (METIS - II) [1], 5th Generation Non-Orthogonal Waveforms for Asynchronous Signalling (5GNOW) [4], 4G Americas

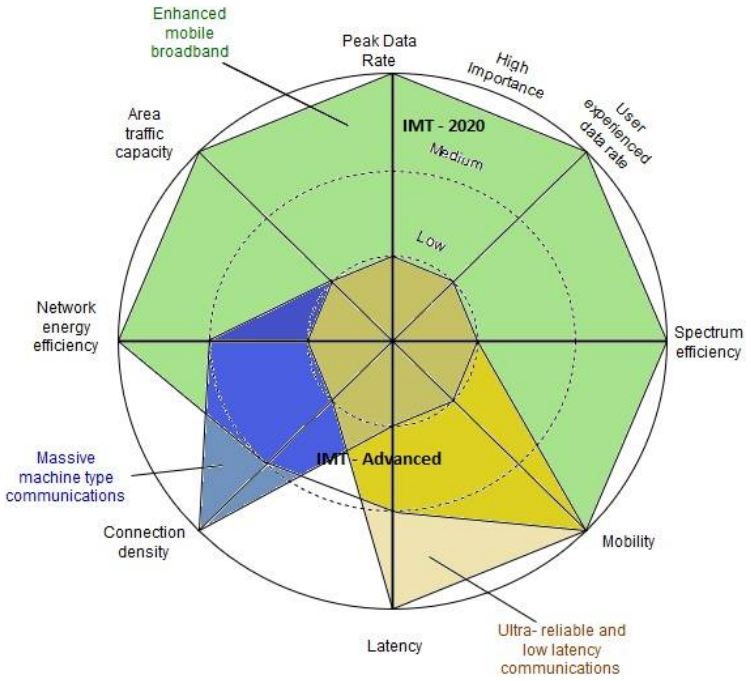

Fig. 1.3 Enhancement of key capabilities from LTE-Advanced to IMT-2020. [111]

[15], Next Generation Mobile Networks (NGMN), 3GPP, International Telecommunication Union - Radio Communication Sector (ITU-R) [111] have attempted to create pioneering scenarios for identifying the requirements of 5G. This process resulted in a large number of scenarios and use cases focusing on diverse requirements. Given the large number of use cases, it would be unrealistic to consider all the use cases proposed by the research community and the standardization bodies and fora for evaluation of the 5G RAN design solutions. Thus, the most representative scenarios are noted below.

1. Mobile broadband and media everywhere and anytime: Mobile broadband is the key use case today and it is expected to continue to be one of the key use cases driving the requirements for 5G. It goes far beyond basic mobile Internet access and covers rich interactive work, media and entertainment applications in the cloud or reality augmentations (both centralized and distributed).

   Data will be one of the key drivers for 5G and in new parts of this system. We may for the first time see no dedicated voice service - in 5G, voice is expected to be handled as an application, simply using the data connectivity provided by the communication system. The main drivers for the increased traffic volume

are the increase in size of content and the number of applications requiring high data rates. Factors include increase in camera resolution, the rise in screen resolution with the recent introduction of 4K (8K is already expected beyond 2020). Streaming services (audio & video), interactive video and mobile Internet connectivity will continue to be used more broadly as more devices connect to the Internet. Many of these applications require always-on connectivity to push real time information and notifications to the users.

Cloud storage and applications are rapidly increasing for mobile communication platforms. This is applicable for both work and entertainment. Cloud storage is one particular use case driving the growth of uplink data rates. In the past, content was mostly downloaded. 5G will also be used for remote work in the cloud which, when done with tactile interfaces, requires much lower end-to-end latencies in order to maintain a good user experience. Entertainment, for example cloud gaming and video streaming, is another key driver for the increasing need for mobile broadband capacity.

With 5G, users will experience broadband access in crowded areas like concerts, sporting events and festivals, alleviating issues with capacity, interference and reliability. 5G customers will also enjoy 4K movies downloaded in just seconds without a WiFi connection. While live TV broadcasts and sporting events will become immersive viewing experiences, as if you were at the event in real-life. For customers, 5G will also maximize their experience in both indoor and outdoor connectivity and offer high QoS broadband even in challenging network conditions.

2. Smart vehicles, transport and infrastructure: The automotive sector is expected to be a very important driver for 5G, with many use cases for mobile communications for vehicles. For example, entertainment for passengers requires simultaneous high capacity and high mobility mobile broadband, because future users will expect to continue their good quality connection independent of their location and speed. Entertainment will be very essential on smart phones and tablets everywhere, including high mobility environments such as trains, cars and air-planes. The key application areas could be for smart infrastructures, connected bus-stops, connected trucks and connected cars. Thus, these applications will be more focused on massive machine type com-

munication. We can consider sensors embedded in roads, railways and airfields to communicate with each other and/or with smart vehicles.

Other use cases for the automotive sector are augmented reality dashboards. These display overlay information on top of what a driver is seeing through the front window, identifying objects in the dark and telling the driver about the distances and movements of the objects.

The previous two use cases are related to content provisioning for the car users, but the cars themselves will also be connected. Many car manufacturers are already adding driver assistance systems based on 3D imaging and built-in sensors. In the future, wireless modules will enable communication between vehicles themselves, information exchange between vehicles and supporting infrastructure and between vehicles and other connected devices, for example, those carried by pedestrians. Additionally, use cases for traffic safety are now widely discussed. These include cars detecting safety critical situations, such as black ice, accidents within reach of the car and other hazardous road conditions. Safety systems will also guide drivers on alternative courses of action to allow them to drive more safely and lower the risks of accidents.

The next phase will be remotely controlled or even self-driven vehicles, which will require ultra reliable and very fast communication between different self-driving cars and between cars and infrastructure. In a plausible future, a self-driving car takes care of all driving activity, allowing the driver to rest and concentrate only on traffic anomalies that the car itself cannot identify. Ideally, reading the morning newspaper while commuting will become possible. The technical requirements for self-driving cars call for ultra-low latencies and ultra-high reliability, increasing traffic safety to levels humans cannot achieve.

3. Human interaction - Internet of Things (IOT): 5G means unlocking the potential for us to interact and connect with machines in unbelievable ways making the networked society and the IOT era a reality by connecting more devices than ever. 5G will become the backbone of IOT, connecting devices in ways we never thought possible. Users will experience smart cars that are capable of communicating with traffic lights, augmented reality and 360 degree immersive gaming and movies, and transmitting touch and texture to realize the tactile internet. The IOT applications that 5G will help enable is truly limitless.

4. Critical control of remote devices: The high reliability and low latency of 5G unlocks the ability to control critical services and infrastructure. This creates new opportunities for public safety, government, city management and utility companies. 5G will be a key enabler of the future digital world. It will bring about new service capabilities for industrial stakeholders thanks to the unprecedented on-demand performance and real-time reactivity. For example, energy and water utilities will be capable of connecting to millions of networked devices, taking real-time, intelligent and autonomous decisions. 5G introduces the ability to remotely control devices and heavy machinery, thus unlocking the potential for improved medical services and surgeries that are otherwise unavailable to rural communities. 5G would also allow for heavy machinery to be controlled from a distance, making hazardous situations safer for humans.

   Wireless and mobile communications are becoming increasingly important for industrial application. Wires are expensive to install and maintain and the possibility of replacing cables with reconfigurable wireless links is a tempting opportunity for many industries. However, achieving this requires that the wireless connection works with a similar delay, reliability and capacity as cables and that its management is simplified. Low delays and very low error probabilities are new requirements that need to be addressed with 5G.

   The health sector has many applications that can benefit from mobile communications. Communications systems enable tele-medicine, which provides clinical health care at a distance. It helps eliminate distance barriers and can improve access to medical services that would often not be consistently available in distant rural communities. It is also used to save lives in critical care and emergency situations.

The vision of the 5G system, key design principles and use cases lead to requirements that the future mobile broadband system will need to meet. Considering all these aspects, the work presented in this thesis addresses in particular the physical layer problems for the use cases defined above. A more detailed description of these problems and their contexts of application is provided next.

1.2 Structure and Contribution of This Thesis

The thesis is organized as follows: all chapters from Chapter 2 to 5 are developed around the need of physical layer algorithms dedicated to above described 5G use cases. In particular:

- Chapter 2 considers the aspect of channel coding algorithms for the ultra-low latency use cases of 5G. In order to achieve low latency for critical control of remote devices use case of 5G system, channel coding and modulation plays an important role in the 5G physical layer. In this work, we enlarge the grid of possible candidates by considering, in particular, short length LBCs (especially eBCH codes) with soft-decision decoding. Specifically, results include:

  1. Statistical analysis of the ordered vector components which highlights and makes evidence to Ordered Statistics Decoding (OSD) property.
  2. Use of novel statistics to derive a further simplified error performance bound.
  3. Analytical study of simplified expressions for the Probability Density Function (pdf) and Cumulative Distribution Function (cdf) of the novel statistic.

- Chapter 3 investigates the aspect of frame synchronization which is very important in achieving the ultra-low latency and ultra reliable communication for smart vehicles, transport and infrastructure and human interaction - IOT use cases of 5G where a M2M communication plays a very important role. Major findings in this chapter include:

  1. Analysis of false-alarm and miss-detection probabilities for both the Massey detector (introduced by Massey in [122]) and the Extended Massey detector.
  2. Introduction of a new test to eliminate a lower bound limitation on the P_{fa} for short pattern lengths.

- Chapter 4 investigate semi-blind detection methods, especially, Energy Detection (ED) and Roy's Largest Root Test (RLRT). Original contributions are performance analysis under practical imperfections of the aforementioned detectors. Specifically, results include:

1. Analysis of false-alarm probability of Hybrid ED and Hybrid RLRT.
2. Performance analysis (detection probability) of the Hybrid ED and Hybrid RLRT.
3. Performance analysis (detection probability) of ED and RLRT under unknown primary user traffic.
4. Comparison of ED and RLRT performance, and quantification of the impact of noise level knowledge.
5. Comparison of ED and RLRT performance, and quantification of the impact of primary user traffic knowledge.

- Chapter 5 investigate a signature matrix for LDS multiplexing. The small number of elements in a spreading sequences are non zero allowing each user to spread its data over small number of chips (tones), thus simplifying the decoding procedure using Message Passing Algorithm (MPA). Major contributions include:

  1. Analysis of upper bound on the normalized minimum euclidean distance of output codewords of a LDS spreading system.
  2. Design of generic spreading matrices for 150% overloading factor which meets the upper bound on the normalized minimum euclidean distance.

Finally, Chapter 6 contains summarizing conclusions and remarks.

Chapter 2

Ordered Statistics Decoding of Linear Block Codes[1]

2.1 Introduction

Current generation of wireless technologies is being evolved toward a fifth generation (5G) for better serving end users and transforming our society [42, 63, 67]. A detailed discussion of the new use cases for 5G wireless communication standards can be found in Chapter 1. Demands for greater capacity and higher data rates are just two of the many factors influencing the evolution of wireless access technologies. The impact of other aspects like energy consumption, device cost, spectrum and latency will be fundamental to the success of future networks. The next evolution of wireless communications is to provide large variety of services with significantly different requirements. For example, in the European Union project Mobile and wireless communications Enablers for the METIS [1], three main service types that are considered for 5G, namely extreme mobile broadband (xMBB), massive Machine-Type Communications (mMTC) and ultra-reliable MTC (uMTC) as well as the five specific use cases for the 5G RAN design which typically represent a mixture of services. It further describes the key requirements on the 5G RAN architecture that have been identified and derived from the diverse service and use case needs, and explicitly elaborates on the requirements posed by the notion of Network Slicing in 5G. Thus, 5G should not be seen as a single solution but rather as a platform on

[1] Part of the work described in this chapter has been previously published in [48].

which multiple different services can be built on using the solutions selected from the 5G toolbox.

M2M communication will make up a large part of the new types of services and use cases that 5G systems will address. From a communication technology perspective, M2M can be divided into two main categories: mMTC is about connectivity for large numbers of low-cost and low-energy devices in the context of the Internet of things; mission-critical MTC is envisioned to enable real-time control and automation of dynamic processes in various fields, such as industrial process automation and manufacturing, energy distribution, intelligent transport systems, traffic safety, infrastructure protection, remote surgery and requires communication with very high reliability and availability, as well as very low end-to-end latency going down to millisecond level. In short, the requirements of mission-critical MTC have to be fulfilled in three dimensions: latency, reliability and availability.

a. Latency refers to the time delay between data being generated – e.g., at a sensor – and the same data being correctly received – e.g., by the actuator. The most stringent requirement on the end-to-end latency may be 1 ms, as explained for example in ITU - Telecommunication Standards Sector (ITU-T) Technology Watch Report on the Tactile Internet [5].

b. Reliability refers to the capability of guaranteeing successful message transmissions within a defined latency budget – or delay. The reliability requirements vary among different mission-critical MTC services, but may go down to one per billion messages as shown in an ETSI TR 101 557 V1.1.1 (2012-02)[2]. As an example, in industrial automation, only one message in one billion data transfers may be lost or delayed within the given latency budget.

c. System availability has to ensure that critical applications are not in outage when they are needed. To equate availability of wireless and wired solutions, an availability of 99.999% can be sought.

Mission-critical MTC, however, is still in the early-development phase, and there are a lot of challenging research problems to solve. Emerging use cases in context to mission-critical MTC along with the anticipated killer apps of the Tactile Internet, like immersive virtual reality, augmented reality and tele-surgery, to name a few, present a need for ultra-low latency mobile networks [72]. Although the current

minimum data plane latency in 4G LTE which is in the order of 20 ms is sufficient for most of the mobile broadband applications, it may however, not be enough for mission critical MTC applications. To ensure support for this kind of mission-critical machine-type connectivity, next-generation wireless access should support latency around 1 ms.

Latency can be interpreted in terms of efficiency of very low-layer procedures allowing for time/frequency synchronization, identification/authentication (Start of/End of frame (SOF/EOF) detection), channel setup time, channel interleaving, channel coding etc. Thus, to enable an end-to-end latency of 1 ms or less, the entire system needs to be designed for low latency. All in all, if we want to address all the potential use cases of mission-critical MTC, the radio technology that we design should also be scalable for these stringent requirements. To achieve the lower delays and higher reliability discussed above, we can identify a number of system modification, for instance, reduced transmission time intervals, e.g., down to $100\mu s$, and short symbol duration enabling fast and efficient data transmission. In addition, redesigning of physical channels allowing early channel estimation, fast detection of SOF/EOF and use of fast encoding-decoding channel codes also help in minimizing the transmission/detection time. In this chapter, we consider the aspect of channel coding algorithms for the ultra-low latency use cases of 5G while in Chapter 3, we will consider the case of frame synchronization for the low latency aspect of 5G use cases.

2.2 Channel Coding for 5G

In terms of error correction coding techniques, a quantum leap from 2G to 3G was achieved of Turbo Codes [25]. However, error correction coding schemes in 3G and 4G are almost same. Another big jump from 4G to 5G is expected because of the several new challenges in 5G.

In order to achieve low latency in 5G system, channel coding and modulation plays an important role in the 5G physical layer. In general, the channel decoder must share the latency budget with many other physical layer components such as synchronization. Owing to this, the channel decoder should target the lowest possible processing latency. Furthermore, since the channel decoder must overcome the uncertainty introduced by noise interference and poor signal strength, it typically

Table 2.1 Turbo codes and duo-binary turbo codes in standards.

Standards	Types of Turbo Codes	Code Rates	Termination
3G (UMTS and CDMA 2000)	Turbo codes	$1/2, 1/3$ and 1/4	Tail Bits
4G (WiMAX)	Duo-binary Turbo code	$1/2 \sim 7/8$	Circular
4G LTE	Turbo Code	$1/2 \sim 7/8$	Tail Bits
DVB-RCS	Duo-binary Turbo code	$1/3 \sim 6/7$	Circular
CCSDS	Turbo codes	1/2, 1/3, 1/4 and 1/6	Tail bits

has a much greater complexity than channel encoder. This is the reason why the channel decoder is typically the main concern when designing a channel code. More specifically, the decoding complexity plays a dominant role in defining decoding delays. Among the most attractive options emerged till now, some of the potential options are discussed hereby.

A. Turbo Codes and Duo-binary Turbo Codes

Turbo codes [25] achieved very low error probability which is close to the Shannon limit. The important design criteria of turbo codes are to find suitable component codes which maximize the effective free distance and to optimize the weight distribution of the codewords at a low EbN0 [53, 52]. One disadvantage of the original turbo codes is that error floor occurs at quite high Bit Error Rate (BER) 10^{-5} due to poor minimum Hamming distance. Possible solutions are to (a) design a good interleaver, (b) increase the number of memories of the consecutive encoder and (c) use the non-binary turbo codes such as duo binary turbo codes[55] or 3D turbo codes. Duo-binary turbo codes are composed of two Circular Recursive Systematic Constituent (CRSC) codes with two inputs. Its information bits are encoded pair wise. CRSC encoders do not need any tail bits.

B. LDPC and Non-binary LDPC

LDPC codes [80], combined with iterative Belief Propagation (BP) decoding, have emerged after 1993 as the most promising method of achieving the goal

set by Shannon [153] in his landmark 1948 paper: to communicate reliably over a noisy transmission channel at a rate approaching channel capacity. Indeed, many applications have recently adopted LDPC codes as industry standards, such as Wireless Local Area Networks (WLANs) (IEEE 802.11n), WiMAX (IEEE 802.16e), Digital Video Broadcasting (DVB) - S2, 10GBase-T Ethernet (IEEE 802.3an), and the ITU-T standard for networking over power lines, phone lines, and coaxial cable (G.hn/G.9960). The key feature that sets LDPC codes apart from other capacity approaching codes is that with suboptimal iterative BP decoding, complexity grows only linearly with code block length, resulting in practically realizable decoder implementations for powerful (long block length) codes. (The decoding complexity of optimum Maximum Likelihood (ML) decoding, on the other hand, grows exponentially with block length, making it impractical for large block lengths.) LDPC block code (LDPC-BC) designs can be classified in two types: regular and irregular. Regular codes, as originally proposed by Gallager [80] in 1962, are asymptotically good in the sense that their minimum distance grows linearly with block length. This guarantees, with ML decoding, that the codes do not suffer from the error floor phenomenon, a flattening of the BER curve that results in poor performance at high signal-to-noise ratios (SNRs), and similar behavior is observed with iterative BP decoding as well.

Non-binary LDPC codes using iterative BP show us good performance at medium code lengths $(500 \leq N \leq 3000)$ and high order modulation communications (greater than 16QAM). However, the decoding complexity remains a major obstacle for their commercial applications.

C. Spatially coupled LDPC (SC-LDPC) codes

SC-LDPC codes have robustly excellent performance over a broad range of channel conditions, including both the waterfall and error floor regions of the BER curve. SC-LDPC codes can be viewed as a type of LDPC convolutional code (LDPC-CC), since spatial coupling is equivalent to introducing memory into the encoding process. In channel coding parlance, the key feature of SC-LDPC codes that distinguishes them from standard LDPC codes is their ability to combine the best features of regular and irregular codes in a single design. An added feature of the SC-LDPC code design is that the resulting Tanner graph retains the essential implementation advantages associated with

the structure of regular codes compared to typical irregular designs. The research establishing the performance characteristics of SC-LDPC codes relies on ensemble average asymptotic methods, that is, the capacity approaching thresholds and asymptotically good minimum distance behavior are shown to hold for typical members of SC-LDPC code ensembles as the block length tends to infinity [61].

D. Other Candidate Channel Codes

Other candidate channel codes are Sparse Regression Codes and Polar Codes. Sparse Regression Codes [24] are new class of codes for Gaussian multi-terminal source They are designed using the statistical framework of high-dimensional linear regression. They are rate-optimal codes with low complexity for compression and transmission. They are suitable for cooperative communications. Polar codes [17] are first constructive coding to provably achieve channel capacity using Kronecker product. Its characteristic can be summarized as follows: (1) the block length of a polar code is normally a power of two but the code length can be adjusted by usual code shortening methods, (2) the rate of a polar code can be adjusted to any number between 0 and 1 in increments of 1/N, (3) polar codes are available in systematic form, (4) polar codes have a recursive structure which makes them suitable for low-complexity implementations and (5) polar codes have no error floor.

While turbo and LDPC codes have brought capacity-approaching performance within reach of implementable systems, implementable does not necessarily mean practical. The complexity of codes that perform well under practical constraints such as limited decoding delay and high spectral efficiency is still a major hurdle for low power implementations in integrated circuits. Furthermore, when codes are short as required by small latency, minimum distance is more important. Turbo codes and LDPC codes are known to have small minimum distance for short length codes. Instead, algebraic designed block codes (e.g., BCH code [28] and Reed-Solomon (RS) codes [145]) are known to have higher minimum distance for short length codes when compared to LDPC and Turbo codes. In this work, we enlarge the grid of possible candidates by considering, in particular, properly designed short length LBCs (especially eBCH codes) with soft-decision decoding.

2.3 Ordered Statistics Decoding

Low complexity decoding of LBCs has long been investigated by many coding theorists: a detailed bibliography of the contributions in this area can be found in [155]. Some examples of decoding algorithms are 1) Exhaustive Decoding: Possible only for very short length codes, 2) Algebraic Decoding: Exploiting the property of algebraic designed block codes, 3) Viterbi decoding [41, 173]: Although all the LBCs possess the trellis structure which is the backbone of Viterbi decoding, the number of states $(\min\{2^k, 2^{n-k}\})$ becomes too large to practically implement for long length codes and 4) Iterative decoding: Iterative decoding of powerful classical codes such as BCH, and RS codes are quite sub-optimal with respect to ideal Maximum-Likelihood Decoding (MLD), due to their structures. As a consequence, sub-optimal (near optimal) soft decision decoding based on the ordered statistic of the received noisy codeword has been proposed [54, 99, 32, 76, 81] proving to be efficient with considerable complexity for short length LBCs.

Since Fossorier and Lin, in their original contribution [76] presented a novel OSD scheme for soft decision decoding of LBCs based on ordered statistics of the received noisy samples (although an algorithm belonging to this set was first proposed by Dorsch [54] and also used by [99] and [32]), OSD is widely being studied in the literature [76, 81, 79, 77, 14]. Over the years, various new methods [175, 75, 165, 106, 176, 97, 101] based on reliability information and many modifications [77, 14] on original OSD have been proposed in the literature to minimize the performance-complexity trade-offs. In addition to wide spread application of ordered Statistic in decoding of LBCs, the contributions in [74, 172, 168, 185] show its use also in decoding of LDPC and convolution codes. In all these optimum and sub-optimum decoding algorithms, a reliability measure of the received symbols has been used to reduce the search space and find the most likely codewords.

The original concept of OSD [76] is basically implemented in two stages, a) determining the Most Reliable Independent (MRI) bits from the Most Reliable Basis (MRB) of the code and b) Order$-I$ reprocessing on MRI using most likely Test Error Patterns (TEPs). Out of these two stages, order$-I$ reprocessing is designed to improve the hard decision decoded codeword progressively until either practically optimum or a desired error performance is achieved. The approach of ML resource test based on the cost function calculated from the soft valued samples of the permuted received sequence is introduced as a stopping criterion after each stage

$j, 0 \leq j \leq I$ of order$-I$ reprocessing. This stopping criterion indeed proved excellent in reducing the average number of computations. An upper bound on the error performance for order$-I$ reprocessing OSD has been derived based on the noise statistics after reordering in [76, 78].

However, there are two major drawbacks of the performance bound derived in [76]. The first drawback is its complexity of evaluation (requiring $(I+1)$ dimensional integral for any order$-I$ reprocessing). The second is the tightness of the bound, since this bound has been derived based on the assumption that the events associated with the reordered vector components are statistically independent, although, this does not hold true in practical scenarios. These issues related to computationally complex error performance bound has been revisited in [79], where a computationally simpler and comparatively tighter upper-bound on the error performance has been derived based on the statistical approach proposed by Agrawal & Vardy in [9]. It has been shown that, compared to $(I+1)$ dimensional integral computation in [76], the expression derived in [79] requires only a $2-$dimensional integral for any order$-I$ reprocessing. Although, the reduction of integral dimension from $(I+1)$ to 2 seems quite impressive, computing $2-$dimensional integral $(n-k-1)$ times as referred to [79] is still computationally complex.

In this chapter, we propose a novel statistic of the ordered vector components which highlights and makes evidence to OSD property. Furthermore, the proposed statics can be applied to derive a further simplified error performance bound. More importantly, simplified expressions for the pdf and cdf of the proposed statistic are derived. Subsequently, we incorporate the properties of this statistic to derive the simplified error performance bound for OSD with order$-I$ reprocessing. The computational complexity of the corresponding bound is found to be even simpler (requiring single dimensional integral evaluation) to that of the bounds derived in [76] and [79]. Furthermore, the error performance bound derived in this work is as tight as the one proposed in [79] and is also derived without any assumption.

2.4 Overview of OSD and Conventional Reprocessing

Given an LBC $C(n,k)$, with a systematic generator matrix $\mathbf{G}$, at the transmitter side, a $k-$bit information vector, $\overline{\mathbf{v}} = (v_1, v_2, \ldots, v_k),\ v_i \in GF(2) = \{0,1\}$ is mapped into a codeword $\overline{\mathbf{c}} = \overline{\mathbf{v}} \cdot \mathbf{G} = (c_1, c_2, \ldots, c_n)$ where GF(2) stands for Galois field of order-2.

Under Binary Phase Shift Keying (BPSK), the codeword is mapped into a real-valued vector as

$$\overline{\mathbf{s}} = (s_1, s_2, \ldots, s_n) \qquad s_i \in \{-1, +1\} \subseteq \mathscr{R}, \tag{2.1}$$

where $c_i = 0 \rightarrow s_i = -1$ and $c_i = 1 \rightarrow s_i = +1$.

The vector $\overline{\mathbf{s}}$ is transmitted over an Additive White Gaussian Noise (AWGN) channel. At the receiver side, we observe the received vector,

$$\overline{\mathbf{r}} = (r_1, r_2, \ldots, r_n) \qquad r_i \in \mathscr{R}, \tag{2.2}$$

where $r_i = s_i + w_i$, w_i is a white Gaussian noise sample with mean zero and variance σ^2.

Given $\overline{\mathbf{r}}$, we want to perform a soft-decision decoding. As already stated in section 2.3, for small-medium block codes (with k upto some hundreds of bits), an effective solution is provided by OSD algorithms, like the Most Reliable Basis (MRB) algorithm [76]. This algorithm starts by reordering the received vector in the descending order of the absolute values. In this way, the first symbols are characterized with a high reliability, i.e., a large probability of being correct.

Given $\overline{\mathbf{r}}$, by reordering its components in decreasing magnitude $\lambda_i = |r_i|$, we obtain a vector,

$$\overline{\mathbf{r}}^* = (r_1^*, r_2^*, \ldots, r_n^*) \qquad r_i^* \in \mathscr{R}, \tag{2.3}$$

such that $|r_i^*| > |r_{i+1}^*|$ for $1 \leq i \leq n$. Let us define ρ_1 as the permutation rule applied on $\overline{\mathbf{r}}$ to obtain $\overline{\mathbf{r}}^*$.

The generator matrix $\mathbf{G}$ is also permuted using the same permutation rule ρ_1, to give a new permuted generating matrix

$$\mathbf{G}^* = \rho_1(\mathbf{G}). \tag{2.4}$$

The matrix $\mathbf{G}^*$ in (2.4) is then processed using elementary row operations to obtain a systematic form $\mathbf{G}'$. As well known in the OSD literature [76, 79], it may happen that the first k columns of $\mathbf{G}^*$ may not be linearly independent, i.e., the k most reliable components do not correspond to an information set. In this case, it is necessary to slightly change the permutation ρ_1 until an information set is obtained. This introduces a second permutation defined as ρ_2 which needs to be applied both on $\overline{\mathbf{r}}^*$ and $\mathbf{G}^*$ to obtain $\overline{\mathbf{r}}'$ and $\mathbf{G}'$ respectively. Thus, the final permutation relations can be written as,

$$\overline{\mathbf{r}}' = \rho_2(\overline{\mathbf{r}}^*) \Leftrightarrow \rho_2(\rho_1(\overline{\mathbf{r}})), \mathbf{G}' = \rho_2(\mathbf{G}^*) \Leftrightarrow \rho_2(\rho_1(\mathbf{G})). \tag{2.5}$$

In the following, we consider ρ_2 as an identity permutation function such that $\rho_2(\overline{\mathbf{x}}) = \overline{\mathbf{x}}$ where $\bar{x}$ is a arbitrary vector. Thus, we suppose $\overline{\mathbf{r}}'$ has exact reliability ordering. We perform a symbol-by-symbol hard decision on $\overline{\mathbf{r}}'$ to obtain the binary vector,

$$\overline{\mathbf{y}}' = (y'_1, \ldots, y'_i, \ldots, y'_n) \qquad y'_i \in GF(2), \tag{2.6}$$

where $r'_i < 0 \rightarrow y'_i = 0$ and $r'_i \geq 0 \rightarrow y'_i = 1$.

Next, we take the first k bits of $\overline{\mathbf{y}}'$ to form the candidate information vector,

$$\overline{\mathbf{v}}' = (v'_1, \ldots, v'_i, \ldots, v'_k) \qquad v'_i \in GF(2). \tag{2.7}$$

Due to reordering, with high probability, $\overline{\mathbf{v}}'$ contains a few errors because its bits have high reliability. One of the objectives of this paper is to provide computationally efficient expression for calculating the number of errors contained in $\overline{\mathbf{v}}'$.

Exploiting the reliability property, OSD algorithm considers a set of patterns,

$$S = \{\overline{\mathbf{p}} = (p_1, \ldots, p_i, \ldots, p_k) \qquad p_i \in GF(2)\}, \tag{2.8}$$

with Hamming weight of the TEP $w_H(\overline{\mathbf{p}})$, $0 \leq w_H(\overline{\mathbf{p}}) \leq I$, where I is called the order of the algorithm. Each pattern is added to the candidate information vector given

by (2.7), which is then encoded by the matrix $\mathbf{G}'$ to obtain a reprocessing codeword $\overline{\mathbf{c}}^*$ in the following way,

$$\forall \overline{\mathbf{p}} \in S : \overline{\mathbf{v}}' \rightarrow \overline{\mathbf{v}}^* = \overline{\mathbf{v}}' + \overline{\mathbf{p}} \rightarrow \overline{\mathbf{c}}^* = \overline{\mathbf{v}}^* \cdot \mathbf{G}'. \tag{2.9}$$

When all patterns are considered, the codeword $\overline{\mathbf{c}}^*$ in (2.9) at minimum Euclidean distance from the permuted received vector $\overline{\mathbf{r}}'$ can be chosen as the received codeword. Obviously, if we set $I = K$ and we test all the corresponding 2^k patterns, we can surely find the ML codeword, but the algorithm becomes equivalent to an exhaustive decoding, which is impossible for non-trivial codes [76]. Then, a key issue for these algorithms is the choice of the order I and the set S to optimize the complexity-performance trade-off. It has been shown that, for small/medium size codes (e.g., $n \leq 150$, code rate $k/n > 0.5$), an order $I \approx d_{\min}/4$ is able to provide nearly-optimal decoding performance, i.e, very close to that of ideal MLD [76].

An approximation of the closed form expression for the upper-bound on the error performance of the order$-I$ reprocessing has been first derived in [76] which requires the computation of an $(I+1)$-dimensional integral for any reprocessing order-I. Later, a relatively simple (requiring $2-$dimensional integral evaluation) and relatively accurate (without any assumption) upper bound on the error performance of OSD for each stage reprocessing is derived in [79] based on the statistics introduced in [9]. In the following sections, we present a new statistics on the error properties of the permuted binary received vector $\overline{\mathbf{y}}'$ which can be applied to evaluate a simplified expression of the OSD error performance bound.

2.5 Proposed New Statistic of Ordered Vector Components

Given an LBC $C(n,k)$, without loss of generality, let us consider an all-zero transmitted codeword, $\overline{\mathbf{c}} = (0,\ldots,0,\ldots,0)$, which after BPSK mapping, corresponds to the transmitted vector, $\overline{\mathbf{s}} = (-1,\ldots,-1,\ldots,-1)$. At the output of the AWGN channel, we observe the received vector $\overline{\mathbf{r}} = (r_1,\ldots,r_i,\ldots,r_n)$, with:

$$r_i = -1 + w_i, \tag{2.10}$$

where w_i is a Gaussian random variable with zero mean and variance σ^2. All w_i noise components are statistically independent.

Each component r_i in (2.10) has a pdf given by,

$$f_r(x) = \frac{1}{\sqrt{2\pi\sigma^2}} e^{-\frac{(x+1)^2}{2\sigma^2}}. \tag{2.11}$$

If we consider the magnitude of the components of $\overline{\mathbf{r}}$ written as $\lambda_i = |r_i|$, the pdf of λ_i is given by,

$$f_{\lambda_i}(x) = \begin{cases} 0 & \text{if } x < 0, \\ \frac{e^{-\frac{(x+1)^2}{2\sigma^2}}}{\sqrt{2\pi\sigma^2}} + \frac{e^{-\frac{(x-1)^2}{2\sigma^2}}}{\sqrt{2\pi\sigma^2}} & \text{if } x \geq 0, \end{cases} \tag{2.12}$$

while its cdf is given by,

$$F_{\lambda_i}(x) = \begin{cases} 0 & \text{if } x < 0, \\ 1 - Q\left(\frac{x+1}{\sigma}\right) - Q\left(\frac{x-1}{\sigma}\right) & \text{if } x \geq 0, \end{cases} \tag{2.13}$$

where $Q(x) \triangleq \int_x^\infty 1/\sqrt{2\pi} exp(-y^2/2) dy$ is the standard normal tail function.

Now, let us focus on the reordered vector $\overline{\mathbf{r}}'$. A first study to estimate the behavior of the components of $\overline{\mathbf{r}}'$ was done in [76], where the pdf of the reordered noise samples conditioned upon the transmitted symbol has been presented.

Given the vector $\overline{\mathbf{r}}$ observed by transmitting the all-zero codeword over an AWGN channel with BPSK modulation and the ordered vector $\overline{\mathbf{r}}'$ obtained by ordering $\overline{\mathbf{r}}$ in decreasing magnitude, we can obtain the pdf of the components of $\overline{\mathbf{r}}'$, and the pdf of the magnitude of the components of $\overline{\mathbf{r}}'$ by using arguments from ordered statistics [78] as follows. The pdf of the i-th component r'_i of $\overline{\mathbf{r}}'$ is given by,

$$\begin{aligned} \forall x : f_{r'_i}(x) = & \frac{n!}{(i-1)!(n-i)!} (1 - F_\lambda(|x|))^{i-1} \\ & \cdot (F_\lambda(|x|))^{n-i} f_r(x). \end{aligned} \tag{2.14}$$

In the similar manner, using the pdf of λ_i, the pdf of the magnitude of i-th component $\lambda_i' = |r_i'|$ of $\bar{\mathbf{r}}'$ is given by,

$$\forall x : f_{\lambda_i'}(x) = \frac{n!}{(i-1)!(n-i)!}(1-F_\lambda(x))^{i-1} \cdot (F_\lambda(x))^{n-i} f_\lambda(x). \tag{2.15}$$

In the following, we define a new random variable E_L which represents the number of errors contained in the first L positions of the permuted received vector $\bar{\mathbf{r}}'$. Furthermore, we present a computationally efficient expression for the pdf of E_L. Normally, under identity permutation rule (which basically doesn't change the position of the vector elements) ρ_2, order$-I$ OSD includes only the chances of having I or less than I errors in MRPs of the permuted received vector. This leaves behind the probability of missing the true codeword by an order$-I$ OSD under ML performance. In this relation, the complementary cdf of E_L at $E_L = I$ actually provides a simplified expression to evaluate the maximum probability of missing a true codeword by an order$-I$ OSD, thus justifying the importance of E_L in evaluating the performance bound of the order$-I$ OSD. Further details are discussed in Section 2.6. We present a new Theorem which provides an exact expression for the pmf of the random variable E_L.

Theorem 1. Given a random variable E_L which represents the number of errors we expect on the first L, $1 \leq L \leq n$, positions of the permuted received vector $\bar{\mathbf{r}}'$, its pmf is given by,

$$p_{E_L}(E_L = j) = \int_0^{+\infty} \binom{l}{j} p(x)^j (1-p(x))^{l-j} f_{\lambda_{l+1}'}(x)dx, \tag{2.16}$$

where,

$$p(x) = \frac{Q\left(\frac{x+1}{\sigma}\right)}{1+Q\left(\frac{x+1}{\sigma}\right)-Q\left(\frac{-x+1}{\sigma}\right)}, \tag{2.17}$$

with $f_{\lambda_{l+1}'}(x)$ given by (2.15) and its cdf is given by,

$$F_{E_L}(E_L = j) = \sum_{i=0}^{j} p_{E_L}(E_L = i). \tag{2.18}$$

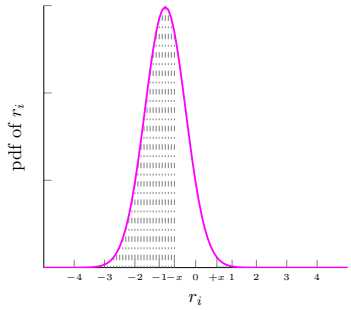

Fig. 2.1 Probability density function of r_i for $E_b/N_0 = 3.5$ dB.

Proof. Fix a value x, and suppose the magnitude of the $(l+1)$-th component of the reordered vector $\bar{\mathbf{r}}'$ is $\lambda'_{l+1} = x$. Then, the vector $\bar{\mathbf{r}}$ contains exactly l components with $|r_i| \geq x$. As can be observed in Fig. 2.1 (the shaded region corresponds to $|r_i| \geq x$), for each of these components, the probability of having an error is,

$$\begin{aligned} p(x) &= P(r_i > 0|_{|r_i| \geq x}) \\ &= \frac{Q\left(\frac{x+1}{\sigma}\right)}{1+Q\left(\frac{x+1}{\sigma}\right)-Q\left(\frac{-x+1}{\sigma}\right)}. \end{aligned} \tag{2.19}$$

Since we are working with the components of $\bar{\mathbf{r}}$ we can use their implicit statistically independent property, which instead does not hold if we try to work with the components of $\bar{\mathbf{r}}'$. As a result, the probability of having j errors among these k components is given by,

$$P(E_L = j|\{\lambda'_{l+1} = x, L = l\}) = \binom{l}{j} p(x)^j (1-p(x))^{l-j}. \tag{2.20}$$

The above result is obtained under the condition $\lambda'_{l+1} = x$. By integrating over all x values by using $f_{\lambda'_{l+1}}(x)$, we obtain the final pmf of E_L as in (2.16) while its cdf at some value $E_L = j$ is obtained as in (2.18) simply by summing the normalized pmf of E_L for all $E_L : 0 \leq E_L \leq j$. □

2.6 OSD Error Performance

In this section, a different look at the error performance of order$-I$ OSD is presented based on the distribution of E detailed in Section 2.5. Let $P_{e_{OSD-I}}$ denote the code error performance of the order$-I$ OSD and $P_e(I)$ denote the probability that the correct codeword is not among the candidate codewords supported by the order$-I$ OSD. The upper bound on the order$-I$ OSD performance can be written as an inequality as

$$\begin{aligned} P_{e_{OSD-I}} &\leq P_{e_{ML}} + P_e(I) \\ &\leq P_{e_{ML}} + P\left(\begin{array}{c}\text{More than } I \text{ errors occur} \\ \text{in } 1^{st}k \text{ positions of } \bar{\mathbf{r}}'\end{array}\right), \end{aligned} \tag{2.21}$$

where $P_{e_{ML}}$ is the MLD code error rate.

In (2.21), the probability of having more than I errors in the first k ordered received symbols in $\bar{\mathbf{r}}'$ given an identity permutation function ρ_2 can be simply evaluated from the cdf of E_L as,

$$P_e(I)|_{\rho_2(x)=x} = 1 - F_{E_L}(I), \tag{2.22}$$

where L in this case is equal to k.

In a real scenario, the permutation function ρ_2 may or may not be identity. In fact, the second permutation ρ_2 directly relates with the number of column permutation required to obtain first k columns of $\mathbf{G}^*$ to be linearly independent. Let us consider d is the number of dependent columns before k^{th} independent one and $P(d)$ be the probability associated with d. It has been shown in [76] that the maximum number of dependent columns that can be found before k^{th} independent one for a given generator matrix is given by,

$$d_{\max} = n - k - d_H^{\min} - 1, \tag{2.23}$$

where $d_H^{\min}$ is the minimum Hamming distance of the considered code.

Thus, $P_e(I)$ can be expressed under all cases of ρ_2 as,

$$\begin{aligned} P_e(I) &= \sum_{d=0}^{d_{\max}} P\left(\begin{array}{c} \text{More than } I \text{ errors occur} \\ \text{in } 1^{st} k+d \text{ positions of } \overline{\mathbf{r}}' \end{array} \right) \cdot P(d) \\ &= \sum_{d=0}^{d_{\max}} P(d) \left(1 - F_{E_{k+d}}(I)\right). \end{aligned} \tag{2.24}$$

where $F_{E_{k+d}}$ is the cdf of E_L at $L = k+d$. The probability $P(d)$ can be evaluated either from simulation or from the approximated distribution proposed in [76].

As stated earlier, the random variable E denotes the number of errors, thus, can only take integer values. Also the reprocessing order$-I$ is always fairly small ($I = \frac{d_H^{\min}}{4} \leq 5$) for LBCs with practical $d_H^{\min}$. Thus, (2.24) can be written in terms of pdf of E_L as,

$$P_e(I) = \sum_{d=0}^{d_{\max}} P(d) \left[1 - \sum_{i=0}^{I} f_{E_{k+d}}(E_{k+d} = i)\right]. \tag{2.25}$$

where $f_{E_{k+d}}(E_{k+d} = i)$ can be evaluated by a single integral given by (2.16).

The above discussion shows that, for all admissible values of order-I, the theoretical upper bound can be evaluated. It is quite clear that the computational complexity of this new upper bound requires a single dimensional integral for any order-I compared to $(I+1)$ and 2 dimensional integral for the one presented in [76] and [79] respectively. Furthermore, this bound is as tight as the one proposed in [79] (see Fig. 2.3 to 2.5) and is also derived without any assumption.

2.7 Numerical Results

For the purpose of comparison and performance evaluation, we adopt the same scenario of BPSK transmissions over an AWGN channel as described in Section 2.4 and Section 2.5. In order to accommodate the code rates of different LBCs, we adopt the ratio of the energy per bit to noise power spectral density ratio E_b/N_0 with $E_b/N_0 = \frac{E_s}{N_0} \cdot \frac{k}{n}$, where E_s is the signal energy and N_0 is the noise power spectral density.

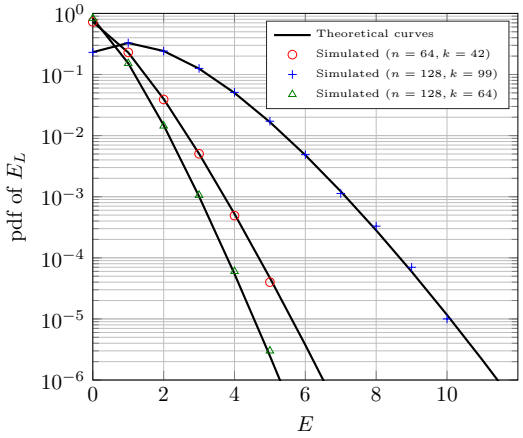

Fig. 2.2 Probability density function of E: $E_b/N_0 = 3.5$ dB, $L = k$.

2.7.1 Pmf of E_L

Figs. 2.2 plots the pmf of random variable E_L for different combinations of n and k. For each (n,k) combinations, the simulation results are plotted and compared with the theoretical result obtained from (2.16). We observe a perfect matching for all permissible values of E_L which justifies the validity of the expression presented in (2.16).

2.7.2 Error Performance

It is worthwhile to mention that the evaluation of (2.21) involves the prior evaluation of the MLD code error rate for the code under consideration. Thus, for our simulation purpose, we use the simplest upper bound, i.e., the union bound [112],

$$P_{e_{ML}}(\overline{\mathbf{c}}) \leq \sum_{d=d_H^{min}}^{n} A_d Q\left(\frac{\sqrt{d}}{\sigma}\right). \tag{2.26}$$

In (2.26), $d : d \geq d_H^{min}$ represents the Hamming weight of the codeword and A_d is the multiplicity (number of codeword with hamming weight equal to d) of the code. For simplicity, we consider at most the first four components of (2.26) which provide a good approximation for medium dimension codes at considerable E_b/N_0. For higher dimensional codes, the total union bound or other tight upper bound alternatives represent more accurate performance measure [112].

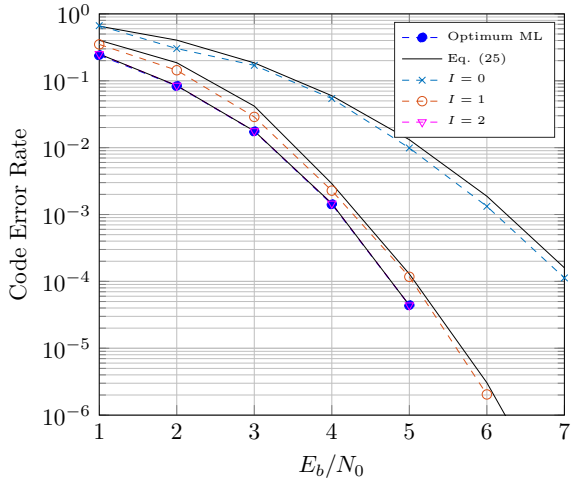

Fig. 2.3 Code Error Rate of OSD with order$-I$ reprocessing for (64,42,8) Reed Muller code

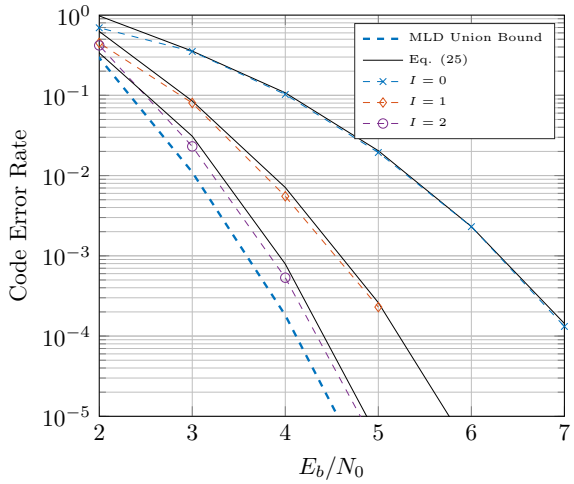

Fig. 2.4 Code Error Rate of OSD with order$-I$ reprocessing for (128,99,10) extended BCH code

Figs. 2.3 to 2.5 depict the error performances of the $(64, 42, 8)$ Reed Muller code, the $(128, 99, 10)$ eBCH code and the $(128, 64, 22)$ eBCH code, respectively. Each plot includes the simulation results and the corresponding upper bounds computed from (2.21). We observe that for all values of reprocessing order-I, the theoretical upper bounds are tight. The bounds are as tight as those derived in [76] and [79]. However, while the error performance bound of order$-I$ reprocessing OSD based on [76] requires the computation of $(I+1)-$dimensional integral and [79] requires the computation of a two-dimensional integral, the new upper bounds require the computation of a single dimensional integral for any reprocessing order-I.

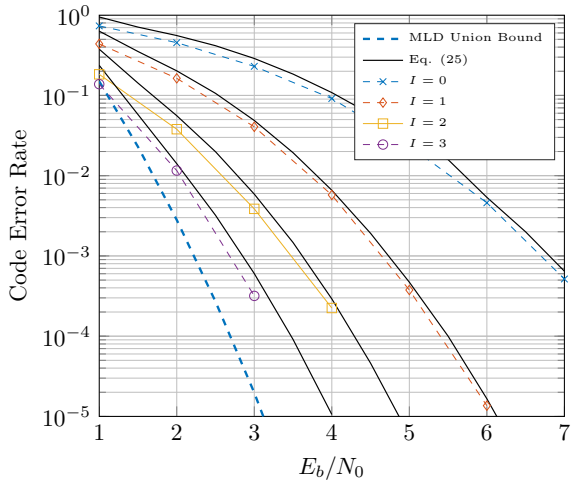

Fig. 2.5 Code Error Rate of OSD with order$-I$ reprocessing for (128,64,22) extended BCH code

Chapter 3

Frame Synchronization[1]

3.1 Introduction

In Chapter 2, we considered the aspect of channel coding in achieving ultra-low latency for 5G use cases. In this chapter, we consider the aspect of frame synchronization which is very important in achieving the ultra-low latency and ultra reliable communication for M2M applications.

3.1.1 Machine to Machine Communication

M2M communication, a promising technology for smart city concept, enables ubiquitous connectivity between one or more autonomous devices without or with minimal human interaction. The most important requirements for M2M communication in 5G systems currently being studied are 1) Maximum allowable end-to-end latency, including jitters/re-transmits less than 1ms. 2) Reliability, for example packet loss rate 10-9 [65, 69, 116]. Similarly, mission critical communications, which can help first responders work safer, smarter and faster in disasters and day-to-day incidents, have similar requirements as well. Among these two requirements for M2M, virtually zero latency, i.e., radio latency lower than 1ms, is very critical for

- achieving higher data rates while keeping equipment cost low.

[1]Part of the work described in this chapter has been previously published in [22].

- ensuring fast procedure response time in the system (e.g. fast wake up and dormancy, fast scheduling, fast link configuration)
- whole new range of use cases like remote control of machines and objects in the cloud or tactile internet etc.

In addition, for real time M2M applications in the area of intelligent transport system, remote monitoring and health will also be requiring very low latency and are become the main focus of many mobile and it operators and vendors as a new revenue opportunity. M2M traffic is bursty, since M2M applicatioin have not been developed with network load shaping in mind. For instance, M2M devices have a much larger ratio of uplink to downlink traffic volume, their traffic typically exhibits different diurnal patterns, they are more likely to generate synchronized traffic resulting in bursty aggregate traffic volumes, and are less mobile compared to smartphones. Thus, burstiness is the result of synchronization effect resulting from several M2M devices simultaneously reporting data [108]. In such application scenario where the data transmission is bursty, a known synchronization/preamble sequence are often periodically or aperiodically embedded in the data in order to aid in

1. data packet location during detection or decoding process,
2. resource scheduling,
3. packet synchronization,
4. determining the boundaries of the transmitted frame.

Thus, frame synchronization is a process by which incoming frame alignment signals are identified, permitting the data bits within the frame to be extracted for decoding and re-transmissions. In addition to the context of M2M application, binary pattern synchronization problem is quite popular in many other scenarios. Some important standards which make use of binary pattern synchronization are noted here.

1. Moving Picture Experts Group (MPEG)-4 data compression standard [100]: It utilizes synchronization patters such as the 24-bit start-code prefix and 17-bit re-synchronization flag.

2. CCSDS (Consultative Committee for Space Data Systems) Telecommand uplink Recommendation [73]: It is used by international space agencies like NASA and ESA for transmission from Earth to satellites/spacecrafts. The transmission is bursty and the frames have variable lengths: every frame is composed by n codewords, with n ranging between 2 and 147. A tail sequence synchronization word of $N = 64$ bits is used to identify the frame end.

3. DVB Terrestrial (DVB-T) standard [95]: In this application we look for the synchronization word inside a sliding window. A N = 8-bit synchronization pattern is used by DVB-T standard for digital television broadcasting.

4. IEEE 802.15.4 standard [8]: Physical layer frame starts with a physical synchronization header (5 bytes) followed by a physical payload upto 127 bytes such that the physical synchronization header is used to alert the receiver that a potentially receivable signal is present.

Another scenario could be in contention free random access procedure in LTE [184], the base station assigns distinct preamble to each UE (user equipment) and hence the concern for collision and other collision related issues are non-existent. Contention-free Random Access are used in areas where low latency is required, such as handover and resumption of down-link traffic for UE.

3.2 Introduction to Frame Synchronization Problem

Binary pattern recognition in a sequence of noisy samples is an important problem in communication and signal processing. As a classical example, Synchronization Word detection is commonly used to determine the boundaries of a transmitted frame for both continuous and burst communication links [23, 157, 82]. Frame synchronization literature covers a number of topics, including optimum and sub-optimum detectors [122, 132, 151, 110, 37], important aspects for communication systems [133, 56, 102, 103, 34–36], and binary pattern design [23, 163].

In this scenario, we focus on the basic detection problem which consists of a known binary pattern, antipodal signaling and Gaussian noise, where soft values are provided to the detector. Under this hypothesis, the optimal solution is provided by the Likelihood Ratio Test (LRT). The LRT for this problem was first derived

by Massey in [122]. A different formulation was provided by Chiani and Martini in [37] (In succeeding section, we present the proof). Both LRT formulations are characterized by a quite high complexity, which may be critical for some practical applications requiring real-time implementation, like frame synchronization at high bit rates and low latency scenario. To overcome this problem, two simplified approaches are often used: hard and soft correlation [82]. Despite their widespread use, they are highly sub-optimal with respect to LRT.

The Massey correlation detector was introduced by Massey in [122] as an asymptotic approximation of LRT which holds for large SNR values. It consists of a modified soft correlation computed only on the components where the sign of observed and pattern symbols differs, therefore it is characterized by a very low complexity. Typically, analytical results on the detectors are not easy to be obtained [132]. However, they are very useful because they highlight the detector properties, and allow to compute the performance without resorting to extremely long simulations. As an example, the LRT analytical performances were presented for the first time by Chiani and Martini in [37] (in the same paper, the analytical performances of hard and soft correlation were reported, too).

3.3 System Model and Problem discussion

We have a fixed, known, binary pattern or Synchronization Word (SW) $\underline{c}$, composed by N binary antipodal symbols:

$$c = (c_1, \cdots, c_i, \cdots, c_N) \text{ with fixed } c_i \in \{-1, +1\}.$$

We observe a window which may contain $\underline{c}$ or random symbols. The observed samples are corrupted by AWGN. We formulate the problem as the binary hypothesis testing of Figure 3.1.

Given the vector $\underline{r}$ composed by N real-value observed samples, there are two alternatives. Under H_1 the SW is present and we observe:

$$\begin{aligned} H_1 : \underline{r} &= (r_1, \cdots, r_i, \cdots, r_N) \\ r_i &= c_i + n_i \text{ with fixed } c_i \in \{-1, +1\}. \end{aligned} \tag{3.1}$$

Under H_0 the SW is absent and we observe random symbols:

$$\begin{aligned} H_0 : \underline{r} &= (r_1, \cdots, r_i, \cdots, r_N) \\ r_i &= d_i + n_i \text{ with i.i.d. } d_i \in \{-1, +1\}. \end{aligned} \tag{3.2}$$

In both cases, n_i are samples of a Gaussian random variable with zero mean and variance σ^2.

The binary pattern recognition problem is quite popular in many scenarios. For communication systems a typical example is frame synchronization: SWs are commonly used to determine the boundaries of a transmitted frame. The observed window where we look for the SW can be fixed or moving [23]-[82]. For example,

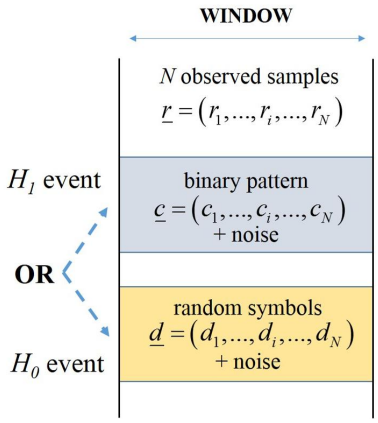

Fig. 3.1 The binary pattern recognition problem under study.

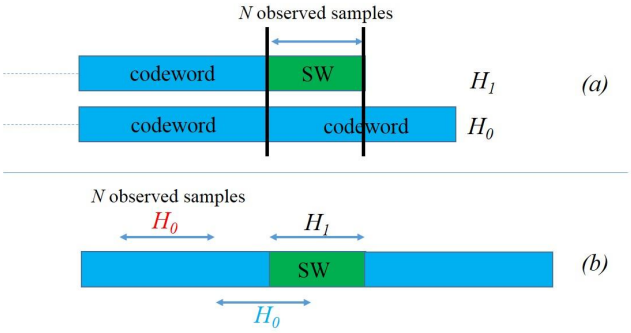

Fig. 3.2 The frame synchronization problem.

it is fixed for the CCSDS Telecommand uplink Recommendation [73], used by international space agencies like NASA and European Space Agency (ESA) for transmission from Earth to satellites/spacecrafts. The transmission is bursty and the frames have variable lengths: every frame is composed by n codewords, with n ranging between 2 and 147. A tail sequence SW of $N = 64$ bits is used to identify the frame end. As shown in Figure 3.2.a, at the end of any codeword the receiver looks for the SW inside a fixed window of 64 symbols. If it is detected, the frame is declared closed, otherwise a new codeword is processed. The problem is very well matched to the considered one. The hypothesis that, under H_0, the binary symbols look as i.i.d. random symbols is well justified by the properties of the transmitted codewords, which typically look as random sequences (see, for example, [31]).

In other applications, we look for the SW inside a sliding window, as in Figure 3.2 (b). Typically, this is the case of continuous systems, where equidistant patterns are introduced to allow block synchronization. The receiver slides a window of N symbols along the received sequence, looking for the SW which starts a frame. If the window is aligned with the SW, we have the H_1 case. In all the other cases, we have the H_0 case. The hypothesis that the binary symbols look random under H_0 is certainly realistic when the window is completely outside the SW (red upper H_0 in Figure 3.2.b). When the window is partially overlapped with the SW (blue lower H_0 in Figure 3.2.b), the hypothesis can still be considered true for well designed SWs with good properties in terms of aperiodic autocorrelation function [23],[163], which look as random symbols when out of sync [37].

In this work we will often refer to frame synchronization as a typical scenario. Obviously, binary pattern recognition problem is much more general and all the presented results hold for a number of different applications, too.

3.4 Likelihood Ratio Test

For the problem presented in Section 3.3, two alternative, equivalent formulations of the optimal LRT solution were derived, respectively by Massey in [122] and by Chiani/Martini in [37].

The Massey formulation [122] is:

$$\Gamma_{LRT_1} = \sum_{i=1}^{N} r_i c_i - \sigma^2 \sum_{i=1}^{N} \log\cosh\left(\frac{r_i}{\sigma^2}\right). \tag{3.3}$$

The Chiani/Martini formulation [37] is:

$$\Gamma_{LRT_2} = \sum_{i=1}^{N} \log\left(1+\exp\left(-\frac{2r_i c_i}{\sigma^2}\right)\right). \tag{3.4}$$

3.4.1 Equivalency of Massey Formulation and Chiani/Martini formulation of LRT

Starting from the final expression of Massey formulation in (3.3), raising both sides of the equation by an exponent, we get,

$$\exp(\Gamma_{LRT_1}/\sigma^2) = \frac{\prod_{i=1}^{N}\exp(\frac{r_i c_i}{\sigma^2})}{\prod_{i=1}^{N}\cosh\left(\frac{r_i}{\sigma^2}\right)} \tag{3.5}$$

Now, we can take a reciprocal of the components on both sides of the (3.5), and using the expansion of hyperbolic cosine function as,

$$\exp(-\Gamma_{LRT_1}/\sigma^2) = \frac{\prod_{i=1}^{N}\left[\exp\left(\frac{r_i}{\sigma^2}\right)+\exp\left(-\frac{r_i}{\sigma^2}\right)\right]}{\prod_{i=1}^{N}\exp(\frac{r_i c_i}{\sigma^2})} \tag{3.6}$$

In order to simplify, we multiply r_i in the exponent at the numerator by c_i which does not change the overall value of the numerator since c_i is +1 or -1. Thus, we obtain,

$$\exp(-\Gamma_{LRT_1}/\sigma^2) = \prod_{i=1}^{N}\left[1+\exp\left(-\frac{2r_i c_i}{\sigma^2}\right)\right] \tag{3.7}$$

Now, taking logarithm on both sides, we obtain,

$$-\Gamma_{LRT_1}/\sigma^2 = \sum_{i=1}^{N} log\left(1+\exp\left(-\frac{2r_i c_i}{\sigma^2}\right)\right) \tag{3.8}$$

Finally, (3.8) proved that the LLR expression in (3.4) is a scaled version of the LLR expression presented by Massey in (3.3).

3.5 Hard and Soft Correlation

By looking at the formulas we observe that both formulations are characterized by non-negligible complexity which makes their application to real-time applications problematic, especially in the case of low latency and high bit-rates system scenario. For this reason, simplified formulations are usually adopted in practice: hard and soft correlation [157],[82],[37].

Given the real-value received vector $\underline{r} = (r_1, \cdots, r_i, \cdots, r_N)$, if a hard decision is taken on each sample by looking at the sign only, it is transformed into the binary vector:

$$\underline{y} = (y_1, \cdots, y_i, \cdots, y_N),$$

where:

$$\begin{aligned} &\text{if } r_i \geq 0 \rightarrow y_i = +1 \\ &\text{if } r_i < 0 \rightarrow y_i = -1. \end{aligned}$$

Given the binary vector $\underline{y}$, it is easy to show that the optimal test for detecting $\underline{c}$ is the *hard correlation* detector:

$$\Gamma_H = \sum_{i=1}^{N} y_i c_i, \tag{3.9}$$

which is equivalent to compute the Hamming distance between the two binary vectors, i.e., the number of different symbols.

Given the hard correlation expression (3.9), we can extend it to the real-value domain. The expression of the *soft correlation* detector is given by:

$$\Gamma_S = \sum_{i=1}^{N} r_i c_i. \tag{3.10}$$

As discussed in [37], soft correlation has no theoretical justification. In fact, there are many set of parameters where hard correlation is better than soft. Both hard and

soft correlation tests are often used in practice. Unfortunately, as shown in the next sections, they are highly sub-optimal with respect to LRT.

3.6 The Massey Correlation Detector

J.L. Massey derived the expression of the *Massey correlation detector* in [122] starting from the optimal LRT given by (3.3) and using this approximation, which holds at high SNR:

$$\cosh\left(\frac{r_i}{\sigma^2}\right) = \frac{\exp\left(+\frac{r_i}{\sigma^2}\right) + \exp\left(-\frac{r_i}{\sigma^2}\right)}{2} \simeq \frac{1}{2}\exp\left(\frac{|r_i|}{\sigma^2}\right). \tag{3.11}$$

By applying it, (3.3) simplifies to:

$$\Gamma_{LRT_1} \simeq \sum_{i=1}^{N} r_i c_i - \sum_{i=1}^{N} |r_i|. \tag{3.12}$$

By noting that:

$$\begin{aligned} &\text{if}\,\text{sgn}(r_i) = c_i \rightarrow |r_i| = r_i c_i \\ &\text{if}\,\text{sgn}(r_i) \neq c_i \rightarrow |r_i| = -r_i c_i, \end{aligned}$$

Massey obtained the following simplified expression:

Definition 1. The Massey Correlation Detector [122]. Given the binary antipodal pattern $\underline{c} = (c_1, \cdots, c_i, \cdots, c_N)$ and the observed real vector $\underline{r} = (r_1, \cdots, r_i, \cdots, r_N)$, the Massey correlation detector computes the statistical test:

$$\Gamma_M = \sum_{\substack{i: \\ \text{sgn}(r_i) \neq \text{sgn}(c_i)}} r_i c_i, \tag{3.13}$$

which is compared against a threshold t:

- If $\Gamma_M \geq t$, the detector declares the event H_1: the SW is present.
- If $\Gamma_M < t$, the detector declares the event H_0: the SW is absent.

Massey correlation is similar to soft correlation (3.10), which is now computed only on the received symbols with a sign different from the pattern symbols, and is much simpler than the LRT. In the next two sections, we present one of the key results of this work: how to analytically compute the Massey detector performances under the two hypotheses H_0 and H_1.

3.7 Analytical computation of the detector performances under H_1

By looking at (3.13) we immediately note that if all r_i symbols have the same sign of the pattern symbols then $\Gamma_M = 0$. Otherwise, if at least one component has a different sign, we have $\Gamma_M < 0$, with a real value depending on the r_i components. This means that Γ_M has a mixed pdf with:

- A discrete component in the origin.
- A continuous component for negative values.

In the following we will express the detector performance as a function of SNR, i.e., $\text{SNR} = \frac{E_s}{N_0} = \frac{1}{2\sigma^2}\,\text{dB}$.

The following theorem computes this pdf under H_1.

Theorem 2. The pdf under H_1 of the Massey correlation detector is a mixed pdf, with:
– A discrete component for $x = 0$ given by

$$P(\Gamma_M = 0|H_1) = (1-p)^N, \tag{3.14}$$

with

$$p = \frac{1}{2}\operatorname{erfc}\sqrt{\frac{1}{2\sigma^2}}.$$

– A continuous component for negative values given by

$$\forall x < 0 \qquad f_{\Gamma_M}(x|H_1) = \sum_{c=1}^{N} \binom{N}{c} p^c (1-p)^{N-c}\, \mathscr{F}^{-1}\left[\mathscr{F}\left(f_y(x)\right)^c\right], \tag{3.15}$$

where $\mathscr{F}$ is the Fourier transform and y is a random variable with pdf:

$$\begin{aligned} f_y(x) &= \frac{1}{p}\frac{1}{\sqrt{2\pi\sigma^2}}e^{-\frac{(x-1)^2}{2\sigma^2}} \quad \text{for } x<0 \\ f_y(x) &= 0 \qquad\qquad\qquad\qquad\quad \text{for } x\geq 0. \end{aligned} \tag{3.16}$$

Proof. Under H_1, every component $r_i = c_i + n_i$ is an independent Gaussian random variable centered around a fixed symbol c_i. Let us suppose (without loss of generality) that $c_i = +1, \forall i$. As a consequence, the condition $\text{sgn}(r_i) \neq \text{sgn}(c_i)$ is equivalent to the condition $r_i < 0$. Then we can write:

$$\Gamma_M = \sum_{\substack{i: \\ \text{sgn}(r_i)\neq\text{sgn}(c_i)}} r_i c_i = \sum_{\substack{i: \\ r_i<0}} r_i. \tag{3.17}$$

The probability that a single component $r_i = 1 + n_i$ is negative is given by:

$$p = P(r_i<0) = P(1+n_i<0) = P(n_i<-1) = \frac{1}{2}\,\text{erfc}\sqrt{\frac{1}{2\sigma^2}}. \tag{3.18}$$

Then, the probability of having C negative components is:

$$P(C=c) = \binom{N}{c} p^c (1-p)^{N-c}. \tag{3.19}$$

From this expression we can compute the discrete component of the pdf in the origin:

$$P(\Gamma_M = 0|H_1) = P(C=0) = (1-p)^N,$$

which is result (3.14). To compute the continuous component of the pdf for $x<0$, we introduce the random variable:

$$\alpha(c) = \sum_{i=1}^{c} y_i \tag{3.20}$$

obtained as the sum of c (with $1 \leq c \leq N$) independent random variables y_i corresponding to negative symbols r_i:

$$y_i = 1 + n_i \quad \text{with} \quad y_i < 0.$$

The pdf of these random variables is depicted in Figure 3.3 and is given by (3.16). Note that the pdf of y_i is written starting from the Gaussian pdf of r_i, but taking into account the condition $y_i < 0$. For this reason, the original pdf is divided by p, which is exactly the factor $p = P(r_i < 0)$.

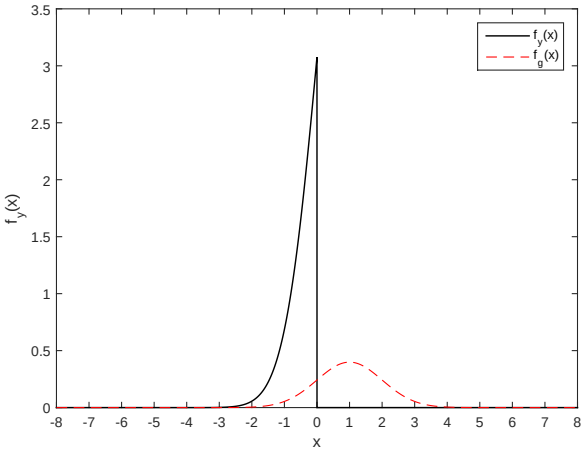

Fig. 3.3 Pdf of random variable y for SNR $= 0$dB. The red dotted curve $f_g(x)$ is the original Gaussian random variable centered in $c_i = +1$.

To derive the pdf of $\alpha(c)$, we can compute the convolution of the c pdfs $f_y(x)$. As an alternative, we can exploit the characteristic function approach by computing the Fourier transform:

$$\Phi_y(f) = \mathscr{F}(f_y(x))$$

and applying:

$$f_{\alpha(c)}(x) = \mathscr{F}^{-1}\left[\Phi_y(f)^c\right]. \tag{3.21}$$

From (3.19) and (3.21) we can finally compute the pdf continuous component, which is result (3.15):

$\forall x < 0$

$$f_{\Gamma_M}(x|H_1) = \sum_{c=1}^{N} P(C=c) f_{\alpha(c)}(x) = \sum_{c=1}^{N} \binom{N}{c} p^c (1-p)^{N-c} \mathscr{F}^{-1}\left[\mathscr{F}\left(f_y(x)\right)^c\right].$$

□

Theorem 2 allows to compute the Massey detector pdf for any pattern length value N and any SNR value $E_S/N_0 = 1/(2\sigma^2)$. As an example, the pdfs (both discrete/continuous components) under H_1 at SNR $= 0$dB are shown in Figure 3.4

for $N = 8$ and in Figure 3.5 for $N = 64$. In the same figures we also verify the perfect agreement with the simulated pdf curves, obtained by generating a sufficiently large number of events H_1 and H_0, applying the Massey detector, and collecting the test results.

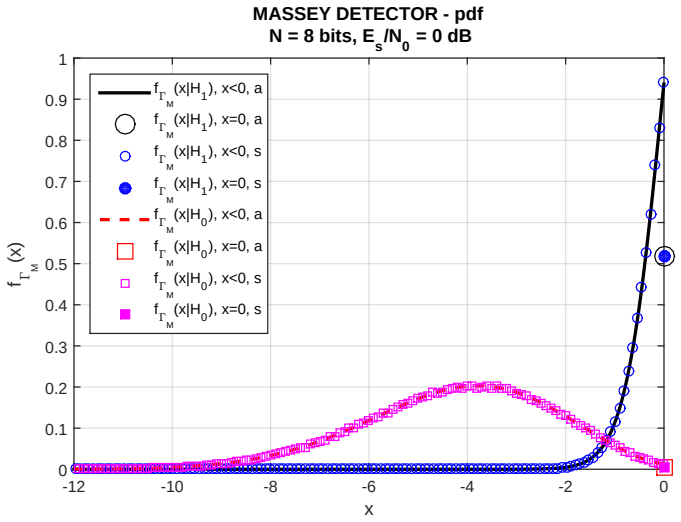

Fig. 3.4 Massey correlation detector: pdfs under H_1 and H_0 for $N = 8$ at SNR $= 0$ dB. Analytical (a) vs. simulated (s) curves.

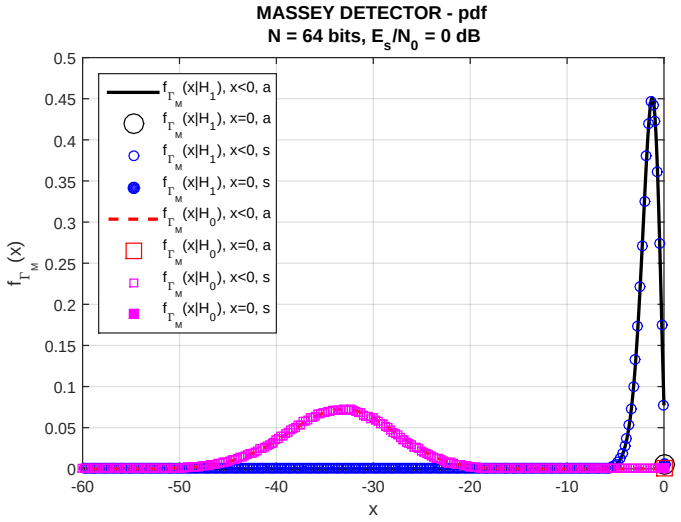

Fig. 3.5 Massey correlation detector: pdfs under H_1 and H_0 for $N = 64$ for SNR $= 0$ dB. Analytical (a) vs. simulated (s) curves.

3.7.1 Miss-Detection Probability

Given the pdf, we can compute the miss-detection probability. We are under H_1, the SW is present, but the test is erroneously below the threshold and the SW is declared absent. The following Corollary of Theorem 2 holds.

Corollary 1. The miss-detection probability of the Massey correlation detector is given by:

$$\begin{aligned} &\text{if } t < 0 : P_{md} = P(\Gamma_M < t | H_1) = \int_{-\infty}^{t} f_{\Gamma_M|H_1}(x)dx \\ &\text{if } t = 0 : P_{md} = P(\Gamma_M < 0 | H_1) = 1 - (1-p)^N \\ &\text{if } t > 0 : P_{md} = P(\Gamma_M < t | H_1) = 1. \end{aligned} \tag{3.22}$$

Proof. The first line is the definition of miss-detection probability, with $f_{\Gamma_M|H_1}(x)$ given by (3.15). For $t = 0$ the integral covers the entire continuous component, then we obtain the complement to one of the discrete component in the origin (3.14). For any positive $t > 0$ the integral covers the entire pdf, then we obtain 1. □

As an example, the miss-detection probability of the Massey detector at SNR $=$ 0 dB is plotted in Figure 3.6 for $N = 8$ and in Figure 3.7 for $N = 64$, where they also compared against the simulated curves. (Clearly, the analytical curves allow to compute very low error rates, without resorting to very long simulations).

3.8 Analytical computation of the detector performances under H_0

In this section, we show how to analytically compute the test performances under H_0. Also in this case, Γ_M has a mixed pdf with a discrete component for $\Gamma_M = 0$ (when all received r_i have the same sign of the pattern symbols) and a continuous component for $\Gamma_M < 0$ (when at least one r_i has a different sign). The following theorem computes this pdf under H_0.

Theorem 3. The pdf under H_0 of the Massey correlation detector is a mixed pdf, with:

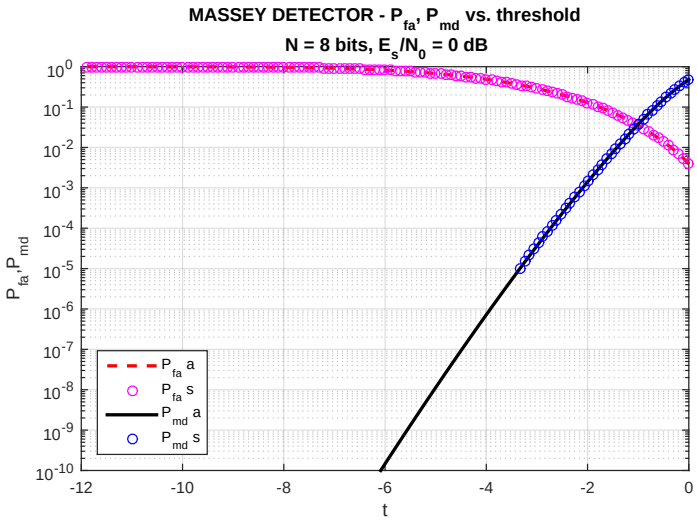

Fig. 3.6 Massey correlation detector: miss-detection and false-alarm performances, for $N = 8$ bits and SNR $= 0$ dB. Analytical (a) and simulated (s) curves.

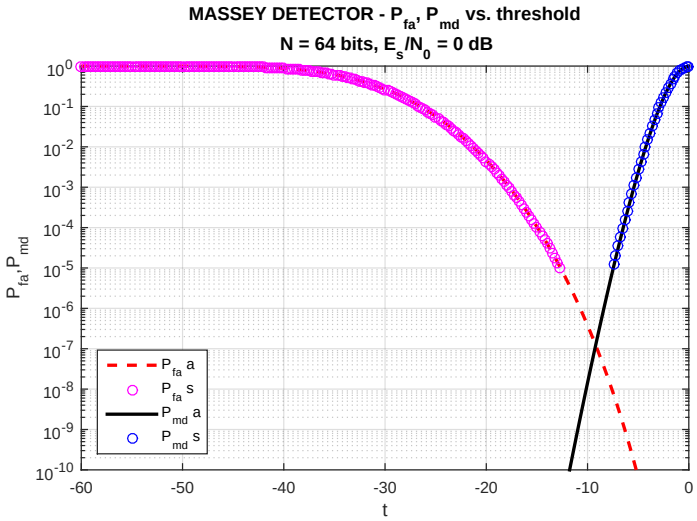

Fig. 3.7 Massey correlation detector: miss-detection and false-alarm performances, for $N = 64$ bits and SNR $= 0$ dB. Analytical (a) and simulated (s) curves.

– A discrete component for $x = 0$ given by

$$P(\Gamma_M = 0|H_0) = \frac{1}{2^N}. \tag{3.23}$$

– A continuous component for negative values given by

$$\forall x<0 \quad f_{\Gamma_M|H_0}(x)=\sum_{i=0}^{N}\frac{1}{2^N}\binom{N}{i}$$
$$\sum_{\substack{c=0\\(c\neq 0)\,\mathrm{OR}\,(c'\neq 0)}}^{i}\sum_{c'=0}^{N-i}\binom{i}{c}p^c(1-p)^{i-c}\binom{N-i}{c'}(1-p)^{c'}p^{N-i-c'}\mathscr{F}^{-1}[\mathscr{F}(f_y(x))^c\mathscr{F}(f_z(x))^{c'}] \quad (3.24)$$

where y is a random variable with pdf given by (3.16), and z is a random variable with pdf given by:

$$\begin{aligned} f_z(x) &= \frac{1}{1-p}\frac{1}{\sqrt{2\pi\sigma^2}}e^{-\frac{(x+1)^2}{2\sigma^2}} && \text{for } x<0 \\ f_z(x) &= 0 && \text{for } x\geq 0. \end{aligned} \quad (3.25)$$

Proof. Under H_0, every component $r_i = d_i + n_i$ is an independent Gaussian random variable centered around a random symbol d_i. We suppose (without loss of generality) that $c_i = +1$. We can write:

$$\Gamma_M = \sum_{\substack{i:\\ \mathrm{sgn}(r_i)\neq\mathrm{sgn}(c_i)}} r_i c_i = \sum_{i:r_i<0} r_i = \sum_{\substack{i:r_i<0\\ d_i=+1}} r_i + \sum_{\substack{i:r_i<0\\ d_i=-1}} r_i. \quad (3.26)$$

Given a random vector $\underline{d} = (d_1, \cdots, d_i, \cdots, d_N)$, composed by i.i.d. symbols, we denote by:

- N^+ the number of symbols with $d_i = +1$.
- $N^- = N - N^+$ the number of symbols with $d_i = -1$.

We have:

$$P(N^+ = i) = \frac{1}{2^N}\binom{N}{i}. \quad (3.27)$$

Given $\underline{r}$, we denote by:

- C the number of negative symbols $r_i < 0$ corresponding to $d_i = +1$.
- C' the number of negative symbols $r_i < 0$ corresponding to $d_i = -1$.

We note that:

$$P(r_i < 0 | d_i = +1) = P(n_i < -1) = p$$
$$P(r_i < 0 | d_i = -1) = P(n_i < +1) = 1 - p.$$

Then the probability that $C = c$ and $C' = c'$ is given by:

$$P(C = c | N^+ = i) = \binom{i}{c} p^c (1-p)^{i-c}$$
$$P(C' = c' | N^+ = i) = \binom{N-i}{c'} (1-p)^{c'} p^{N-i-c'}.$$

When both $c = c' = 0$, all symbols r_i are positive and $\Gamma_M = 0$. This allows to compute the pdf discrete component under H_0:

$$P(\Gamma_M = 0 | H_0) = \sum_{i=0}^{N} P(N^+ = i) P(C = 0, C' = 0 | N^+ = i) = \sum_{i=0}^{N} \frac{1}{2^N} \binom{N}{i} (1-p)^i p^{N-i} = \frac{1}{2^N},$$

which is result (3.23). Even if this procedure is useful for the remaining part of the proof, we note here that it is possible to compute this value in a simpler way. Let us consider the output of a binary symmetric channel when the input vector is random. The output vector is a random vector, too, and $1/2^N$ is exactly the probability that all its symbols are positive.

To compute the continuous component of the pdf, when at least one symbol r_i is negative, i.e., $[(c \neq 0) \,\mathrm{OR} (c' \neq 0)]$, let us consider:

$$\gamma(c, c') = \alpha(c) + \beta(c') = \sum_{i=0}^{c} y_i + \sum_{i=0}^{c'} z_i. \tag{3.28}$$

The first term $\alpha(c)$ corresponds to the negative symbols $r_i < 0$ with $d_i = +1$. It can be studied as in the previous section and its pdf is given by (3.21).

The second term $\beta(c')$ is obtained as the sum of c' independent random variables z_i corresponding to negative symbols r_i with $d_i = -1$:

$$z_i = -1 + n_i \text{ with } z_i < 0.$$

The pdf of each of them is depicted in Figure 3.8 and is given by (3.25).

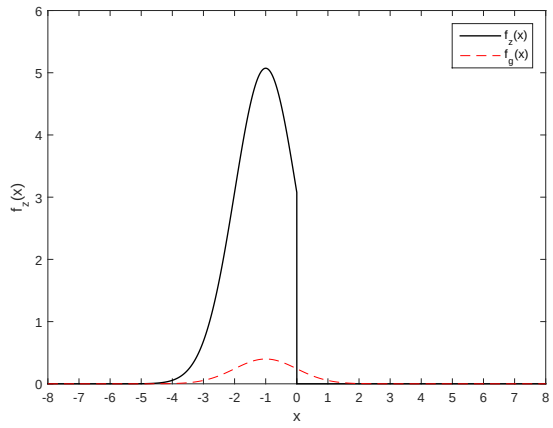

Fig. 3.8 Pdf of random variable z for SNR $= 0$dB. The red dotted curve $f_g(x)$ is the original Gaussian random variable centered in $d_i = -1$.

The pdf of $\gamma(c,c')$ can be computed by using the characteristic function approach:

$$f_{\gamma(c,c')}(x) = \mathscr{F}^{-1}\left[\mathscr{F}(f_y(x))^c \mathscr{F}(f_z(x))^{c'}\right].$$

Finally, we can group together all these results to get the pdf continuous component:

$$\forall x < 0 \quad f_{\Gamma_M|H_0}(x) = \sum_{i=0}^{N} P(N^+ = i) \sum_{\substack{c=0 \\ (c\neq 0)\,\mathrm{OR}\,(c'\neq 0)}}^{i} \sum_{c'=0}^{N-i} P(C = c, C' = c' | N^+ = i) f_{\gamma(c,c')}(x) =$$

$$= \sum_{i=0}^{N} \frac{1}{2^N} \binom{N}{i} \sum_{\substack{c=0 \\ (c\neq 0)\,\mathrm{OR}\,(c'\neq 0)}}^{i} \sum_{c'=0}^{N-i} \binom{i}{c} p^c (1-p)^{i-c} \binom{N-i}{c'} (1-p)^{c'} p^{N-i-c'} \mathscr{F}^{-1}[\mathscr{F}(f_y(x))^c \mathscr{F}(f_z(x))^{c'}],$$

which is result (3.24). □

Theorem 3 allows to compute the detector pdf for any pattern length value N and any SNR value. As an example the pdfs (discrete and continuous components) under H_0 at SNR $= 0$dB are shown in Figure 3.4 for $N = 8$ and in Figure 3.5 for $N = 64$, where we have also plotted the simulated curves.

3.8.1 False-Alarm Probability

Given the pdf, we can compute the false-alarm probability. We are under H_0, the SW is absent, but the test is erroneously above the threshold and the SW is declared present. The following Corollary of Theorem 3 holds.

Corollary 2. The False-Alarm probability of the Massey detector is given by:

$$\begin{aligned} &\text{if } t < 0 : P_{fa} = P(\Gamma_M \geq t | H_0) = \int_t^{0^-} f_{\Gamma_M|H_0}(x)dx + \frac{1}{2^N} \\ &\text{if } t = 0 : P_{fa} = P(\Gamma_M \geq 0 | H_0) = \frac{1}{2^N} \\ &\text{if } t > 0 : P_{fa} = P(\Gamma_M \geq t | H_0) = 0 \end{aligned} \tag{3.29}$$

Proof. The false-alarm probability is obtained by integrating the detector pdf given by Theorem 3, which has a continuous component for negative values and a discrete component in the origin equal to $1/2^N$. When $t = 0$, P_{fa} is equal to the discrete component. For positive thresholds it goes to zero. □

As an example, the false-alarm probability of the Massey detector at SNR $= 0$ dB is plotted in Figure 3.6 for $N = 8$ and in Figure 3.7 for $N = 64$, where they are also compared against the simulated pdf.

3.8.2 False-alarm lower bound

By looking at Corollary 1 and 2, we can observe that:

- For $t = 0$ we have $P_{fa} = 1/2^N$ and $P_{md} = 1 - (1-p)^N$.
- For $t > 0$ we have $P_{fa} = 0$ and $P_{md} = 1$.

This means that it is useless to set a positive threshold, because the pattern is never detected. As a consequence, it is impossible to achieve a value $P_{fa} < 1/2^N$: the false-alarm rate is always lower bounded by the term due to the pdf discrete component under H_0:

$$P_{fa} \geq P_{fa}^{(LB)} = \frac{1}{2^N}. \tag{3.30}$$

This is an important issue for practical applications, because the term $1/2^N$ is not negligible for small N. As an example, the lower bound values for some SW

lengths N are reported in Table 3.1, which shows that the bound is quite high for small lengths (e.g., $N \leq 16$).

Table 3.1 Massey correlation detector: false-alarm lower bound values for different lengths N.

N	$P_{fa}^{(LB)}$
8	$3.90 \cdot 10^{-3}$
16	$1.53 \cdot 10^{-5}$
32	$2.33 \cdot 10^{-10}$
64	$5.42 \cdot 10^{-20}$

Indeed, the lower bound impact is clearly visible in Figure 3.6 for $N = 8$, while it is negligible in Figure 3.7 for $N = 64$. This limitation for small values of N can be a problem for some applications which require very low false-alarm rates. This issue will be further discussed in Section 3.10, where we present a solution to eliminate it.

3.9 ROC curves

Given the miss-detection and the false-alarm probability analytical expressions derived in Section 3.8 and Section 3.7, we can now compute the ROC performances of the Massey detector, *i.e.*, the miss-detection vs. false-alarm curves. As an example, Figure 3.9 and Figure 3.10 present the ROC for $N = 8$ and $N = 64$ for different SNR values. As another example, the ROC curves at SNR $= 0$ dB for different values of N are shown in Figure 3.11. Also in this case, the impact of the false-alarm lower bound values is clearly visible in Figure 3.9 and Figure 3.11 for $N = 8$, and in Figure 3.11 for $N = 16$.

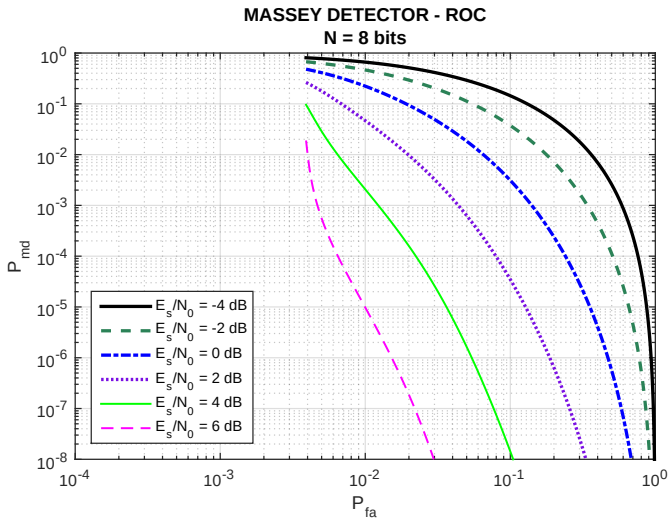

Fig. 3.9 Massey correlation detector: ROC curves for N=8 bits and different SNR values.

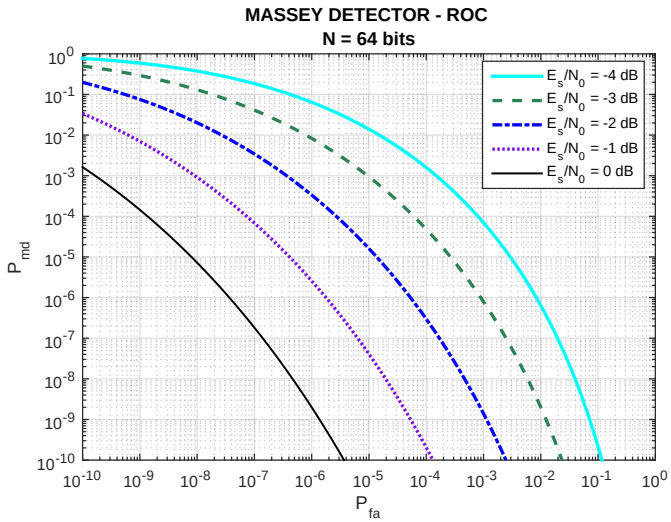

Fig. 3.10 Massey correlation detector: ROC curves for N=64 bits and different SNR values.

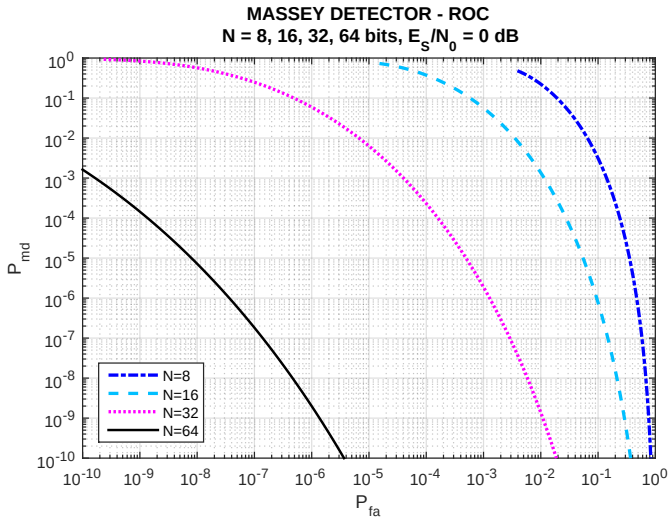

Fig. 3.11 Massey correlation detector: ROC curves for SNR $= 0$ dB and different pattern lengths.

3.10 The Extended Massey correlation detector

As explained in Section 3.8.2, for the Massey detector we have a false-alarm lower bound $P_{fa}^{(LB)} = 1/2^N$. For applications requiring low false-alarm rates, this limitation may be a problem. As an example, a target $P_{fa} = 10^{-6}$ (which is a realistic values for some applications, e.g. [73]) cannot be achieved by $N < 32$. Unfortunately, in some cases the use of a synchronization word with $N \geq 32$ can be a problem, because the introduced overhead may be too large, especially for small data frames. In this section we introduce a new solution, which allows to overcome this limitation.

The lower bound is due to the pdf discrete component in zero, which is induced by the Massey detector definition. If we have $\mathrm{sgn}(r_i) = \mathrm{sgn}(c_i)$ for any received symbol (an event with probability $1/2^N$), the test result is equal to zero. As a consequence, there is no way to further reduce the false-alarm probability from the lower bound: for positive thresholds we have $P_{fa} = 0$, but $P_{md} = 1$; so the pattern cannot be revealed and the detector is useless.

We now propose an enhanced definition of the Massey detector, that we call the *Extended Massey correlation detector*, which is based on the following idea. If at least one received symbol r_i has a sign different from the corresponding c_i symbol, the Massey correlation is applied. If all the signs agree, the soft correlation (which takes into account all the marker symbols) is applied.

Definition 2. The Extended Massey Correlation Detector. Given the binary antipodal pattern $\underline{c} = (c_1, \cdots, c_i, \cdots, c_N)$ and the observed real vector

$$\underline{r} = (r_1, \cdots, r_i, \cdots, r_N) \tag{3.31}$$

the Extended Massey correlation detector computes the statistical test:

$$\text{if } \exists i : \mathrm{sgn}(r_i) \neq \mathrm{sgn}(c_i) \;\rightarrow\; \Gamma_E = \sum_{\substack{i: \\ \mathrm{sgn}(r_i) \neq \mathrm{sgn}(c_i)}} r_i c_i \tag{3.32}$$

$$\text{if } \forall i : \mathrm{sgn}(r_i) = \mathrm{sgn}(c_i) \;\rightarrow\; \Gamma_E = \sum_i r_i c_i. \tag{3.33}$$

For negative thresholds, the test is identical to the Massey detector. As we will show afterwards:

- Since we can use positive thresholds, too, the lower bound limitation is eliminated.
- For positive thresholds the Extended test is better than or equal to the soft correlation.
- Overall, it is nearly optimal for both positive and negative thresholds, very close to the LRT.

To analyze this new test, we start from the analytical computation of its pdfs. We note that:

- We apply (3.32) if and only if $\Gamma_E < 0$.
- We apply (3.33) if and only if $\Gamma_E \geq 0$.

Then, for negative threshold values, the pdfs are equal to the continuous component of the Massey detector pdf computed in Section 3.7 (H_1) and Section 3.8 (H_0). For zero and positive threshold values we present two theorems to compute them.

3.10.1 Analytical computation of the Extended Massey detector pdf under H_1

Under H_1, the following theorem provides the pdf of the new test.

Theorem 4. The pdf under H_1 of the Extended Massey correlation detector is given by:
– For negative values:

$$\forall x < 0 \quad f_{\Gamma_E|H_1}(x) = f_{\Gamma_M|H_1}(x) \quad \text{given by (3.15).}$$

– For zero and positive values:

$$\forall x \geq 0 : f_{\Gamma_E|H_1}(x) = (1-p)^N \mathscr{F}^{-1}\left[\mathscr{F}\left(f_s(x)\right)^N\right]. \tag{3.34}$$

where s is a random variable with pdf given by

$$\begin{aligned} f_s(x) &= \frac{1}{1-p}\frac{1}{\sqrt{2\pi\sigma^2}}e^{-\frac{(x-1)^2}{2\sigma^2}} && \text{for} x \geq 0 \\ f_s(x) &= 0 && \text{for} x < 0. \end{aligned} \tag{3.35}$$

Proof. We suppose, without loss of generality, that all $c_i = +1$. For positive thresholds we have:

$$\forall x \geq 0 \; \Gamma_E = \sum_{i=1}^{N} r_i c_i = \sum_{i=1}^{N} r_i \;\; (\text{iff all } r_i \geq 0). \tag{3.36}$$

The probability that all $r_i \geq 0$ is equal to $(1-p)^N$.

We introduce the random variable

$$\delta(N) = \sum_{i=1}^{N} s_i \tag{3.37}$$

obtained as the sum of N independent random variables s_i corresponding to positive r_i with $c_i = +1$, i.e.,

$$s_i = 1 + n_i \;\; \text{with} \;\; s_i \geq 0.$$

The pdf of each of them is given by (3.35). (Note that this pdf is similar to the pdf of the random variable y depicted in Figure 3.3, only reflected on the positive axis.)

To derive the pdf of $\delta(N)$ we can apply the characteristic function approach:

$$f_{\delta(N)}(x) = \mathscr{F}^{-1}\left[\mathscr{F}(f_s(x))^N\right]. \tag{3.38}$$

Finally, the pdf of Γ_E under H_1 for positive values is given by:

$$\forall x \geq 0 : f_{\Gamma_E|H_1}(x) = (1-p)^N \mathscr{F}^{-1}\left[\mathscr{F}\left(f_s\left(x\right)\right)^N\right], \tag{3.39}$$

which is result (3.34).

For negative values we have $f_{\Gamma_E|H_1}(x) = f_{\Gamma_M|H_1}(x)$ given by (3.15) because we apply (3.32) if and only if $\Gamma_E < 0$: in this region the definitions of the Massey detector and the Extended Massey detector coincide. □

Given the pdf, we can compute the miss-detection probability.

Corollary 3. The miss-detection probability of the Extended Massey detector is given by:

$$\begin{aligned}
&\text{if } t<0: P_{md}=P(\Gamma_E<t|H_1)=\int_{-\infty}^{t} f_{\Gamma_M|H_1}(x)dx \\
&\text{if } t=0: P_{md}=P(\Gamma_E<0|H_1)=1-(1-p)^N \\
&\text{if } t>0: P_{md}=P(\Gamma_E<t|H_1)=1-(1-p)^N+\int_{0}^{t} f_{\Gamma_E|H_1}(x)dx
\end{aligned} \tag{3.40}$$

Proof. For negative thresholds, the pdf is equal to the Massey continuous pdf. For $t=0$, we obtain the integral of the Massey continuous component, which is the complement to one of its discrete component, *i.e.*, $1-(1-p)^N$ as in Corollary 1. For positive thresholds we sum to this term the integral of the Extended Massey pdf, which is distributed on the entire positive axis. For t going to infinity, the probability goes to one. □

3.10.2 Analytical computation of the Extended Massey detector pdf under H_0

The following theorem provides the pdf of the new test under H_0.

Theorem 5. The pdf under H_0 of the Extended Massey detector is given by:
– For negative values:

$$\forall x<0 \quad f_{\Gamma_E|H_0}(x)=f_{\Gamma_M|H_0}(x) \text{ given by (3.24).}$$

– For zero and positive values:

$$\forall x\geq 0 \;\; f_{\Gamma_E|H_0}(x)=\frac{1}{2^N}\sum_{d=0}^{N}\binom{N}{d}(1-p)^d p^{N-d}\mathscr{F}^{-1}[\mathscr{F}(f_s(x))^d\mathscr{F}(f_t(x))^{N-d}], \tag{3.41}$$

where s is a random variable with pdf given by (3.35) and t is a random variable with pdf:

$$\begin{aligned}
f_t(x)&=\frac{1}{p}\frac{1}{\sqrt{2\pi\sigma^2}}e^{-\frac{(x+1)^2}{2\sigma^2}} && \text{for } x\geq 0 \\
f_t(x)&=0 && \text{for } x<0.
\end{aligned} \tag{3.42}$$

Proof. We suppose without loss of generality that all $c_i = +1$. For positive thresholds we have:

$$\forall x \geq 0 \quad \Gamma_E = \sum_{i=1}^{N} r_i c_i = \sum_{i=1}^{N} r_i \ \ (\text{iff all } r_i \geq 0). \tag{3.43}$$

Under H_0 we have $r_i = d_i + n_i$, where d_i are random symbols. All the r_i are positive. Let us denote by:

- D the number of positive symbols r_i corresponding to $d_i = +1$.
- $D' = N - d$ the number of positive symbols r_i corresponding to $d_i = -1$.

We note that:

$$P(D = d) = \frac{1}{2^N} \binom{N}{d} (1-p)^d p^{N-d}, \tag{3.44}$$

where the first two terms are the probability that an $N-$bit random vector contains d symbols equal to $+1$ and the last two are the probability that all the symbols of the corresponding observed vector are positive. Let us consider:

$$\zeta(d, d') = \delta(d) + \varepsilon(d') = \sum_{i=0}^{d} s_i + \sum_{i=0}^{d'} t_i. \tag{3.45}$$

The first term $\delta(d)$ corresponds to the components with $r_i \geq 0$ and $d_i = +1$. It is the sum of d random variables s_i with pdf (3.35) introduced for studying H_1. The pdf of $\delta(d)$ is then given by:

$$f_{\delta(d)}(x) = \mathscr{F}^{-1}\left[\mathscr{F}(f_s(x))^d\right]. \tag{3.46}$$

The second term $\varepsilon(d')$ corresponds to the components with $r_i \geq 0$ and $d_i = -1$ is obtained as the sum of d' independent random variables t_i,

$$t_i = -1 + n_i \ \text{ with } \ t_i \geq 0.$$

The pdf of each of them is given by (3.42). (Note that this pdf is similar to the pdf of the random variable z depicted in Figure 3.8, only reflected on the positive axis.)

The pdf of $\varepsilon(d')$ can be computed by using the characteristic function approach:

$$f_{\varepsilon(d')}(x) = \mathscr{F}^{-1}\left[\mathscr{F}(f_t(x))^{d'}\right].$$

Finally, we can group together all these results to get the pdf of the Extended detector under H_0 for $x \geq 0$:

$$f_{\Gamma_E|H_0}(x) = \sum_{d=0}^{N} P(D=d) f_{\zeta(d,N-d)}(x)$$
$$= \sum_{d=0}^{N} \frac{1}{2^N} \binom{N}{d} (1-p)^d p^{N-d} \mathscr{F}^{-1}[\mathscr{F}(f_s(x))^d \mathscr{F}(f_t(x))^{N-d}],$$

which is result (3.41).

As for Theorem 4, for negative thresholds we have $f_{\Gamma_E|H_0}(x) = f_{\Gamma_M|H_0}(x)$ given by (3.24), because we apply (3.32) if and only if $\Gamma_E < 0$, then in this region the two definitions coincide. □

Given the pdf, we can compute the false-alarm probability.

Corollary 4. The false-alarm probability of the Extended Massey detector is given by:

$$\begin{aligned} &\text{if} t < 0 : P_{fa} = P(\Gamma_E \geq t | H_0) = \int_t^{0^-} f_{\Gamma_M|H_0}(x)dx + \frac{1}{2^N} \\ &\text{if} t = 0 : P_{fa} = P(\Gamma_E \geq 0 | H_0) = \frac{1}{2^N} \\ &\forall t > 0 \;\; P_{fa} = P(\Gamma_E \geq t | H_0) = \int_t^{+\infty} f_{\Gamma_E|H_0}(x)dx. \end{aligned} \tag{3.47}$$

Proof. For negative thresholds we have the same false-alarm rate of the Massey detector. For $t = 0$, the integral covers all the non-negative values then it is equal to $1/2^N$ (for the Massey detector this probability is concentrated in the origin, while for the Extended detector it is distributed on the entire non-negative axis). For positive thresholds the integral is applied only to the positive portion of the Extended detector pdf. □

3.10.3 Extended Massey detector performances

For negative thresholds, the Extended Massey detector has the same performances of the Massey detector, but it overcomes the lower bound limitation on the P_{fa} because the threshold can assume positive values, too. As an example, the Extended detector performances in terms of P_{fa} and P_{md} vs. thresholds are reported in Figure 3.12 for

SNR = 6 dB and $N = 8$ bits. For comparison, in the same figure we have also plotted the performances of the Massey detector and the soft correlation (3.10). By looking at these results we observe that:

- For negative thresholds the Extended Massey performances are identical to those of the Massey detector. In fact, in this region the detector rules are exactly the same.
- For the Extended Massey detector, the lower bound limitation no longer applies: for positive thresholds the P_{fa} becomes smaller than the lower bound $P_{fa}^{(LB)} = 1/2^N = 3.90 \cdot 10^{-3}$ where the Massey detector curve stops.
- For positive thresholds the Extended Massey performances becomes similar to the soft correlation ones for large thresholds. In this region, the two detectors use the same correlation rule but their pdfs are different. To explain this behavior let us suppose again (without loss of generality) that all $c_i = +1$. The Extended Massey detector applies the soft correlation rule under the condition that all r_i are positive. Instead, the soft correlation detector always applies it, for any received vector. In this second case, small positive values of the test are generated by vectors $\underline{r}$ with both negative and positive r_i, while large positive values are generated by vectors $\underline{r}$ that, with high probability, have all positive symbols. Then, the performances of the two tests are different for small positive values, and become similar for large values.

3.11 Comparison against LRT, soft and hard correlation

In this section we compare the performances of the Massey detector and the Extended Massey detector against the optimal LRT, the soft correlation and the hard correlation. As an example, the ROC curves of these detectors for SNR $= 0$ dB are compared in Figure 3.13 for $N = 8$ bits and in Figure 3.14 for $N = 64$ bits. By looking at Figure 3.13 we can observe that:

- As expected, the Massey detector curve stops at the lower bound $P_{fa}^{(LB)} = 1/2^N = 3.90 \cdot 10^{-3}$ (where also the hard correlation curve stops). The Extended Massey detector does not suffer this limitation.

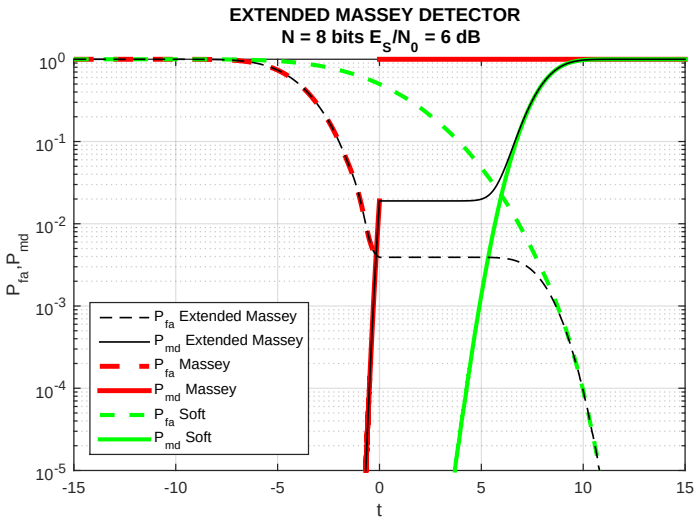

Fig. 3.12 Extended Massey correlation detector: P_{fa} and P_{md} vs. threshold, for $N = 8$ bits and SNR $= 6$dB.

- Even if the SNR is quite low, the Extended Massey detector ROC is essentially coincident with the optimal LRT ROC curve and much better than the soft and hard correlation curves.

These results are confirmed by Figure 3.14 for $N = 64$ bits. For this length, there is no need to use the Extended Massey detector, because the lower bound $P_{fa}^{(LB)} \geq 5.42 \cdot 10^{-20}$ is negligible. Also in this case, the Massey detector performances are very close to the optimal LRT ones and much better than the soft and hard correlation curves.

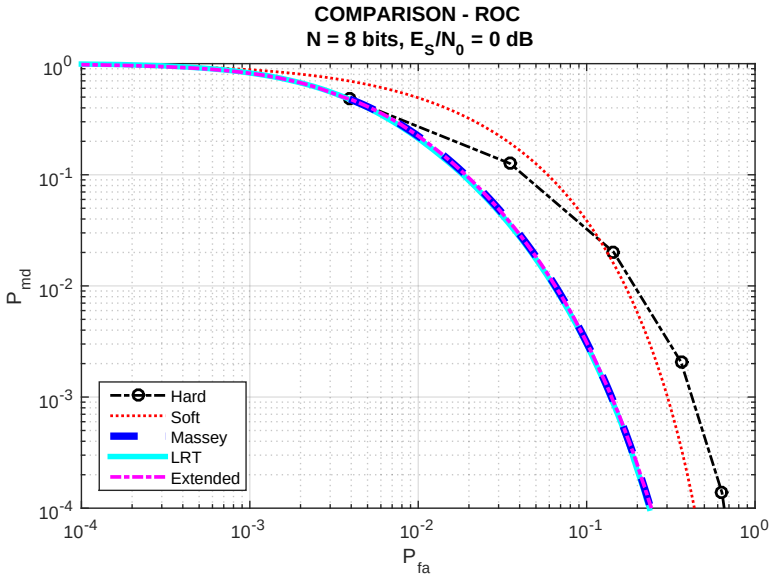

Fig. 3.13 ROC curves for $N = 8$ bits and SNR $= 0$ dB: comparison between Extended Massey detector, Massey detector, LRT, Soft correlation, Hard correlation.

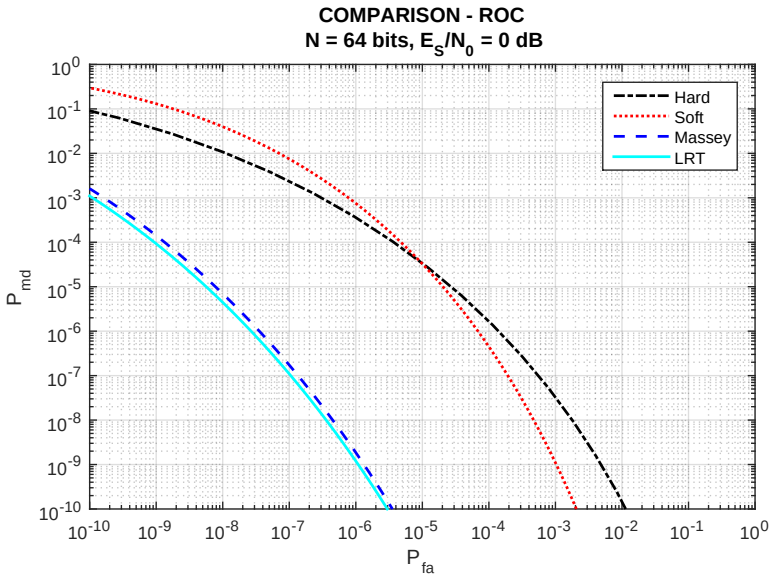

Fig. 3.14 ROC curves for $N = 64$ bits and SNR $= 0$ dB: comparison between Massey detector, LRT, Soft correlation, Hard correlation.

3.11.1 Miss-detection vs. SNR performances

To better quantify the differences between the detectors, we now consider the miss-detection vs. SNR performances at fixed false-alarm rate. Fixed a target value for P_{fa}, by using Corollary 2 for the Massey detector or Corollary 4 for the Extended Massey detector we can compute the minimum value of the threshold t which guarantees to achieve it. Given t, by using Corollary 1 for the Massey detector or Corollary 3 for the Extended Massey detector, we can compute the corresponding value of the P_{md}. In this way, we can plot the miss-detection probability as a function of the SNR, for the chosen target false-alarm probability value.

These curves are very useful for practical applications, where the systems are typically designed for achieving a given value P_{fa} (the so-called CFAR (Constant False-Alarm Rate) property): these results show which are the corresponding P_{md} values obtained for different SNR values. Moreover, fixed the target P_{fa} and the target P_{md} they provide the SNR value necessary to achieve them.

As an example, Figure 3.15 and Figure 3.16 show the results for $N = 8$ and $N = 64$, with different target false-alarm rates. In Figure 3.15, since $N = 8$ is a small value, we have considered the Extended Massey detector. We can observe that it is very close to the optimal LRT, with a penalty limited to a small fraction of dB even when the SNR is low, which disappears at higher SNR values. The gains achieved by the Extended Massey detectors with respect to hard and soft correlation are large. If we fix target $P_{md} = P_{fa} = 10^{-2}$ the gain is 3 dB from hard and more than 6 dB from soft (that in this scenario is worse than hard correlation, which is not surprising because the soft correlation is not derived as an optimal test). The gains are larger for lower miss-detection probabilities.

In Figure 3.16, since $N = 64$ is a large value and the lower bound is negligible, we have considered the Massey detector. It shows a limited penalty from the optimal LRT, even when the SNR is low. At target $P_{md} = P_{fa} = 10^{-6}$ the Massey detector gains 2.5 dB with respect to the hard correlator and 3 dB from the soft. Higher gains are achieved at lower miss-detection probabilities.

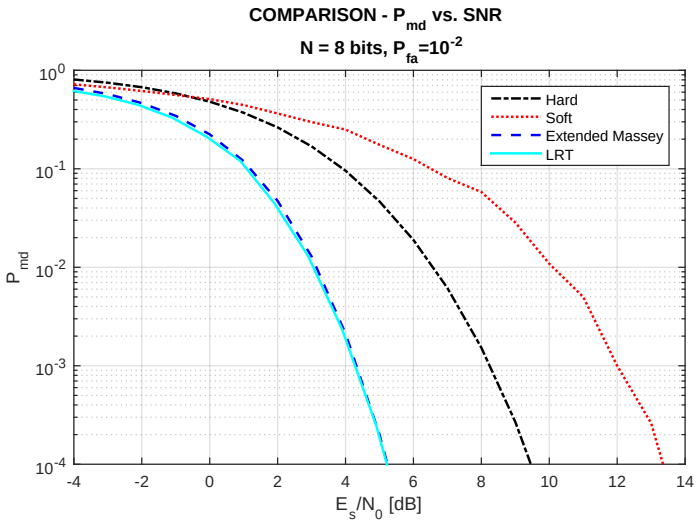

Fig. 3.15 Extended Massey detector: P_{md} vs. SNR, for $N = 8$ bits and $P_{fa} = 10^{-2}$.

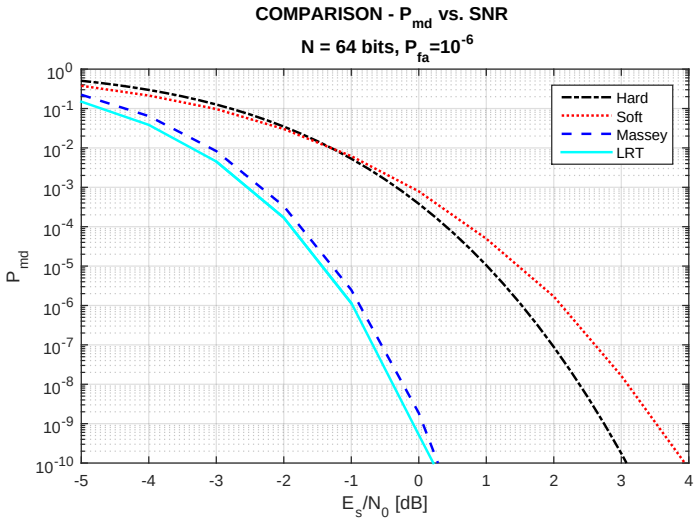

Fig. 3.16 Massey detector: P_{md} vs. SNR, for $N = 64$ bits and $P_{fa} = 10^{-6}$.

3.12 Some Aspects for Practical Implementation

The presented results show that the Extended Massey and the Massey detector:

- are nearly optimal tests at both low and high SNR values, with penalty in the order of a fraction of dB from the optimal LRT.
- are much better than the popular hard and soft correlation tests.

The choice between the two Massey detectors depends on the target false alarm rate. If it is below the lower bound $1/2^N$ we use the Extended Massey detector, otherwise we use the Massey detector. As a consequence, the Extended Massey detector looks more appropriate for small N (e.g., for $N \leq 16$) and the Massey detector for large N.

The complexity of the two Massey detectors is very low. Obviously it is slightly higher than the complexity of the hard correlation which works on bits, but it is essentially identical to soft correlation complexity and much lower than LRT complexity, which may be a serious issue for high bit rate applications.

Moreover, if we look at the false-alarm and miss-detection vs. threshold curves of the Massey detectors shown in Figures 3.6, 3.7, and 3.12, we can see that they have a favorable behavior for threshold setting, because the curves slope is not too pronounced. Having fixed the target error rate to be achieved, the threshold can be easily obtained by inverting the analytical curves.

Chapter 4

Cognitive Radio: Spectrum Sensing[1]

4.1 Introduction

3G and 4G technologies have mainly focused on the mobile broadband use case, providing enhanced system capacity and offering higher data rates. This focus will clearly continue in the future 5G era where they will provide mobile telephony and mobile broadband with wide area coverage. Moreover, they will be extended by lot of new applications and lot of new use cases and new scenarios. Some of them can be the evolution of existing technologies but some of them will need new technologies. In addition, the upcoming '5G wireless networks' is sought to offer wireless access to anyone and anything. Thus, in the future, wireless access will go beyond humans and expand to serve any entity and device that may benefit from being connected. Thus, 5G networks will undoubtedly explore unlimited possibilities until an official standard by telecommunications standardisation bodies such as ITU-R, IMT and the 3GPP.

Machine type communications will be more and more important in the future. This will include communications for electronics and home appliances, communications for transports, communications for medical equipments, internet of things and many more. A lot of dense communications will be probably carried by existing wireless access technologies but some of these use cases will have so high requirements that they will require new wireless access technologies. For example, ultra

[1] Part of the work described in this chapter has been previously published in [49, 44, 146, 147, 45–47]

reliable communications may be needed for critical infrastructure, or for industrial processes. This may very well require new radio access technologies. Car-to-car or car-to roadside communication will be introduced for traffic safety and traffic control. And new ways to communicate will be exploited for example, communicating directly between devices. All these factors, including new technological advancements, emergence of new applications and growth in user demand for wireless services and number of devices contribute to the need for additional licensed or in some respect repurposed spectrum to accommodate new capabilities of 5G wireless systems.

Moreover, each use cases of 5G have specific technical requirements that need to be addressed through adequate design of the 5G radio interface(s) and access to appropriate frequency ranges. While some of these applications, such as high resolution video, would require ultra-fast connection speeds, others might need very robust performance and wide reaching range. It should be noted that some of the 5G applications will be supported by evolved 4G systems with existing spectrum. However, 5G systems will provide additional capabilities and as a result, consideration of required spectrum for 5G should include all applications foreseen for future networks.

To provide an example for factors affecting the amount of spectrum, ultra-high speed connections in the range of multi-gigabit per second could potentially be achieved through using ultra-wide carrier bandwidths in the order of up to several hundred MHz or more. An example could be fast downloads of 4k/8k video content, which using wide channels and multi-gigabit speeds, would take seconds. Another example of factors affecting the spectrum choice is the case of ultra-reliable communications for mission critical applications such as public safety, where obstacle and ground penetration for ubiquitous coverage in critical times would require use of lower frequencies such as those in the lower Ultra-High Frequency (UHF) band. In order to come up with a mapping between applications and required spectrum, Table 4.1 lists potential spectrum-related implications of various high- level requirements for future 5G systems. Licensed spectrum is currently available for mobile uses in small chunks (contiguous 50 MHz at most), which fails to meet the 5G target data rate. In fact, predicted spectrum demands from ITU-R suggests the extra spectrum requirements in 2020 will be 12801720 MHz [15] to supplement the current allocated spectrum in mobile networks. Significant portion of sub-6GHz bands (with ideal propagation characteristics for mobile uses), is currently allocated to non-mobile spectrum users, e.g., military, radar, etc., across the globe.

Table 4.1 Potential Spectrum-Related Implications of various 5G Requirements [15]

High-Level Requirement	Potential Spectrum-Related Implications
Ultra-high speed radio links	Ultra-wide carrier bandwidths, e.g. 500 MHz Multi-gigabit fronthaul/backhaul
High speed radio links	Wide carrier bandwidths, e.g. 100 MHz Gigabit fronthaul/backhaul
Support for low to high-Doppler environment	Depends on the throughput requirement
Ultra-low latency	Short range implications
Low latency	Mid-short range implications
Ultra-high reliability radio links	Severe impact of rain and other atmospheric effects on link availability in higher freq., e.g. mm-wave for outdoor operations
High reliability radio links	Impact of rain and other atmospheric effects on link availability in higher freq., e.g. mm-wave for outdoor operations
Short range	Higher frequencies, e.g. mm-wave
Long range	Lower frequencies, e.g. sub-3 GHz
Ground/obstacle penetration	Lower frequencies, e.g. sub-1 GHz
Operation in cluttered environment	Diffraction dominated env. in lower freqs. Reflection dominated env. in higher freqs.
Operation near fast moving obstacles	Frequency-selective fading channels
Mesh networking	High-speed distributed wireless backhaul operating in-band or out-of band

Wireless channels are usually characterized by a fixed spectrum assignment policy. Electromagnetic spectrum is strictly regulated and licensed by governmental entities, for instance, Federal Communications Commission (FCC) in US, Office of Communications (OFCOM) in UK, Ministero dello Sviluppo Economico - Dipartimento per le Comunicazioni in Italy and Nepal telicom Authority (NTA) in Nepal. The rapid development in the field of wireless communications certainly creates a big challenge for every licensing organization to accommodate all the new applications, services and use cases of 5G with the limited electromagnetic spectrum. The frequency allocation chart of UK [57] (see Figure 4.1), Italy [57] and US [71] shows that large portion of the radio spectrum is already assigned to traditional services (Mobile, Maritime Mobile, Fixed Satellite Services, Radio Navigation). Even though there are few genuinely unlicensed bands, a good example of which is Industrial

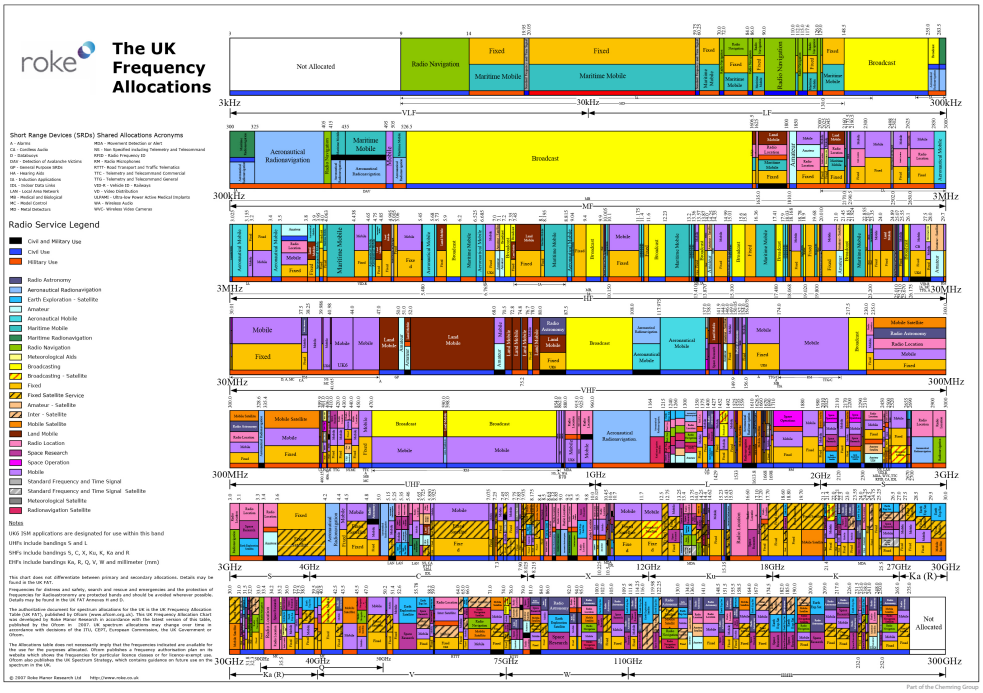

Fig. 4.1 OFCOM frequency allocation chart for UK [57]

Scientific & Medical (ISM) band in 2.4 GHz, available which could be the possible solution for accommodating new services, but there are already multiple wireless technologies in these bands such as 802.11 WLAN, Cordless Phones, Bluetooth, Wireless Personal Area Network (WPAN), HIPERLAN etc. Some other examples of unlicensed frequency bands include UNII-1 and UNII-2 bands where systems such as IEEE802.11a WLAN and IEEE802.11n WLAN operate. This rapid expansion in the field of Wireless Communications has led to a common belief that the day is not too far when the increasing demands of the spectrum access will lead to the spectrum scarcity.

Frequency spectrum is a scarce resource in the field of wireless communication. Thus, its utilization efficiency should be made as efficient as possible. In contrast, several measurements carried out to verify the spectrum utilization in different countries have shown significant under-utilization of the allocated frequency bands. Noticeably, the Digital Television (DTV) band is an example of inefficient spectrum use, since depending on the geographical location, only certain channels are always occupied both in the temporal and spatial domains. Concerning the same, FCC Spectral Policy Task Force reported that typical radio channel occupancy is less than

15% while the peak occupancy is close to 85% in US [70]. Similar measurements carried out in various countries show that most of the radio frequency spectrum is inefficiently utilized with spectrum utilization mostly in the range of 5% to 50% [96, 166]. These thought-provoking statistics in synergy provide the drive for main challenges facing the spectral world. Experts around the world are interested in tackling how we can manage future spectrum more effectively to serve for 5G use cases. A number of technologies and techniques have been identified as enablers for the 5G wireless networks and among them is Cognitive Radio technology. Many studies are suggesting that 5G could exploit Cognitive Radio approaches to increase band availability, especially for very small cells.

4.1.1 Cognitive Radio Technology

Cognitive Radio was first officially proposed by Joseph Mitolla II at the Royal Institute of Technology [123, 124] but the idea of using learning and sensing machines to improve radio spectrum was envisioned several decades earlier. Now, Cognitive Radio is seen as an emerging solution to the problem of spectrum scarcity. It has an implicit mechanism of spectrum sensing intelligence and decision making that enables opportunistic access to the under-utilized frequency slots of licensed or unlicensed frequency bands which is also evident from the definitions of Cognitive Radio adopted by FCC: [40]

> *"A radio or system that senses its operational electromagnetic environment and can dynamically and autonomously adjust its radio operating parameters to modify system operation, such as maximize throughput, mitigate interference, facilitate interoperability, access secondary markets."*

There are some more definitions of Cognitive Radio which are similar in theme. Cognitive Radio defined by Haykin [87] is:

> *"Cognitive radio is an intelligent wireless communication system that is aware of its surrounding environment (i.e., outside world), and uses the methodology of understanding by building to learn from the environment and adapt its internal states to statistical variations in the incoming RF*

> *stimuli by making corresponding changes in certain operating parameters (e.g., transmit-power, carrier-frequency, and modulation strategy) in real-time, with two primary objectives in mind: highly reliable communication whenever and wherever needed: efficient utilization of the radio spectrum."*

Being a multidisciplinary nature of subject, working on Cognitive Radio is more challenging and therefore exciting to most of the researchers. However, Cognitive Radio Technology is still in its infancy, better to say in a research phase, despite few attempts are done in developing wireless communication standards based on the concept of Cognitive Radio. IEEE 802.22 Wireless Regional Area Network (WRAN) [3] is the first international standard exploiting TV white spaces using Cognitive Radio Technology. WRAN is envisioned to operate in Very High Frequency (VHF) and Ultra High frequency (UHF) ($54 - 862$ MHz) bands currently licensed for analog and digital television broadcasting and wireless microphones. ECMA TC48-TG1 [64], IEEE 802.11 [94], Dynamic Spectrum Access Networks Standards Committee (DySPAN - SC) [156], IEEE 802.16 [7], and IEEE 802.19 [6] are some other emerging standardization initiatives based on the platform of Cognitive Radio concept.

The Cognitive Radio Network paradigm defines two user environments coexisting in a common spatial location exploiting the same radio environment in a quasi-cooperative manner. In Cognitive Radio terminology, a Primary User (PU) refers to incumbent licensees, which have a legal priority to use the allocated spectrum whereas a Secondary User (SU) refers to unlicensed users who seek opportunity to use the spectrum when primary users are idle. The user territory of primary users and secondary user corresponds to primary user environment and secondary user environment respectively. Some of the common technologies operated using legacy rights are Global System for Mobile (GSM), Worldwide Interoperability for Microwave Access (WiMAX) and LTE.

The concept behind Cognitive Radio (CR) is to exploit the underutilized spectral resources by reusing them in an opportunistic manner. SU adjust its carrier frequency, transmit power, modulation, coding etc to make best use of the available spectrum and to achieve the desired quality of service. Even though PU no doubt can use the spectrum as per their requirements, SU can access spectral resources of PU, when PU is not using it and vacate the frequency band as soon as the PU becomes active

without causing any interference. It is required that the unlicensed secondary users should not cause harmful interference to the licensed primary users. Therefore, SU have to make sure that the licensed spectrum bands are not utilized by the PU before they access these bands, which makes spectrum sensing one of the key technologies for the implementation of CR.

4.1.2 Spectrum Sensing

Among the functionalities provided by Cognitive Radio, Opportunistic Spectrum Access (OSA) is devised as a dynamic method to increase the overall spectrum efficiency by allowing SUs to utilize unused licensed spectrum. For this purpose, a correct identification of channel vacuity conditions by means of spectrum awareness techniques becomes fundamental. Spectrum sensing is defined as "*The task of finding underutilized bands both in temporal and spatial domain, by sensing the radio spectrum in the local neighborhood of the Cognitive Radio receiver in an unsupervised manner*" [88]. Literature referring to these underutilized portions of spectrum as *spectrum holes* or *white spaces*.

Specifically, the task of spectrum sensing may involve the following sub-tasks: [88]

- Detection of spectrum holes;
- Spectral Resolution of each spectrum hole;
- Estimation of spatial directions of incoming interferes;
- Signal classification;

In essence, spectrum hole detection is a very critical component of Cognitive Radio Concept. Table 4.2 shows the currently understood requirements about the secondary devices (CPEs) sensitivity for three signal types. According to 802.22 Working Group [3], for a receiver noise figure of 11 dB, the resulting required SNR for the secondary receiver is listed, where noise power is calculated over a bandwidth of 6 MHz for a TV signals and over a bandwidth of 200 KHz for wireless microphones. It is also clear from above Table 4.2 that each SU sensors is required to operate under very low SNR values. In general, such low SNR values must be expected in all deployment scenarios of CR to protect the primary users from undue

Table 4.2 Receiver Parameter for 802.22 WRAN [3]

Parameter	Analog TV	Digital TV	Wireless Microphone
Probability of Detection	0.9	0.9	0.9
Probability of false alarm	0.1	0.1	0.1
Channel Detection Time	$\leq$ 2s	$\leq$ 2s	$\leq$ 2s
Incumbent Detection Threshold	-94dBm	-116dBm	-107dBm
SNR	1dB	-21dB	-12dB

interference. Thus, the goal is to design detection algorithm that meet the given sensing constraint at very low SNR.

Spectrum sensing is the most challenging task which should be taken with prime importance for the Dynamic spectrum Access (DSA) and autonomous exploitation of locally unused spectrum, to provide new paths for spectrum access. It is the enabling unit of SU for the accurate identification and exploitation of the PU spectrum. Moreover, the detection performance of the spectrum sensing device quantifies the interference level caused to the PU transmission in the spectrum band.

Several spectrum sensing methods have been considered for Cognitive Radio applications including Energy Detection (ED) [164], Match Filtering [29], Feature Detection Algorithms [33], proposed for individual SU and their cooperative counterpart for multiple SU sensing. A survey of different spectrum sensing methodologies for Cognitive Radio [18, 16] shows that a remarkable spectrum sensing performance can be attained with feature detection (e.g., Cyclic Prefix (CP) based detector and Pilot Based Detector) that exploit some known characteristic of PU signals at the expense of long observation time. Even more, Matched Filtering is assumed to perform best with high processing gain at the constraint of knowledge of PU signal properties [141]. ED is considered to be the simplest detector which does not make any assumption on the PU signal statistics. Feature detection lies in the middle of these two extremes and only makes certain assumptions on the statistical properties of the PU signal while designing the PU signal. Even though Match filtering and feature detection algorithms are known to outperform ED algorithm, the requirement

of knowledge of the PU signal characteristics at the expense of long observation time make them less suitable for spectrum sensing in Cognitive Radio Network, where knowledge of primary user signal is usually unavailable.

In recent years, sensing techniques based on the eigenvalues of the received signal co-variance matrix evolved as a promising solution for spectrum sensing [139]. EBD schemes can be categorized as "semi-blind EBD schemes": which assume knowledge of noise level and "blind EBD schemes": which do not assume noise level knowledge. Methods belonging to the first class provide better performance when the noise variance is known exactly, whereas blind methods are more robust to uncertain or varying noise level.

Semi-blind detection algorithms like ED and EBD achieve very good performance in a known noise power level scenario. Thus, knowledge of noise power level plays prime role for the better performance ED and EBD spectrum sensing algorithms. Unfortunately, in real practice, the noise uncertainty is very often present.

4.1.3 Spectrum sensing under practical imperfection

The spectrum awareness problem for a CR system is different from the legacy wireless communication ststems, for these reseasons: (i) no prior knowledge of the PU signal structure, channel and noise variance is available (ii) the information on spectrum occupancy, SNR, etc. must be acquired at the shortest possible time, (iii) primary SNR may be very low due to fading and multi-path phenomenon, and (iv) noise/interference power may vary in time giving rise to noise/interference power uncertainty. Thus, despite the significant volume of available literature on spectrum sensing under ideal scenarios, investigation under practical constraints and imperfections are still lacking [154].

In this direction, the main focus of this chapter is to provide a comprehensive analysis of the popular Semi-blind' spectrum techniques (ED and EBD) under two of the most important practical imperfections.

1. Noise uncertainty
2. Uncertainty on PU traffic

4.2 Semi-blind SS techniques under noise uncertainty

In real world scenario, the information about the PU signal is generally not available and, even if available, Match Filtering and Feature Detection algorithms needs sensing receivers for all types of signals. Thus, for CR application the most popular sensing algorithms are semi-blind spectrum sensing techniques which requires the knowledge of noise floor. Performance of these algorithms over AWGN and different fading channels has been studied in many works including [164, 180, 50, 51, 105, 162, 161]. These works assumed a perfect knowledge of the noise power at the receiver, which allows for a perfect threshold design. However, in real systems the detector does not have a prior knowledge of the noise level. In recent years, variation and unpredictability of the precise noise level at the sensing device have been identified as a critical issue, which is also known as *noise uncertainty*.

Noise is an unwanted random process which may arise from several sources in the external environment as well as from every components of a receiver chain. In real world scenarios, noise distribution is not known to infinite precision and the noise is neither perfectly Gaussian, perfectly white, nor perfectly stationary [159]. Therefore, the noise variance in practice has to be estimated by using a proper noise calibration method. The noise calibration can be done either during the sensing process or by carrying out on-site Out of Bands (OoB) measurements. Another option for noise calibration is to use inband measurements at the frequencies where the pilot is absent so that the noise statistics can be calibrated at the pilot frequencies [158].

The noise estimation can be perfect in the ideal case, however, in practice, accurate estimation of the noise variance is not possible, thus limiting the performance of the semi blind sensing techniques like E and EBD, at low SNRs. For ED, the noise variance uncertainty may lead to SNR wall phenomenon due to which it is not possible to achieve the robust detection performance beyond a certain SNR value even by increasing the sensing duration [158]. In this work, we present two alternative for the estimation of the noise variance:

1. Offline noise estimation: In this approach, a maximum likelihood noise variance is used under the assumption that pure noise samples are available in prior. The pure noise samples can be obtained from inband measurement or from out of band measurements as stated above.

2. Online noise estimation: In this approach, noise variance is estimated implicitly from auxiliary received signal slots which are declared noise only samples by the detection algorithms.

Thus, in this section we introduce the idea of auxiliary noise variance estimation for noise uncertainty. Later Hybrid approach of ED and EBD are presented and the impact assessment of noise power estimation is then analysed.

4.2.1 Energy Detection and its performance under Noise Uncertainty (State-of-art)

For CR application, the most popular sensing algorithm is the simple ED that compares the energy of the received signal with the noise variance σ_v^2. ED requires the knowledge of σ_v^2 value. Performance of ED in AWGN and different fading channels has been studied in many works including [164, 50, 51, 105]. These works assumed a perfect knowledge of the noise power at the receiver, which allows for perfect threshold design. In that case ED can work with arbitrarily small value of false alarm probability P_{Fa} and Miss-detection Probability P_{Md}, by using sufficiently large observation time, even in low SNR environment [159].

With the scope of reducing the impact of noise uncertainty on the signal detection performance of ED, several researches have been proposed including [158, 159, 118, 119]. Hybrid Spectrum Sensing Algorithms based on the combination of ED and Feature Detection techniques have been proposed for the reduction of the effect of noise variance uncertainty [125]. Similar Hybrid Spectrum Sensing approach was discussed in [19] utilizing the positive points of ED and Covariance Absolute Value detection methods while Sequeira et al. [152] used Akaike Information Criteria (AIC), Minimum Description Length (MDL) and Rank Order Filtering (ROF) methods for noise power estimation in presence of signal for energy based sensing. In [159] the fundamental bounds of signal detection in presence of noise uncertainty are analyzed. This study showed that there are some SNR thresholds under noise uncertainty known as *SNR Wall*, that prevents achieving the desired performance even if the detection interval is made infinitely large. It concludes that the robustness of any detector can be quantified in terms of the *SNR Wall* giving the threshold below which weak signals cannot be detected reliably no matter how many samples are taken. In [119] authors performed the asymptotic analysis of the Estimated Noise Power

(ENP) to derive the condition of *SNR Wall* phenomenon for ED. They suggested that the *SNR Wall* can be avoided if the variance of the noise power estimator can be reduced while the observation time increases. Yonghong Zeng [182] proposed a uniform noise power distribution model for the noise uncertainty study of ED in low SNR regime. Similarly, [109] proposed a discrete-continuous model of the noise power uncertainty for the performance analysis of the ED in presence of noise uncertainty. Performance of ED using Bartlett's estimate is studied in [85].

4.2.2 Eigenvalue Based Detection and its performance in Noise Uncertainty (State-of-art)

Indeed, in recent years various new algorithms able to outperform ED have been applied to CR, mostly based on Random Matrix Theory (RMT) and information theoretic criteria. Two thorough reviews have been presented in [183] and [180]. Different diversity enhancing techniques such as multiple antenna, cooperative and oversampling techniques have been introduced in the literature to enhance the spectrum sensing efficiency in the wireless fading channels [143, 162, 181, 117, 169]. Most of these methods use the properties of the eigenvalues of the received signal's co-variance matrix and use results from advanced RMT. In particular, sensing techniques based on the eigenvalues of the received signals co-variance matrix recently emerges as a promising solution, as they also do not require a prior assumption on the signal to be detected, and typically outperform the popular ED method when multiple sensors are available. The various EBD algorithms can be divided in two classes:

A. Those that require the prior knowledge of the noise variance σ_v^2 (called"semi-blind" in [180]). This class includes channel independent tests [183], and Roy's Largest Root Test (RLRT) [148] which shows the best performance in this class (see Sub-Section 4.2). [This class also includes classical ED]

B. Those that do not require knowledge of σ_v^2 (called "blind" in [180]). This class includes the Eigenvalue Ratio Detection (ERD) [179], channel and noise-independent tests [183], information theoretic criteria detectors like the AIC and the MDL [169], and the Generalized Root Test (GLRT) [26], which shows the best performance in this class.

Methods belonging to the first class provide better performance when the noise variance is known exactly, whereas blind methods are more robust to uncertain or varying noise level. Recently, few research works have studied the impact of noise variance uncertainty and their effect in semi-blind EBD including [129, 139, 104]. In [129] author showed the importance of the accurate noise estimation for the EBD algorithms performance.

4.2.3 Model Scenario

This chapter focuses on the scenario described below:

- Single, unknown, primary signal. Its samples are modelled as Gaussian and independent.
- Flat-fading channel, constant over the entire sample window.
- Additive Gaussian white noise.

The problem is formulated as a simple binary test between the mutually exclusive hypotheses:

$\mathscr{H}_0$ (single primary signal absent) and $\mathscr{H}_1$ (single primary signal present).

This model is mostly used in detection theory because it allows a clear analytical approach and represents a benchmark for the case of non-parametric analysis of a single unknown primary signal. In particular relating to CR applications, where it is very popular and it was adopted by many relevant papers (including work by Debbah [26], and many others). The reason is that, despite of its simplicity, it is well matched to many practical situations:

1. *Single primary user.* In many CR scenarios, the primary signal of interest for a secondary opportunistic CR network is unique. This is the case, for example, in reuse of TV signal bands [3] or the coexistence between a Wi-Fi access point and a Wireless Sensor Network (WSN) or Bluetooth in the 2.4 GHz band, two typical CR applications that can already be realized in practice. Moreover, when multiple sources are present, the performance essentially depends on the component with the highest received power.

2. *Gaussian primary signal*. Most CR sensing algorithms working on the time-axis use non-parametric detection that does not exploit the (complete or limited) knowledge of the signal shape. This is a realistic assumption for several CR wireless applications: even if we know that the primary signal has a PSK/QAM/OFDM format, the secondary network is not synchronized, neither in carrier nor in time (this would require a great amount in complexity, not available for most applications). Then, the I/Q samples does not corresponds to the constellation signals and do not have special properties (e.g. constant envelope for PSK signals). Under these conditions, the Gaussian approximation for the signal amplitude turns out to be appropriate for many practical situations.

3. *Uncorrelated signal samples*. In practical CR sensing, some correlation between adjacent samples may be present , but (a) it strongly depends on the shape of the transmitting and the receiver filters and (b) the sampling frequency is completely asynchronous with respect to the received signal. For this reason, it is difficult to be modelled. Furthermore, including it into the framework is expected to have a negligible impact on the detector performance.

4. *Channel and noise*. The flat fading channel assumption is rather realistic when the sampling window time is relatively short and the system mobility is limited, which is the typical scenario for current CR applications. Finally, the Gaussian model for the noise is appropriate in general. (Impulsive noise is usually of secondary importance for CR wireless applications.)

4.2.4 Mathematical framework

The detector builds its test statistic from K sensors (receivers, nodes or antennas) and N time samples for each of them. Let,

$$\boldsymbol{y}(n) = [y_1(n) \cdots y_k(n) \cdots y_K(n)]^T, \tag{4.1}$$

be the $K \times 1$ received vector at time n, where the element $y_k(n)$ is the discrete baseband complex (I/Q) sample at receiver k and time n. Under $\mathscr{H}_0$, the received vector contains only noise and consists of K independent complex Gaussian noise

samples with zero mean and variance σ_v^2:

$$\boldsymbol{y}(n)|_{\mathscr{H}_0} = \boldsymbol{v}(n), \tag{4.2}$$

where $\boldsymbol{v}(n) \sim \mathscr{N}_{\mathbb{C}}(\boldsymbol{0}_{K\times 1}, \sigma_v^2 \boldsymbol{I}_{K\times K})$.
Under $\mathscr{H}_1$, the received vector contains signal plus noise:

$$\begin{aligned} \boldsymbol{y}(n) &= \boldsymbol{x}(n) + \boldsymbol{v}(n), \\ &= \boldsymbol{h}s(n) + \boldsymbol{v}(n), \end{aligned} \tag{4.3}$$

where,

- $s(n)$ is the transmitted signal sample at time n, modeled as Gaussian with zero mean and variance σ_s^2 : $s(n) \sim \mathscr{N}_{\mathbb{C}}(0, \sigma_s^2)$
- $\boldsymbol{h}$ is the channel complex vector $\boldsymbol{h} = [h_1 \cdots h_K]^T$; assumed to be constant and memoryless during the sampling window.

Under $\mathscr{H}_1$, the average SNR at the receiver is defined as

$$\rho \triangleq \frac{E\|\boldsymbol{x}(n)\|^2}{E\|\boldsymbol{v}(n)\|^2} = \frac{\sigma_s^2 \|\boldsymbol{h}\|^2}{K\sigma_v^2} \tag{4.4}$$

where, $\|.\|^2$ denotes the Frobenius norm and $E[.]$ is the mean operator. The received samples are stored by the detector in the $K \times N$ received matrix

$$\boldsymbol{Y} \triangleq [\boldsymbol{y}(1) \cdots \boldsymbol{y}(n) \cdots \boldsymbol{y}(N)] \tag{4.5}$$

Let us introduce the $1 \times N$ signal matrix $\boldsymbol{S} \triangleq [s(1) \cdots s(n) \cdots s(N)]$ and the $K \times N$ noise matrix $\boldsymbol{V} \triangleq [\boldsymbol{v}(1) \cdots \boldsymbol{v}(n) \cdots \boldsymbol{v}(N)]$. All the signals samples of $\boldsymbol{S}$ and the noise samples of $\boldsymbol{V}$ are assumed statistically independent. The detector must distinguish between

$$\boldsymbol{Y}|_{H_0} = \boldsymbol{V} \qquad \text{and} \qquad \boldsymbol{Y}|_{H_1} = \boldsymbol{h}\boldsymbol{S} + \boldsymbol{V}.$$

The sample covariance matrix is given by

$$\boldsymbol{R} \triangleq \frac{1}{N}\boldsymbol{Y}\boldsymbol{Y}^H, \tag{4.6}$$

and we will denote by $\lambda_1 \geq \cdots \geq \lambda_K$ its **eigenvalues** sorted in decreasing order.

4.2.5 Detection Performance Parameters

Let T be the **test statistic** employed by a detector to distinguish between $\mathscr{H}_0$ and $\mathscr{H}_1$. To make the decision, the detector compares T against a pre-defined **threshold** t: if $T > t$ it decides for $\mathscr{H}_1$, otherwise for $\mathscr{H}_0$. As a consequence, the probability of false alarm is defined as $P_{Fa} = Pr(T > t|_{\mathscr{H}_0})$ and the probability of detection as $P_D = Pr(T > t|_{\mathscr{H}_1})$. (see Figure 4.2).

Both P_{Fa} and P_D are key quantities for practical CRN: P_{Fa} must be low to maximize the spectrum exploitation by the secondary user and P_D must be high to minimize the interference caused by the opportunistic user to the primary one. As an example, the WRAN standard [3] imposes stringent requirements on both of them: $P_{Fa} < 0.1$ and $P_D > 0.9$. In practical applications, the decision threshold t is typically computed as a function of the target P_{Fa}: this ensures the so-called Constant False Alarm Rate (CFAR) detection.

Receiver Operating Characteristics

In order to compare the performances for different threshold values ROC curves can be used. The ROC curve is obtained by plotting the probability of correct detection versus the probability of false alram. ROC curves allow us to explore the relationship between the sensitivity (Probability of detection) and specificity (Probability of false alarm) of a sensing method for a variety of different threshold, thus allowing the determination of an optimal threshold.

The Neyman-Pearson test

The usual criterion for comparing two tests is to fix the false alarm rate P_{Fa} and look for the test achieving the higher P_D. The Neyman-Pearson (NP) lemma [130] is known to provide the Uniformly Most Powerful (UMP) test, achieving the maximum possible P_D for any given value of P_{Fa}. The NP criterion is applicable only when both $\mathscr{H}_0$ and $\mathscr{H}_1$ are simple hypotheses. In our setting this is the case when both the

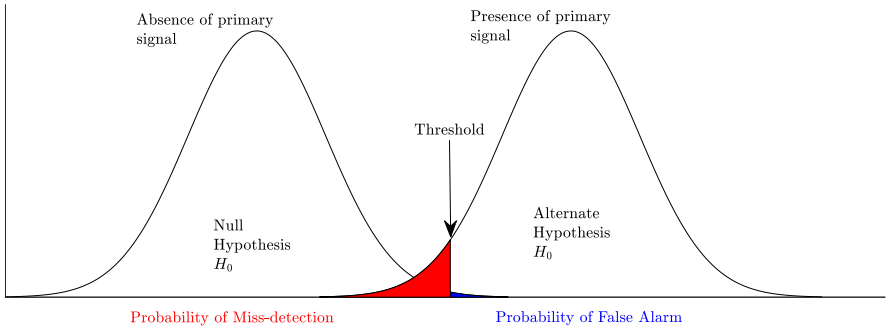

Fig. 4.2 Probability of false alarm P_{Fa} and Probability of Miss-detection P_D

noise level σ_v^2 and the channel vector $\boldsymbol{h}$ are a prior known. The NP test is given by the following likelihood ratio:

$$T_{NP} = \frac{p_1(\boldsymbol{Y}; \boldsymbol{h}, \sigma_s^2, \sigma_v^2)}{p_0(\boldsymbol{Y}; \sigma_v^2)}. \tag{4.7}$$

The NP test provides the best possible performance, but requires exact knowledge of both $\boldsymbol{h}$ and σ_v^2. For most practical applications, the knowledge of h is questionable. The noise variance is somewhat easier to know: since we only consider thermal noise, if the temperature is constant some applications may possess an accurate estimation of it.

4.2.6 Maximum Likelihood Noise Estimation Model

Maximum Likelihood Estimation (MLE) is a method of estimating the parameters of a statistical model. When applied to a given statistical model of received noise samples, maximum-likelihood provides estimates for the variance of a data set. Maximum-likelihood estimation gives a unified approach to estimation, which is well-defined in the case of the normal distribution and many other problems.

Consider Independent and Identically Distributed (IID) Gaussian noise samples with mean zero and unknown variance. For N time samples of noise $v(n)$ taken by the nodes in a given detection interval, the MLE of the variance is given by the formula [92].

$$\hat{\sigma}_v^2 = \frac{1}{KM} \sum_{k=1}^{K} \sum_{m=1}^{M} |v_k(m)|^2. \tag{4.8}$$

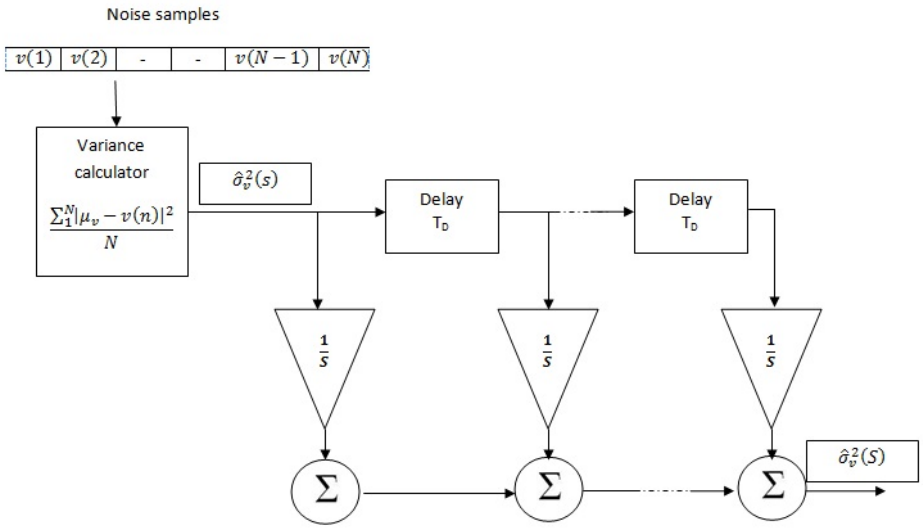

Fig. 4.3 Block diagram of Maximum Likelihood Noise Estimation

From N noise samples in one detection interval (one slot), one MLE noise estimate is generated. To make the estimate more accurate, S such estimates are averaged after getting new estimate of the noise variance forming a Moving Average System (MAS) as shown in Figure 4.3. Thus, the final expression for the noise variance estimation is given by,

$$\hat{\sigma}_v^2(S) = \frac{1}{KSM} \sum_{s=1}^{S} \sum_{k=1}^{K} \sum_{m=1}^{M} |v_k(m)|^2. \tag{4.9}$$

Hybrid approach of noise estimation

Basically, there are two approaches of noise variance estimation depending on the availability of the noise signal samples. Based on the noise variance estimation approach, two types of hybrid techniques of ED/RLRT are proposed in this dissertation, namely,

A. Offline Estimation (Hybrid Approach-1)

B. Online Estimation (Hybrid Approach-2)

These methods are described in the following subsections.

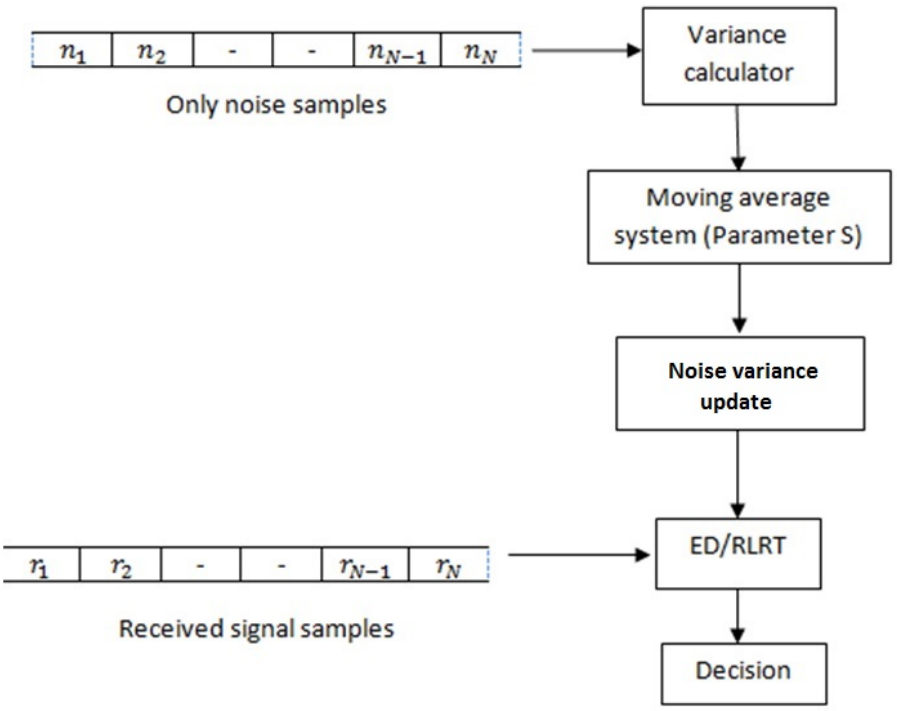

Fig. 4.4 Hybrid approach-1: Noise variance estimated from S auxiliary noise only slots.

A Offline Estimation

In this approach, noise variance is estimated explicitly assuming pure noise samples are available. As can be seen from the block diagram shown in Figure 4.4, noise variance is estimated from explicitly available noise only samples taking N samples at a time. Accurate estimate of the noise variance is obtained by averaging S variances from S noise-only slots using the MAS. The average noise variance estimate is then used in detecting the received primary signals using ED/RLRT detectors. After each detection interval, the average noise variance estimate is updated using one new noise variance estimate and the process is repeated. For ED and RLRT algorithm using this approach of noise estimation, Hybrid Energy Detection (HED1) and Hybrid Roy's Largest Root Test (HRLRT1) is named respectively.

B Online Estimation

In this approach, noise variance is estimated implicitly from S auxiliary re-

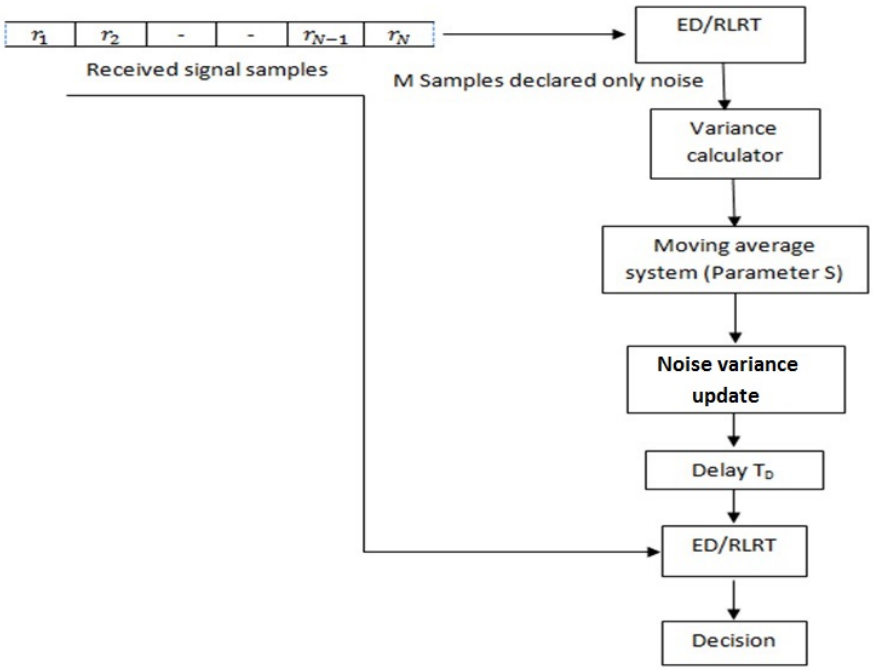

Fig. 4.5 Hybrid approach-2: Noise variance estimated in S auxiliary slots from received signal samples declared only noise samples by ED/RLRT

ceived signal slots which are declared only noise samples by the same algorithm. As can be seen from the block diagram shown in Figure 4.5, noise variance is calculated from signal samples implicitly declared as noise only samples by ED/RLRT taking M samples at a time. Accurate estimate of the noise variance is obtained by averaging S variances using a Moving Average taking S slots into consideration. The average noise variance estimate is then used in detecting the received primary signals using ED/RLRT detectors in the next detection interval. Thus, after the encounter of the noise only slots, the system updates the noise variance estimate and the process is repeated. For ED and RLRT algorithms using this approach of noise estimation, Hybrid Energy Detection-2 (HED2) and Hybrid Roy's Largest Root Test-2 (HRLRT2) are named respectively.

4.2.7 Energy Detection

Objective of every spectrum sensing scheme is to find out the detection statistic which can be used in the decision making by properly comparing against a threshold

value. ED is a spectrum sensing techniques that evaluates the signal energy over a certain time interval and compare it with the threshold to decide whether the spectrum is in use or not. The presence of noise in the signal may affect the decision of energy detector thus causing false alarm or even miss detection.

Formulation of the Decision Statistic

Using the information of the received signal matrix $\boldsymbol{Y}$ to develop a test statistic T_{ED}, which is the measure of the average energy of the received signal over a sensing interval N, the detector compares T_{ED} against a predefined threshold t. If $T_{ED} < t$ then it decides in favour of Null Hypothesis $\mathscr{H}_0$ otherwise in favor of Alternate Hypothesis $\mathscr{H}_1$. The average energy of the received signal vector $\boldsymbol{Y}$ normalized by the noise variance σ_v^2 can be represented as,

$$T_{ED} = \frac{1}{KN\sigma_v^2} \sum_{k=1}^{K} \sum_{n=1}^{N} |y_k(n)|^2. \tag{4.10}$$

Case 1: Null Hypothesis

For Null Hypothesis, rearranging (4.10) using $y_k(n) = v_k(n)$,

$$T_{ED}|_{H_0} = \frac{1}{KN\sigma_v^2} \sum_{k=1}^{K} \sum_{n=1}^{N} |v_k(n)|^2 \tag{4.11}$$

$$= \frac{1}{2KN} \sum_{k=1}^{K} \sum_{n=1}^{N} \left| \frac{v_k^R(n)}{\frac{\sigma_v}{\sqrt{2}}} + j\frac{v_k^C(n)}{\frac{\sigma_v}{\sqrt{2}}} \right|^2 \tag{4.12}$$

$$= \frac{1}{2KN} \sum_{k=1}^{K} \sum_{n=1}^{N} \left| \beta^R + j\beta^C \right|^2 \tag{4.13}$$

$$= \frac{1}{2KN} \sum_{k=1}^{K} \sum_{n=1}^{N} \beta_R^2 + \beta_C^2, \tag{4.14}$$

where $v_k^R(n)$ and $v_k^C(n)$ are real and imaginary part of the noise signal $v_k(n)$ respectively. $\beta_R = \sqrt{2}v_k^R(n)/\sigma_v$ and $\beta_C = \sqrt{2}v_k^C(n)/\sigma_v$. As $v_k(n)$ is a zero mean and σ_v^2 variance complex valued Gaussian Random Variable, β_R and β_C are Standard Normal Random Variables with mean zero and unity variance. The numerator of T_{ED} in (4.14) is sum of square of $2KN$ Standard Normal Random Variable with mean zero and variance 1, thus, the decision statistic $T_{ED}|_{H_0}$ follows the Chi Square Distribution with $2KN$ degrees of freedom

scaled by the factor $(1/2KN)$. Thus, (4.14) can be written as,

$$T_{ED}|_{H_0} = \frac{1}{2KN}\chi^2_{2KN}. \tag{4.15}$$

Case 2: Alternate Hypothesis

For Alternate Hypothesis, rearranging the (4.10) using $y_k(n) = h_k s_k(n) + v_k(n)$,

$$T_{ED}|_{H_1} = \frac{1}{KN\sigma_v^2}\sum_{k=1}^{K}\sum_{n=1}^{N}|h_k s_k(n) + v_k(n)|^2 \tag{4.16}$$

$$= \sum_{k=1}^{K}\frac{\sigma_{t_k}^2}{KN\sigma_v^2}\sum_{n=1}^{N}\left|\frac{h_k s_k(n) + v_k(n)}{\frac{\sigma_{t_k}}{\sqrt{2}}}\right|^2 \tag{4.17}$$

$$= \sum_{k=1}^{K}\frac{\sigma_{t_k}^2}{2KN\sigma_v^2}\sum_{n=1}^{N}|\alpha|^2, \tag{4.18}$$

where $\alpha = \frac{h_k s_k(n)+v_k(n)}{\sigma_{t_k}/\sqrt{2}}$. As h_k is assumed to be constant for the sensing interval and both the signal and noise are Complex Valued Gaussian Signals with variances σ_v^2 and σ_s^2 respectively and both are independent signals, $h_k s_k(n) + v_k(n)$ is also Complex Valued Gaussian Signal with mean zero and variance $\sigma_{t_k}^2$. It is clear that α is also a Complex Valued Standard Normal Random Variable with mean zero and unity variance. So the sum $\sum_{n=1}^{N}|\alpha|^2$ in (4.18) follows the Chi Square Distribution with $2N$ degrees of freedom. And we have:

$$T_{ED}|_{H_1} = \sum_{k=1}^{K}\left(\frac{|h_k|^2\sigma_s^2 + \sigma_v^2}{2KN\sigma_v^2}\right)\chi^2_{2N} \tag{4.19}$$

$$= \sum_{k=1}^{K}\left(\frac{|h_{t_k}|^2\sigma_s^2}{2KN\sigma_v^2}\right)\chi^2_{2N} + \sum_{k=1}^{K}\frac{1}{2KN}\chi^2_{2N} \tag{4.20}$$

$$T_{ED}|_{H_1} = \frac{K\rho\chi^2_{2N}}{2KN} + \frac{\chi^2_{2KN}}{2KN}. \tag{4.21}$$

Normal Approximation of ED Decision Statistic

According to the Central Limit Theorem, when N is sufficiently large, the Chi Squared Distributed Random Variable in (4.21) converges to a Gaussian Distribution.

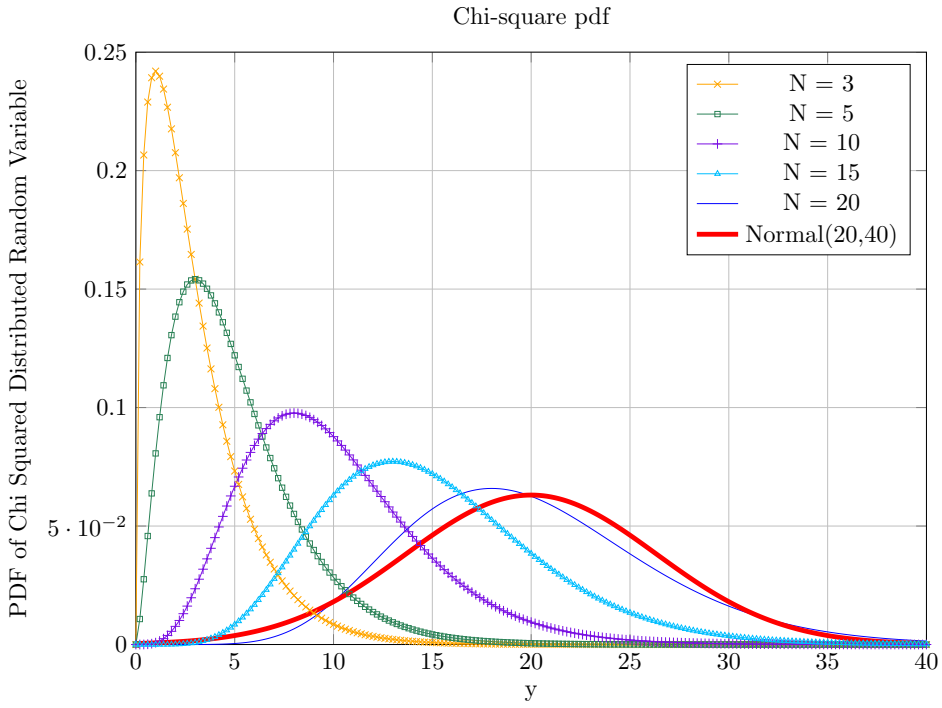

Fig. 4.6 χ^2_N distribution with 5, 10, and 20 degrees of freedom. A normal distribution is superimposed to illustrate a good approximation to χ^2_N by $N_{\mathbb{R}}(20,40)$ for N large

Figure 4.6 shows the pdf plot of the Chi Squared Distribution for $3,5,10$, and 20 degrees of freedom superimposing $N_{\mathbb{C}}(10,20)$ to illustrate a good approximation of χ^2_N by a Gaussian $N_{\mathbb{C}}(N/2,2N) \cong N_{\mathbb{R}}(N,2N)$ for large N. It is clear fron Figure 4.6 that Chi Square Distribution Variable with Degrees of Freedom 20 $(N = 20)$ shows a similarity with the Normal Distribution with mean and variance 20 and 40 (N and $2N$).

To get an insight of accuracy of the approximation, simulation of Gaussian approximation of Chi Square Distribution for different values of N is carried out. Figure 4.7 shows the *pdf* of Chi Square Random Variable and its Gaussian Approximation counterpart for N taking values $5,10,20$ and 40. Also Figure 4.8 shows the plot of the Mean Square Error (MSE) of the approximation considering Probability Density Functions of distribution functions as a comparison criteria for varying N. The approximation shows perfect matching for N greater than 40 and it is clear that the MSE is nearly zero, i.e. the Gaussian approximation is very accurate for $N > 40$, which indicated that a degree of freedom greater than 40 is sufficient for

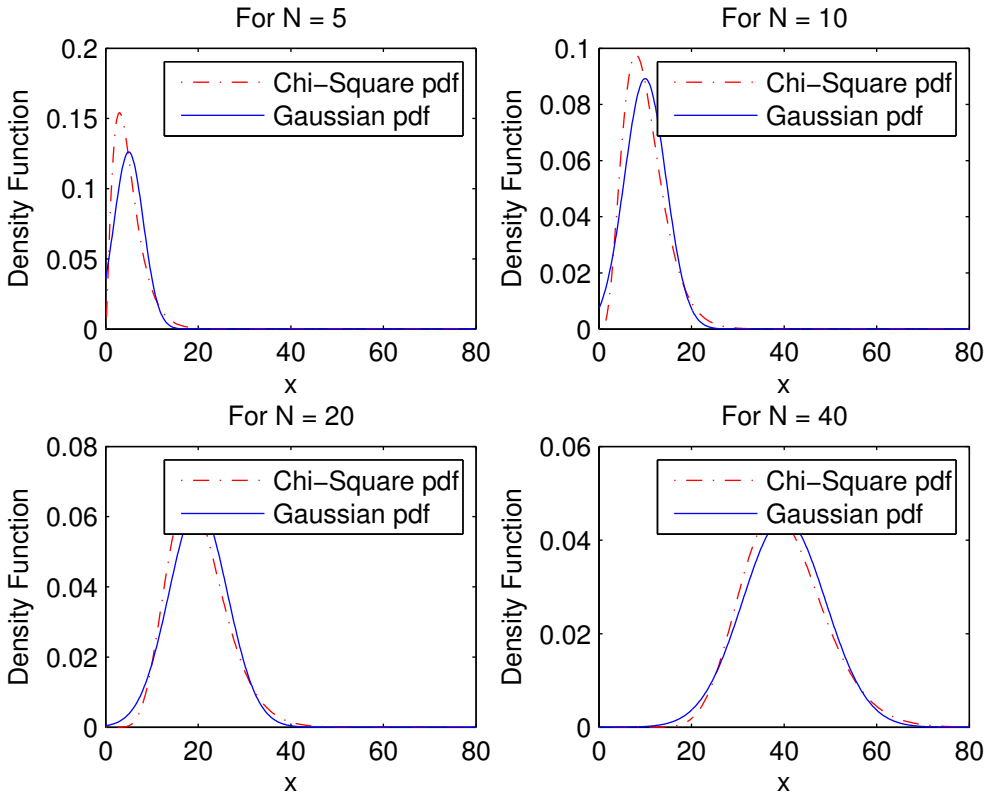

Fig. 4.7 Comparison of Chi Square Distribution with Gaussian approximation for different N

approximating Chi Squared Distribution of the detection statistic to a Gaussian distribution.

For good approximation, different models have been developed such as Edell's Model [58], Torrieri's Model [161] and Berkeley Model [30] which have analyzed the accuracy of different models in approximating the exact solution of the T_{ED} and concluded that these models almost have the same performance for such scenario. Thus, for the result in (4.21) and (4.15), using Berkeley Model [30] the Chi Squared Distribution Function can be approximated to a Normal Distribution Function as,

$$T_{ED} = \begin{cases} N_{\mathbb{R}}\left(1, \frac{1}{KN}\right) & \mathscr{H}_0, \\ N_{\mathbb{R}}\left((\rho+1), \frac{K\rho^2+2\rho+1}{KN}\right) & \mathscr{H}_1 \end{cases}. \tag{4.22}$$

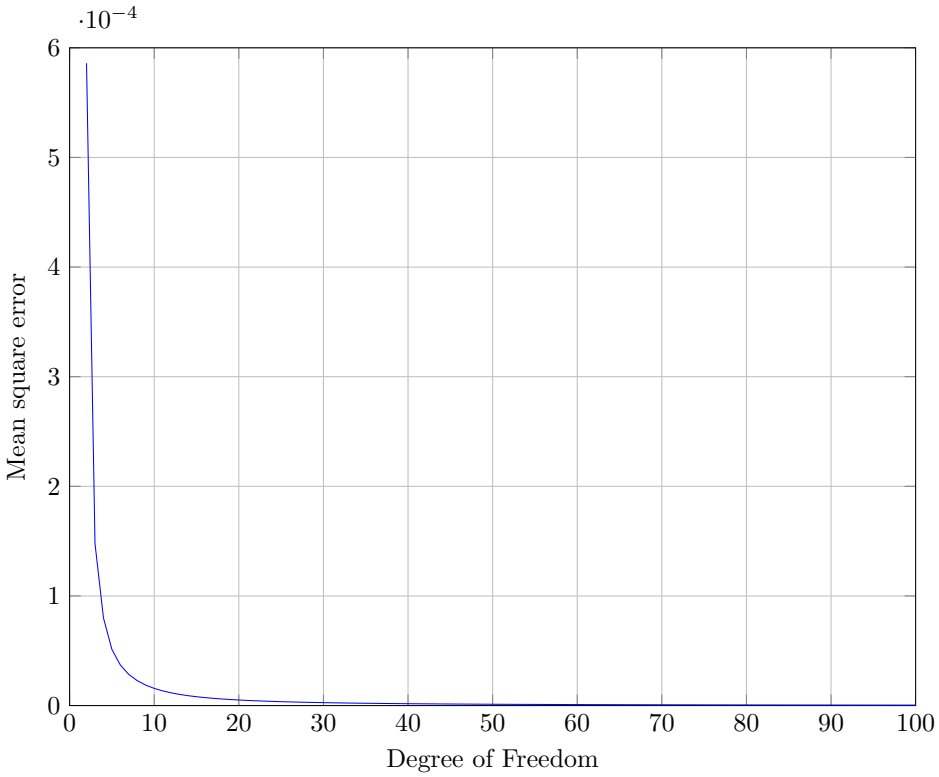

Fig. 4.8 MSE of the approximation considering Probability Density Function approximation

Detection and False Alarm Probabilities

A numerical study shows that ED ROC curves based on chi-squared distributions may be accurately represented by binomial ROC curves. This allows the detector accuracy and the ROC shape to be expressed simply in terms of distribution parameters [86]. For any description model, it would be useful to have a concise description of the ROC curves that is meaningful in terms of underlying signal and noise distributions. Such a description would facilitate the comparison between model and experiments, and help in studying the effect of changing model parameter.

Hypothesis test is a procedure which divides the space of observations into 2 regions, Rejection Region (R) and Acceptance Region (A). The two important characteristics of a test are called significance and power, referring to errors of type I and II in hypothesis testing which relates to Probability of false alarm and probability of detection respectively. The probabilities of false alarm P_{Fa} and probability of

detection P_D for a given decision statistic referring to ED test is given by:

$$P_{Fa} = Prob\{T_{ED} > t|_{H_0}\} \tag{4.23}$$
$$P_D = Prob\{T_{ED} > t|_{H_1}\}. \tag{4.24}$$

Based on the statistics of T_{ED} shown in (4.22), P_{Fa} can be evaluated as,

$$P_{Fa} = \int_t^{\infty} T_{ED}|_{H_0} dt \tag{4.25}$$
$$= 1 - \phi(t) \equiv 1 - \frac{1}{2}\left[1 + erf\left[\frac{t-\mu}{\sqrt{2\sigma^2}}\right]\right] \tag{4.26}$$
$$= \frac{1}{2}\left[1 - erf\left[\frac{t-\mu}{\sqrt{2\sigma^2}}\right]\right] \tag{4.27}$$
$$= \frac{1}{2} erfc\left[\frac{t-\mu}{\sqrt{2\sigma^2}}\right] \tag{4.28}$$
$$P_{Fa} = Q\left(\frac{t-\mu}{\sqrt{2\sigma^2}}\right), \tag{4.29}$$

where $\phi(t)$ is the cdf of Normal Distribution, $erf()$ is the error function, $erfc()$ is the complementary error function and $Q()$ is the complementary cdf of Normal Random Variable. Now putting the value of mean and variance for $\mathscr{H}_0$ from (4.22), We have

$$P_{Fa} = Q\left[(t-1)\sqrt{KN}\right]. \tag{4.30}$$

Following the same line of reasoning, the expression of P_D is given by,

$$P_D = Q\left[\frac{(t-1-\rho)\sqrt{KN}}{\sqrt{K\rho^2 + 2\rho + 1}}\right]. \tag{4.31}$$

Simulation Result

This Sub-Section discusses the simulation of ED in single sensor and multi-sensor environment. Signal, channel and noise environment are set to matche the scenario explained in Sub-Section 4.2.3.

Figure 4.9 illustrates the ROC plot of ED with its detection statistic following Normal distribution. Analytical result of ROC for ED computed using (4.30) and (4.31)

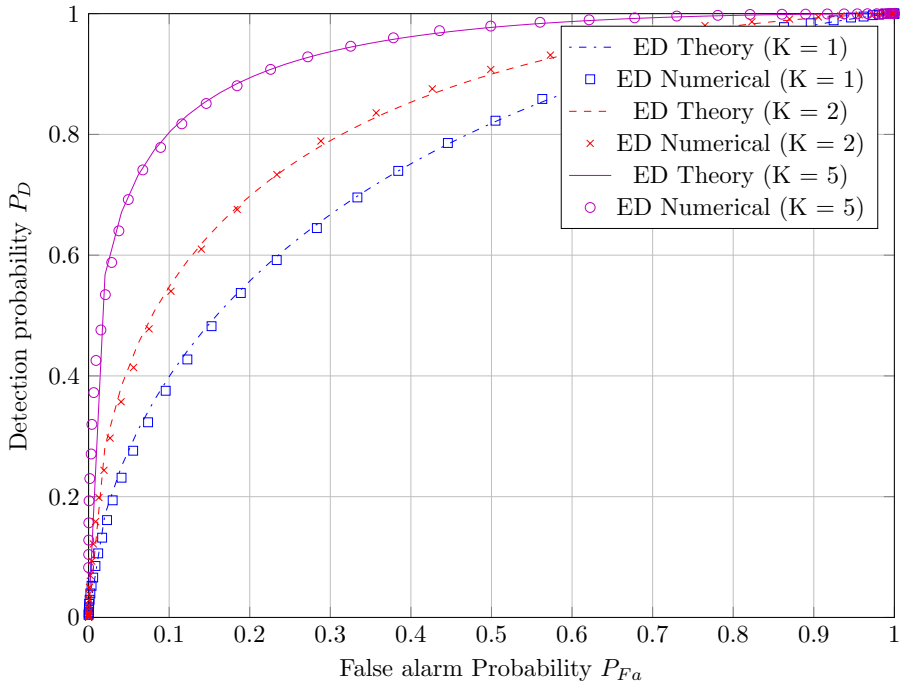

Fig. 4.9 ROC plot of ED for Normal Approximation of the Decision Statistics for $N = 100$, and $SNR = -10$dB for varying number of sensors K

for $SNR = -10\ dB$, $N = 100$, and number of sensors $K = 1$ (*Single Sensor*), 5 and 10 are compared with the numerical simulation for the same parameters. The plots overlap with each other and model proves to be very accurate. With the increase in number of sensors from 1 to 10, the performance of ED is greatly enhanced. The graph converges to $P_D = 1$ with steep slope for $K = 10$ if compared to the case of $K = 1$ which shows that co-operative(*"soft combining"*) spectrum sensing can greatly enhance the performance.

SNR performance of ED for a given P_{Fa} is illustrated in Figure 4.10. The accuracy of the the closed-form expression derived in (4.30) and (4.31) is confirmed by the results presented in Figure 4.10, where the theoretical formula is compared against simulated detection performance for different SNR values. The considered parameters are ($K = 5, 10, 15, N = 50$), at a false alarm rate of 5%. As shown in the figure, the theoretical expressions are quite accurate even for a small number K of sensors.

Figure 4.11 shows the variation of Probability of Detection vs. SNR performance for different uncertainty in noise variance described as as the ratio between estimated

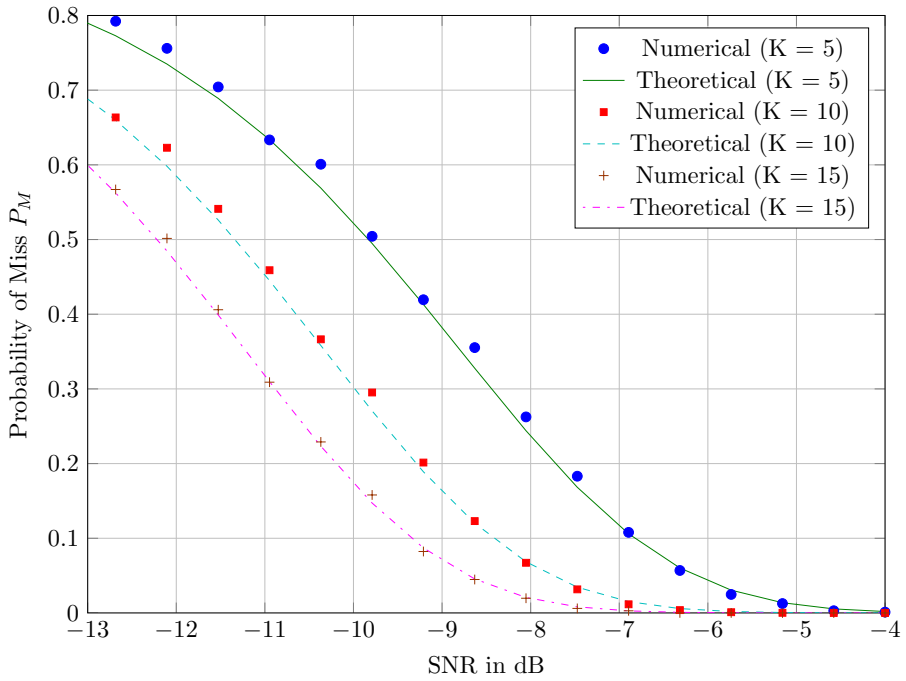

Fig. 4.10 Probability of Miss vs. SNR for varying number of sensors. Parameters: $N = 50, P_{Fa} = 0.05$ and $K = 5, 10$ and 15

noise variance and true variance level. Even though the increase in number of sensors from 1 to 5 increases the performance of ED significantly, there is still a big gap between known and unknown noise variance curves. This result makes it clear that, the knowledge of exact noise variance is the crucial part for ED.

4.2.8 Hybrid ED (HED1)

From the results of previous section, it is evident that the knowledge of the noise power (noise variance for zero mean Gaussian Noise) is imperative for achieving the optimum ED performance. Unfortunately, the variation and the unpredictability of noise power is unavoidable. Thus, the knowledge of the noise power is one of the critical limitations of ED for its operation in low SNR. The only option is to estimate the noise power. This chapter deals with the study of detection performance of the

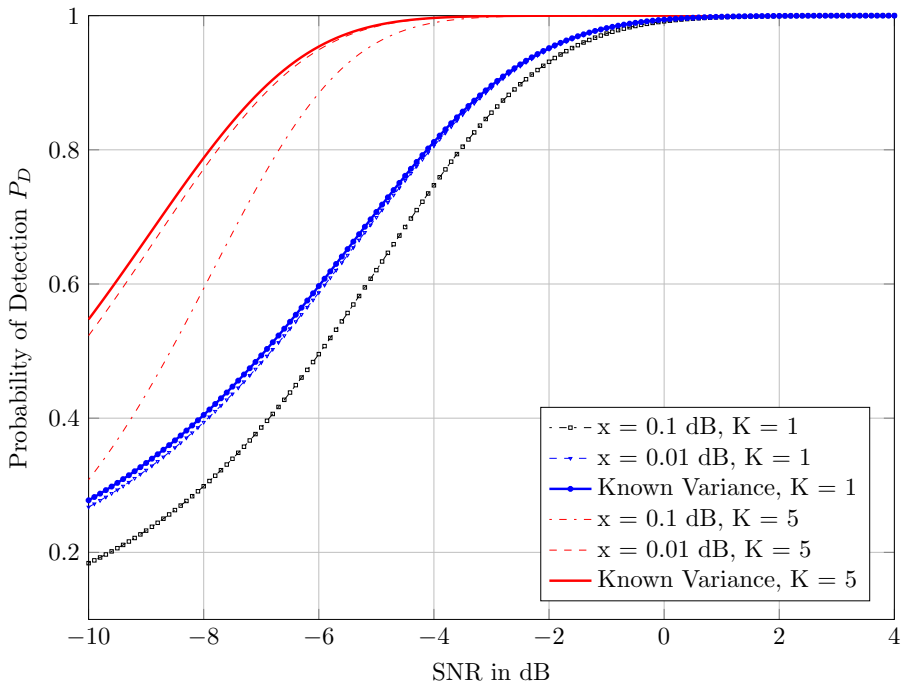

Fig. 4.11 Probability of Detection vs. SNR for varying amount of noise uncertainty measured as $\beta = \frac{\hat{\sigma}_v^2}{\sigma_v^2}$, and $x = 10\log_{10}(\beta)$, Parameters: $N = 40, P_{Fa} = 0.1$ and $K = 1,5$ and S

ED algorithm using estimated noise variance. Noise variance is estimated from S auxiliary noise-only slots where we are sure that the primary signal is absent. For ED with noise power estimation from noise only slots, which we call HED1 model, the analytical expression of performance parameters P_D and P_{Fa} in a multi-sensor[2] environment is derived and simulated.

Formulation of the Decision Statistic

In this chapter, a concept of noise variance estimation from noise only samples is proposed so as to fulfill the gap of unavailability of the noise variance. In this technique called HED1, noise variance is estimated on S auxiliary noise only slots, under the hypothesis that noise variance is constant over the adjacent slots.

Consider a sampling window of length M before and adjacent to the detection window which is containing noise only samples for sure. Then the estimated noise variance from these noise-only samples using a Maximum Likelihood noise power

[2]For single sensor performance evaluation, set the number of sensors K to 1.

estimate can be written as,

$$\hat{\sigma}_v^2 = \frac{1}{KM} \sum_{k=1}^{K} \sum_{m=1}^{M} |v_k(m)|^2. \tag{4.32}$$

If the noise variance is constant, the estimation can be averaged over S successive noise-only slots. And (4.32) becomes:

$$\hat{\sigma}_v^2(S) = \frac{1}{KSM} \sum_{s=1}^{S} \sum_{k=1}^{K} \sum_{m=1}^{M} |v_k(m)|^2. \tag{4.33}$$

Now, the ED Test Statistic in (4.10) can be modified to HED1 test statistic using (4.33) as,

$$T_{HED1} = \frac{1}{KN\hat{\sigma}_v^2(S)} \sum_{k=1}^{K} \sum_{n=1}^{N} |y_k(n)|^2. \tag{4.34}$$

Here, T_{HED1} denotes the detection statistics for the HED1 scheme and the statistical distribution of T_{HED1} depends upon the particular estimation technique considered.

Moreover, (4.34) can be considered as the parametric likelihood ratio test when the signal to be detected is assumed to be Gaussian with zero mean and variance σ_s^2.

Proposition 1. The false alarm probability P_{Fa} of HED1 for number of sensors K, number of samples N, number of auxiliary slots S and threshold t is given by,

$$P_{Fa} = Q\left[\frac{t-1}{\sqrt{\frac{MS+Nt^2}{KMNS}}}\right]. \tag{4.35}$$

Similarly, the Probability of detection P_D of HED1 for number of sensors K, number of samples N, number of auxiliary slots S and threshold t is given by,

$$P_D = Q\left[\frac{(t-1-\rho)}{\sqrt{\frac{t^2}{KMS} + \frac{K\rho^2+2\rho+1}{KN}}}\right]. \tag{4.36}$$

The analytical proof of **Proposition** 1 is given below.

Case 1: Null Hypothesis H_0

For Null Hypothesis, rearranging (4.34) using $y_k(n) = v_k(n)$, we have:

$$T_{HED1}|_{H_0} = \frac{1}{KN\hat{\sigma}_v^2} \sum_{k=1}^{K} \sum_{n=1}^{N} |v_k(n)|^2 \tag{4.37}$$

$$= \frac{2KMS}{2KN} \left[\frac{\sum_{k=1}^{K} \sum_{n=1}^{N} \left| \frac{v_k^R(n)}{\frac{\sigma_v}{\sqrt{2}}} + j\frac{v_k^C(n)}{\frac{\sigma_v}{\sqrt{2}}} \right|^2}{\sum_{s=1}^{S} \sum_{m=1}^{M} \left| \frac{v_k(m)}{\sigma_v/\sqrt{2}} \right|^2} \right] \tag{4.38}$$

$$= \frac{2KMS}{2KN} \left[\frac{\sum_{k=1}^{K} \sum_{n=1}^{N} |\beta_1|^2}{\sum_{s=1}^{S} \sum_{k=1}^{K} \sum_{n=1}^{N} |\beta_2|^2} \right], \tag{4.39}$$

where $v_k^R(n)$ and $v_k^C(n)$ are real and imaginary part of the noise signal $v_k(n)$ respectively, $\beta_1 = \sqrt{2}v_k(n)/\sigma_v$ and $\beta_2 = \sqrt{2}v_k(m)/\sigma_v$.

As $v_k(n)$ is a zero mean and σ_v^2 variance complex valued Gaussian Random variable, β_1 and β_2 are Standard Normal Random Variables with zero mean and unity variance. Both numerator and denominator of T_{HED1} in (4.39) are the sum of square $2KMS$ and $2KN$ Standard Normal Random variables with zero mean and variance 1. Thus, the numerator and the denominator of the decision statistic $T_{HED1}|_{H_0}$ follows the Chi Square Distribution with $2KMS$ and $2KN$ degrees of freedom respectively, scaled by the factor $\frac{2KMS}{2KN}$.

Finally, (4.39) can be modified as,

$$T_{HED1}|_{H_0} = \frac{2KMS}{2KN} \frac{\chi_{2KN}^2}{\chi_{2KMS}^2} \tag{4.40}$$

Case 2: Alternate Hypothesis H_1

For Alternate Hypothesis, rearranging (4.34) using $y_k(n) = h_k s_k(n) + v_k(n)$, we have:

$$T_{HED1}|_{H_1} = \frac{1}{KN\hat{\sigma}_v^2} \sum_{k=1}^{K} \sum_{n=1}^{N} |h_k s_k(n) + v_k(n)|^2 \tag{4.41}$$

$$= \frac{\sum_{k=1}^{K} \left(\frac{KMS\sigma_{t_k}^2}{KN\sigma_v^2} \right) \sum_{n=1}^{N} \left| \frac{h_k s_k(n) + v_k(n)}{\sigma_{t_k}/\sqrt{2}} \right|^2}{\sum_{s=1}^{S} \sum_{k=1}^{K} \sum_{m=1}^{M} \left| \frac{v_k(m)}{\sigma_v/\sqrt{2}} \right|^2} \tag{4.42}$$

$$= \frac{\sum_{k=1}^{K} \left(\frac{KMS\sigma_{t_k}^2}{KN\sigma_v^2} \right) \sum_{n=1}^{N} |\alpha|^2}{\sum_{s=1}^{S} \sum_{k=1}^{K} \sum_{m=1}^{M} |\beta_2|^2}, \tag{4.43}$$

where $\alpha = \frac{h_k s_k(n) + v_k(n)}{\sigma_{t_k}/\sqrt{2}}$ and $\beta_2 = \sqrt{2} v_k(m)/\sigma_v$.

The channel coefficient h_k is assumed to be constant for the sensing interval and both signal and noise are independent Complex Valued Gaussian variable with variances σ_v^2 and σ_s^2 respectively. Then, $h_k s_k(n) + v_k(n)$ is a Complex Valued Gaussian variable with zero mean and variance $\sigma_{t_k}^2$. It is clear that α and β_2 are also Complex Valued Standard Normal Random Variables with zero mean and unity variance. So the sum $\sum_{n=1}^{N} |\alpha|^2$ and $\sum_{s=1}^{S} \sum_{k=1}^{K} \sum_{m=1}^{M} |\beta|^2$ in an expression of (4.43) follows the Chi Square Distribution with $2N$ and $2SKM$ degrees of freedom respectively. Thus, (4.43) can be re-written as,

$$T_{HED1}|_{H_1} = 2KMS \frac{\sum_{k=1}^{K} \left(\frac{|h_k|^2 \sigma_s^2 + \sigma_v^2}{2KN\sigma_v^2} \right) \chi_{2N}^2}{\chi_{2KMS}^2} \tag{4.44}$$

$$= 2KMS \frac{\sum_{k=1}^{K} \left(\frac{|h_{t_k}|^2 \sigma_s^2}{2KN\sigma_v^2} \right) \chi_{2N}^2 + \sum_{k=1}^{2} \frac{1}{2KN} \chi_{2N}^2}{\chi_{2KMS}^2} \tag{4.45}$$

$$T_{HED1}|_{H_1} = \frac{KMS}{KN} \left[\frac{K\rho\chi_{2N}^2 + \chi_{2KN}^2}{\chi_{2KMS}^2} \right]. \tag{4.46}$$

Normal Approximation of HED1 Decision Statistic

For large values of N and M, the Chi Squared Random Variables in (4.40) and (4.46) can be replaced by their normal approximates with $\chi_N^2 \sim N_{\mathbb{R}}(N, 2N)$. Thus, decision

statistics $T_{ED}|_{H_0}$ and $T_{ED}|_{H_1}$ in (4.40) and (4.46) can be re-written as,

$$T_{HED1}|_{H_0} = \left(\frac{KMS}{KN}\right) \frac{N_{\mathbb{R}}(2KN, 4KN)}{N_{\mathbb{R}}(2KMS, 4KMS)} \tag{4.47}$$

$$T_{HED1}|_{H_1} = \frac{N_{\mathbb{R}}\left(\rho+1, \frac{K\rho^2+2\rho+1}{KN}\right)}{N_{\mathbb{R}}\left(1, \frac{1}{KMS}\right)}. \tag{4.48}$$

Now, the ratio of two normal random variables in (4.47) and (4.48) can be transformed to a single normal random variables as shown below under the assumption that the denominator is always positive [121].

$$T_{HED1} = \begin{cases} N_{\mathbb{R}}\left(1, \frac{1}{KN} + \frac{t^2}{KMS}\right) & \mathscr{H}_0, \\ N_{\mathbb{R}}\left((\rho+1), \frac{t^2}{KMS} + \frac{K\rho^2+2\rho+1}{KN}\right) & \mathscr{H}_1 \end{cases}. \tag{4.49}$$

Detection and False Alarm Probabilities

A numerical study shows that ED ROC curves based on chi-squared distributions may be accurately represented by binomial ROC curves. This allows the detector accuracy and the ROC shape to be expressed simply in terms of distribution parameters [86]. For any description model, it would be useful to have a concise description of the ROC curves that is meaningful in terms of underlying signal and noise distributions. Such a description would facilitate the comparison between model and experiments, and help in studying the assessment of effect of changing model parameter.

Hypothesis test is a procedure which divides the space of observations into 2 regions, Rejection Region (R) and Acceptance Region (A). The two important characteristics of a test are called significance and power, referring to errors of type I and II in hypothesis testing which relates to probability of false alarm and probability of detection respectively. The probabilities of false alarm P_{Fa} and probability of detection P_D for a given decision statistic referring to HED1 test is given by:

$$P_{Fa} = Prob\{T_{HED1} > t|_{H_0}\} \tag{4.50}$$

$$P_D = Prob\{T_{HED1} > t|_{H_1}\}. \tag{4.51}$$

Based on the statistics of T_{HED1} shown in (4.49), P_{Fa} can be evaluated as,

$$P_{Fa} = \int_{t}^{\infty} T_{ED}|_{H_0} dt \tag{4.52}$$

$$= 1 - \phi(t) \equiv 1 - \frac{1}{2}\left[1 + erf\left[\frac{t-\mu}{\sqrt{2\sigma^2}}\right]\right] \tag{4.53}$$

$$= \frac{1}{2}\left[1 - erf\left[\frac{t-\mu}{\sqrt{2\sigma^2}}\right]\right] \tag{4.54}$$

$$= \frac{1}{2} erfc\left[\frac{t-\mu}{\sqrt{2\sigma^2}}\right] \tag{4.55}$$

$$P_{Fa} = Q\left(\frac{t-\mu}{\sqrt{2\sigma^2}}\right), \tag{4.56}$$

where $\phi(t)$ is the cdf of Normal Distribution, $erf(.)$ is the error function $erfc()$ is the complementary error function and $Q(.)$ is the complementary cdf of Normal Random Variable.

Now putting the value of mean and variance for $\mathscr{H}_0$ from (4.49), we have:

$$P_{Fa} = Q\left[\frac{t-1}{\sqrt{\frac{MS+Nt^2}{KMNS}}}\right]. \tag{4.57}$$

Similarly, for the detection probability:

$$P_D = Q\left[\frac{(t-1-\rho)}{\sqrt{\frac{t^2}{KMS} + \frac{K\rho^2+2\rho+1}{KN}}}\right]. \tag{4.58}$$

Simulation Result

This Sub-Section shows the comparison between simulated ROC curves and analytical curves based on (4.35) and (4.36). The accuracy of the closed-form expression derived in Proposition 1 is confirmed by the results presented in Figure 4.12, where the theoretical formulas (4.35) & (4.36) are compared against simulated performance over S auxiliary noise only slots (S ranges from 1 to 10). It can be realized from Figure 4.12 that the analytical and the numerical curves are perfectly matched

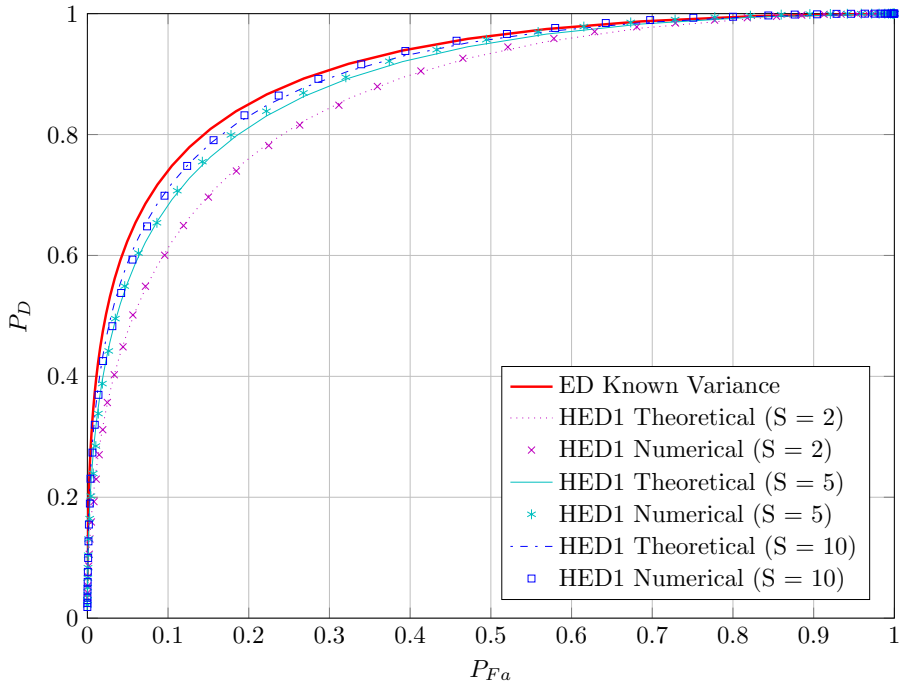

Fig. 4.12 ROC of Multi Sensor HED1, Parameters: $N = 100$, $M = 100$, $K = 5$, $S = 1, 2, 5, 10$, and $SNR = -10\ dB$

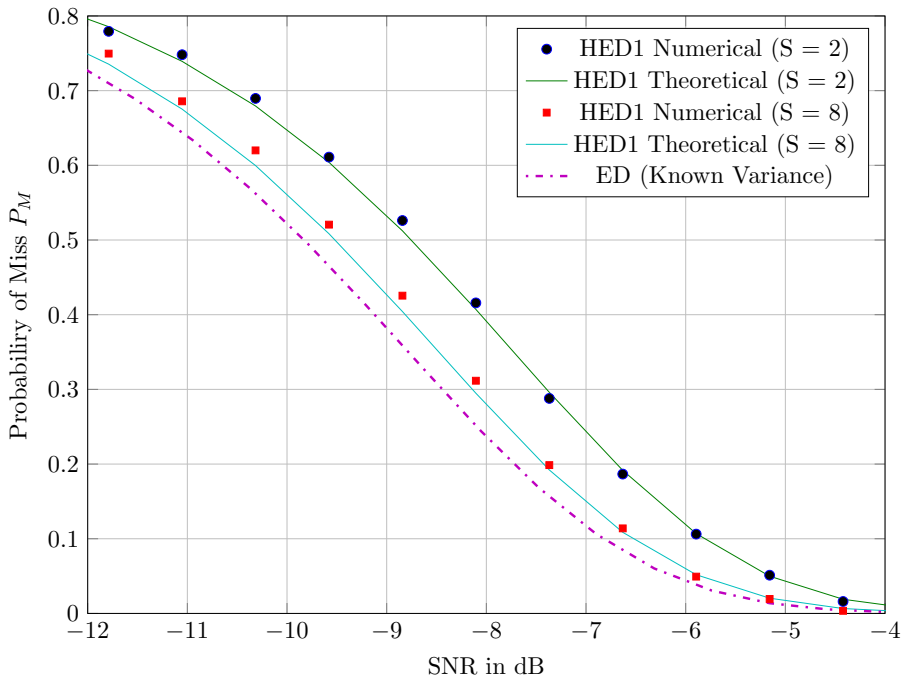

Fig. 4.13 Probability of Miss vs SNR, Parameters: $N = 50$, $M = 50$, $K = 5$, $S = 2, 8$, and $SNR = -10dB$

and this validates the analytical expressions. Also, it can be noted that the increase in number of slots for noise variance estimation correspondingly increases the performance of HED1 and approaches closer to the optimal one (ED with known noise variance). Under the considered scenario with $M = N = 100$ which is the number of noise samples in each slot, just $S = 10$ (i.e., 1000 samples) provides very near convergence to ideal performance.

Fixed the probability of false alarm $P_{Fa} = 0.05$, the simulated and analytical performance of HED1 in terms of probability of miss-detection is plotted against different values of SNR in Figure 4.13. The considered parameters are ($K = 5$, $N = 50, M = 50$). As shown in the figure, the theoretical expressions is quite accurate even for a small number K of sensors. The figure clearly shows the performance gap between ED (known variance) and HED1 with estimated noise variance from S auxiliary noise only slots.

4.2.9 Hybrid ED-2(HED2)

As discussed, optimum performance of ED can be achieved even in the absence of noise power knowledge in prior by estimating it from sufficient number of noise samples which is also clear from the result of Sub-Section 4.2.8. But in reality, it is difficult to guarantee the availability of signal free samples so as to estimate the noise variance. Some literature analyzed the performance of ED using estimated noise variance setting aside a separate frequency channel for the measurement of the noise power [178]. Even though setting a separate frequency channel for the measurement of the noise power is good enough for accurate noise estimation, it's also a waste of frequency resource. Wireless channels may show variation in the amount of noise on different frequency slots. Since SU needs to scan and make decision on a large band of frequencies about the presence or absence of PU, it is not always safe to assume uniformly distributed noise in all the frequency band of concern. Similarly, Mariani et al. [120] put forwarded the two-step sensing scenario where basic ED is used for small sensing period whose decision promotes the periodic estimation of the noise variance from the noise only samples decided by ED, and some other sophisticated techniques can be used for fine sensing using long observation time.

HED2 is somewhat similar to the method of Mariani et al. [120]: HED2 does not resort on the existence of auxiliary noise only slots, but estimates the noise variance

information from the previous slots declared as $\mathscr{H}_0$ by the algorithm. Now, the noise variance estimated from S previous slots which are declared $\mathscr{H}_0$ is used in current detection interval to get the decision about the presence or absence of the primary signal. The derivation of the analytical expression of performance parameters P_D and P_{Fa} in a multi-sensor environment for HED2 is now presented using different probability distribution models.

Formulation of Decision Statistic

The information on the received signal matrix $\boldsymbol{Y}$ is used to develop a test statistic T_{HED2}, which measures the average energy of the received signal over a sensing interval N and compares it against an estimated noise variance. The detector compares T_{HED2} against a predefined threshold t. If $T_{HED2} < t$ then it decides in favor of Null Hypothesis $\mathscr{H}_0$ otherwise in favor of Alternate Hypothesis $\mathscr{H}_1$. The average energy of the received signal vector $\boldsymbol{Y}$ normalized by the estimated noise variance $\hat{\sigma}_v^2$ can be represented as,

$$T_{HED2} = \frac{1}{KN\hat{\sigma}_v^2} \sum_{k=1}^{K} \sum_{n=1}^{N} |y_k(n)|^2. \tag{4.59}$$

Proposition 2. Let, P_S be the probability of receiving primary signal plus noise, P_D^{ED} the probability of detection of first stage ED, and S the number of slots. The Maximum Likelihood noise variance estimate $\hat{\sigma}_v^2$ using M received signal samples declared noise samples by ED from K receivers each is given by,

$$\hat{\sigma}_v^2(S) = \frac{\left[\sum_{s=1}^{S_s} \sum_{k=1}^{K} \sum_{m=1}^{M} |h_k s(m) + v(m)|^2 + \sum_{s=1}^{S_N} \sum_{k=1}^{K} \sum_{m=1}^{M} |v_k(m)|^2\right]}{KMS}, \tag{4.60}$$

where, $S_S = SP_S\left(1 - P_D^{ED}\right)$ is the number of primary signal slots missed by ED and $S_N = S - S_S$ is the number of noise samples successfully detected.

Proof. Consider a window of length S containing slots declared H_0 by the detector. In case of error, the estimated noise variance from the noise only samples using a Maximum Likelihood Noise Power Estimate can be written as,

$$\hat{\sigma}_v^2 = \frac{1}{KM}\left[\sum_{k=1}^{K} \sum_{m=1}^{M} |h_k s(m) + v(m)|^2\right]. \tag{4.61}$$

If a slot is slot are declared noise only by ED, there is a chance with probability $(1-P_D^{ED})$ that ED decides in favor of $\mathscr{H}_0$ even if it was H_1. If the estimated variance is the mean of S successive noise variances calculated from the noise only slots decided by ED, then out of S noise only slots decided by ED, $P_S(1-P_D^{ED})S$ noise variance estimates are calculated from H_1 slots. Thus, the average noise variance can now be written as the mean of the noise variance estimated from H_0 slots declared $\mathscr{H}_0$ by ED and the H_1 slots declared $\mathscr{H}_0$ by ED. Finally, (4.61) can be modified and rewritten as,

$$\hat{\sigma}_v^2(S) = \frac{\left[\sum_{s=1}^{S_s}\sum_{k=1}^{K}\sum_{m=1}^{M}|h_k s(m)+v(m)|^2 + \sum_{s=1}^{S_N}\sum_{k=1}^{K}\sum_{m=1}^{M}|v_k(m)|^2\right]}{KMS}. \tag{4.62}$$

□

Proposition 3. The false alarm probability P_{Fa} of HED2 for number of sensors K, number of samples N, number of auxiliary slots S for noise estimation using (4.62) and threshold t is given by,

$$P_{Fa} = Q\left[\frac{t-\frac{S}{S+\rho S_S}}{\sqrt{\frac{t^2N(S_SK\rho^2+\rho S_S+S)+MS^2}{KMN(S+\rho S_S)^2}}}\right]. \tag{4.63}$$

Similarly, the Probability of Detection P_D of HED2 for number of sensors K, number of samples N, number of auxiliary slots S for noise estimation using (4.62) and threshold t is given by,

$$P_D = Q\left[\frac{t-\frac{S(\rho+1)}{S+\rho S_S}}{\sqrt{\frac{t^2N(S_SK\rho^2+\rho S_S+S)+MS^2(K\rho^2+2\rho+1)}{KMN(S+\rho S_S)^2}}}\right]. \tag{4.64}$$

The analytical proof of **Proposition** 3 is given below.

Case 1: Null Hypothesis

For Null Hypothesis, rearranging (4.59) using $y_k(n) = v_k(n)$, we have:

$$T_{HED2}|_{H_0} = \frac{1}{KN\hat{\sigma}_v^2}\sum_{k=1}^{K}\sum_{n=1}^{N}|v_k(n)|^2 \tag{4.65}$$

$$= \left(\frac{1}{\hat{\sigma}_v^2/\sigma_v^2}\right)\left(\frac{1}{KN}\sum_{k=1}^{K}\sum_{n=1}^{N}\frac{|v_k(n)|^2}{\sigma_v^2}\right) \tag{4.66}$$

$$= \frac{\mathbf{B}}{\mathbf{A}}, \tag{4.67}$$

where,

$\mathbf{A} = \hat{\sigma}_v^2/\sigma_v^2$ and,

$\mathbf{B} = \frac{1}{KN}\sum_{k=1}^{K}\sum_{n=1}^{N}\frac{|v_k(n)|^2}{\sigma_v^2}$.

$\mathbf{A}$ can be simplified using the expression of $\hat{\sigma}_v^2$ in (4.62) as,

$$\mathbf{A} = \frac{\hat{\sigma}_v^2}{\sigma_v^2} \tag{4.68}$$

$$= \frac{\sum_{s=1}^{S_s}\sum_{k=1}^{K}\sum_{m=1}^{M}|h_k s(m)+v(m)|^2 + \sum_{s=1}^{S_N}\sum_{k=1}^{K}\sum_{m=1}^{M}|v_k(m)|^2}{MKS\sigma_v^2}. \tag{4.69}$$

$$A = \frac{1}{2MKS}\left[\left(\sum_{s=1}^{S_S}\sum_{k=1}^{K}\frac{\sigma_{t_k}^2}{\sigma_v^2}\chi_{2M}^2\right) + \chi_{2KMS_N}^2\right], \tag{4.70}$$

where, $\sigma_{t_k}^2$ is the total variance of $h_k s_k(n) + v_k(n)$.

We have:

$$\mathbf{A} = \frac{1}{2MKS}\left[\left(\sum_{s=1}^{S_S}\sum_{k=1}^{K}\frac{|h_k|^2\sigma_s^2+\sigma_v^2}{\sigma_v^2}\chi_{2M}^2\right) + \chi_{2KMS_N}^2\right] \tag{4.71}$$

$$= \frac{1}{2MKS}\left[\left(\sum_{s=1}^{S_S}\left(K\rho\chi_{2M}^2 + \chi_{2KM}^2\right)\right) + \chi_{2KMS_N}^2\right] \tag{4.72}$$

$$= \frac{1}{2MKS}\left[\rho\chi_{2MS_S}^2 + \chi_{2MKS_S}^2 + \chi_{2MKS_N}^2\right] \tag{4.73}$$

$$= \frac{1}{2MKS}\left[\rho\chi_{2MS_S}^2 + \chi_{2(K-1)MS_S} + \chi_{2MS_S}^2 + \chi_{2MS_N}^2\right] \tag{4.74}$$

$$= \frac{1}{2MKS}\left[(K\rho+1)\chi_{2MS_S}^2 + \chi_{2KMS}^2 - \chi_{2MS_S}^2\right]. \tag{4.75}$$

After approximating each Chi Squared Random Variables to Normal Random Variable using $\chi^2_N \sim N_{\mathbb{R}}(N,2N)$ transformation for $2MS_S \geq 50$, (4.75) above can be approximated to Normal Random Variable as,

$$\mathbf{A} = \frac{N_{\mathbb{R}}\left(K\rho S_S + S_S + KS - S_S, \frac{S_S K^2\rho^2 + K\rho S_S + S_S + KS - S_S}{M}\right)}{KS} \tag{4.76}$$

$$= N_{\mathbb{R}}\left(\frac{S+\rho S_S}{S}, \frac{S_S K\rho^2 + \rho S_S + S}{KMS^2}\right). \tag{4.77}$$

Similarly **B** can be simplified as,

$$\mathbf{B} = \frac{1}{KN}\sum_{k=1}^{K}\sum_{n=1}^{N}\frac{|v_k(n)|^2}{\sigma_v^2} \tag{4.78}$$

$$= \frac{1}{2KN}\sum_{k=1}^{K}\sum_{n=1}^{N}\beta_1^2, \tag{4.79}$$

where $\beta_1 = \frac{v_k(n}{\sigma_v/\sqrt{2}}$ is a Standard Normal Random Variable with zero mean and unitary variance.

Now, the sum in (4.79) is the sum of square of KN Complex Standard Normal Random variables, thus the sum follows a Chi Square Distribution of $2KN$ degrees of freedom, i.e.

$$\mathbf{B} = \frac{1}{2KN}\chi^2_{2KN}. \tag{4.80}$$

Again, using an Normal Approximation to a Chi Square Random variable, (4.80) can be written in the form

$$\mathbf{B} = N_{\mathbb{R}}\left(1, \frac{1}{KN}\right). \tag{4.81}$$

Finally, using (4.77) and (4.81) in (4.66), the expression of $T_{HED2}|_{H_0}$ can be written as the ratio of two Normal Random variables as,

$$T_{HED2}|_{H_0} = \frac{N_{\mathbb{R}}\left(1, \frac{1}{KN}\right)}{N_{\mathbb{R}}\left(\frac{S+\rho S_S}{S}, \frac{S_S K\rho^2 + \rho S_S + S}{KMS^2}\right)}. \tag{4.82}$$

Case 2: Alternative Hypothesis

For Alternate Hypothesis, rearranging (4.59) using $y_k(n) = h_k s(n) + v_k(n)$, we have:

$$T_{HED2}|_{H_1} = \frac{1}{KN\hat{\sigma}_v^2} \sum_{k=1}^{K} \sum_{n=1}^{N} |h_k s(n) + v_k(n)|^2 \tag{4.83}$$

$$= \left(\frac{1}{\hat{\sigma}_v^2/\sigma_v^2} \right) \left(\frac{1}{KN} \sum_{k=1}^{K} \sum_{n=1}^{N} \frac{|h_k s(n) + v_k(n)|^2}{\sigma_v^2} \right) \tag{4.84}$$

$$= \frac{\mathbf{C}}{\mathbf{A}}, \tag{4.85}$$

where,
$\mathbf{C} = \frac{1}{KN} \sum_{k=1}^{K} \sum_{n=1}^{N} \frac{|h_k s(n) + v_k(n)|^2}{\sigma_v^2}$ and,
$\mathbf{A} = \hat{\sigma}_v^2/\sigma_v^2$.

$\mathbf{C}$ can be simplified as,

$$\mathbf{C} = \frac{1}{KN} \sum_{k=1}^{K} \sum_{n=1}^{N} \frac{|h_k s_k(n) + v_k(n)|^2}{\sigma_v^2} \tag{4.86}$$

$$= \sum_{k=1}^{K} \left(\frac{\sigma_{t_k}^2}{2KN\sigma_v^2} \right) \sum_{n=1}^{N} \left| \frac{h_k s_k(n) + v_k(n)}{\sigma_{t_k}/\sqrt{2}} \right|^2 \tag{4.87}$$

$$= \sum_{k=1}^{K} \left(\frac{\sigma_{t_k}^2}{2KN\sigma_v^2} \right) \sum_{n=1}^{N} |\alpha|^2, \tag{4.88}$$

where $\alpha = \frac{h_k s_k(n) + v_k(n)}{\sigma_{t_k}/\sqrt{2}}$.

As h_k is assumed to be constant for the sensing interval and both the signal and noise are independent Complex Valued Gaussian samples with variances σ_v^2 and σ_s^2 respectively, $h_k s_k(n) + v_k(n)$ is also Complex Valued Gaussian samples with zero mean and variance $\sigma_{t_k}^2$. It is clear that α is a Complex Standard Normal Random Variable with zero mean and unitary variance. So the sum $\sum_{n=1}^{N} |\alpha|^2$ in (4.88) follows the Chi Square Distribution with $2N$ and $2SKM$

degrees of freedom respectively. Thus, (4.88) can be re-written as,

$$\mathbf{C} = \sum_{k=1}^{K} \left(\frac{|h_k|^2 \sigma_s^2 + \sigma_v^2}{2KN\sigma_v^2} \right) \chi_{2N}^2 \tag{4.89}$$

$$= \sum_{k=1}^{K} \left(\frac{|h_{t_k}|^2 \sigma_s^2}{2KN\sigma_v^2} \right) \chi_{2N}^2 + \sum_{k=1}^{2} \frac{1}{2KN} \chi_{2N}^2 \tag{4.90}$$

$$= \frac{1}{2KN} \left[K\rho \chi_{2N}^2 + \chi_{2KN}^2 \right]. \tag{4.91}$$

Simplifying (4.91) to a Normal Distributed Random Variable, we obtain

$$\mathbf{C} = N_{\mathbb{R}} \left(\rho + 1, \frac{K\rho^2 + 2\rho + 1}{KN} \right). \tag{4.92}$$

Using expression of $\mathbf{A}$ from (4.77) and $\mathbf{C}$ from (4.92) in (4.85), $T_{HED2}|_{H_1}$ can be written as the ratio of two Normal Random Variables as,

$$T_{HED2}|_{H_1} = \frac{N_{\mathbb{R}} \left(\rho + 1, \frac{K\rho^2 + 2\rho + 1}{KN} \right)}{N_{\mathbb{R}} \left(\frac{S + \rho S_S}{S}, \frac{S_S K\rho^2 + \rho S_S + S}{KMS^2} \right)}. \tag{4.93}$$

Noting the result,

$$T_{HED2} = \begin{cases} \dfrac{N_{\mathbb{R}} \left(1, \frac{1}{KN} \right)}{N_{\mathbb{R}} \left(\frac{S + \rho S_S}{S}, \frac{S_S K\rho^2 + \rho S_S + S}{KMS^2} \right)} & \mathscr{H}_0, \\ \dfrac{N_{\mathbb{R}} \left(\rho + 1, \frac{K\rho^2 + 2\rho + 1}{KN} \right)}{N_{\mathbb{R}} \left(\frac{S + \rho S_S}{S}, \frac{S_S K\rho^2 + \rho S_S + S}{KMS^2} \right)} & \mathscr{H}_1 \end{cases}. \tag{4.94}$$

This shows that, for both $\mathscr{H}_0$ and $\mathscr{H}_1$, the decision statistic is the ratio of two normal random variables which can be simplified to single Normal Random

Variable as,

$$T_{HED2} = \begin{cases} N_{\mathbb{R}}\left(\dfrac{S}{S+\rho S_S}, \dfrac{t^2 N(S_S K\rho^2+\rho S_S+S)+MS^2}{KMN(S+\rho S_S)^2}\right) & \mathscr{H}_0, \\ N_{\mathbb{R}}\left(\dfrac{S(\rho+1)}{S+\rho S_S}, \dfrac{t^2 N(S_S K\rho^2+\rho S_S+S)+MS^2(K\rho^2+2\rho+1)}{KMN(S+\rho S_S)^2}\right) & \mathscr{H}_1 \end{cases}. \tag{4.95}$$

Formulation of Detection and False Alarm Probabilities

Based on the statistics of T_{HED2} given by (4.95), probability of false alarm can be written in terms of Q-function as,

$$P_{Fa} = Q\left[\frac{t-\dfrac{S}{S+\rho S_S}}{\sqrt{\dfrac{t^2 N(S_S K\rho^2+\rho S_S+S)+MS^2}{KMN(S+\rho S_S)^2}}}\right]. \tag{4.96}$$

Similarly, based on the statistics of T_{HED2} given by (4.95), probability of detection can be written in terms of Q-function as,

$$P_D = Q\left[\frac{t-\dfrac{S(\rho+1)}{S+\rho S_S}}{\sqrt{\dfrac{t^2 N(S_S K\rho^2+\rho S_S+S)+MS^2(K\rho^2+2\rho+1)}{KMN(S+\rho S_S)^2}}}\right]. \tag{4.97}$$

Simulation Result

This Sub-Section shows the comparison between HED2 simulated curves and analytical ROC curves based on (4.63) and (4.64). Figure 4.14 shows perfect match between theoretical and numerical curves validating the considered model. Figure 4.15 illustrates the comparison of ED, HED1 and HED2 performance in varying SNR. Performance of HED1 and HED2 varies typically around 0 dB SNR but no big difference can be noted in extreme higher or lower SNR values. Since, there is a chance of mis-interpretation of noise plus primary signal as only noise signal in case of HED2, performance of HED2 is slightly lower than HED1 near 0 dB SNR. With the increase in the number of slots used for the estimation of the noise variance,

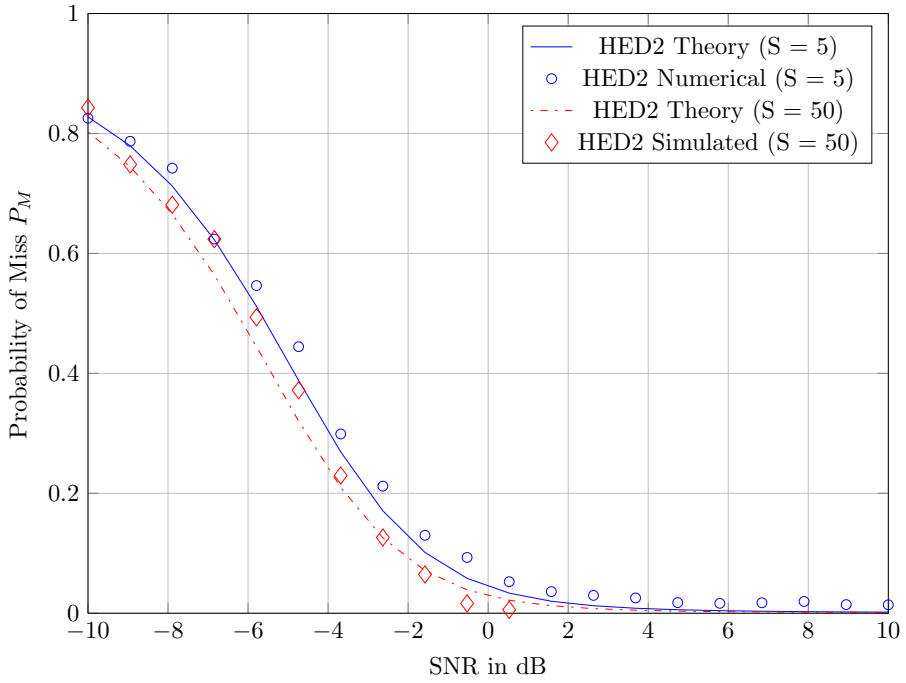

Fig. 4.14 Comparison of simulated and analytical detection performance curves of HED2 method for $N = 10$, $M = 10$, $K = 5$, $S = 5$ and 50

the probability of miss of HED1 and HED2 is decreases and goes near to that of ED-known variance.

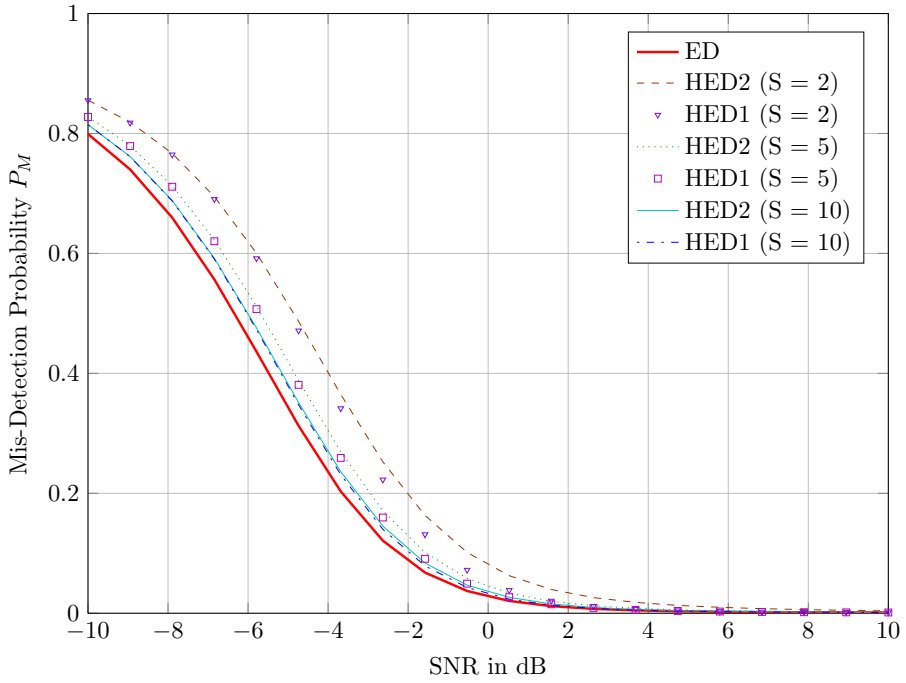

Fig. 4.15 Comparison of performance curves of HED2, ED and HED1 for $N = 10$, $M = 10$, $K = 5$, $S = 2, 5$ and 10

4.2.10 RLRT

RLRT is a "semi-blind" eigenvalue based detection scheme originally proposed in [148] and introduced in CR by [107]. It is a multi-sensor detection algorithm which requires the prior knowledge of noise variance for optimum performance.

Formulation of Decision Statistic

Using the information on the received signal matrix $\boldsymbol{Y}$ and assuming a perfect knowledge of noise variance σ_v^2 and the channel parameter $\boldsymbol{h}$, a test statistic T is developed. The detector compares T against a predefined threshold t. If $T < t$ it decides in favor of Null Hypothesis $\mathscr{H}_0$ otherwise in favor of Alternate Hypothesis $\mathscr{H}_1$. In context of perfect knowledge of noise and channel parameters, the most accurate and uniformly most powerful test of the above hypothesis is the Neyman-Pearson Test (NP Test) [131]. Using NP test, the expression of the test statistic can be written as

$$T_{NP} = \frac{p_1(\boldsymbol{Y}; \boldsymbol{h}, \sigma_s^2, \sigma_v^2)}{p_0(\boldsymbol{Y}; \sigma_v^2)}. \tag{4.98}$$

Using (4.98) probability of false alarm P_{Fa} and probability of detection P_D for a given decision statistic are given by,

$$P_{Fa} = Prob\{T > t|_{H_0}\} \tag{4.99}$$

$$P_D = Prob\{T > t|_{H_1}\}, \tag{4.100}$$

where t is the detection threshold. Since (4.98) in asymptotic regime $N \to \infty$ converges to depend on the largest Eigenvalue [128, 107] λ_1, resulting test is also known as RLRT [148]. Thus, the test statistic of the RLRT test is given by,

$$T_{RLRT} = \frac{\lambda_1}{\sigma_v^2}. \tag{4.101}$$

Formulation of Detection and False alarm Probabilities

1) False alarm probability: Concerning the Null hypothesis where $\boldsymbol{Y} = \boldsymbol{V}$, the sample covariance matrix $\boldsymbol{R}$ follows a Wishart Distribution of degree N. From (4.99) and (4.101), it is clear that, the false alarm rate depends upon the distribution of the largest eigenvalue λ_1 of the sample covariance matrix $\boldsymbol{R}$. According to recent results involving RMT, the detection statistic T_{RLRT} under Null Hypothesis for sufficiently large N and K follows a Tracy Widom Distribution of order 2 [98]. Thus,

$$Prob\left[\frac{T_{RLRT}|_{H_0} - \mu}{\xi} < t\right] \to F_{TW2}(t), \tag{4.102}$$

where $F_{TW2}(t)$ is the Cumulative Distribution Function of the Tracy Widom Distribution of order 2 with suitably chosen centering and scaling parameters given by:

$$\mu = \left[\left(\frac{K}{N}\right)^{\frac{1}{2}} + 1\right]^2 \tag{4.103}$$

$$\xi = N^{-2/3}\left[\left(\frac{K}{N}\right)^{\frac{1}{2}} + 1\right]\left[\left(\frac{K}{N}\right)^{-\frac{1}{2}} + 1\right]^{1/3}. \tag{4.104}$$

For (4.99), the probability of false alarm can be written as

$$P_{Fa} = Prob\left(P_{RLRT} > t|_{H_0}\right) \tag{4.105}$$

$$= Prob\left(\frac{T_{RLRT}|_{H_0} - \mu}{\xi} > \frac{t-\mu}{\xi}\right) \tag{4.106}$$

$$P_{Fa} = 1 - F_{TW2}\left(\frac{t-\mu}{\xi}\right). \tag{4.107}$$

2) Detection probability: Under alternate hypothesis H_1, the asymptotic distribution of λ_1 in the joint limit $N, K \to \infty$ is characterized by a phase transition phenomenon for smaller SNR [21]. For single signal detection, a critical detection threshold was identified [139] in terms of SNR as, $\rho_{Cric} = \frac{1}{\sqrt{KN}}$. This suggests that when SNR is lower than the critical value, the limiting distribution of the detection statistics T_{RLRT} is the same of the largest noise eigenvalue, thus nullifying the statistical power of a largest eigenvalue test. For $\rho > \rho_{Cric}$ the distribution of T_{RLRT} was found to be asymptotically Gaussian [107, 21] as shown below,

$$\frac{\lambda_1}{\sigma_v^2} \sim N_{\mathbb{R}}(\mu_1, \sigma_1^2), \tag{4.108}$$

where,

$$\mu_1 = (1 + K\rho)\left(1 + \frac{K-1}{NK\rho}\right) \tag{4.109}$$

$$\sigma_1^2 = \frac{1}{N}(K\rho + 1)^2\left(1 - \frac{K-1}{NK^2\rho^2}\right). \tag{4.110}$$

Thus, using the above normal approximation in (4.100), the probability of detection of RLRT can be written as

$$P_D = Prob\left[T_{RLRT}|_{H_1} < t\right], \tag{4.111}$$

$$P_D = Q\left(\frac{t-\mu_1}{\sigma_1}\right). \tag{4.112}$$

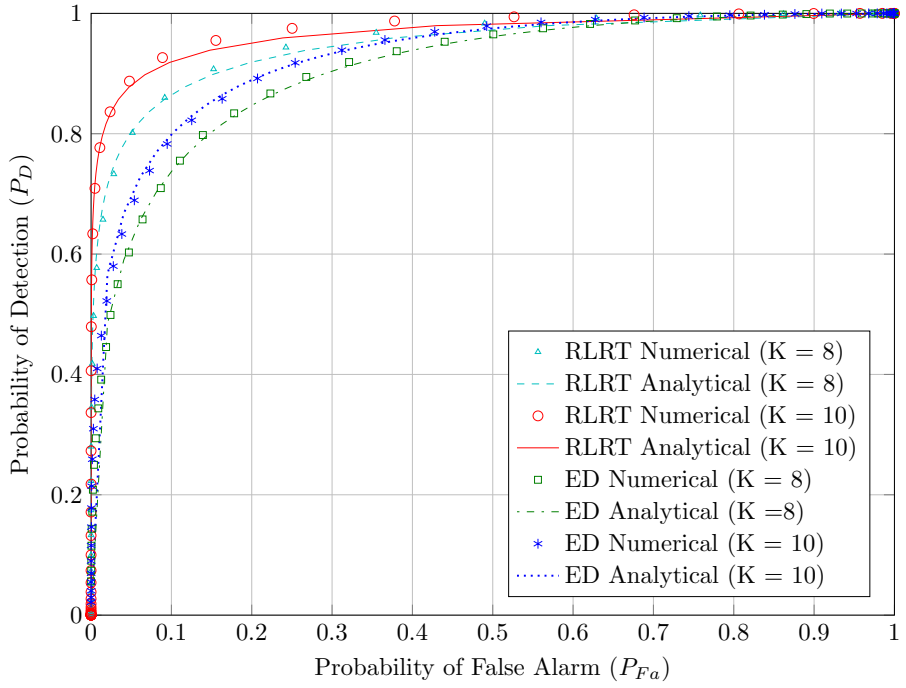

Fig. 4.16 Comparison of simulated and analytical ROC performance curves of RLRT method for $N = 50, K = 8$ and 10, $SNR = -10\ dB$

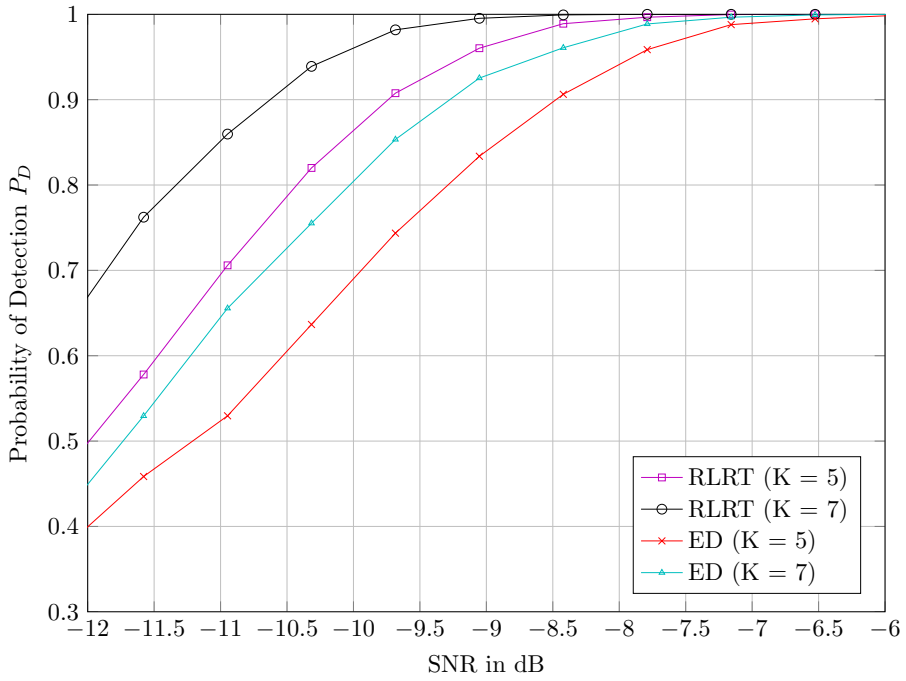

Fig. 4.17 P_D vs. SNR performance of RLRT. Parameters: $N = 100, K = 5, 7$, $P_{Fa} = 0.05$

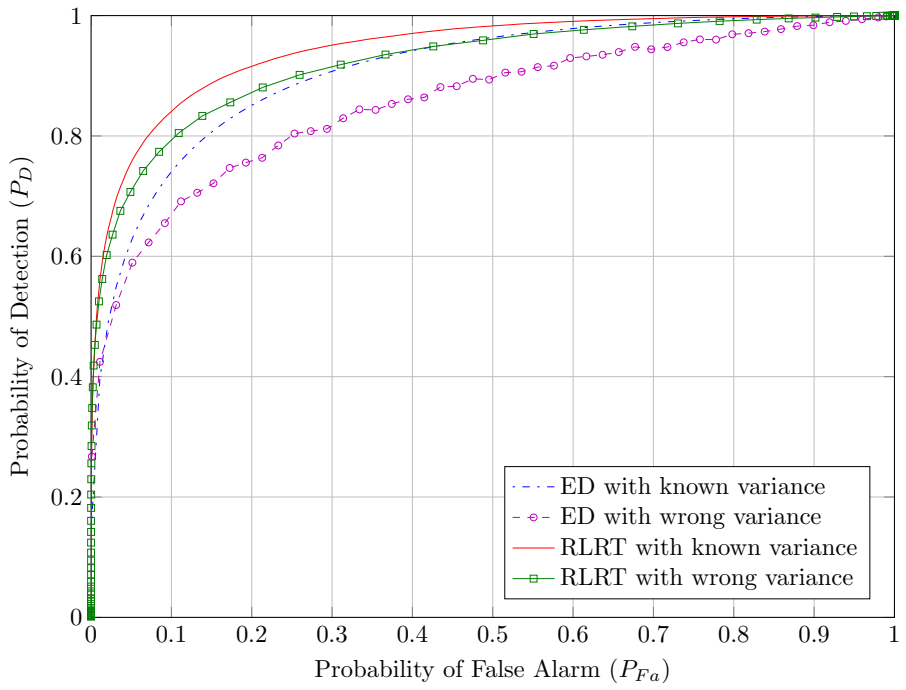

Fig. 4.18 Effect of Noise Variance fluctuation on ED and RLRT. Parameters: $N = 100, K = 4, var(\hat{\sigma}_v^2) = 0.0032(-25dB)$ given nominal variance $\sigma_v^2 = 1$

Simulation Result

The ROC performance of RLRT is shown in Figure 4.16 along with its comparison with ED for the same simulation parameters. The accuracy of the closed-form expression derived in (4.107) and (4.112) is confirmed by the results presented in Figure 4.16, which shows a perfect match between analytical and ùàsimulated curves. The considered parameters are $(K = 8, N = 50)$ at $-10dB$ SNR. As shown in the figure, the theoretical expressions is quite accurate even for small number of sensors K. The figure also shows the performance gap between ED and RLRT.

For given probability of false alarm $P_{Fa} = 0.05$, the performance of RLRT in terms of probability of miss-detection is plotted against different values of SNR in Figure 4.17. The considered parameters are ($K = 5, 7$ and $N = 50$). A comparison between ED and RLRT can also be realized from Figure 4.17. It can be noted that the detection performance of RLRT is far more better than that of ED for same simulation parameters.

The effect of the noise variance fluctuation on ED and RLRT algorithms is considered in Figure 4.18. Assuming Gaussian Distribution of the noise variance estimate with mean equal to nominal value, ROC for ED and RLRT is being plotted, setting $var(\hat{\sigma}_v^2) = 0.0032(-25dB)$ for $N = 100$ and $K = 4$. The result showed that, for the same fluctuation on the noise variance estimate, the performance gap between the ideal curve and the curve with wrong variance is larger for ED as compared to RLRT. Thus, it could be figured out that RLRT is more robust to noise variance fluctuation as compared to ED algorithm.

4.2.11 Hybrid RLRT (HRLRT1)

HRLRT1 addresses the problem of a priori knowledge of the noise power in RLRT. HRLRT1 is a hybrid approach of RLRT similar to HED1 in which estimated noise variance is used instead of nominal noise variance so as to normalize the received signal in order to detect the primary signal.

Formulation of Decision Statistic

HRLRT1 explores the concept of noise variance estimation from noise only samples so as to fulfill the gap of unavailability of the noise variance. Assuming the noise variance is constant over the adjacent slots, independent noise estimation in auxiliary "noise only" slots is performed.

Consider a sampling window of M samples before and adjacent to the detection window which is containing only noise samples for sure. The estimated noise variance from the noise only samples using a Maximum Likelihood noise power estimation can be written as,

$$\hat{\sigma}_v^2 = \frac{1}{KM} \sum_{k=1}^{K} \sum_{m=1}^{M} |v_k(m)|^2. \tag{4.113}$$

If the noise variance is constant over each slots, the estimation can be averaged over S successive noise-only slots. Thus, above (4.113) can be modified by averaging over S successive noise-only slots as,

$$\hat{\sigma}_v^2 = \frac{1}{KSM} \sum_{s=1}^{S} \sum_{k=1}^{K} \sum_{m=1}^{M} |v_k(m)|^2. \tag{4.114}$$

Now, the HRLRT1 Test Statistic can be derived from (4.101) by replacing the exact noise variance with the estimated noise variance using (4.114), i.e.,

$$T_{HRLRT1} = \frac{\lambda_1}{\hat{\sigma}_v^2}. \tag{4.115}$$

Equation (4.115) can be considered as the parametric likelihood ratio test when the signal to be detected is assumed to be Gaussian with zero mean and variance σ_s^2.

Proposition 4. Consider the HRLRT1 test working with K sensors, N samples, SNR value ρ and threshold t. Asymptotically in N and K, the false alarm and detection probability of HRLRT1 are given by,

$$P_{Fa} = 1 - F_0(t) \tag{4.116}$$

$$P_D = Q\left(\frac{t-1}{\sqrt{\frac{2t^2}{D} + \sigma_1^2}}\right), \tag{4.117}$$

where $F_0(t)$, is the cdf of the pdf shown below:

$$f_0(t) = \frac{1}{2\xi}\sqrt{\frac{D}{\pi}}\int_{-\infty}^{\infty} |x| f_{TW2}\left(\frac{tx-\mu}{\xi}\right)\exp\left(-\frac{D}{4}(x-1)^2\right)\mathrm{d}x. \tag{4.118}$$

The proof of the above Proposition 4 can be found in following Sub-Section.

Formulation of Detection and False Alarm Probability

For the ease of simplification, consider the test statistic of the HRLRT1 as shown below,

$$T_{HRLRT1}|_{H_0} = \frac{\lambda_1|H_0}{\sigma_v^2} \times \frac{1}{\hat{\sigma}_v^2/\sigma_v^2}. \tag{4.119}$$

1) False alarm probability: Under Null hypothesis H_0 where $\boldsymbol{Y} = \boldsymbol{V}$, the sample covariance matrix $\boldsymbol{R}$ follows a Wishart Distribution of degree N. From (4.115) and (4.119) it is clear that the false alarm rate depends upon the distribution of the largest eigenvalue λ_1 of the sample covariance matrix $\boldsymbol{R}$.

Now, for sufficiently large N and K, $\frac{\lambda_1|_{H_0}}{\sigma_v^2}$ follows a Tracy Widom Distribution of order 2 [98] with suitably chosen centering and scaling parameters as shown below:

$$\mu = \left[\left(\frac{K}{N}\right)^{\frac{1}{2}} + 1\right]^2 \tag{4.120}$$

$$\xi = N^{-2/3}\left[\left(\frac{K}{N}\right)^{\frac{1}{2}} + 1\right]\left[\left(\frac{K}{N}\right)^{-\frac{1}{2}} + 1\right]^{1/3}. \tag{4.121}$$

Let us denote the Probability Density Function of the Tracy Widom Distribution of order 2 as,

$$pdf\left\{F_{TW2}\left(\frac{z-\mu}{\xi}\right)\right\} = \frac{1}{\xi} f_{TW2}\left(\frac{z-\mu}{\xi}\right). \tag{4.122}$$

Similarly, for sufficiently large value of $D = 2KSM$, $\hat{\sigma}_v^2/\sigma_v^2$ follows a Normal distribution $N_{\mathbb{R}}\left(1, \frac{2}{D}\right)$ with Probability Density Function,

$$f_{1,2/D}(x) = \frac{1}{2}\sqrt{\frac{D}{\pi}} \exp\left(-\frac{D(x-1)^2}{4}\right). \tag{4.123}$$

Thus, using above distribution, the test statistic $T_{HRLRT1}|_{H_0}$ in (4.119) can be re-written as,

$$T_{HRLRT1}|_{H_0} = \frac{F_{TW2}\left(\frac{\frac{\lambda_1|_{H_0}}{\sigma_v^2} - \mu}{\xi}\right)}{N_{\mathbb{R}}\left(1, \frac{2}{D}\right)}. \tag{4.124}$$

Since the two random variables in (4.124) are statistically independent, the probability density functions of the detection statistic $T_{HRLRT1}|_{H_0}$ can be written as,

$$f_0(t) = \frac{1}{2\xi}\sqrt{\frac{D}{\pi}} \int_{-\infty}^{\infty} |x| f_{TW2}\left(\frac{tx-\mu}{\xi}\right) \exp\left(-\frac{D}{4}(x-1)^2\right) \mathrm{d}x. \tag{4.125}$$

Now, using the result in (4.125), the probability of false alarm can be written as,

$$P_{Fa} = 1 - F_0(t), \tag{4.126}$$

where $F_0(t)$, is the Cumulative Distribution Function of the probability distribution function shown in (4.125).

2) Detection probability: Under alternate hypothesis H_1, the asymptotic distribution of λ_1 in the joint limit $N,K \to \infty$ is characterized by a phase transition phenomenon for small SNR [21]. For single signal detection, the critical detection threshold can be expressed in terms of SNR as [139],

$$\rho_{Cric} = \frac{1}{\sqrt{KN}}, \tag{4.127}$$

which in fact suggests that when SNR is lower than the critical value, the limiting distribution of $\frac{\lambda_1|_{H_1}}{\sigma_v^2}$ is the same as that of the largest noise eigenvalue, thus, nullifying the statistical power of a largest eigenvalue test.

For $\rho > \rho_{Cric}$ the distribution of $\frac{\lambda_1|_{H_1}}{\sigma_v^2}$ was found to be asymptotically Gaussian [107, 21] as shown below,

$$\frac{\lambda_1|_{H_1}}{\sigma_v^2} \sim N_{\mathbb{R}}(\mu_1, \sigma_1^2), \tag{4.128}$$

where,

$$\mu_1 = (1+K\rho)\left(1+\frac{K-1}{NK\rho}\right) \tag{4.129}$$

$$\sigma_1^2 = \frac{1}{N}(K\rho+1)^2\left(1-\frac{K-1}{NK^2\rho^2}\right). \tag{4.130}$$

Thus, the expression in (4.119) can be written as,

$$T_{HRLRT1}|_{H_1} = \frac{N_{\mathbb{R}}(\mu_1, \sigma_1^2)}{N_{\mathbb{R}}\left(1, \frac{2}{D}\right)}. \tag{4.131}$$

The above ratio of normal distributed random variable can be approximated with a single Normal Random Variable as,

$$T_{HRLRT1}|_{H_1} = N_{\mathbb{R}}\left(\mu_1, \frac{2t^2}{D} + \sigma_1^2\right). \tag{4.132}$$

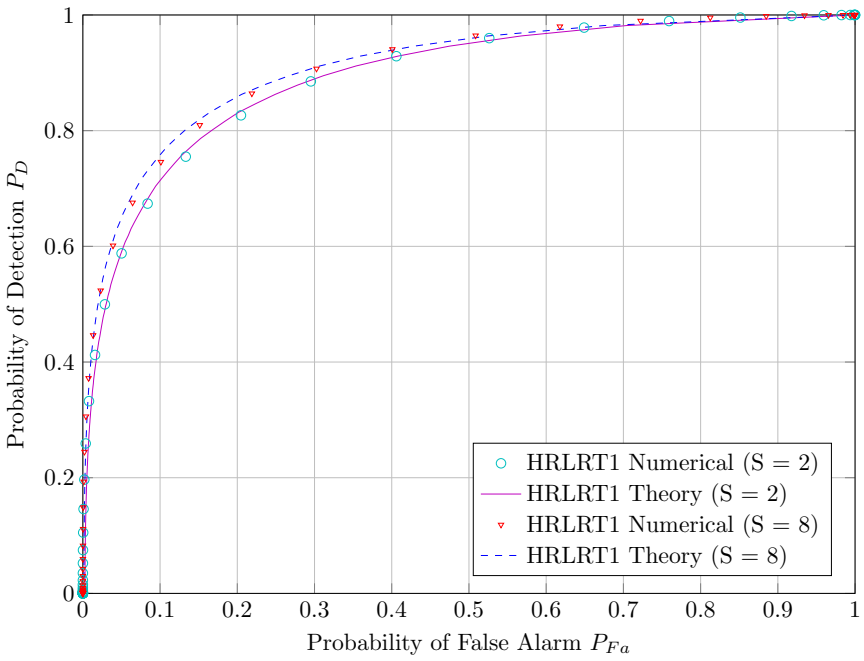

Fig. 4.19 Comparison of simulated and analytical performance curves of HRLRT1 method for $N = 80, K = 4$ and $S = 2\ 8$, $SNR = -10\ dB$

Thus, using the above normal approximation, the probability of detection of HRLRT1 can be computed,

$$P_D = Prob\left[T_{HRLRT1}|_{H_1} > t\right] \tag{4.133}$$

$$= Q\left(\frac{t-\mu_1}{\sqrt{\frac{2t^2}{D}+\sigma_1^2}}\right). \tag{4.134}$$

Simulation Result

The accuracy of the closed-form expression derived in Proposition 4 is confirmed by the results presented in Figure 4.19, where the analytical curves obtained by applying theoretical formula in (4.126) and (4.134) are compared against simulated detection performance. The considered parameters are ($K = 4, N = 80, S = 2, 8$ and SNR $= -10\ dB$). As shown in the figure, the theoretical expressions is quite accurate even for a small number of sensors.

The performance of HED1 and HRLRT1 is compared in Figure 4.20 and Figure 4.21. The noise variance is estimated by (4.114) in S auxiliary pure noise slots

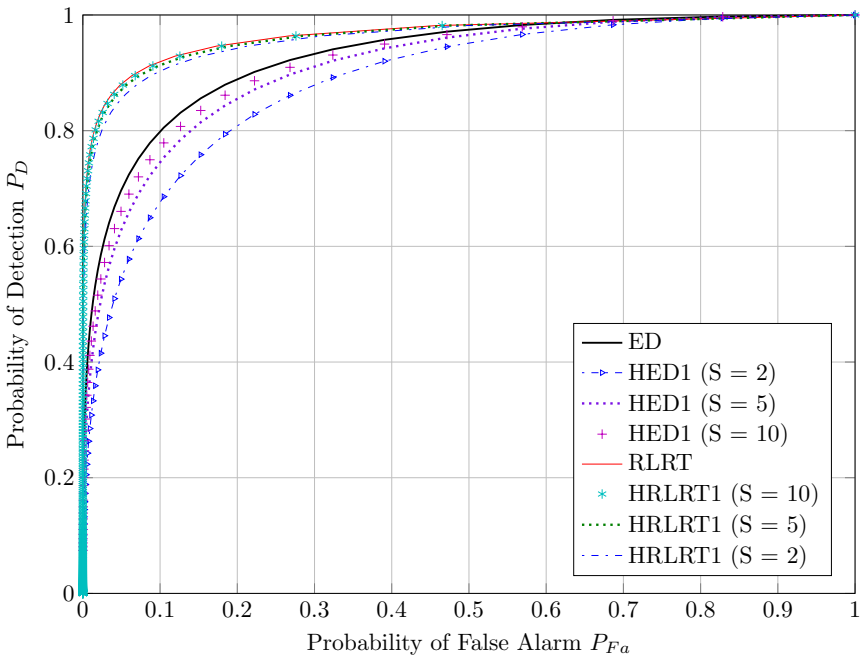

Fig. 4.20 ROC performance of RLRT and ED methods compared with their hybrid counterparts. Parameters: $N = 80, K = 4$ and $S = 2, 5, 10$, $SNR = -10\ dB$

and the value is then used within the two tests for all the other slots. The curves approach the ideal ED and RLRT curves by increasing the number of auxiliary slots S, but the rate of convergence of HED1 is slower.

4.2.12 Hybrid RLRT-2(HRLRT2)

It is evident that the knowledge of the noise power is imperative for achieving RLRT the optimum performance. Unfortunately, the variation and the unpredictability of precise noise power is a critical issue for using RLRT in sensing signals with low SNR. In Sub-Section 4.2.11, we discussed the detection performance of RLRT with estimated noise variance, where noise variance was estimated from the noise only slots. In reality, within the same channel, there is a serious problem in finding noise only samples so as to estimate the variance of the noise samples. As an alternative, HRLRT2 does not resort on the existence of auxiliary noise only slots,

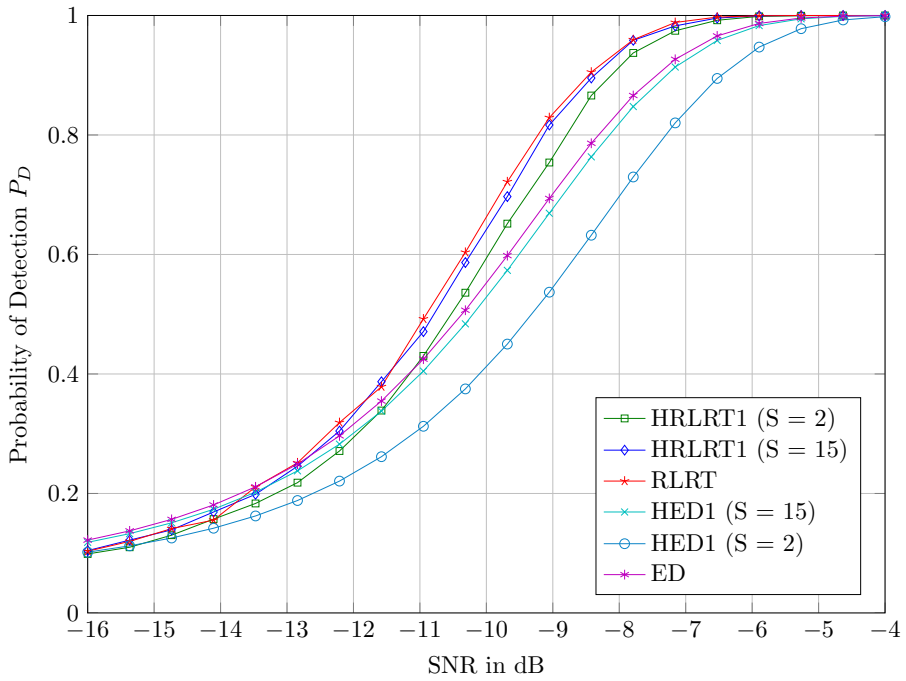

Fig. 4.21 Comparison of HRLRT1 and HED1 performance curves. Parameters: $N = 80, K = 4$ and $S = 2$ and 15, $SNR = -10\ dB$

but estimated the noise variance information from the previous slots declared as $\mathscr{H}_0$ by the algorithm. Now, for the RLRT scheme using noise variance estimated from S preceding slots which are declared $\mathscr{H}_0$ by same algorithm, which we call Hybrid RLRT-2 (HRLRT2) model, we derive the analytical expression of performance parameters P_D and P_{Fa} in a multi-sensor environment.

Formulation of the Decision Statistic

Using the information on the received signal matrix $\boldsymbol{Y}$ to develop a test statistic T_{HRLRT2} which is a modification of the RLRT test statistic considering noise variance is estimated in S slots declared $\mathscr{H}_0$ by RLRT in the first stage. The detector compares T_{HRLRT2} against a predefined threshold t. If $T_{HRLRT2} < t$ then it decides in favor of Null Hypothesis $\mathscr{H}_0$ otherwise in favor of Alternate Hypothesis $\mathscr{H}_1$. The ratio of largest eigenvalue of the covariance matrix $\boldsymbol{R}$ and the estimated noise variance is given by,

$$T_{HRLRT2} = \frac{\lambda_1}{\hat{\sigma}_v^2}. \tag{4.135}$$

Proposition 5. Let us denote by P_S the probability of receiving primary signal plus noise, P_D^{RLRT} the probability of detection of first stage RLRT, and S the number of slots. The Maximum Likelihood noise variance estimate $\hat{\sigma}_v^2$ using M received signal samples declared noise samples by RLRT from K receivers is given by,

$$\hat{\sigma}_v^2(S) = \frac{\left[\sum_{s=1}^{S_s}\sum_{k=1}^{K}\sum_{m=1}^{M}|h_k s(m)+v(m)|^2 + \sum_{s=1}^{S_N}\sum_{k=1}^{K}\sum_{m=1}^{M}|v_k(m)|^2\right]}{KMS}, \tag{4.136}$$

where, $S_S = SP_S\left(1-P_D^{RLRT}\right)$ is the number of H_1 primary signal slots missed by RLRT and $S_N = S - S_S$ is the number of H_0 noise slots successfully detected.

Proof. Consider a sampling window of length M before and adjacent to the detection window which contains slota declared $\mathscr{H}_0$ by first stage RLRT. But instead are H_1 slots for them the estimated noise variance from the noise only samples using a Maximum Likelihood Noise Power Estimate can be written as,

$$\hat{\sigma}_v^2 = \frac{1}{KM}\left[\sum_{k=1}^{K}\sum_{m=1}^{M}|h_k s(m)+v(m)|^2\right]. \tag{4.137}$$

If the noise variance is constant, the estimation can be averaged over S successive noise-only slots. Noting that since slots are declared noise only slot by RLRT, there is a chance with probability $(1-P_D^{RLRT})$ that RLRT decides in favor of $\mathscr{H}_0$ even if the received signal is the sum of noise and the primary signal. If the estimated variance is the mean of S successive noise variances calculated from the noise only slots decided by ED, then out of S noise variance estimates from S noise only slots decided by RLRT, $P_S(1-P_D^{RLRT})S$ noise variance estimates are calculated from H_1 slots containing noise and the primary signal. Thus, the estimated noise variance can be written as the mean of the noise variance estimated from noise signal slots declared $\mathscr{H}_0$ by RLRT given $\mathscr{H}_0$ and the noise signal slots declared $\mathscr{H}_0$ by RLRT given $\mathscr{H}_1$. Finally, (4.137) could be modified and rewritten as,

$$\hat{\sigma}_v^2(S) = \frac{\left[\sum_{s=1}^{S_s}\sum_{k=1}^{K}\sum_{m=1}^{M}|h_k s(m)+v(m)|^2 + \sum_{s=1}^{S_N}\sum_{k=1}^{K}\sum_{m=1}^{M}|v_k(m)|^2\right]}{KMS}. \tag{4.138}$$

□

Proposition 6. Consider the HRLRT2 test working with K sensors, N samples, SNR value ρ, number of auxiliary slots S for noise estimation using (4.138) and threshold t. Asymptotically in N and K, the false alarm and detection probability of HRLRT2 are respectively given by,

$$P_{Fa} = 1 - F_0(t) \tag{4.139}$$

$$P_D = Q\left(\frac{t - \mu_x/\mu_1}{\sqrt{\frac{t^2\sigma_1^2+\sigma_x^2}{\mu_1^2}}}\right), \tag{4.140}$$

where $F_0(t)$, is the cumulative distribution function of the probability distribution function shown below:

$$f_0(t) = \frac{1}{\xi\sigma_1^2\sqrt{2\pi}}\int_{-\infty}^{\infty}|x| f_{TW2}\left(\frac{tx-\mu}{\xi}\right)\exp\left(-\frac{1}{2\sigma_1^2}(x-\mu_1)^2\right)\mathrm{d}x. \tag{4.141}$$

The proof of the above Proposition 6 could be found in following Sub-Section.

Formulation of Detection and False Alarm Probability

The test statistic of HRLRT2 can be written as

$$T_{HRLRT2}|_{H_0} = \frac{\lambda_1|H_0}{\sigma_v^2} \times \frac{1}{\hat{\sigma}_v^2/\sigma_v^2}. \tag{4.142}$$

1) Probability of false alarm: Cosider the Null hypothesis H_0 where $\boldsymbol{Y} = \boldsymbol{V}$ and the sample covariance matrix $\boldsymbol{R}$ follows a Wishart Distribution of degree N. For sufficiently large N and K, $\frac{\lambda_1|_{H_0}}{\sigma_v^2}$ follows a Tracy Widom Distribution of order 2 [98] with suitably chosen centering and scaling parameters given by.

$$\mu = \left[\left(\frac{K}{N}\right)^{\frac{1}{2}}+1\right]^2 \tag{4.143}$$

$$\xi = N^{-2/3}\left[\left(\frac{K}{N}\right)^{\frac{1}{2}}+1\right]\left[\left(\frac{K}{N}\right)^{-\frac{1}{2}}+1\right]^{1/3}. \tag{4.144}$$

Let us denote the pdf of the Tracy Widom Distribution of order 2 as

$$pdf\left\{F_{TW2}\left(\frac{z-\mu}{\xi}\right)\right\} = \frac{1}{\xi} f_{TW2}\left(\frac{z-\mu}{\xi}\right). \tag{4.145}$$

For sufficiently large value of $2KS_SM$, $\hat{\sigma}_v^2/\sigma_v^2$ follows a Normal distribution given by(See (4.77)),

$$N_{\mathbb{R}}\left(\mu_1, \sigma_1^2\right), \tag{4.146}$$

where,

$$\mu_1 = \frac{S+S_S}{S} \tag{4.147}$$

$$\sigma_1^2 = \frac{S+2\rho S_S+\rho^2 KS_S}{KMS^2}. \tag{4.148}$$

Thus, following above distributions, the test statistic $T_{HRLRT2}|_{H_0}$ in (4.135) can be re-written as,

$$T_{HRLRT2}|_{H_0} = \frac{F_{TW2}\left(\frac{1}{\xi}\left(\frac{\lambda_1|_{H_0}}{\sigma_v^2}-\mu\right)\right)}{N_{\mathbb{R}}\left(\mu_1, \sigma_1^2\right)}. \tag{4.149}$$

Since the two random variables in (4.149) are statistically independent, the probability density functions of the detection statistic $T_{HRLRT2}|_{H_0}$ can be written as,

$$f_0(t) = \frac{1}{\xi\sigma_1^2\sqrt{2\pi}} \int_{-\infty}^{\infty} |x| f_{TW2}\left(\frac{tx-\mu}{\xi}\right) \exp\left(-\frac{1}{2\sigma_1^2}(x-\mu_1)^2\right) \mathrm{d}x. \tag{4.150}$$

Finally, the probability of false alarm can be written as,

$$P_{Fa} = 1 - F_0(t), \tag{4.151}$$

where $F_0(t)$, is the Cumulative Distribution Function of the Probability Distribution Function shown in (4.150).

2) Probability of detection: Under alternate hypothesis, the asymptotic distribution of λ_1 in the joint limit $N, K \to \infty$ is characterized by a phase transition phenomenon for small SNR [21]. For single signal detection, the critical detection threshold was expressed in terms of SNR as [139],

$$\rho_{Cric} = \frac{1}{\sqrt{KN}}, \tag{4.152}$$

This suggests that when SNR is lower than the critical value, the limiting distribution of $\frac{\lambda_1|_{H_1}}{\sigma_v^2}$ is the same as that of the largest noise eigenvalue, thus nullifying the statistical power of a largest eigenvalue test. For $\rho > \rho_{Cric}$ the distribution of $\frac{\lambda_1|_{H_1}}{\sigma_v^2}$ was found to be asymptotically Gaussian [107, 21] with,

$$\frac{\lambda_1|_{H_0}}{\sigma_v^2} \sim N_{\mathbb{R}}(\mu_x, \sigma_x^2), \tag{4.153}$$

where,

$$\mu_x = (1+K\rho)\left(1+\frac{K-1}{NK\rho}\right) \tag{4.154}$$

$$\sigma_x^2 = \frac{1}{N}(K\rho+1)^2\left(1-\frac{K-1}{NK^2\rho^2}\right). \tag{4.155}$$

Thus, the expression in (4.135) can be written as,

$$T_{HRLRT2}|_{H_1} = \frac{N_{\mathbb{R}}(\mu_x, \sigma_x^2)}{N_{\mathbb{R}}\left(\mu_1, \sigma_1^2\right)}. \tag{4.156}$$

The above ratio of normal distributed random variable can be approximated with a single Normal Random Variable as,

$$T_{HRLRT2}|_{H_1} = N_{\mathbb{R}}\left(\frac{\mu_x}{\mu_1}, \frac{t^2\sigma_1^2+\sigma_x^2}{\mu_1^2}\right). \tag{4.157}$$

Thus, using the above normal approximation, the probability of detection of HRLRT2 can be written as

$$P_D^{HRLRT2} = Q\left(\frac{t-\mu_x/\mu_1}{\sqrt{\frac{t^2\sigma_1^2+\sigma_x^2}{\mu_1^2}}}\right). \tag{4.158}$$

Simulation Result

Figure 4.22 shows the comparison of simulated and analytical performance curves of HRLRT2 algorithm. Analytical evaluation of HRLRT2 ROC curves is carried out in two phases. In first phase, the pdf in (4.150) is evaluated numerically. In second phase, for a given probability of false alarm, corresponding threshold is

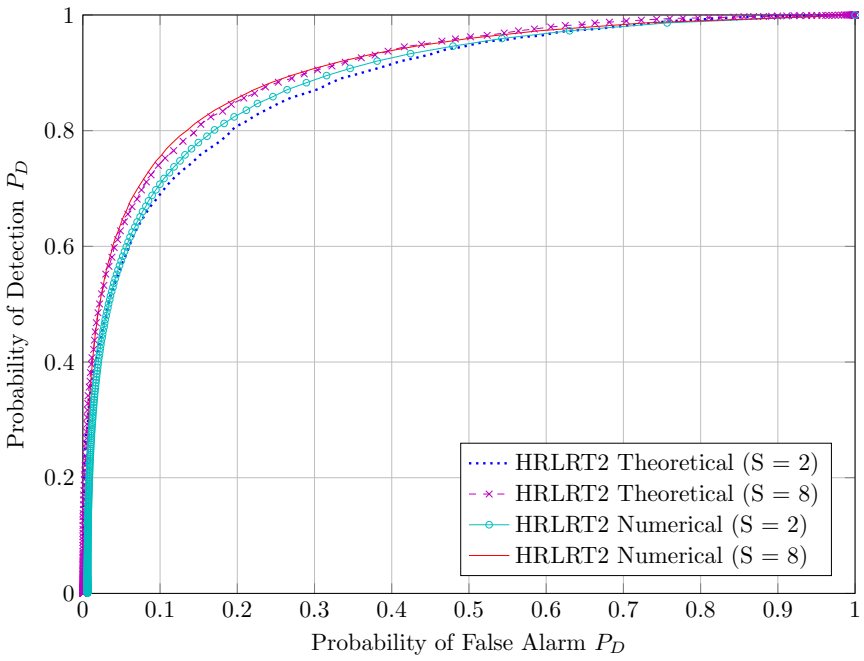

Fig. 4.22 Comparison of simulated and analytical performance curves of HRLRT2 method. Parameters: $N = 80, K = 4$ and $S = 2$ and 8, $SNR = -10\ dB$

evaluated. Finally, the probability of detection is calculated for each threshold value using (4.158). The simulated ROC curves of HRLRT2 are superimposed to the analytically generated ROC to measure the accuracy of the closed form expression presented by Proposition 6.

Convergence of the Hybrid approach of RLRT detection to ideal RLRT (with known variance) is illustrated in Figure 4.23. With the increase in number of auxiliary slots used for noise variance estimation, the performance of HRLRT1 and HRLRT2 converge to the ideal RLRT performance.

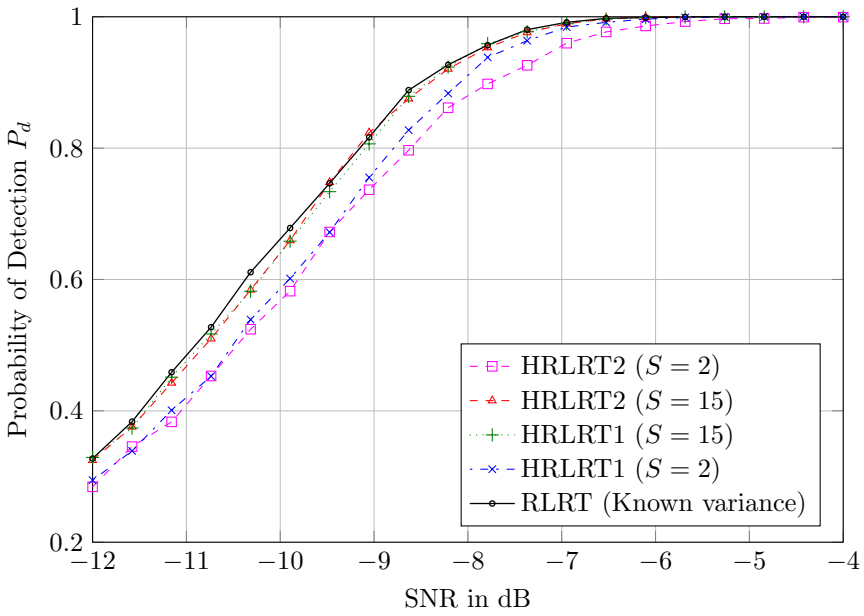

Fig. 4.23 Probability of detection vs. SNR for RLRT, HRLRT1 and HRLRT2, Parameters: $N = 80, K = 4$ and $S = 2$ and 15, $SNR = -10$ to -4 dB

4.2.13 SNR Wall Analysis of ED and HED1

For CR application the most popular sensing algorithm is the simpler ED that compares the energy of the received signal against the noise variance σ_v^2 as discussed before. ED requires the perfect knowledge of the noise power at the receiver [164, 50, 51, 105], however, in real systems the detector does not have a prior knowledge of the noise level. It is known from [159] that there is a certain SNR threshold in case of noise uncertainty known as SNR wall, which prevents ED from achieving the desired performance even if the detection interval tends to infinity.

In this work, starting from the contributions of [159, 118], we extend the condition of SNR Wall [159] to multi-sensor hybrid ED with auxiliary noise variance estimation (offline method) described in Sub-Section 4.2.6. For auxiliary noise variance estimation of White Gaussian Noise samples, the distribution of the estimated variance is studied and linked to the uncertainty bound referred to [159]. The SNR Wall expression is derived for multisensor ED and proved to be independent of the number of sensors. It is concluded that the noise uncertainty can be reduced by increasing the number of samples used for noise variance estimation, but the number of samples/slots used for noise estimation exponentially increases as the SNR Wall condition becomes more stringent.

With reference to the system model of Sub-Section 4.2.4 we briefly summarize the main results of ED presented in Sub-Section 4.2.7. Using the information on the received signal matrix Y, ED test statistic T_{ED} is employed by a detector to distinguish between $\mathscr{H}_0$ and $\mathscr{H}_1$. T_{ED} is the measure of the average energy of the received signal over a sensing interval N from K receivers which can be represented as,

$$T_{ED} = \frac{1}{KN\sigma_v^2} \sum_{k=1}^{K} \sum_{n=1}^{N} |y_k(n)|^2. \tag{4.159}$$

Here, the total energy estimated by T_{ED} is the normalized average energy over the sensing interval. In order to make a decision, the detector compares T_{ED} against a predefined threshold t: if $T_{ED} > t$ it decides for $\mathscr{H}_1$, otherwise for $\mathscr{H}_0$. As a consequence, the false alarm and detection probabilities are defined as,

$$P_{Fa} = Pr(T > t|_{\mathscr{H}_0}), \qquad P_D = Pr(T > t|_{\mathscr{H}_1}). \tag{4.160}$$

In practical applications, the decision threshold t is typically computed as a function of the target P_{Fa}: this ensures CFAR detection.

If the noise variance is assumed to be perfectly known, then T_{ED} in (4.159) can be simplified using a Gaussian approximation as,

$$T_{ED} = \begin{cases} N_{\mathbb{R}}\left(1, \frac{1}{KN}\right) & \mathscr{H}_0, \\ N_{\mathbb{R}}\left((\rho+1), \frac{K\rho^2+2\rho+1}{KN}\right) & \mathscr{H}_1 \end{cases}. \tag{4.161}$$

Based on the above approximation, P_{Fa} and P_D of ED can be easily simplified as,

$$P_{Fa} = Q\left[(t-1)\sqrt{KN}\right] \tag{4.162}$$

$$P_D = Q\left[\frac{(t-1-\rho)\sqrt{KN}}{\sqrt{K\rho^2+2\rho+1}}\right], \tag{4.163}$$

where $Q(.)$ is the standard normal complementary cdf.

If we eliminate the threshold t by using a similar approach as in [159] from (4.162) and (4.163) to calculate the number of samples in a sensing slot to achieve the re-

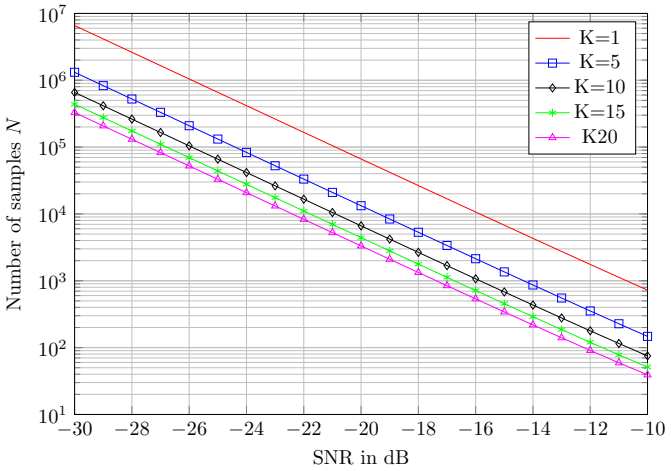

Fig. 4.24 Comparison of sample complexity N to achieve given P'_D and P'_{Fa} for single antenna vs. multi antenna environment for different SNR assuming perfect knowledge of noise variance. Parameters: $K = 5, 10, 15$ and 20, $P'_D = 0.9, P'_{Fa} = 0.1$

quired P_D and P_{Fa}, we get:

$$N = \frac{\left[\sqrt{(K\rho^2 + 2\rho + 1)}Q^{-1}(P_D) - Q^{-1}(P_{Fa})\right]^2}{K\rho^2}. \tag{4.164}$$

The expression of N in (4.164) exactly matches the expression of N derived in [159] when $K = 1$(single antenna) and with real signals. Figure 4.24 plots the sample complexity N for different SNR in single and multi antenna scenario. The plot clearly unveil that multi-sensor ED requires relatively less number of samples to achieve the given P'_D and P'_{Fa}. It is also clear that, given a priori information on the noise variance, received signal can be detected for any SNR maintaining the detection interval accordingly.

Now, let us consider the case in which the noise variance is not precisely known but its deviation is known to be bounded in the interval [159] $\left[\frac{1}{\beta}\sigma_v^2, \beta\sigma_v^2\right]$, i.e.,

$$\hat{\sigma}_v^2 \in \left[\frac{1}{\beta}\sigma_v^2, \beta\sigma_v^2\right], \tag{4.165}$$

where σ_v^2 is the nominal (true) noise power and $\beta > 1$ is the parameter that quantifies the level of uncertainty. It is evident that the knowledge of the noise variance is imperative for the optimum performance of ED. In practice it is not possible to know

the exact value of the noise variance, so the only option is to estimate it from the noise samples. The performance of ED with auxiliary noise variance estimation known as Hybrid ED (HED1) using Maximum Likelihood Estimation (MLE) was studied in previous sections. If we denote the estimate of the noise variance with $\hat{\sigma}_v^2$ and consider the ED detection statistic as,

$$\tilde{T}_{ED} = \frac{1}{KN} \sum_{k=1}^{K} \sum_{n=1}^{N} |y_k(n)|^2, \tag{4.166}$$

the Gaussian approximation of the detection statistic in (4.166) can be written as,

$$\tilde{T}_{ED} = \begin{cases} N_{\mathbb{R}}\left(\hat{\sigma}_v^2, \frac{\hat{\sigma}_v^4}{KN}\right) & \mathscr{H}_0, \\ N_{\mathbb{R}}\left(\|\boldsymbol{h}\|\sigma_s^2 + \hat{\sigma}_v^2, \frac{K\|\boldsymbol{h}\|^2\sigma_s^4 + 2\|\boldsymbol{h}\|\sigma_s^2\hat{\sigma}_v^2 + \hat{\sigma}_v^4}{KN}\right) & \mathscr{H}_1, \end{cases} \tag{4.167}$$

whose performance parameters can be written as,

$$P_{Fa} = Q\left[\frac{(t - \hat{\sigma}_v^2)\sqrt{KN}}{\hat{\sigma}_v^2}\right] \tag{4.168}$$

$$P_D = Q\left[\frac{(t - \hat{\sigma}_v^2 - \|\boldsymbol{h}\|\sigma_s^2)\sqrt{KN}}{\sqrt{K\|\boldsymbol{h}\|^2\sigma_s^4 + 2\|\boldsymbol{h}\|\sigma_s^2\hat{\sigma}_v^2 + \hat{\sigma}_v^4}}\right]. \tag{4.169}$$

Now, the worst case scenario of P_D and P_{Fa}, represented by the notations P'_D and P'_{Fa}, can be analyzed as,

$$P'_{Fa} = \max_{\hat{\sigma}_v^2 \in \left[\frac{1}{\beta}\sigma_v^2, \beta\sigma_v^2\right]} Q\left[\frac{(t - \hat{\sigma}_v^2)\sqrt{KN}}{\hat{\sigma}_v^2}\right] \tag{4.170}$$

$$P'_{Fa} = Q\left[\frac{\left(\frac{t}{\sigma_v^2} - \beta\right)\sqrt{N}}{\beta}\right] \tag{4.171}$$

$$P'_D = \min_{\hat{\sigma}_v^2 \in \left[\frac{1}{\beta}\sigma_v^2, \beta\sigma_v^2\right]} Q\left(\frac{(t - \hat{\sigma}_v^2 - \|\boldsymbol{h}\|\sigma_s^2)\sqrt{KN}}{\sqrt{K\|\boldsymbol{h}\|^2\sigma_s^4 + 2\|\boldsymbol{h}\|\sigma_s^2\hat{\sigma}_v^2 + \hat{\sigma}_v^4}}\right) \tag{4.172}$$

$$P'_D = Q\left[\frac{\left(\frac{t}{\sigma_v^2} - \rho\frac{1}{\beta}\right)\sqrt{KN}}{\sqrt{K\rho^2 + 2\rho\frac{1}{\beta} + \frac{1}{\beta^2}}}\right]. \tag{4.173}$$

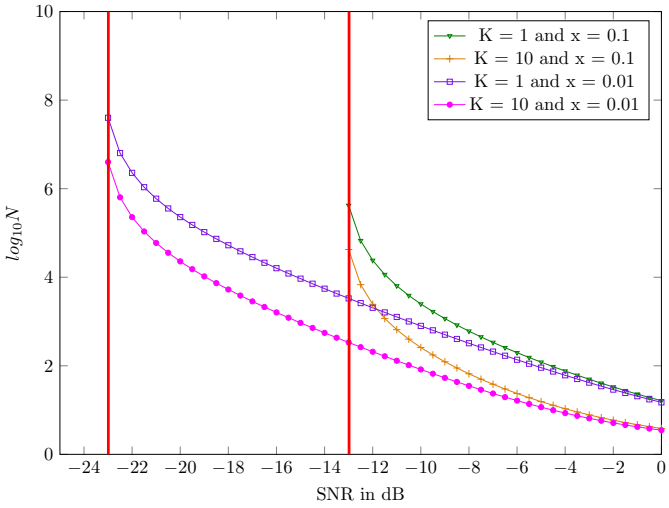

Fig. 4.25 Variation of sample complexity N as the SNR approaches SNR wall for ED, Parameters: $K = 5, P'_D = 0.9, P'_{Fa} = 0.1$ [use $x = 10\log_{10}\beta$ in Equation (4.174)]

By solving (4.171) and (4.173) and eliminating t, we get,

$$N = \frac{\left[\beta Q^{-1}(P'_{Fa}) - Q^{-1}(P'_D)\sqrt{K\rho^2 + 2\rho\frac{1}{\beta} + \frac{1}{\beta^2}}\right]^2}{K\left[\rho - \left(\beta - \frac{1}{\beta}\right)\right]^2}. \tag{4.174}$$

Equation (4.174) gives the expression of the number of samples in a sensing slot for given SNR condition to achieve the required performance in terms of P_{Fa} and P_D, which is also an extension of the result in [159] for a multi-sensor ED. The number of samples N goes to infinity as SNR approaches $\beta - \frac{1}{\beta}$. This condition is known as SNR Wall condition, which means that under this SNR wall value we cannot achieve the required performance in a given level of noise uncertainty even if the sample number is made sufficiently large. Thus, SNR Wall is given by the expression as shown below,

$$SNR_{wall}^{ED} = \left(\beta - \frac{1}{\beta}\right). \tag{4.175}$$

SNR wall makes clear that the Energy Detector cannot robustly detect the signal if the signal power is less than the uncertainty of the noise power, i.e.,

$$\sigma_s^2 < \left(\beta - \frac{1}{\beta}\right)\sigma_v^2. \tag{4.176}$$

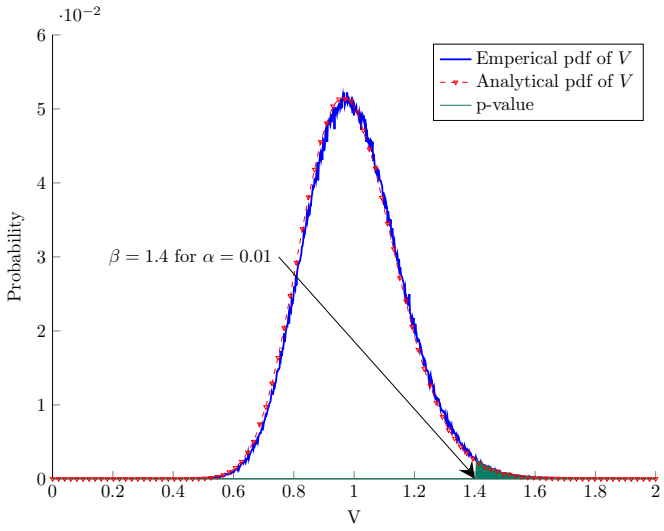

Fig. 4.26 Probability distribution of normalized noise variance estimate V. Parameters: $S = 2$, $K = 2$, $M = 10$

Our study shows that there is no difference in the SNR wall expression by using a multi antenna or a single antenna in ED. Figure 4.25 illustrates the SNR wall condition for single/multi antenna case and the variation of the sample complexity N, as SNR approaches SNR wall for different levels of noise uncertainty.

Noise Uncertainty Distribution and Formulation of Uncertainty Bound

Let us suppose that noise variance is estimated in S auxiliary slots with M noise only samples in each slot. Then the ML noise variance estimate using SKM noise-only samples obtained from K receivers with S slots each can be written as,

$$\hat{\sigma}_v^2(S) = \frac{1}{KSM} \sum_{s=1}^{S} \sum_{k=1}^{K} \sum_{m=1}^{M} |v_k(m)|^2. \tag{4.177}$$

If we focus on noise variance distribution under the same scenario, let us consider a random variable V (normalized noise variance estimate), which associates a unique numerical value from $\left(\frac{\hat{\sigma}_v^2}{\sigma_v^2}\right)$ for each noise variance estimation, where $\hat{\sigma}_v^2$ corresponds to (4.177).

Now, V can be written as

$$V = \left(\frac{\hat{\sigma}_v^2}{\sigma_v^2}\right) \tag{4.178}$$

$$= \left(\frac{1}{2KMS}\sum_{s=1}^{S}\sum_{k=1}^{K}\sum_{m=1}^{M}\left|\frac{v_k(m)}{\sqrt{\sigma_v/2}}\right|^2\right). \tag{4.179}$$

It can be noted that the expression in (4.179) is the sum of squared standard normal noise samples, thus it has a Chi-Square Distribution with $2KMS$ degrees of freedom. Then we have

$$V = \left(\frac{\chi^2_{2KMS}}{2KMS}\right), \tag{4.180}$$

where χ^2_{2KMS} represents a Chi-Squared random variable with $2KMS$ degrees of freedom.

Figure 4.26 shows the pdf of the random variable V according to (4.180) compared to its empirical pdf. Now, the uncertainty bound β can easily related with V using (4.165) and (4.180) as,

$$\beta = \max(V) \tag{4.181}$$

$$= \frac{F^{-1}_{Chi}(1-\alpha, 2KMS)}{2MKS}, \tag{4.182}$$

where $F^{-1}_{Chi}()$ is the Inverse Cumulative Distribution Function of a Chi Square Distributed Random Variable and α is the significance level of a Chi Square Distribution. As we know, a Chi Square Distributed Random variable can take any values in the range $(-\infty, +\infty)$, which leads (4.182) to infinity. In (4.182), $(1-\alpha)$ is the significance level, which gives an insight of percentage coverage of all possible values smaller than the value given by the inverse cdf. Thus,

$$\beta = \frac{F^{-1}_{Chi}(1-\alpha, 2KMS)}{2MKS}. \tag{4.183}$$

Finally, β can be expressed in terms of the total number of noise samples (i.e. KMS) considered for variance estimation as shown in (4.183) and can be easily

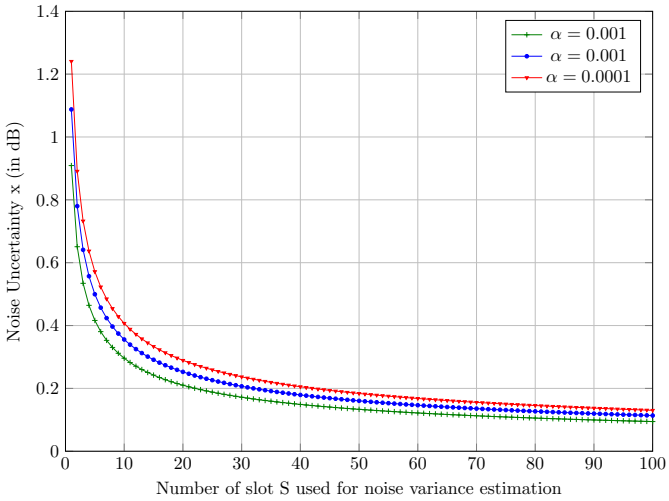

Fig. 4.27 Variation of noise uncertainty level with number of slots S used for noise variance estimation.

evaluated. For example, for $\alpha = 0.01$, β is found to be 1.4 as shown in Figure 4.26. It is clear from (4.183) that the level of noise uncertainty decreases with the increase of the number of samples and the number of slots averaging the estimation of the noise variance.

Simulation Result

The variation of the noise uncertainty bound β with number of slots S used in noise variance estimation for different significance level, is presented in Figure 4.27. The plot seems to have a steep slope ($\sim$ - 0.08dB/slot) for small values of S, but for larger number of estimation slots S ($S > 30$) the slope starts to flatten suggesting large changes in S are required for small gain in noise uncertainty bound. Figure 4.28 illustrates the variation of SNR wall as a function of the number of slots used for noise variance estimation. Curves are plotted for different significance parameter α. As expected, the level of SNR Wall decreases with the increase in the number of slots used in noise estimation but curve saturates for low values of SNR Wall ($< -12dB$). As a matter of fact, for given parameters ($M = 100, K = 5$ and $\alpha = 0.01$), the number of slots required to overcome the SNR Wall condition for SNR $\leq$ to $-12dB$ is $S > 80$.

Similarly, Figure 4.29 plots the SNR wall condition and the sample complexity as a function of the number of auxiliary slots S. It shows that the minimum attainable SNR wall value of -12 dB obtained for $S = 100$ and $\alpha = 10^{-5}$. Moreover, for

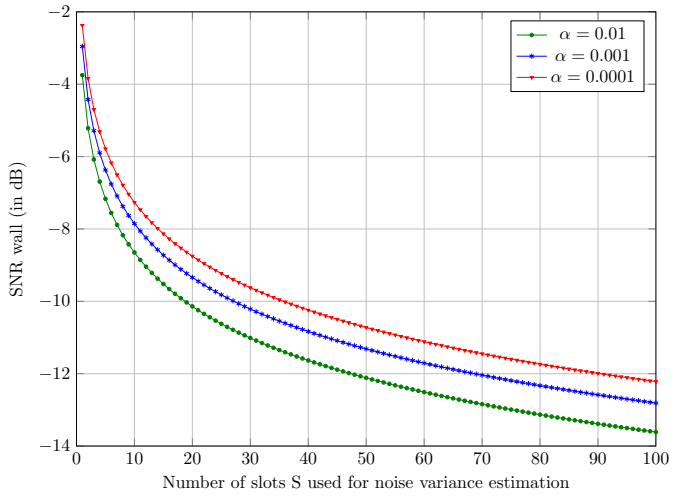

Fig. 4.28 Variation of SNR wall level with number of auxiliary slots S used for noise variance estimation

asymptotic number of slots S (then asymptotic of total number of samples KMS), the noise uncertainty x (in dB) decreases to zero with $\hat{\sigma}_v^2 = \sigma_v^2$ resulting no SNR wall, proving the finding of [119].

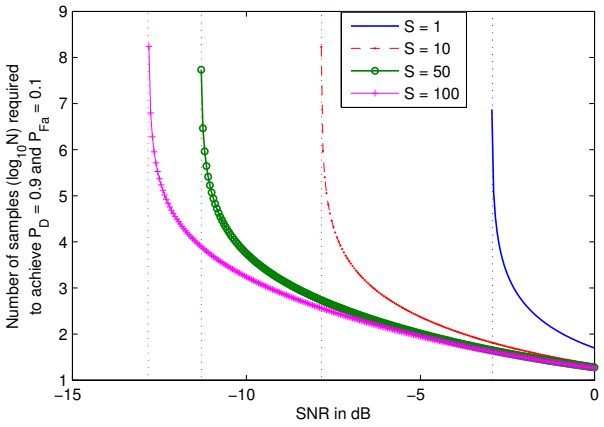

Fig. 4.29 Variation of sample complexity N as the SNR approaches SNR wall for varying number of auxiliary slots used for noise variance estimation in HED1

4.3 Semi-blind sensing techniques under unknown Primary User Traffic

Among many practical imperfections and constraints for spectrum sensing in CR scenarios mentioned in the literature, the unknown PU traffic is one of the most important constraints which significantly limits the sensing performance of the secondary user. In the existing literature on spectrum sensing, the SUs are assumed to have a perfect knowledge of the exact time slot structure of PU transmissions providing a solid basis for guaranteeing that PU traffic transitions occur only at the beginning of the SU sensing slots. However, in practice, the SU may not have the knowledge of exact time slot structure of PU transmissions. Moreover, it is also possible that the communications among PUs are not based on synchronous schemes at all [73, 186]. It means, under practical scenarios that the primary traffic transition may occur during the sensing period, especially when a long sensing period is used to achieve a good sensing performance, or when spectrum sensing is performed for a network with high traffic load. Thus, it is necessary to analyze the sensing performance of existing spectrum sensing techniques under unknown PU traffic.

Among a limited number of literature including[138, 113, 170, 140, 174, 160] that deal with unknown primary traffic scenario, [138] was the first one to study the performance of well known semi-blind spectrum sensing algorithms including ED and Roy's Largest Root Test (RLRT) under bursty primary traffic, in which

the burst interval is comparable to or smaller than the spectrum sensing interval. The traffic model used is limited to constant length bursts of the PU data, whose length is smaller than the SU sensing duration. However, the burst length of the PU may be varying with time following some stochastic models [137, 84]. A more general scenario, in which the PUs traffic transition is completely random, may affect the spectrum sensing performance. The analysis of the spectrum sensing performance has been presented in [170, 140, 174, 160] by modeling the PU traffic as an independent and identically distributed two state Markov's model. Using this primary traffic model, authors in [170, 174, 160] analyzed the effect of PU traffic on the sensing performance and the sensing-throughput trade-off considering ED as a sensing technique under the half duplex scenario. Moreover, the effect of multiple PUs traffic on the sensing-throughput trade-off of the secondary system has been studied in [140]. Although all the aforementioned contributions recognized the fact that the PU traffic might affect the sensing performance including sensing-throughput trade-off, none of them considered the realistic scenario of multi-antenna spectrum sensing in a complex signal sample domain and the sensing performance of other spectrum sensing techniques including Eigenvalue Based Detection (EBD) techniques under unknown primary user traffic.

In this section we study the effect of PU traffic on the performance of multi-antenna spectrum sensing especially ED and RLRT under the complex domain of PU signal, noise and channel. In contrast to commonly used continuous time Markov model in the existing literature, a novel technique of modeling PU traffic is proposed which is only based on discrete time distribution of PU free and busy periods. The proposed model is more realistic and simple compared to the continuous time Markov model proposed in the previous literature [170, 140, 174, 160]. Moreover, an analytical performance evaluation of the decision statistic in terms of ROC under the considered scenario is carried out.

Mathematical Framework

We consider a single source scenario (single primary transmitter) whereas multiple antennas are employed by an SU. Suppose the SU has K antennas and each antenna receives N samples in each sensing slot. In a given sensing frame, the detector calculates its decision statistic T_D by collecting N samples from each one of the K antennas. Subsequently, the received samples are collected by the detector in the

form of a $K \times N$ matrix $\mathbf{Y}$. When the primary transmissions are not based on some synchronous schemes or the sensing unit at the SU does not have any information about the primary traffic pattern, the received vector at the sensing unit may consist in part by the samples from one PU state and the remaining part by alternate PU state. To simplify the scenario, we begin with the following classification of the sensing slots based on the PU traffic status, which is also illustrated in Fig. 4.30.

1. Steady State (SS) sensing slot: In such type of sensing slot, all the received samples in one sensing slot are obtained from the same PU state.
2. Transient State (TS) sensing slot: In such type of sensing slot, a part of the received samples within the sensing slot are obtained from one PU state and the remaining from the another PU state.

In general, the probabilities of observing SS and TS sensing slots are dependent on the PUs traffic model. In contrast to the commonly used hypothesis definition in spectrum sensing literature, we define two hypotheses in the following way:

$\mathscr{H}_0$: the channel is going to be free,
$\mathscr{H}_1$: the channel is going to be busy.

This hypothesis formulation implies that the decision is based on the PU status at the end of the sensing interval. Thus, in a TS sensing slot, a transition from the PU busy state to the PU free state is considered $\mathscr{H}_0$, while a transition from the PU free state to the PU busy state is considered $\mathscr{H}_1$. In the considered scenario, in an SS sensing interval, the generic received signal matrix under each hypothesis can be written as,

$$Y_{SS} = \begin{cases} V_{[K,N]} & (\mathscr{H}_0), \\ S_{[K,N]} & (\mathscr{H}_1), \end{cases} , \tag{4.184}$$

where $V_{[K,N]} \triangleq [v(1) \cdots v(n) \cdots v(N)]$ is the $K \times N$ noise matrix ,$S_{[K,N]} = \mathbf{h}_{[K,1]}\mathbf{s}_{[1,N]} + \mathbf{V}_{[K,N]}$ is the $K \times N$ received noisy signal matrix when PU signal is present, $h_{[K,1]} = [h_1 \cdots h_K]^T$ is the channel vector and $s_{[1,N]} \triangleq [s(1) \cdots s(n) \cdots s(N)]$ is a $1 \times N$ PU signal vector. In the TS sensing interval, the generic received signal matrix under each hypothesis can be written as,

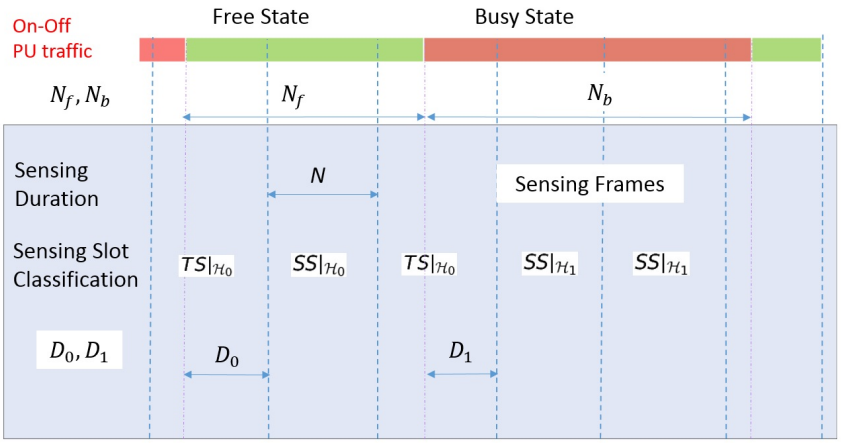

Fig. 4.30 Primary user traffic scenario and sensing slot classification

$$Y_{TS} = \begin{cases} [\mathbf{S}_{[K,N-D_0]} | \mathbf{V}_{[K,D_0]}] & (\mathscr{H}_0), \\ [\mathbf{V}_{[K,N-D_1]} | \mathbf{S}_{[K,D_1]}] & (\mathscr{H}_1), \end{cases} . \tag{4.185}$$

where D_0 represents the number of pure noise samples in TS sensing slot under $\mathscr{H}_0$, D_1 represents the number of noise plus PU signal samples in TS sensing slot under $\mathscr{H}_1$, $\mathbf{S}_{[K,N-D_0]} = \mathbf{h}_{[K,1]}\mathbf{s}_{[1,N-D_0]} + \mathbf{V}_{[K,N-D_0]}$ is the $(K \times N - D_0)$ received noisy signal matrix when PU signal is present only for $(N - D_0)$ sample periods. Similarly, $\mathbf{S}_{[K,D_1]} = \mathbf{h}_{[K,1]}\mathbf{s}_{[1,D_1]} + \mathbf{V}_{[K,D_1]}$ is the $K \times D_1$ received noisy signal matrix when PU signal is present only for D_1 sample periods. In each of them, the unknown primary transmitted signal $s(n)$ at time instant n is modelled as independent and identically distributed (IID) complex Gaussian with zero mean and variance σ_s^2 : $s(n) \sim \mathscr{N}_{\mathbb{C}}(0, \sigma_s^2)$. The noise sample $v_k(n)$ at the k^{th} antenna of the SU at the time instant n is also modelled as complex Gaussian with mean zero and variance $\sigma_v^2 : v_k(n) \sim \mathscr{N}_{\mathbb{C}}(0, \sigma_v^2)$. The channel coefficient h_k of the k^{th} antenna is assumed to be constant and memory-less during the sensing interval. The average SNR at the receiver is defined as, $\rho = \frac{\sigma_s^2 \|h\|^2}{K\sigma_v^2}$, where $||.||$ denotes the Euclidean norm.

4.3.1 Characterization of Primary user traffic

In this sub-section, we characterize the mathematical model of PU traffic. Based on the proposed stochastic PU traffic model, we build the PU's probability transition

matrix, which leads to analytical formulation of the SU's probability of receiving SS sensing frame and TS sensing frame under null and alternate hypothesis.

In this work, we model the PU traffic as a two state Markov process (On-Off process: PU 'On' representing busy state and PU 'Off' representing free state). The length of free as well as busy period are independent geometrically distributed random variables with parameters α and β, respectively. Essentially, the parameters α and β represent the state transition probabilities in single sample duration. The mean length of free period M_f and busy period M_b of PU traffic can be related to parameters α and β as, $M_f = \frac{1}{\alpha}$ and $M_b = \frac{1}{\beta}$, respectively.

At any time instant, the PU is in free state with probability $P_f = \frac{M_f}{M_b+M_f}$ and, similarly, in the busy state with probability, $P_b = \frac{M_b}{M_b+M_f}$. We further assume that the parameters (α and β) of geometrically distributed length of PU free and busy periods are constant over time. Thus, the corresponding two-state Markovs process can be considered homogeneous in nature. Using this homogeneity property and the Chapman-Kolmogorov equation, the PU n-step transition probability matrix is given by:

$$\begin{aligned} P^n &= \begin{bmatrix} p_{00}^n & p_{01}^n \\ p_{10}^n & p_{11}^n \end{bmatrix} \\ &= \frac{1}{\alpha+\beta} \begin{bmatrix} \beta+\alpha(1-\alpha-\beta)^n & \alpha-\alpha(1-\alpha-\beta)^n \\ \beta-\beta(1-\alpha-\beta)^n & \alpha+\beta(1-\alpha-\beta)^n \end{bmatrix}, \end{aligned} \tag{4.186}$$

which reduces to (4.187) for single step transition matrix:

$$P = \begin{bmatrix} p_{00} & p_{01} \\ p_{10} & p_{11} \end{bmatrix} = \begin{bmatrix} 1-\alpha & \alpha \\ \beta & 1-\beta \end{bmatrix}. \tag{4.187}$$

As already mentioned earlier in Sub-Section 4.3, the stochastic nature of the PU state transition gives a mixed nature of received signals in a TS sensing slot resulting in random variables (RVs) D_0 and D_1. Thus, in each PU state transition from *Busy* to *Free State*, the sensing unit has to decide based on D_0 pure noise samples and $(N-D_0)$ noise plus primary signal samples which actually affects the overall sensing performance. Thus, with the support of above analysis and also keeping (4.184) and

(4.185) in reference, it is clear that to find the distribution of the decision statistic under different hypotheses, the prior deduction of the probability of occurrence of SS sensing slot, TS sensing slot, probability mass function (*pmf*) of D_0 and the *pmf* of D_1 are inevitable.

The following Lemmas compute the *pmf*s of D_0 and D_1 based on the two state PU traffic model described above.

Lemma 1. Given the N number of samples in a sensing slot, the probability transition matrix P as in (4.187) with comparable mean parameters M_f and M_b,

1. The probability of having D_0 noise only (PU signal free) samples in a TS sensing slot under $\mathscr{H}_0$ reduces to,

$$P_{D_0}(d_0)|_{\mathscr{H}_0} = \frac{1}{N-1}. \tag{4.188}$$

2. The probability of having D_1 noise-plus-PU-signal samples in a TS sensing slot under $\mathscr{H}_1$ reduces to,

$$P_{D_1}(d_1)|_{\mathscr{H}_1} = \frac{1}{N-1}. \tag{4.189}$$

Proof. As mentioned earlier during binary hypothesis formulation, the PU state transition from *Busy State* to *Free State* corresponds to $\mathscr{H}_0$ sensing slot and viceversa for $\mathscr{H}_1$. We consider thus, without loss of generality, while dealing with a $\mathscr{H}_0$ sensing slot, that the TS sensing slot occurs at the beginning of the PU *Free State*. Thus, given that the PU is initially in *Busy State*, the probability of having a PU state transition after $N-D_0$ samples, leading to D_0 pure noise samples in a TS sensing slot under $\mathscr{H}_0$ is given by,

$$P(TS, D_0, \mathscr{H}_0) = p_b \cdot p_{11}^{N-D_0-1} p_{10} p_{00}^{D_0}. \tag{4.190}$$

The probability in (4.190) is the PU state transition probability after $N-D_0$ sample instances from a busy PU state to a free PU one. This probability can be normalized

by the sum of the transition probabilities for all range of D_0 and we obtain

$$P_{D_0}(d_0)|_{\mathscr{H}_0} = \frac{p_b \cdot p_{11}^{N-d_0-1} p_{10} p_{00}^{d_0}}{\sum_{a=1}^{N-1} p_b \cdot p_{11}^{N-a-1} p_{10} p_{00}^{a}} \tag{4.191}$$

$$= \frac{(1-\beta)^{N-d_0-1}(1-\alpha)^{d_0}}{\sum_{a=1}^{N-1}(1-\beta)^{N-a-1}(1-\alpha)^{a}}. \tag{4.192}$$

When the mean parameters M_f and M_b are close (4.192) can be approximated to:

$$P_{D_0}(d_0)|_{\mathscr{H}_0} = \frac{(1-\alpha)^{N-d_0-1}(1-\alpha)^{d_0}}{\sum_{a=1}^{N-1}(1-\alpha)^{N-a-1}(1-\alpha)^{a}} \tag{4.193}$$

$$= \frac{1}{N-1}. \tag{4.194}$$

This proves the first claim. By using the same line of reasoning, the proof of the second claim is straightforward. □

The following Lemmas compute the probability of occurrence of SS sensing slot $p_{SS}|_{\mathscr{H}_0}$ under $\mathscr{H}_0$ and the probability of occurrence of TS sensing slot, which is the complementary, i.e., $p_{TS}|_{\mathscr{H}_0} = 1 - p_{SS}|_{\mathscr{H}_0}$.

Lemma 2. Given the number of samples in a sensing slot$N$ and the probability transition matrix P as in (4.187),

1. The probability of receiving SS sensing slot under $\mathscr{H}_0$ is given by:

$$P_{SS}|_{\mathscr{H}_0} = \frac{1}{1+\alpha\sum_{d_0=1}^{N}(1-\beta)^{N-d_0-1}(1-\alpha)^{d_0-N}}. \tag{4.195}$$

2. The probability of receiving SS sensing slot under $\mathscr{H}_1$ is given by:

$$P_{SS}|_{\mathscr{H}_1} = \frac{1}{1+\beta\sum_{d_1=1}^{N}(1-\alpha)^{N-d_1-1}(1-\beta)^{d_1-N}}. \tag{4.196}$$

Proof. First of all, the probability of having no PU state transition under $\mathscr{H}_0$is given by:

$$P(SS, \mathscr{H}_0) = p_f \cdot p_{00}^{N}. \tag{4.197}$$

Similarly, the probability of having a PU state transition from *Busy State* to *Free State* is given by,

$$P(TS,\mathscr{H}_0) = P\left(\begin{array}{c}\text{PU is in}\\ \textit{Busy State}\end{array}\right)\cdot P\left(\begin{array}{c}\text{PU transits from } \textit{Busy} \text{ to } \textit{Free}\\ \textit{State} \text{ during sensing interval}\end{array}\right). \quad (4.198)$$

Essentially, the PU state transition may occur at any time during the sensing duration,

$$P(TS,\mathscr{H}_0) = p_b \cdot \sum_{d_0}^{N-1} p_{11}^{N-d_0-1} p_{10} p_{00}^{d_0}. \quad (4.199)$$

Thus, by using (4.187) and (4.199), the probability of having a SS sensing slot belonging to $\mathscr{H}_0$ is given by,

$$P_{SS}|_{\mathscr{H}_0} = \frac{P(SS,\mathscr{H}_0)}{P(SS,\mathscr{H}_0)+P(TS,\mathscr{H}_0)} \quad (4.200)$$

$$= \frac{p_f \cdot p_{00}^N}{p_f \cdot p_{00}^N + p_b \cdot \sum_{d_0}^{N-1} p_{11}^{N-d_0-1} p_{10} p_{00}^{d_0}}. \quad (4.201)$$

By replacing p_f, p_b and the elements of the probability transition matrix by their respective expressions in terms of α and β, further simplification yields (4.195) and proves claim 1 of Lemma 2.

Through the same line of reasoning, the proof of claim 2 of Lemma 1 is straightforward.

□

Corollary 5. When the mean parameters M_f and M_b are comparable, the probabilities in (4.195) and (4.196) reduce to simple expressions given by,

$$P_{SS}|_{\mathscr{H}_0} = \frac{1}{1+(N-1)\alpha} \quad (4.202)$$

$$P_{SS}|_{\mathscr{H}_1} = \frac{1}{1+(N-1)\beta}. \quad (4.203)$$

In Figure 4.31, the pdf of the decision statistic under ideal PU-SU sensing slot synchronization is compared with the pdf of the decision statistic under unknown PU traffic considering both hypotheses. In addition, the accuracy of the derived

analytical pdf expressions is confirmed by the results presented in Figure 4.31b, where the theoretical formulas are compared against the numerical results obtained by Monte-Carlo simulation. The perfect match of the theoretical and the numerical pdfs validates the derived analytical expressions.

4.3.2 ED under Unknown PU Traffic

ED computes the average energy of the received signal matrix Y normalized by the noise variance σ_v^2 and compares it against a predefined threshold T_{ED}:

$$T_{ED} = \frac{1}{\sigma_v^2} \sum_{k=1}^{K} \sum_{n=1}^{N} |y_k(n)|^2. \tag{4.204}$$

To analyze ED performance, it is necessary to express the pdf of the decision statistic in case of unknown primary traffic. The following theorem computes the pdf of the ED decision statistic under both H_0 and H_1, by using the PU traffic characterization presented Sub-Section 4.3.1.

Theorem 6. Given a multi-antenna sensing unit with K receiving antennas, N received samples in each slot and a random PU traffic with geometrically distributed free state duration, the pdf of the ED decision statistic under $\mathscr{H}_0$ and $\mathscr{H}_1$ is given by (4.205) and (4.206), respectively, where $f_{\mathscr{G}}(x,\alpha,\beta)$ is the pdf of a Gamma distribution with shape parameter α and rate parameter β and $f_{\mathscr{N}}(x,\mu,\sigma^2)$ is the pdf of Gaussian distribution with mean μ and variance σ^2.

$$\begin{aligned} f_{T_{ED}|_{H_0}}(x) = {} & p_{SS}|_{H_0} f_{\mathscr{G}}(x,KN,1) + p_{TS}|_{H_0} \sum_{d_0=1}^{N-1} P_{D_0}(d_0) \left[f_{\mathscr{G}}(x,2Kd_0,1) + f_{\mathscr{G}}(x,N-d_0,K\rho) \right. \\ & \left. + \; f_{\mathscr{G}}(x,K(N-d_0),1) + f_{\mathscr{N}}(x,0,2\rho K(N-d_0)) \right], \end{aligned} \tag{4.205}$$

$$\begin{aligned} f_{T_{ED}|_{H_1}}(x) = {} & p_{SS}|_{\mathscr{H}_1} \left(f_{\mathscr{G}}(x,N,K\rho) + f_{\mathscr{G}}(x,KN,1) + f_{\mathscr{N}}(x,0,2\rho KN) \right) \\ & + p_{TS}|_{\mathscr{H}_1} \sum_{d_1=1}^{N-1} P_{D_1}(d_1) \left[f_{\mathscr{G}}(x,d_1,K\rho) + f_{\mathscr{G}}(x,Kd_1,1) \right. \\ & \left. + \; f_{\mathscr{N}}(x,0,2\rho Kd_1) + f_{\mathscr{G}}(x,K(N-d_1),1) \right]. \end{aligned} \tag{4.206}$$

Proof. As noted from Sub-Section 4.3, the term within the summation in (4.204) is different for the SS sensing slot and TS sensing slot. Under the null hypothesis

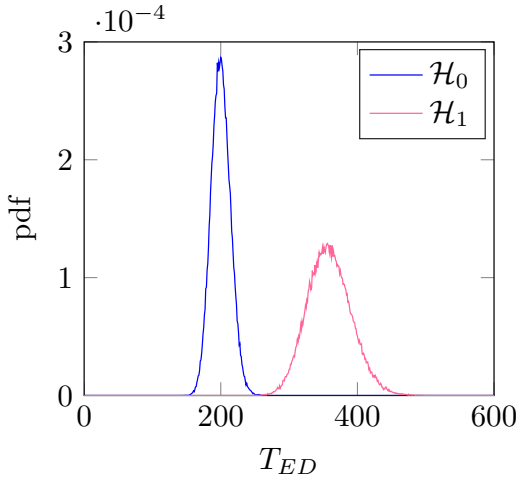

(a) Known PU Traffic (synchronized PU-SU sensing slots)

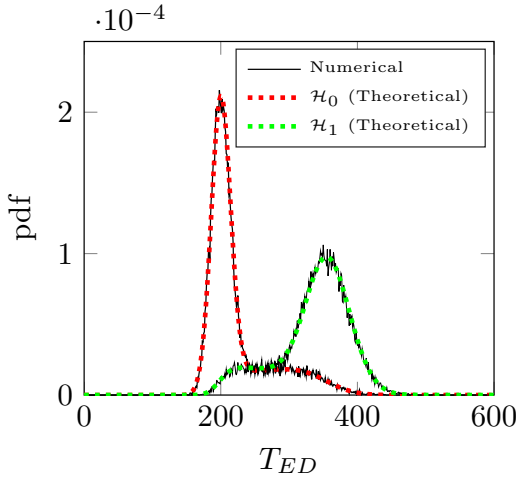

(b) Unknown PU Traffic

Fig. 4.31 Pdfs of the ED decision statistic: Parameters: $N = 50$, $K = 4$, $M_f = 150$, $M_b = 150$ and SNR $= -6$ dB

$\mathscr{H}_0$, the ED decision statistic in (4.204) can be decomposed as a probabilistic sum of $T_{ED}^{SS}|_{\mathscr{H}_0}$ and $T_{ED}^{TS}|_{\mathscr{H}_0}$.

$$T_{ED}|_{\mathscr{H}_0} = \frac{p_{SS}|_{\mathscr{H}_0}}{2}\sum_{k=1}^{K}\sum_{n=1}^{N}\left|\frac{v_k(n)}{\sigma_v/\sqrt{2}}\right|^2 + \frac{p_{TS}|_{\mathscr{H}_0}}{2}\left[\sum_{k=1}^{K}\sum_{n=1}^{D_0}\left|\frac{v_k(n)}{\sigma_v/\sqrt{2}}\right|^2 + \sum_{k=1}^{K}\sum_{n=N-D_0+1}^{N}\left|\frac{h_k s(n)+v_k(n)}{\sigma_v/\sqrt{2}}\right|^2\right]. \tag{4.207}$$

Next, the distribution of each sum in (4.207) can be derived as [46],

$$T_{ED}|_{\mathscr{H}_0} = \frac{p_{SS}|_{\mathscr{H}_0}}{2}\chi^2_{2KN} + \frac{p_{TS}|_{\mathscr{H}_0}}{2}\sum_{d_0=1}^{N-1}P_{D_0}(d_0)\left[\chi^2_{2Kd_0} + K\rho\chi^2_{2(N-d_0)} + \chi^2_{2K(N-d_0)} + \mathscr{N}(0,2\rho(N-d_0)K)\right], \tag{4.208}$$

where χ^2_A represents a Chi-squared random variable with A degrees of freedom. and $\mathscr{N}(\mu,\sigma^2)$ represents the Normal random variable with mean μ and variance σ^2.

In fact, the product of a Chi-squared RV with a constant is a Gamma RV, thus, with this replacement we obtain,

$$T_{ED}|_{\mathscr{H}_0} = p_{SS}|_{\mathscr{H}_0}\mathscr{G}(KN,1) + p_{TS}|_{\mathscr{H}_0}\sum_{d_0=1}^{N-1}P_{D_0}(d_0)\left[\mathscr{G}(Kd_0,1) + \mathscr{G}(N-d_0,K\rho) + \mathscr{G}(K(N-d_0),1) + \mathscr{N}(0,2\rho(N-d_0)K)\right]. \tag{4.209}$$

In addition, $\mathscr{G}(\alpha,\beta)$ represents a Gamma random variable with a shape parameter α and a rate parameter β. Since the goal is to find the pdf of the sum in (4.204) under $\mathscr{H}_0$, we replace the random variables in (4.209) with their respective pdfs to obtain (4.205).

Similarly, under the alternate hypothesis $\mathscr{H}_1$, the ED decision statistic in (4.204) can be decomposed as a probabilistic sum of $T_{ED}^{SS}|_{\mathscr{H}_1}$ and $T_{ED}^{TS}|_{\mathscr{H}_1}$.

$$T_{ED}|_{\mathscr{H}_1} = \frac{p_{SS}|_{\mathscr{H}_1}}{2} \sum_{k=1}^{K} \sum_{n=1}^{N} \left| \frac{h_k s(n) + v_k(n)}{\sigma_v/\sqrt{2}} \right|^2 + \frac{p_{TS}|_{\mathscr{H}_1}}{2} \cdot \left[\sum_{k=1}^{K} \sum_{n=1}^{D_1} \left| \frac{h_k s(n) + v_k(n)}{\sigma_v/\sqrt{2}} \right|^2 + \sum_{k=1}^{K} \sum_{n=N-D_1+1}^{N} \left| \frac{v_k(n)}{\sigma_v/\sqrt{2}} \right|^2 \right]. \tag{4.210}$$

Using the fact that D_1 is a random variable,

$$T_{ED}|_{\mathscr{H}_1} = \frac{p_{SS}|_{\mathscr{H}_1}}{2} \sum_{k=1}^{K} \sum_{n=1}^{N} \left| \frac{h_k s(n) + v_k(n)}{\sigma_v/\sqrt{2}} \right|^2 + \frac{p_{TS}|_{\mathscr{H}_1}}{2} \sum_{d_1=1}^{N-1} P_{D_1}(d_1) \cdot \left[\sum_{k=1}^{K} \sum_{n=1}^{d_1} \left| \frac{h_k s(n) + v_k(n)}{\sigma_v/\sqrt{2}} \right|^2 + \sum_{k=1}^{K} \sum_{n=N-d_1+1}^{N} \left| \frac{v_k(n)}{\sigma_v/\sqrt{2}} \right|^2 \right]. \tag{4.211}$$

Deriving the distribution of each sum in (4.211) using [46], we obtain:

$$\begin{aligned} T_{ED}|_{\mathscr{H}_1} = p_{SS}|_{\mathscr{H}_1} & \left(\mathscr{G}(N, K\rho) + \mathscr{G}(KN, 1) + \mathscr{N}(0, 2\rho KN)\right) \\ & + p_{TS}|_{\mathscr{H}_1} \sum_{d_1=1}^{N-1} P_{D_1}(d_1) \left[\mathscr{G}(d_1, K\rho) + \mathscr{G}(Kd_1, 1)\right. \\ & \left. + \mathscr{N}(0, 2\rho Kd_1) + \mathscr{G}(K(N-d_1), 1)\right]. \end{aligned} \tag{4.212}$$

Finally, we replace the random variables in (4.212) with their respective pdfs to obtain (4.206). □

In essence, the pdfs in (4.205) and (4.206) consist of the sum of independent random variables. From a statistical point of view, the pdf of the sum of two independent pdfs can be realized as the convolution of these pdfs [92]. Thus, the sum of pdfs can be computed using convolution as an alternative, we can exploit the characteristic function approach by computing Fourier transform. In conclusion, (4.205) and (4.206) can be easily evaluated by using standard Fast Fourier Transform (FFT) techniques.

A. Probability of False Alarm: Given the pdf of the decision statistic in (4.205), we can compute the false alarm probability. Under $\mathscr{H}_0$, the PU is in free state at

the end of the sensing interval, but the decision statistic is erroneously above the threshold τ and the PU signal is declared present. For false alarm P_{Fa}, the following Corollary of Theorem 6 holds.

Corollary 6. The false-alarm probability of the ED test under unknown PU traffic and complex signal space scenario is:

$$P_{Fa} = P(T_{ED}|_{\mathscr{H}_0} \geq \tau) \equiv \int_{\tau}^{+\infty} f_{T_{ED}|_{H_0}}(x)dx. \tag{4.213}$$

B. Probability of Detection: Given the pdf of the decision statistic in (4.206), we can compute the detection probability. Under $\mathscr{H}_1$, i.e., the PU is in busy state at the end of the sensing interval. Under this scenario, if the decision statistic is above the threshold, the PU signal is declared present. The following Corollary of Theorem 6 holds for defines the probability of detection P_D.

Corollary 7. The detection probability of the ED test under unknown PU traffic and the complex signal space scenario is given by:

$$P_D = P(T_{ED}|_{\mathscr{H}_1} \geq \tau) \equiv \int_{\tau}^{+\infty} f_{T_{ED}|_{H_1}}(x)dx. \tag{4.214}$$

Simulation Results

In this Sub-Section, the effect of PU traffic on the multi-antenna ED is analyzed based on the the traffic model developed in Sub-Section 4.3.1. The analytical expressions derived are validated via numerical simulation. The length of the free and busy periods of the PU traffic are measured in terms of the discrete number of samples where each of them has Geometric distribution with probability of success parameters p_f and p_b, respectively. Here, we use mean and busy period denoting $M_f = \frac{1}{p_f}$ and $M_b = \frac{1}{p_b}$, respectively. Under multiple antenna sensing scenario, the average SNR at the receiver is defined as, $\rho = \frac{\sigma_s^2 \|h\|^2}{K\sigma_v^2}$, where $||.||$ denotes the Euclidean norm.

Figure 4.32 illustrates the ED ROC performance for different values of the mean free and busy period of the PU traffic. It shows that as the mean free and busy periods of the primary traffic increases, the detection performance of SU also

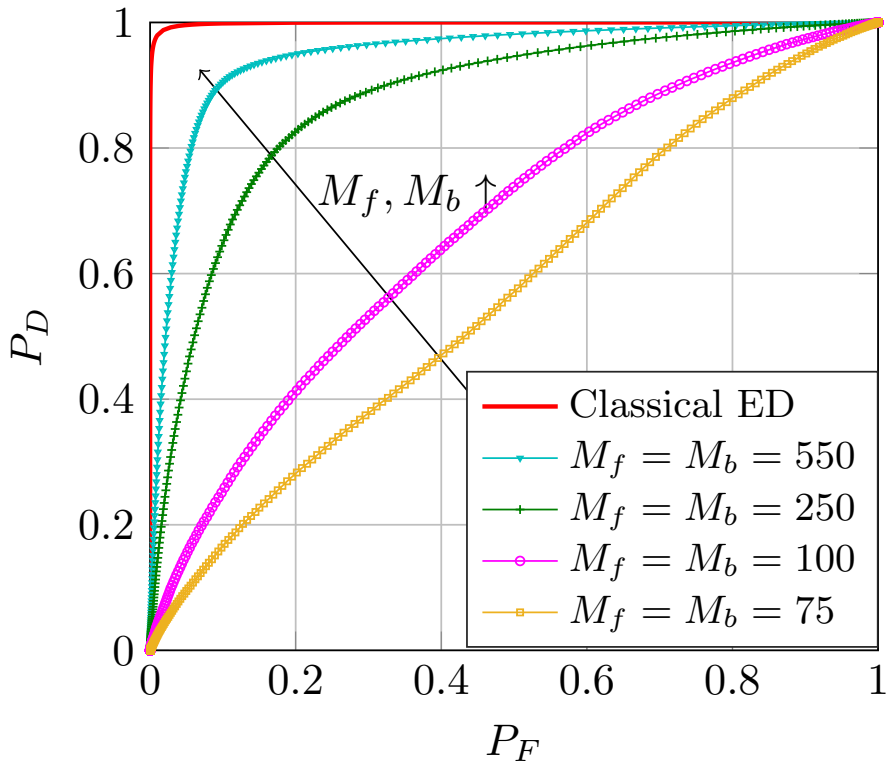

Fig. 4.32 ROC performance for the considered scenario. Parameters: $N = 100$, $K = 4$ and SNR $= -6$ dB

increases. Clearly, the conventional model with perfect synchronization of the PU-SU sensing slots performs better than the one with unknown PU traffic.

The behaviour variation of the sensing performance for different number of receiving antennas is plotted in Figure 4.33. It can be observed that unlike the rapid increase in sensing performance with increasing number of receiving antennas under synchronized PU-SU sensing slot scenario (rapid decrease in missed-detection probability with increasing number of receiving antennas), the sensing performance is almost constant even if we increase the number of antennas under unknown PU traffic. During a TS sensing slot, from each receiving antenna, the received signal samples are a mixture of pure noise samples and the samples with both noise and PU signal. Thus, even if we use multiple antennas, the nature of the received signal doesn't change much which is the reason why the sensing performance improvement is suppressed by the unknown PU traffic (more specifically, the TS sensing performance) when the length of the free and busy periods of PU traffic are quite small (a few multiples of the sensing window length).

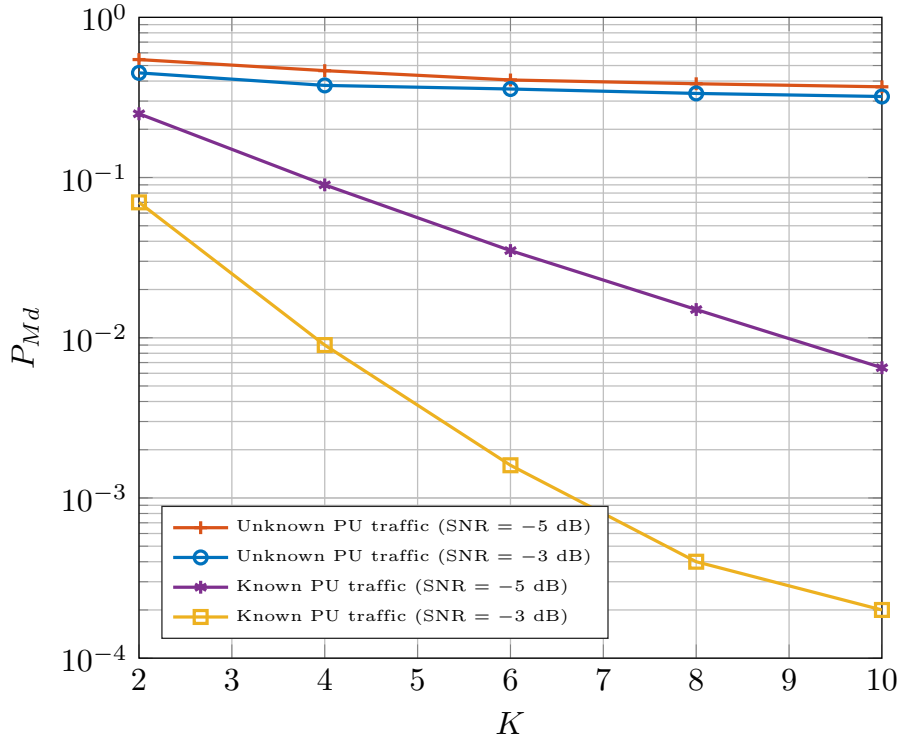

Fig. 4.33 Probability of missed detection vs. the number of Antennas, Parameters: $N = 25$, $M_f = 62$, $M_b = 62$ and $P_F = 0.1$

4.3.3 EBD under Unknown PU Traffic

In this Sub-Section, we consider the performance under unknown PU traffic of an another important class of detection techniques designed for multi-sensor detectors, based on the eigenvalues of the received signal covariance matrix. Receive diversity can be achieved either by multiple users (cooperative detection) or by multiple antennas. Given a $K \times N$ received signal matrix $\mathbf{Y}$, the sample covariance matrix is defined as $\mathbf{R} \triangleq \frac{1}{N}\mathbf{Y}\mathbf{Y}^{\mathrm{H}}$ and $\lambda_1 \geq \cdots \geq \lambda_k$ are its eigenvalues sorted in the decreasing order.

Eigenvalue based detection techniques infer the presence of signal from eigenvalues λ_i. In particular, as already mentioned the detection technique which considers the largest one (λ_1) and compare it against the noise variance is known as RLRT [149] and its test statistics is,

$$T_{RLRT} \triangleq \frac{\lambda_1}{\sigma_v^2}. \tag{4.215}$$

RLRT is a "semi-blind" algorithm, as it requires the exact knowledge of noise variance and is considered to be asymptotically optimum test in this setting[46].

Here, we analyze in detail the RLRT method. However, the results can be extended to the other eigenvalue methods as well. To analyze the RLRT performance, it is necessary to express the test statistics pdf for the case of unknown PU traffic. The following theorem computes the RLRT decision statistic pdf under both the hypotheses H_0 and H_1 using the PU traffic characterization presented in Sub-Section 4.3.1.

Theorem 7. Given a multi-antenna sensing unit with K receive antennas, N received samples in each slot and a random PU traffic with geometrically distributed free and busy state duration, let $c = K/N$, N_s a independent parameter and define:

$$\mu_1(N_s) = \left(\frac{N_s}{N}K\rho + 1\right)\left(1 + \frac{K-1}{N_s K\rho}\right), \quad \sigma_1^2(N_s) = \frac{N_s}{N^2}(K\rho+1)\left(1 - \frac{K-1}{N_s K^2\rho^2}\right) \tag{4.216}$$

$$\mu_{N,K} = \left[1+\sqrt{c}\right]^2, \quad \sigma_{N,K} = N^{-2/3}\left[1+\sqrt{c}\right]\left[1 + \frac{1}{\sqrt{c}}\right]^{1/3}. \tag{4.217}$$

Then, the pdfs of RLRT decision statistic under $\mathscr{H}_0$ and $\mathscr{H}_1$ are given by (4.218) and (4.219) respectively:

$$f_{T_{RLRT}|_{H_0}}(x) = P_{SS}|_{H_0} f_{TW2}\left(\frac{x-\mu_{N,K}}{\sigma_{N,K}}\right) + P_{TS}|_{H_0}\sum_{d_0=1}^{N-1} P_{D_0}(d_0) f_D(x, N-d_0), \tag{4.218}$$

$$f_{T_{RLRT}|_{H_1}}(x) = P_{SS}|_{\mathscr{H}_1} f_D(x,N) + P_{TS}|_{\mathscr{H}_1}\sum_{d_1=1}^{N-1} P_{D_1}(d_1) f_D(x,d_1). \tag{4.219}$$

where,

$$f_D(x,d) = \begin{cases} f_{\mathscr{N}}(\mu_1(d), \sigma_1^2(d)) & \text{if, } d > \frac{K-1}{K^2\rho^2}, \\ f_{TW2}(\mu_{N,K}, \sigma_{N,K}) & \text{otherwise.} \end{cases}. \tag{4.220}$$

In (4.220), $f_{\mathscr{N}}(\mu_1(d), \sigma_1^2(d))$ denotea a Gaussian pdf with mean $\mu_1(N_s)$ and variance $\sigma_1^2(N_s)$ provided in (4.216) at $N_s = d$. Next, $f_{TW2}(\mu_{N,K}, \sigma_{N,K})$ is the pdf of Tracy-Widom distribution of order 2 with parameters $\mu_{N,K}$ and $\sigma_{N,K}$ provided in (4.217).

Proof. As noted from Sub-Section 4.3, the nature of the received signal matrix is different for the SS sensing slot and TS sensing slot. Under null hypothesis $\mathscr{H}_0$,

received sample covariance matrix $\mathbf{R}|_{\mathscr{H}_0}$ can be decomposed as a probabilistic sum of $\mathbf{R}_{SS}|_{\mathscr{H}_0}$ and $\mathbf{R}_{TS}|_{\mathscr{H}_0}$ in the following way,

$$\mathbf{R}|_{\mathscr{H}_0} = P_{SS}|_{\mathscr{H}_0}\mathbf{R}_{SS}|_{\mathscr{H}_0} + P_{TS}|_{\mathscr{H}_0}\mathbf{R}_{TS}|_{\mathscr{H}_0}. \tag{4.221}$$

Since sensing slots are independent from each other, we treat each covariance matrix in (4.221) independently. Given an SS sensing slot under null hypothesis, all the received samples $y_k(n)$ are homogeneous in nature comprising the i.i.d. Gaussian noise samples with mean zero and variance σ_v^2. Thus, the sample covariance matrix $\mathbf{R}_{SS}|_{\mathscr{H}_0}$ follows a Wishart distribution whose largest eigenvalue normalized by noise variance can be expressed by a Tracy-Widom distribution of second order [46, 20].

$$\frac{\lambda_1^{SS}|_{\mathscr{H}_0}}{\sigma_v^2} = f_{TW2}\left(\frac{x-\mu_{N,K}}{\sigma_{N,K}}\right), \tag{4.222}$$

where $\mu_{N,K}$ and $\sigma_{N,K}$ are given in (4.217).

Next, given a TS sensing slot under null hypothesis, all the received samples $y_k(n)$ are not homogeneous in nature. To provide a better understanding, we express the covariance matrix in a TS sensing slot under $\mathscr{H}_0$ as,

$$\mathbf{R}_{TS}|_{\mathscr{H}_0} = \mathbf{R}_S(N-D_0) + \mathbf{R}_N(D_0), \tag{4.223}$$

where,

$$\mathbf{R}_S(N-D_0) \triangleq \frac{1}{N-D_0}\mathbf{S}_{[K,N-D_0]}\mathbf{S}^H_{[K,N-D_0]}, \tag{4.224}$$

$$\mathbf{R}_N(D_0) \triangleq \frac{1}{D_0}\mathbf{V}_{[K,D_0]}\mathbf{V}^H_{[K,D_0]}, \tag{4.225}$$

are the partial covariance matrices built respectively from signal-plus-noise and only-noise samples. $\mathbf{R}_S(N-D_0)$ is a standard spiked population covariance matrix of rank-1 and $\mathbf{R}_N(D_0)$ is Wishart matrix. The largest eigenvalue of $\mathbf{R}_N(D_0)$ is negligible compared to the largest eigenvalue of $\mathbf{R}_S(N-D_0)$ given a signal identifiability condition is met [138]. It is known that the fluctuation of the largest eigenvalue of a rank-1 spiked population matrix normalized by the noise variance are asymptotically Gaussian [46, 139] if the signal identifiability condition is met, otherwise its distribution is again a Tracy-Widom of order 2.

$$\frac{\lambda_1^{TS}|_{\mathscr{H}_0}}{\sigma_v^2} = f_D\left(x,(N-D_0)\right) \tag{4.226}$$

Using the results from (4.222) and (4.226), the RLRT decision statistic under null hypothesis can be written as:

$$T_{RLRT}|_{\mathscr{H}_0} = \frac{\lambda_1|_{\mathscr{H}_0}}{\sigma_v^2} \tag{4.227}$$

$$= p_{SS}|_{\mathscr{H}_0}\frac{\lambda_1^{SS}|_{\mathscr{H}_0}}{\sigma_v^2} + p_{TS}|_{\mathscr{H}_0}\frac{\lambda_1^{TS}|_{\mathscr{H}_0}}{\sigma_v^2} \tag{4.228}$$

$$= p_{SS}|_{\mathscr{H}_0} f_{TW}\left(\frac{t-\mu_{N,K}}{\sigma_{N,K}}\right) + p_{TS}|_{\mathscr{H}_0} f_D(x,N-D_0). \tag{4.229}$$

Using the fact that D_0 is a random variable distributed as in (4.188), we obtain the final distribution of the decision statistic of RLRT test under null hypothesis as in (4.218).

We consider now the case when the PU signal is present (hypothesis $\mathscr{H}_1$). In this case, an error is made if the presence of PU signal is not detected. Under alternate hypothesis $\mathscr{H}_1$, the received sample covariance matrix $\mathbf{R}|_{\mathscr{H}_1}$ can be decomposed as the probabilistic sum of $\mathbf{R}_{SS}|_{\mathscr{H}_1}$ and $\mathbf{R}_{TS}|_{\mathscr{H}_1}$.

$$\mathbf{R}|_{\mathscr{H}_1} = p_{SS}|_{\mathscr{H}_1}\mathbf{R}_{SS}|_{\mathscr{H}_1} + p_{TS}|_{\mathscr{H}_1}\mathbf{R}_{TS}|_{\mathscr{H}_1}. \tag{4.230}$$

Since $\mathbf{R}_{SS}|_{\mathscr{H}_1}$ is a standard spiked population covariance matrix of rank-1, the distribution of the largest eigenvalue normalized by the noise variance in a SS sensing slot under $\mathscr{H}_1$ can be approximated as [46, 139],

$$\frac{\lambda_1^{SS}|_{\mathscr{H}_1}}{\sigma_v^2} = f_D(x,N). \tag{4.231}$$

Using the same line of reasoning as in $\mathscr{H}_0$, we get,

$$\frac{\lambda_1^{TS}|_{\mathscr{H}_1}}{\sigma_v^2} = f_D(x,D_1). \tag{4.232}$$

Using (4.231) and (4.232), the distribution of the RLRT decision statistic under alternate hypothesis can be written as,

$$T_{RLRT}|_{\mathscr{H}_1} = \frac{\lambda_1|_{\mathscr{H}_1}}{\sigma_v^2} \tag{4.233}$$

$$= p_{SS}|_{\mathscr{H}_1} \frac{\lambda_1^{SS}|_{\mathscr{H}_1}}{\sigma_v^2} + p_{TS}|_{\mathscr{H}_1} \frac{\lambda_1^{TS}|_{\mathscr{H}_1}}{\sigma_v^2} \tag{4.234}$$

$$= p_{SS}|_{\mathscr{H}_1} f_D(x,N) + p_{TS}|_{\mathscr{H}_1} f_D(x,D_1). \tag{4.235}$$

Incorporating the pmf of D_1 (derived in (4.189)) in (4.235) yields (4.219).

□

A. Probability of False Alarm: Given the pdf of the decision statistic in (4.218), we can now compute the false alarm probability. Under $\mathscr{H}_0$, the PU is in free state at the end of the sensing interval, but the decision statistic is erroneously above the threshold τ and the PU signal is declared present. For the probability of false-alarm P_{Fa}, the following Corollary of Theorem 7 holds.

Corollary 8. The false-alarm probability of the RLRT test under unknown PU traffic and complex signal space scenario is given by:

$$P_{Fa} = P(T_{RLRT}|_{\mathscr{H}_0} \geq \tau) \equiv \int_{\tau}^{+\infty} f_{T_{RLRT}|_{H_0}}(x)dx. \tag{4.236}$$

B. Probability of Detection: Given the pdf of the decision statistic in (4.219), we can now compute the detection probability. Under $\mathscr{H}_1$, i.e., the PU is in busy state at the end of the sensing interval. Under this scenario, if the decision statistic is above the threshold, the PU signal is declared present. The following Corollary of Theorem 7 defines the probability of detection P_D.

Corollary 9. The detection probability of the RLRT test under unknown PU traffic and the complex signal space scenario is given by:

$$P_D = P(T_{RLRT}|_{\mathscr{H}_1} \geq \tau) \equiv \int_{\tau}^{+\infty} f_{T_{RLRT}|_{H_1}}(x)dx. \tag{4.237}$$

Simulation Results

In this Sub-Section, the effect of PU traffic on the RLRT detection method is analyzed based on the the traffic model developed in Sub-Section 4.3.1. The length of the free and busy periods of the PU traffic are measured in terms of the discrete number of samples where each of them has Geometric distribution with mean parameters M_f and M_b, respectively. Under multiple antenna sensing scenario, the average SNR at the receiver is defined as, $\rho = \frac{\sigma_s^2 \|h\|^2}{K\sigma_v^2}$, where $||.||$ denotes the Euclidean norm. The analytical expressions derived are validated via numerical simulations.

In Fig. 4.34, the sensing performance of RLRT under unknown PU traffic is compared with the ideal RLRT performance. It can be well understood that the conventional model with perfect synchronization of the PU-SU sensing slots performs better than the one with unknown PU traffic. The perfect match of the theoretical and Monte-Carlo numerical curves validates the derived analytical expressions of P_{Fa} and P_D. The ROC performance of RLRT in the considered PU traffic model for different PU traffic parameters is presented in Figure 4.34a. The sensing performance degrades significantly when the mean lengths of busy and free periods are comparable with the length of the sensing interval or in a few multiples of it. However, an improvement in the sensing performance can be seen if the length of the mean parameters M_f and M_b is increased. In Figure 4.34b we present the missed detection probability (P_{Md}) as a function of SNR. From this figure, we can see that, for a given PU traffic parameters, increasing the SNR improves the sensing performance for certain lower range of SNR. However, in contrast to RLRT sensing performance under known PU traffic , the RLRT sensing performance under unknown PU traffic levels to some point ($1 > P_{Md} >> 0$) above certain SNR. This is due to the effect of the PU signal-plus-noise and only-noise samples mixing in the TS sensing slot.

In Fig. 4.35, the RLRT sensing performance is plotted as a function of sensing parameters N and K. The variation of the sensing performance of RLRT detector for different number of receiving antennas (K) is plotted in Figure 4.35a. It can be observed that, unlike the rapid increase in sensing performance (decrease in missed-detection probability) with the increasing number of receiving antennas under synchronized PU-SU sensing slot scenario, the RLRT sensing performance under unknown PU traffic is almost constant even if we increase the number of antennas. During a TS sensing slot, from each receiving antenna the received signal samples are the mixture of pure noise samples and samples with both noise and PU signal. Thus,

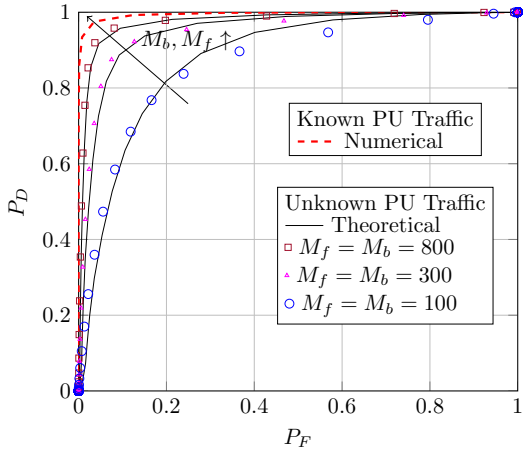

(a) ROC performance. Parameters: $N = 50$, $K = 4$ and SNR $= -6$ dB

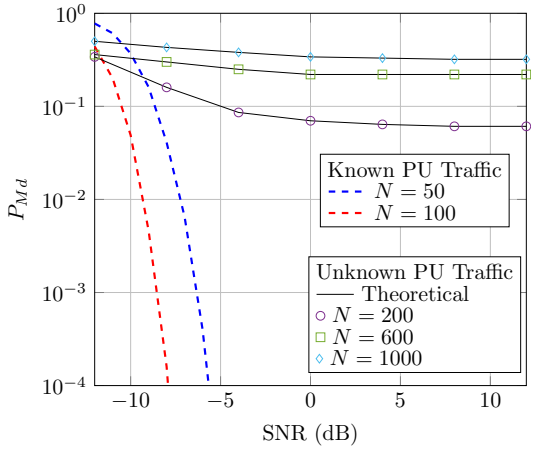

(b) Probability of Missed detection vs. SNR, Parameters: $K = 8$, $P_{Fa} = 0.01$ and $M_f = M_b = 3000$.

Fig. 4.34 Sensing performance of RLRT under unknown PU traffic.

even if we use multiple antennas, the nature of the received signal doesn't change much. This is the reason why the sensing performance improvement is suppressed by the unknown PU traffic (more specifically, the TS sensing performance) when the length of the free and busy periods of PU traffic are quite small (a few multiples of the length of the sensing window). Furthermore, we present in Figure 4.35b, the numerical simulation of detection probability (P_D) as a function of sensing window (N). Note that, unlike RLRT detection probability under known PU traffic which monotonically increases indefinitely until '$P_D = 1$' with increasing length of sensing window, the detection probability of RLRT under unknown PU traffic do not have a monotonic property as a function of the sensing window length.

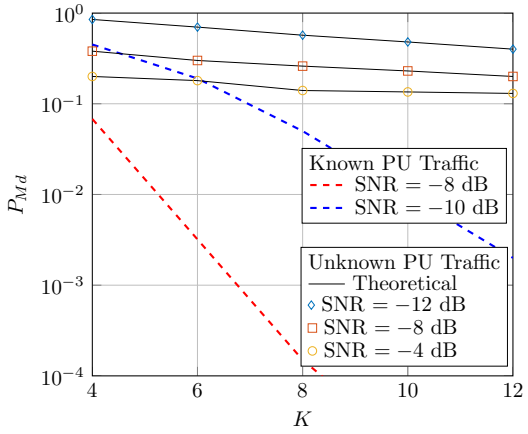

(a) Prob. of Missed Detection vs. the number of receiving antennas (K). Parameters: $N = 100$, $P_F = 0.01$ and $M_f = M_b = 1500$

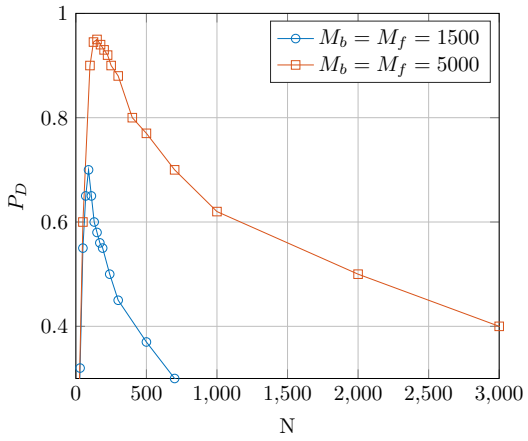

(b) Detection Probability for increasing N. Parameters: SNR $= -10$ dB, $K = 8$ and $P_F = 0.01$

Fig. 4.35 RLRT under unknown PU traffic sensing performance comparison for different sensing parameters (N and K).

Chapter 5

Low Density Spreading (LDS) Multiplexing for NOMA

Low Density Spreading (LDS) Multiplexing for Non-orthogonal Multiple Access

5.1 Introduction

5G wireless networks are expected to support very diverse services - from very low latency to very high delay tolerant, and from very small to very large packets in different applications. An important 5G requirement is will be to support massive connectivity with a large number of devices such as smart phones, tablets and machines. The current LTE [43] system is not able to efficiently support massive connectivity, especially in uplink. While fundamental research for 5G is now well under way [1, 10], the question what actually makes a 5G system and what are the drivers is still open and part of intensive discussions.

A new flexible and adaptable interface is proposed to meet the complex and diverse application requirements of air interface technology. New air interface consists of building blocks and configuration mechanisms such as adaptive waveforms, adaptive protocols, adaptive frame structures, adaptive coding and modulation family, and adaptive multiple access schemes. With these blocks and mechanisms, the air interface will be able to accommodate the future wide variety of user services, spectrum bands and traffic levels. The quest of improving the spectral efficiency has

been regarded as the most important but yet challenging task in the design of future wireless communication system due to the fact that the rapid growth of multimedia services, such as interactive game and television applications, cannot be coped with the scarce radio frequency (RF) spectrum resources. As a result, multiple access schemes will play a critical role in providing the increasing demand in services for future terminals and applications.

Multiple access (MA) technique is a major building block of cellular systems. Through the MA technique, the users can simultaneously access the physical medium and share the finite resources of the system, such as spectrum, time and power. Due to the rapid growth in data demand in mobile communications, there has been extensive research to improve the efficiency of cellular systems. A significant part of this effort focuses on developing and optimizing the MA techniques. As a result, many MA techniques have been proposed systematically over the years, and some of these MA techniques are already been adopted in the cellular system standards such as Time Division Multiple Access (TDMA), Frequency Division Multiple Access (FDMA), Orthogonal Frequency Division Multiple Access (OFDMA) and Code Division Multiple Access (CDMA). There are many factors that determine the efficiency of MA techniques, including spectral efficiency, low complexity implementation as well low envelope fluctuations.

OFDM and OFDMA are the modulation technique and the multiple access strategy adopted in LTE fourth genereation (4G) cellular network standards, respectively [83]. OFDM and OFDMA succeeded CDMA, employed in third generation (3G) networks for several reasons, such as the ease of implementation of both transmitter and receiver thanks to the use of FFT and inverse FFT (IFFT) blocks; the ability to counteract multipath distortion, the orthogonality of subcarriers which eliminates intercell interference; the possibility of adapting the transmitted power and the modulation cardinality; and the ease of integration with multi-antenna hardware, both at the transmitter and receiver. Nonetheless, despite such a pool of positive properties, OFDM/ OFDMA are not exempt of defects, and their adoption in the forthcoming generation of wireless networks is not taken for granted. Indeed, the spectral efficiency of OFDM is limited by the need of a CP and by its large sidelobes (which require some null guard tones at the spectrum edges). OFDM signals may exhibit large peak-to-average-power ratio values [136] and the impossibility of having strict frequency synchronization among subcarriers makes OFDM and OFDMA not really orthogonal techniques. In particular, synchronization is a key issue in the uplink of a

cellular network wherein different mobile terminals transmit separately [127], and, also, in the downlink when base station coordination is used [93, 68]. For instance, with regard to the spectral efficiency loss of side lobes and the CP, in an LTE system operating at 10 MHz bandwidth, only 9 MHz of the band is used. In addition, the loss of the CP is around 7%, so the accumulated loss totals at 16%. These drawbacks, which invalidate many of the above-mentioned OFDM/OFDMA advantages, form the basis of an open and intense debate on what the modulation format and multiple access strategy should be in next-generation cellular networks.

The limitations of OFDM-based waveforms were identified as research topics for future 5G waveforms. One aspect is the requirement for much shorter latency to enable new services and applications like autonomous driving, that demands an ultra-low latency and a highly resilient communication link. Another approach is to make the cyclic prefix optional and work with shorter symbol durations. All this has led to several candidate waveforms, such as Generalized frequency division multiplexing (GFDM), Filter bank multi-carrier (FBMC), Universal filtered multi-carrier (UFMC), Filtered OFDM (f-OFDM), etc [142]. The performance of these waveform candidates is currently being analyzed and evaluated. At the same time new multiple access schemes are also being researched, including Sparse Code Multiple Access (SCMA) [134], Non-Orthogonal Multiple Access (NOMA) [150] and Resource Spread Multiple Access (RSMA) [142].

However, it has not been decided yet which of these waveform candidates or multiple access schemes will be utilized in a future 5G system. It is up to the standardization committees to evaluate different proposal to the IMT-2020 group within the ITU.

Moreover, 3GPP has already started the first study items for the choice of the new Radio Access Technology (RAT) for next generation 5G mobile networks. Currently, there is a lot of interest in Non-Orthogonal Multiple Access (NOMA) schemes, which allow to distribute resources among users without a strict orthogonal division. For non-orthogonal MA techniques, all the users share the entire signal dimension, and there is a Multiple Access Interference (MAI). Thus, for non-orthogonal transmission, more complicated receivers are required to deal with the MAI comparing to orthogonal transmission. NOMA is more practical in the uplink scenario because the base station can afford the Multi-user Detection (MUD) complexity. On the other hand, for downlink, orthogonal MA is more suitable due

to the limited processing power at the user equipment. Many non-orthogonal MA techniques have been overlooked due to the implementation complexity. Clearly, the recent advancements in signal processing have opened up new possibilities for developing more sophisticated and efficient MA techniques. Thus, more advanced MA techniques have been proposed lately. However, in order to adopt these new MA techniques in the mobile communication systems, many challenges and opportunities need to be studied.

To better understand the problem, let us consider 4G LTE, which uses an OFDM (Orthogonal Frequency Division Multiplexing) radio access. In LTE, a resource block is made of 12 OFDM carriers (corresponding to 180 kHz of band), which are allocated for a TTI (Transmission Time Interval) 1ms long. In LTE, different users receive disjoints sets of resource blocks, so they transmit on disjoint bands. Instead, in a non-orthogonal approach, the same resource block may be jointly assigned to different users. Therefore, two or more users may transmit simultaneously on the same band.

Examples of non-orthogonal schemes under discussion for 5G access schemes are super-position modulation [89], Low Density Signature-OFDM [91] and Sparse Code Multiple Access [134]. In this chapter, we focus on Low Density Signature schemes, which look very promising thanks to their simplicity.

5.2 Multiplexing with Low Density Spreading

Low Density Spreading is one of the promising multiplexing scheme for NOMA techniques proposed for 5G multiple access [171, 11, 12]. In LDS-Multiplexing, low density spreading codes are used for transmission, where each user spreads its data on a small set of sub-carriers. Due to the low density structure, every data symbol will be spread over a small subset of sub-carriers (effective processing gain) and also every sub-carrier will only be used by small subset of data symbols that could belong to different users. There is no exclusivity in the sub-carriers allocation and more than one user can share each sub-carrier. Therefore, each user transmission on a given sub-carrier will only be interfered by a small number of other user's transmission. The LDS structure can be captured by a low density graph thus similar to application of LDS for CDMA system, thus the detection of LDS symbols could be based on the MPA presented in [90]. The LDS system can be understood as a system which

applies LDS as multiplexing technique together with any orthogonal multi-carrier modulation.

The main features of the LDS scheme can be summarized as follow [171]

- At each sub-carrier, a user will have relativity small number of interferers comparing to the total number of users. Consequently, the search space will be smaller and more complex MUD techniques can be implemented.
- Higher Signal to Interference plus Noise Ratio (SINR) can be achieved at each sub-carrier, which results in reliable detection process.
- Each user will experience interference from different users at different sub-carriers, which results in interference diversity by avoiding strong interferers to destroy the signal of a user on all the sub-carriers.
- Belief propagation based MUD can be implemented with linear complexity in the number of sub-carriers [126].

Spreading sequences of the low-density type (containing many zeros) were conceptually introduced in [38] for the purpose of allowing low-complexity multiuser detection, while for the multicarrier system they were introduced in [90]. These sequences, when designed in accordance with appropriate rules [126], allow application of a belief propagation algorithm at the receiver. This was shown to yield promising performance for overloaded systems - systems with more spreading sequences than chips for BPSK modulated data. Later, the concept of LDS-OFDM was introduced as an uplink multi-carrier multiple access scheme and a close-to-optimum MUD receiver performance was analyzed using EXIT charts [91]. The Performance comparison with other existing multiple access techniques like OFDMA and SC-FDMA were investigated together with their suitability for next generation cellular system in [144, 13].

The focus of above literature was on the conceptual multiuser receiver structure rather than on the particular choice of the set of spreading sequences. Bypassing details of spreading sequence synthesis, low-density sequences were found by trial and error. Moreover, user-specific pseudo-random phases were applied in the evaluation of the receiver structure [90].

In this chapter we address the design of the user's spreading sequences. We refer to them as signatures sets assuming they have the low-density structure of [90].

Instead of relying on trial-and-error searches and on pseudo-random design steps, we take a structured approach towards the design of spreading sequences. We focus on their performance on the AWGN channel which is a good model for downlink multiple access systems operating in a flat, slowly fading radio environment. In the downlink scenario, a single physical transmitter can simultaneously transmit multiple information streams, each information stream intended to a separate user, i.e., to a separate receiver. Thus, from a single user reception performance perspective, the situation is equivalent to have multiple users transmitting simultaneously.

We investigate here a signature matrix of the low-density type, which has non-zero entries only in positions indicated by a low-density spreading binary-matrix [90]. The design of this kind of matrices has been subject of extensive research over the past years in a completely different context (the design of LDPC codes [114]) than the one addressed here (multiple-access signatures). Binary matrices designed for good error-correction performance usually have a large girth-value (defined as the length of the smallest cycle in the factor graph associated with the binary matrix). We anticipate that matrices designed according to these principles also are beneficial when used for signature design and we therefore adopt these binary matrices as the basis for further signature design. We assume perfect synchronization of the transmitted signatures, typically accomplished when any orthogonal modulation scheme is the carrier transmission technology for the transmitted chip sequences. Demodulation is done by the near-optimally belief-propagation structure of [90]. We evaluate the performance of our sequence constructions and we show that they have beneficial properties in terms of their distance spectrum.

5.3 System Model

We consider a NOMA Scheme in order to allow N simultaneously users to share K orthogonal carriers where $N > K$. We define the ratio $\gamma = \frac{N}{K}$ as the overload factor of the scheme. A simple factor graph representation of the LDS spreading system is shown in Figure 5.1.

Let us denote by $\underline{x}$, a complex symbol vector of length N generated by N users,

$$\underline{x} = (x_1, \cdots, x_n, \cdots, x_N) \quad x_n \in \mathbb{C}, \tag{5.1}$$

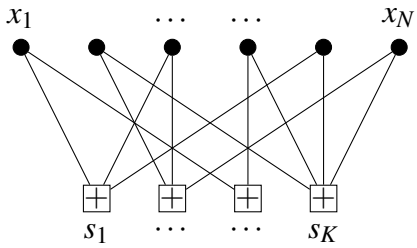

Fig. 5.1 Factor Graph representation of LDS spreading

and K complex symbols transmitted on the K tones by $\underline{s}$,

$$\underline{s} = (s_1, \cdots, s_k, \cdots, s_K) \quad s_k \in \mathbb{C}. \tag{5.2}$$

The problem of distributing $N > K$ symbols can be approached by transmitting on each tone a linear combination of the N user symbols.

$$s_i = \sum_{n=1}^{N} x_n \alpha_{nk} \quad x_k \in \mathscr{C}, \tag{5.3}$$

where α_{nk} is a linear combination coefficient. This equation can be written by using vector representation as,

$$\underline{s} = \underline{x}\mathbf{A}. \tag{5.4}$$

where the $N \times K$ matrix $\mathbf{A}$ known as Spreading Matrix, contains the linear combination coefficients as its columns, known as spreading sequence, i.e., $\mathbf{A} = [\underline{a}_1 \cdots \underline{a}_k \cdots \underline{a}_K]$ and $\underline{a}_k = [\alpha_{1k} \cdots \alpha_{nk} \cdots \alpha_{Nk}]^T$. The spreading sequences are assigned uniquely to each user and are completely shared among the transmitter/receiver.

In LDS multiplexing, a small number of elements of a spreading sequences are non zero allowing each user to spread its data over small number of tones. The relationship between the LDS matrix $\mathbf{A}$ and the user spreading can be better explained using following elements:

- Binary Matrix: A binary matrix $\mathbf{B}$ is given by $\mathbf{B} = [\underline{b}_1, \cdots, \underline{b}_K]$ where $\underline{b} \in \mathbb{B}_2^K$ is a binary vector for each tone. The n^{th} element of $\underline{b}$ is denoted by b_{nk} and is given by,

$$b_{nk} = \begin{cases} 0, & \text{if} \quad \alpha_{nk} = 0 \\ 1, & \text{if} \quad \alpha_{nk} \neq 0 \end{cases} \quad ; \quad n = 1, \ldots, N. \tag{5.5}$$

  The set of positions of 1's in the n^{th} row denotes the set of output tones over which user n spread its data, while the set of positions of 1's in the k^{th} column represents the set of users that can contribute with their data at the k^{th} tone. Note that the $1'$s components of the binary matrix $\mathbf{B}$ represents the non zero components of the matrix $\mathbf{A}$ and the non zero components of matrix $\mathbf{A}$ can take any complex values.

- Row Weight and Column Weight: Let us define the cardinality of the set of tones over which any user spreads its data as w_r, known as row weight, and the cardinality of the set of users that can contribute their data at any tone as w_c, known as column weight. If the parameters w_r and w_c are constant for all users and tones respectively, then the resulting Spreading Matrix is known as regular spreading matrix. In the following, we discuss the problem of constructing optimum performing Spreading Matrix **A**. For simplicity, focus on a regular Spreading Matrix for the rest of the discussion.

- Column Correlation Factor: Let us define a variable w_f, which denotes the maximum correlation among the non-zero positions in two columns of the binary matrix and is given by,

$$w_f = \max_{k_1,k_2} \sum_{\substack{n=1 \\ k_1 \neq k_2}}^{n} b_{nk_1} b_{nk_2}. \tag{5.6}$$

- Non-zero elements: We consider non-zero elements of the spreading matrix taken from a small and finite complex-valued constellation $\underline{v} = \{v_k\}$ referred to as signature constellation. Signature constellation are taken from the ring of constant magnitude in a 2-D complex state space. A constant amplitude is considered so as to keep the power of each input symbols constant during a linear combination. Each output symbol is the linear combination of few input symbols for each entry α_{kn} in **A**,

$$\alpha_{kn} \in \underline{v} \cup \{0\}. \tag{5.7}$$

5.4 Calculation of average energy per bit (E_b)

It is clear that the output symbol vector is the complex linear combination of the input symbols. The output energy per bit varies depending on the overloading factor, the number of input symbols linearly combined to form an output and energy per bit at the input modulated symbol. In order to derive the upper bound on minimum

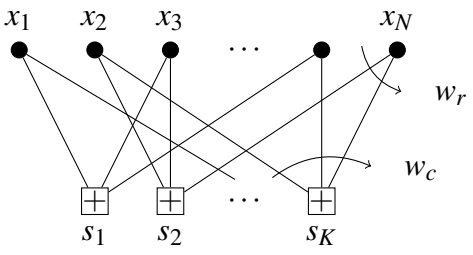

Fig. 5.2 Regular LDS spreading system

Euclidean distance achieved by these schemes, we first derive the expression for the output average energy per bit for a regular LDS spreading system employing BPSK as input modulation scheme.

Proposition 7. For an LDS system with system parameters (N, K, w_r, w_c) employing BPSK as an input modulation scheme, the output average energy is given by,

$$E_b = \frac{Kw_c}{N} E_{bi} \Rightarrow w_r \times E_{bi}. \tag{5.8}$$

Proof. Consider a LDS system with system parameters (N, K, w_r, w_c) employing BPSK as an input modulation scheme, $x_n \in \{+\sqrt{E_{bi}}, -\sqrt{E_{bi}}\}$ with input energy per bit E_{bi}.

The average energy at one of the output symbol can be calculated as the sum of the energy of every possible output symbol normalized by their number. If w_c different inputs are linearly combined to form an output symbol s_k (see Figure 5.2), it means there are 2^{w_c} different possible s_k: $s_k \in \{s_k^1, \cdots, s_k^{2^{w_c}}\}$. If w_c inputs linearly sums to an output s_k, the remaining $N - w_c$ inputs can give 2^{N-w_c} possible input combinations that can give the same output s_k, thus the average energy of the output symbol is given by:

$$E_O(k) = \frac{2^{N-w_c} \sum_{i=1}^{2^{w_c}} |s_k^i|^2}{2^N}. \tag{5.9}$$

Since there are K output symbols and N inputs, the output average energy per bit can be written as

$$E_b = \frac{1}{N} \sum_{k=1}^{K} E_O(k). \tag{5.10}$$

Since w_c is constant for all the output symbols s_k, the average output energy per symbol is constant, thus:

$$E_b = \frac{K2^{N-w_c}}{N2^N} \sum_{i=1}^{2^{w_c}} |s_k^i|^2. \tag{5.11}$$

It can easily be found that the sum $\sum_{i=1}^{2^{w_c}} |s_k^i|^2$ is equal to $w_c \times E_{bi} \times 2^{w_c}$.

This leads to a simplified expression of the Average Output energy per bit as in (5.8).

□

Next, the following proposition derives the upper bound on minimum euclidean distance using the above derived average output energy per bit.

Proposition 8. For an LDS system with system parameters (N, K, w_r, w_c) employing BPSK as an input modulation scheme, the upper bound on minimum Euclidean distance is given by,

$$\frac{d_{\min}^2}{E_b}|_{\max}| = 4. \tag{5.12}$$

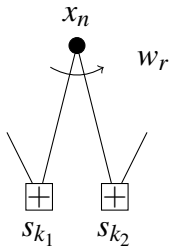

Fig. 5.3 Euclidean distance relationship

Proof. In a considered LDS system with parameters (N, K, w_c, w_r), the least possible Hamming distance among two different binary input sequence is 1. Since each input is connected to w_r number of output tones for a regular LDS spreading system (See Figure 5.3), the difference in one bit corresponds to an Euclidean distance of at most $2 \times \sqrt{E_{bi}}$ in each connected output tones. Thus, the maximum squared Euclidean distance we can achieve is,

$$d_{\min}^2|_{\max} = w_r \times 4E_{bi}. \tag{5.13}$$

Thus, the upper bound on the normalized minimum Euclidean distance expressed in (5.12) can be easily obtained using (5.13) and (5.8). □

5.5 Spreading Matrix Design

The performance of the LDS system directly depends on the Euclidean distance profile of the considered spreading matrix **A** for the given LDS system parameters. In essence, the BER performance depends mostly on the minimum Euclidean distance provided by the spreading matrix and partly on the multiplicity of other distances (distance distribution).

The design of a spreading matrix **A** with parameters (N, K, w_c, w_r) involves the separate design of three different components, which are:

- Binary Matrix
- Non-zero elements
- Distribution of non-zero elements in a binary matrix

5.5.1 Binary Matrix Design

Binary matrix serves as a way to relate the input symbol sets with output tones. The LDS binary matrix **B** must be designed to meet the system parameters, i.e., N, K, w_r and w_c. Like for LDPC matrices, a factor graph can be associated to a binary matrix **B** by constructing the edges connecting factor (i.e. column) nodes and variable (i.e. row) nodes. In a factor graph a loop (or cycle) is a closed path with no repeated nodes, and must therefore be of even length. There is at most one edge between any two nodes, and so the shortest length a loop can have is 4, the next largest is 6, and so on. We refer to such loops as 4-loops, 6-loops, etc., and in general a loop of length n is an $n-$loop. The girth of a graph is the length of the shortest loop. The main problem with a loop is that the value of an incorrect bit is propagated back to itself, effectively reinforcing itself and resisting the efforts of the algorithm to correct it. Thus, an important consideration in designing a binary matrix is to avoid small loops. In this work, we introduce a novel design concept for the construction of a binary matrix, which completely avoids 4-loops.

Given a binary matrix **B**, it is very simple to check the presence of 4-loops by using the column correlation factor w_f defined in Section 5.3. As we know that the column position of a binary matrix corresponds to a factor node in a factor graph, this

means that the correlation in the non-zero position of a two column pair represents the edge of a factor graph. Thus, considering any two columns of a binary matrix, a column correlation factor greater than one confirms the presence of 4-loops in the binary matrix. It is important to note that it may not be possible to construct the binary matrix **B** for all the matrix size and overloading factor with a column correlation factor $w_f = 1$. The following relation, which is derived based on the t-design [115] concept, helps us to check the possibility of constructing the binary matrix with $w_f = 1$ for given LDS system parameters.

For an LDS system with system parameters (N, K, w_r, w_c), if $\left\lfloor \frac{K-1}{w_r-1} \right\rfloor \times \frac{K}{w_r} \geq N$, there exists at least one binary matrix design which has a column correlation factor $w_f = 1$. Design guidelines are provided for every overloading factor in next sections.

5.5.2 Design of non-zero symbols

The concept behind Low Density Spreading is to uniquely distribute the spreading codes which contains less number of non-zero elements allowing each user to spread its data over a small number of chips (tones, carriers, channels). In order to uniquely decode the linearly combined output symbols, the one-to-one mapping relationship between input and output is a must. This necessitates a careful design of non-zero symbols of a spreading matrix. In addition, the choice of non-zero symbols should not change the overall magnitude of the input symbols while spreading. Thus, it is obvious that the non-zero symbols must be chosen from the unit circle of a complex 2-dimensional space which can be written in a complex exponential form as,

$$v_k = \exp(\theta_k i). \tag{5.14}$$

We distribute these symbols in the position of 1's of each column in the binary matrix. Let us consider the set of unique elements which are to be distributed as signature constellation set. One of the easiest way to ensure a one to one relationship between input and output of a LDS system is to ensure one-to-one relationship among the inputs corresponding to single channel outputs [167].

As presented before, the objective of this work is to find a design rule for the construction of a complete spreading matrix which ensures the achievement of upper bound on the minimum normalized Euclidean distance. In the following we present

a theorem that proves that for $w_c > 2$, there is no such unitary magnitude signature constellation for a single channel output that gives a one to one mapping matching the upper bound on the minimum normalized Euclidean distance.

Lemma 3. Given an LDS binary matrix with parameters N, $K = 1$, w_c,

- there exists a signature constellation for $w_c = 2$ to obtain the upper bound on the normalized Euclidean distance, and the angle separation among the signature constellation points should fall in the following range.

$$\begin{aligned} &-2\pi/3 \leq \theta_1 - \theta_2 \leq -\pi/3, -5\pi/3 \leq \theta_1 - \theta_2 \leq -4\pi/3, \\ &\pi/3 \leq \theta_1 - \theta_2 \leq 2\pi/3, 4\pi/3 \leq \theta_1 - \theta_2 \leq 5\pi/3, \end{aligned} \tag{5.15}$$

  where θ_1 and θ_2 are the angles of the signature constellation points.

- no signature constellation exists that gives an upper bound on the normalized minimum Euclidean distance for $w_c \geq 3$

Proof. Let $(x_1, \cdots, x_{w_c})$ and $(y_1, \cdots, y_{w_c})$ be two input sets that correspond to non-zero positions of the considered column of a binary matrix. Single channel outputs corresponding to these input sets can be written as,

$$O_1 = v_1 x_1 + v_2 x_2 + \cdots + v_{w_c} x_{w_c} \tag{5.16}$$

$$O_2 = v_1 y_1 + v_2 y_2 + \cdots + v_{w_c} y_{w_c}. \tag{5.17}$$

A first and a simple case would be to consider $w_c = 2$, thus,

$$O_1 = v_1 x_1 + v_2 x_2 \tag{5.18}$$

$$O_2 = v_1 y_1 + v_2 y_2. \tag{5.19}$$

Now, the squared Euclidean distance among these outputs can be written as,

$$(O_1 - O_2)^2 = |v_1(x_1 - y_1) + v_2(x_2 - y_2)|^2. \tag{5.20}$$

Table 5.1 Relationship of A and B with input $\mathbf{x}$ and $\mathbf{y}$.

x_1	x_2	y_1	y_2	A	B
-1	-1	-1	-1	0	0
-1	+1	-1	+1	$-2E_{bi}$	$-2E_{bi}$
+1	-1	+1	-1	$2E_{bi}$	$2E_{bi}$
+1	+1	+1	+1	0	0

Substituting the values of v_1 and v_2 with their exponential form as in (5.14), we have,

$$(O_1 - O_2)^2 = |(\cos\theta_1 + i\sin\theta_1)(x_1 - y_1) + (\cos\theta_2 + i\sin\theta_2)(x_2 - y_2)|^2. \quad (5.21)$$

Let $A = x_1 - y_1$ and $B = x_2 - y_2$, then simplifying we get,

$$(O_1 - O_2)^2 = A^2 + B^2 + 2AB\cos(\theta_1 - \theta_2). \quad (5.22)$$

For BPSK modulated input symbols with bit energy of E_{bi}, Table 5.1 shows the different values of A and B for different combinations of x_1, x_2 and y_1, y_2. As explained above, the squared Euclidean distance should be greater or equal to $4E_{bi}^2$ for two distinct output tones:

$$A^2 + B^2 + 2AB\cos(\theta_1 - \theta_2) \geq 4E_{bi}^2. \quad (5.23)$$

Now, we define different cases based on the combination of these input sequences.

Case 1: $x_1 = x_2$ and $y_1 = y_2$ (corresponds to the first and the last rows of the above table)

When the inputs are same then, A and B becomes zero, thus $(O_1 - O_2) = 0$ which is a obvious result.

Case 2: If one of the input is equal and the other is different, $x_1 = x_2$ and $y_1 = -y_2$ OR $x_1 = -x_2$ and $y_1 = y_2$

$A = 0$ and $B = \pm 2E_{bi}$ OR $A = \pm 2E_{bi}$ and $B = 0$, thus the inequality turns to

$$4E_{bi}^2 = 4E_{bi}^2, \quad (5.24)$$

which is also an obvious result.

Case 3: When both the inputs are different, $x_1 = -x_2$ and $y_1 = -y_2$ OR $x_1 = -x_2$ and $y_1 = y_2$, i.e., $A = \pm 2E_{bi}$ and $B = \pm 2E_{bi}$ thus the inequality turns to

$$4E_{bi}^2 + 4E_{bi}^2 + 2(\pm 2E_{bi})(\pm 2E_{bi})\cos(\theta_1 - \theta_2) \geq 4E_{bi}^2. \tag{5.25}$$

Here are two sub-cases,

Sub-case 1: When both A and B are positive or both negative, the product AB is always positive, thus,

$$8E_{bi}^2 + 8E_{bi}^2\cos(\theta_1 - \theta_2) \geq 4E_{bi}^2 \tag{5.26}$$

$$\cos(\theta_1 - \theta_2) \geq -0.5. \tag{5.27}$$

Sub-case 2: When A and B are of opposite sign, the product AB is always negative, thus,

$$8E_{bi}^2 - 8E_{bi}^2\cos(\theta_1 - \theta_2) \geq 4E_{bi}^2 \tag{5.28}$$

$$-\cos(\theta_1 - \theta_2) \geq -0.5 \tag{5.29}$$

$$\cos(\theta_1 - \theta_2) \leq 0.5. \tag{5.30}$$

From (5.27) and (5.30),

$$-0.5 \leq cos(\theta_1 - \theta_2) \leq 0.5 \tag{5.31}$$

$$-2\pi/3 \leq \theta_1 - \theta_2 \leq -\pi/3, -5\pi/3 \leq \theta_1 - \theta_2 \leq -4\pi/3,$$
$$\pi/3 \leq \theta_1 - \theta_2 \leq 2\pi/3, 4\pi/3 \leq \theta_1 - \theta_2 \leq 5\pi/3. \tag{5.32}$$

Thus, if $(\theta_1 - \theta_2)$ falls in the above range, then the squared Euclidean distance among two different outputs is always greater or equal to $4E_{bi}^2$. This proves the first claim.

Next, we consider $w_c = 3$.

$$O_1 = v_1x_1 + v_2x_2 + v_3x_3 \tag{5.33}$$

$$O_2 = v_1y_1 + v_2y_2 + v_3y_3. \tag{5.34}$$

The squared Euclidean distance between O_1 and O_2 is,

$$(O_1 - O_2)^2 = |v_1(x_1 - y_1) + v_2(x_2 - y_2) + v_3(x_3 - y_3)|^2. \tag{5.35}$$

Substituting the values of v_1, v_2 and v_3 with their exponential form as in (5.14), we have,

$$\begin{aligned}(O_1 - O_2)^2 = |&(\cos\theta_1 + i\sin\theta_1)(x_1 - y_1) + (\cos\theta_2 + i\sin\theta_2)(x_2 - y_2) \\ &+ (\cos\theta_3 + i\sin\theta_3)(x_3 - y_3)|^2.\end{aligned} \tag{5.36}$$

Let $A = x_1 - y_1$, $B = x_2 - y_2$ and $C = x_3 - y_3$, then simplifying we get,

$$(O_1 - O_2)^2 = A^2 + B^2 + C^2 + 2AB\cos(\theta_1 - \theta_2) + 2BC\cos(\theta_2 - \theta_3) + 2AC\cos(\theta_3 - \theta_1). \tag{5.37}$$

Our objective is to obtain the angle parameters relationship in order to obtain the maximum possible normalized euclidean distance. The inequality to satisfy can be written as

$$(O_1 - O_2)^2 \geq 4E_{bi}^2. \tag{5.38}$$

We consider the values of A, B and C based on the above table. Based on the input situation here we define three cases:

Case 1: When all the inputs are equal giving $A = B = C = 0$, then $(O_1 - O_2)^2 = 0$ which is obvious.

Case 2: When one of them is different and two of them are equal, i.e., $A = \pm 2E_{bi}$ and $B = C = 0$ OR $B = \pm 2E_{bi}$ and $A = C = 0$ OR $C = \pm 2E_{bi}$ $B = A = 0$, In each case,

$$(O_1 - O_2)^2 = 4E_{bi}^2, \tag{5.39}$$

which satisfies (5.38)

Case 3: When two of them are different and one is equal, i.e., $A = B = \pm 2E_{bi}$ and $C = 0$ OR $A = C = \pm 2E_{bi}$ and $B = 0$ OR $B = C = \pm 2E_{bi}$ $A = 0$, In each case,

$$(O_1 - O_2)^2 = 8E_{bi}^2 + 2(\pm 2E_{bi})(\pm 2E_{bi})\cos(\theta_1 - \theta_2), \tag{5.40}$$

$$(O_1 - O_2)^2 = 8E_{bi}^2 + 2(\pm 2E_{bi})(\pm 2E_{bi})\cos(\theta_1 - \theta_3), \tag{5.41}$$

$$(O_1 - O_2)^2 = 8E_{bi}^2 + 2(\pm 2E_{bi})(\pm 2E_{bi})\cos(\theta_2 - \theta_3). \tag{5.42}$$

When conditioned with $(S_1 - S_2)^2 \geq 4E_{bi}^2$, we obtain

$$-2\pi/3 \leq \theta_1 - \theta_2 \leq -\pi/3, -5\pi/3 \leq \theta_1 - \theta_2 \leq -4\pi/3,$$
$$\pi/3 \leq \theta_1 - \theta_2 \leq 2\pi/3, 4\pi/3 \leq \theta_1 - \theta_2 \leq 5\pi/3. \tag{5.43}$$
$$-2\pi/3 \leq \theta_2 - \theta_3 \leq -\pi/3, -5\pi/3 \leq \theta_2 - \theta_3 \leq -4\pi/3,$$
$$\pi/3 \leq \theta_2 - \theta_3 \leq 2\pi/3, 4\pi/3 \leq \theta_2 - \theta_3 \leq 5\pi/3. \tag{5.44}$$
$$-2\pi/3 \leq \theta_3 - \theta_1 \leq -\pi/3, -5\pi/3 \leq \theta_3 - \theta_1 \leq -4\pi/3,$$
$$\pi/3 \leq \theta_3 - \theta_1 \leq 2\pi/3, 4\pi/3 \leq \theta_3 - \theta_1 \leq 5\pi/3. \text{ respectively.} \tag{5.45}$$

We know that the complex angle at the exponent is symmetric over a multiples of 2π. Thus, to simplify the above range in (5.43), (5.44) and (5.45), let us consider,

$$\theta_1 - \theta_2 = \frac{\pi}{3} \text{ and } \theta_2 - \theta_3 = \frac{\pi}{3} + \varepsilon. \tag{5.46}$$

Since $\theta_3 - \theta_1 = (-(\theta_2 - \theta_3) - (\theta_2 - \theta_3)$, we have,

$$\theta_3 - \theta_1 = -\pi/3 - \pi/3 - \varepsilon \tag{5.47}$$
$$\theta_3 - \theta_1 = -2\pi/3 - \varepsilon. \tag{5.48}$$

It can easily be shown that the only values of ε that satisfies above inequalities are $\varepsilon = 0, -\pi$. It means that the values of $\theta_1 - \theta_2, \theta_2 - \theta_3$ and $\theta_3 - \theta_1$ are fixed and are given Table 5.2,

Case 4: When all the inputs are different, i.e., $A = B = C = \pm 2E_{bi}$.

Sub-Case 1: One is positive and two are negative, i.e., $A = -2E_{bi}$, $B = -2E_{bi}$ and $C = +2E_{bi}$ OR $A = -2E_{bi}$, $B = +2E_{bi}$ and $C = -2E_{bi}$ OR $A = +2E_{bi}$, $B = -2E_{bi}$ and $C = -2E_{bi}$.

Sub-Case 2: One is negative and two are positive, i.e., $A = +2E_{bi}$, $B = +2E_{bi}$ and $C = -2E_{bi}$ OR $A = +2E_{bi}$, $B = -2E_{bi}$ and $C = +2E_{bi}$ OR $A = -2E_{bi}$, $B = +2E_{bi}$ and $C = +2E_{bi}$

Table 5.2 Set of angles satisfying (5.43), (5.44) and (5.45).

Sets	$\theta_1-\theta_2$	$\theta_2-\theta_3$	$\theta_3-\theta_1$
Set1	$\frac{-\pi}{3}$	$\frac{-\pi}{3}$	$\frac{2\pi}{3}$
Set2	$\frac{-\pi}{3}$	$\frac{2\pi}{3}$	$\frac{-\pi}{3}$
Set3	$\frac{2\pi}{3}$	$\frac{-\pi}{3}$	$\frac{-\pi}{3}$
Set4	$\frac{\pi}{3}$	$\frac{\pi}{3}$	$\frac{-2\pi}{3}$
Set5	$\frac{\pi}{3}$	$\frac{-2\pi}{3}$	$\frac{\pi}{3}$
Set6	$\frac{-2\pi}{3}$	$\frac{\pi}{3}$	$\frac{\pi}{3}$
Set7	$\frac{-4\pi}{3}$	$\frac{2\pi}{3}$	$\frac{2\pi}{3}$
Set8	$\frac{2\pi}{3}$	$\frac{-4\pi}{3}$	$\frac{2\pi}{3}$
Set9	$\frac{2\pi}{3}$	$\frac{2\pi}{3}$	$\frac{-4\pi}{3}$
Set10	$\frac{-2\pi}{3}$	$\frac{-2\pi}{3}$	$\frac{4\pi}{3}$
Set11	$\frac{-2\pi}{3}$	$\frac{4\pi}{3}$	$\frac{-2\pi}{3}$
Set12	$\frac{4\pi}{3}$	$\frac{-2\pi}{3}$	$\frac{-2\pi}{3}$

For both of these sub-cases we have,

$$(O_1-O_2)^2 = 12E_{bi}^2+8E_{bi}^2\cos(\theta_1-\theta_2)-8E_{bi}^2\cos(\theta_2-\theta_3) - 8E_{bi}^2\cos(\theta_3-\theta_1) \tag{5.49}$$

$$(O_1-O_2)^2 = 12E_{bi}^2-8E_{bi}^2\cos(\theta_1-\theta_2)-8E_{bi}^2\cos(\theta_2-\theta_3) + 8E_{bi}^2\cos(\theta_3-\theta_1) \tag{5.50}$$

$$(O_1-O_2)^2 = 12E_{bi}^2-8E_{bi}^2\cos(\theta_1-\theta_2)+8E_{bi}^2\cos(\theta_2-\theta_3) - 8E_{bi}^2\cos(\theta_3-\theta_1) \text{ respectively.} \tag{5.51}$$

After simplification we get,

$$\frac{(O_1-O_2)^2}{E_{bi}^2} = 4-32\sin\left(\frac{\theta_2-\theta_3}{2}\right)\sin\left(\frac{\theta_3-\theta_1}{2}\right)\cos\left(\frac{\theta_1-\theta_2}{2}\right) \text{ OR} \tag{5.52}$$

$$= 4-32\sin\left(\frac{\theta_2-\theta_3}{2}\right)\cos\left(\frac{\theta_3-\theta_1}{2}\right)\sin\left(\frac{\theta_1-\theta_2}{2}\right) \text{ OR} \tag{5.53}$$

$$= 4-32\cos\left(\frac{\theta_2-\theta_3}{2}\right)\sin\left(\frac{\theta_3-\theta_1}{2}\right)\sin\left(\frac{\theta_1-\theta_2}{2}\right) \tag{5.54}$$

Table 5.3 Inequality check of angle sets.

Sets	$\theta_1-\theta_2$	$\theta_2-\theta_3$	$\theta_3-\theta_1$	(5.55)	(5.56)	(5.57)
Set1	$\frac{-\pi}{3}$	$\frac{-\pi}{3}$	$\frac{2\pi}{3}$	$\times$	$\surd$	$\surd$
Set2	$\frac{-\pi}{3}$	$\frac{2\pi}{3}$	$\frac{-\pi}{3}$	$\surd$	$\times$	$\surd$
Set3	$\frac{2\pi}{3}$	$\frac{-\pi}{3}$	$\frac{-\pi}{3}$	$\surd$	$\surd$	$\times$
Set4	$\frac{\pi}{3}$	$\frac{\pi}{3}$	$\frac{-2\pi}{3}$	$\times$	$\surd$	$\surd$
Set5	$\frac{\pi}{3}$	$\frac{-2\pi}{3}$	$\frac{\pi}{3}$	$\surd$	$\times$	$\surd$
Set6	$\frac{-2\pi}{3}$	$\frac{\pi}{3}$	$\frac{\pi}{3}$	$\surd$	$\surd$	$\times$
Set7	$\frac{-4\pi}{3}$	$\frac{2\pi}{3}$	$\frac{2\pi}{3}$	$\surd$	$\surd$	$\surd$
Set8	$\frac{2\pi}{3}$	$\frac{-4\pi}{3}$	$\frac{2\pi}{3}$	$\surd$	$\surd$	$\surd$
Set9	$\frac{2\pi}{3}$	$\frac{2\pi}{3}$	$\frac{-4\pi}{3}$	$\surd$	$\surd$	$\surd$
Set10	$\frac{-2\pi}{3}$	$\frac{-2\pi}{3}$	$\frac{4\pi}{3}$	$\surd$	$\surd$	$\surd$
Set11	$\frac{-2\pi}{3}$	$\frac{4\pi}{3}$	$\frac{-2\pi}{3}$	$\surd$	$\surd$	$\surd$
Set12	$\frac{4\pi}{3}$	$\frac{-2\pi}{3}$	$\frac{-2\pi}{3}$	$\surd$	$\surd$	$\surd$

Considering the expressions in (5.52), (5.53) and (5.54) which when conditioned with $(S_1-S_2)^2 \geq 4E_{bi}^2$, we obtain,

$$\sin\left(\frac{\theta_2-\theta_3}{2}\right)\sin\left(\frac{\theta_3-\theta_1}{2}\right)\cos\left(\frac{\theta_1-\theta_2}{2}\right) \leq 0 \tag{5.55}$$

$$\sin\left(\frac{\theta_2-\theta_3}{2}\right)\cos\left(\frac{\theta_3-\theta_1}{2}\right)\sin\left(\frac{\theta_1-\theta_2}{2}\right) \leq 0 \tag{5.56}$$

$$\cos\left(\frac{\theta_2-\theta_3}{2}\right)\sin\left(\frac{\theta_3-\theta_1}{2}\right)\sin\left(\frac{\theta_1-\theta_2}{2}\right) \leq 0. \tag{5.57}$$

We can check easily if the above explained sets satisfy these inequalities in Table 5.3,

Sub-case 3: All values are positive OR all are negative

$$\frac{(S_1-S_2)^2}{E_{bi}^2} = 4+32\cos\left(\frac{\theta_2-\theta_3}{2}\right)\cos\left(\frac{\theta_3-\theta_1}{2}\right)\cos\left(\frac{\theta_1-\theta_2}{2}\right). \tag{5.58}$$

When (5.58) is conditioned with $(S_1-S_2)^2 \geq 4E_{bi}^2$, we obtain

$$\cos\left(\frac{\theta_2-\theta_3}{2}\right)\cos\left(\frac{\theta_3-\theta_1}{2}\right)\cos\left(\frac{\theta_1-\theta_2}{2}\right) \geq 0. \tag{5.59}$$

Table 5.4 Set of difference angles satisfying inequalities presented in (5.55), (5.56), (5.57) and (5.59)

Sets	$\theta_1-\theta_2$	$\theta_2-\theta_3$	$\theta_3-\theta_1$	(5.55)	(5.56)	(5.57)	(5.59)
Set1	$\frac{-\pi}{3}$	$\frac{-\pi}{3}$	$\frac{2\pi}{3}$	×	√	√	√
Set2	$\frac{-\pi}{3}$	$\frac{2\pi}{3}$	$\frac{-\pi}{3}$	√	×	√	√
Set3	$\frac{2\pi}{3}$	$\frac{-\pi}{3}$	$\frac{-\pi}{3}$	√	√	×	√
Set4	$\frac{\pi}{3}$	$\frac{\pi}{3}$	$\frac{-2\pi}{3}$	×	√	√	√
Set5	$\frac{\pi}{3}$	$\frac{-2\pi}{3}$	$\frac{\pi}{3}$	√	×	√	√
Set6	$\frac{-2\pi}{3}$	$\frac{\pi}{3}$	$\frac{\pi}{3}$	√	√	×	√
Set7	$\frac{-4\pi}{3}$	$\frac{2\pi}{3}$	$\frac{2\pi}{3}$	√	√	√	×
Set8	$\frac{2\pi}{3}$	$\frac{-4\pi}{3}$	$\frac{2\pi}{3}$	√	√	√	×
Set9	$\frac{2\pi}{3}$	$\frac{2\pi}{3}$	$\frac{-4\pi}{3}$	√	√	√	×
Set10	$\frac{-2\pi}{3}$	$\frac{-2\pi}{3}$	$\frac{4\pi}{3}$	√	√	√	×
Set11	$\frac{-2\pi}{3}$	$\frac{4\pi}{3}$	$\frac{-2\pi}{3}$	√	√	√	×
Set12	$\frac{4\pi}{3}$	$\frac{-2\pi}{3}$	$\frac{-2\pi}{3}$	√	√	√	×

Again checking the inequality for the above explained sets in Table 5.3, we get,

None of the sets satisfy all the inequalities thus proving that there is no such set of angles that can achieve the upper bound on the normalized Euclidean distance.

□

5.5.3 Distribution of non-zero symbols in a binary matrix

It is clearly evident that an optimal signature constellation doesn't exist for a single channel output this means that a smart distribution rule should be designed in order to obtain an optimal overall Euclidean distance for a given spreading matrix. This distribution rule depends both on the arrangement of the binary matrix and the signature constellation points, thus in next section we present in detail the unique distribution rule for each considered spreading matrices type in next section.

5.6 Optimal Design

In the previous section, we have shown that a unitary signature constellation doesn't exist for a single channel output. In this section we show that by carefully selecting the signature constellation distribution rule, we can still achieve the upper bound on normalized minimum Euclidean distance for the signature constellation set having one of the angle separation among the list of sets presented in Table 5.4. Next, we provide a complete guide to the design of spreading matrix for an LDS system to achieve the overloading capacity of 150%.

To design a spreading matrix to achieve the upper bound on the normalized minimum Euclidean distance, we start from the signature constellation. This gives some hint for the design of binary matrix and a signature constellation distribution rule.

We have $w_c = 3$, for which we have already proved in previous section that an optimal signature constellation doesn't exist for single channel output. However, it can be observed from Table 5.4 that there are some sets for which the number of output overlapping is limited to a pair. Thus, in the following design, we choose a signature constellation whose angle separations fall under one of the sets provided in the Table 5.4. In the following we consider a signature constellation,

$$v_1 = \exp(i\theta_1), \quad v_2 = \exp(i\theta_2) \text{ and } v_3 = \exp(i\theta_3), \tag{5.60}$$

such that

$$\theta_1 - \theta_2 = -\frac{\pi}{3}, \quad \theta_2 - \theta_3 = \frac{\pi}{3} \text{ and } \theta_3 - \theta_1 = -\frac{\pi}{3}. \tag{5.61}$$

For these angle parameters, next we discuss the nature of the single channel output and the input conditions which lead to non-optimal Euclidean distances.

With these angle parameters, the squared Euclidean distance among single channel outputs from two different inputs can be written as

$$(O_1 - O_2)^2 = A^2 + B^2 + C^2 + 2AB\cos(\theta_1 - \theta_2) + 2BC\cos(\theta_2 - \theta_3) + 2AB\cos(\theta_3 - \theta_1). \tag{5.62}$$

By replacing the values of the angle separation parameters from (5.62) using (5.62), we obtain

$$(O_1 - O_2)^2 = A^2 + B^2 + C^2 + AB + BC - AB. \tag{5.63}$$

We know that when all the inputs are different, the magnitude of A, B and C are equal. Thus, when the last three products in (5.63) provide a negative contribution to the sum, then $(O_1 - O2)^2$ may end up with zero. This happens when,

$$\begin{aligned} &A \text{ is positive, } B \text{ is negative and } C \text{ is positive} \quad \text{OR} \\ &A \text{ is negative, } B \text{ is positive and } C \text{ is negative .} \end{aligned} \tag{5.64}$$

Thus, for the above angle parameters, the single channel output is not one to one since for the input conditions given by (5.64), the squared Euclidean distance is zero.

Next, we look forward to design a binary matrix which gives a one-to-one I/O mapping for the above set of signature constellation. By looking at the input conditions that gives a squared euclidean distance zero, we can rewrite the conditions as:

- A (corresponding to θ_1) and C (corresponding to θ_3) should be non-zero and have same sign.
- B (corresponding to θ_2) should be non-zero and having a sign different from A and C

With above criterion in hand, we choose to consider $w_f = 1$. While keeping $w_f = 1$, a single column is connected with other three columns in only one position, in this way all the columns are interlinked by $w_f = 1$ position. Thus, in a worst case scenario, when one of the column is giving a zero Euclidean distance, the overall Euclidean distance is zero only when all the input symbols are different and satisfy the condition (5.64) for all column outputs.

Thus, when the Euclidean distances from two separate output channels are zero at the same time and if we can avoid the Euclidean distance from the third output channel to be zero, then the final spreading matrix will have a one-to-one I/O relationship. For this, we have to identify three columns such that the two non-zero

positions are linked to other two columns at one position each. For example,

$$\mathbf{A} = \begin{bmatrix} 1 & 1 & 0 & \cdots \\ 0 & 0 & 1 & \cdots \\ 0 & 1 & 1 & \cdots \\ 1 & 0 & 0 & \cdots \\ 1 & 0 & 1 & \cdots \\ 0 & 1 & 0 & \cdots \\ \vdots & \vdots & \vdots & \ddots \end{bmatrix} \tag{5.65}$$

Now we distribute the signature constellation points as shown below,

$$\mathbf{A} = \begin{bmatrix} v_1 & v_2 & 0 & \cdots \\ 0 & 0 & v_3 & \cdots \\ 0 & v_3 & v_2 & \cdots \\ v_3 & 0 & 0 & \cdots \\ v_2 & 0 & v_1 & \cdots \\ 0 & v_1 & 0 & \cdots \\ \vdots & \vdots & \vdots & \ddots \end{bmatrix} \tag{5.66}$$

Next we check when these Euclidean distances of each column are zero.

- An Euclidean distance from first column is zero when A, B and C corresponding to input positions I_1, I_5 and I_4 are with $A =$ positive, $B =$ negative and $C =$ positive.
- For second column, from first column it is fixed that B is positive corresponding to I_1 and v_2. Thus, an Euclidean distance from second column is zero when A and C corresponding to input positions I_3 and I_6 respectively are with $A =$ negative and $C =$ negative.
- For third columns the input positions corresponding to I_3 and I_5 are already negative. Thus, if we replace these positions in the third column of the binary matrix with v_1 and v_2, when they are of the same sign they will never give a zero Euclidean distance.

$$\mathbf{A} = \begin{bmatrix} I_1 & v_1(+) & v_2(+) & 0 & \cdots \\ I_2 & 0 & 0 & v_3 & \cdots \\ I_3 & 0 & v_3(-) & v_2 & \cdots \\ I_3 & v_3(+) & 0 & 0 & \cdots \\ I_4 & v_2(-) & 0 & v_1 & \cdots \\ I_5 & 0 & v_1(-) & 0 & \cdots \\ I_{\cdot} & \vdots & \vdots & \vdots & \ddots \end{bmatrix} \tag{5.67}$$

It is also important to note that when all A, B and C have non-zero magnitude and the single channel squared Euclidean distance is non-zero, it is always greater than or equal to $8E_{bi}^2$.

5.7 Simulation Result

In this section, we present the simulation result for the LDS spreading system. We consider the 150%-load signature matrices $\mathbf{A}_{6,4}$ and $\mathbf{A}_{9,6}$ which were designed based on the criterion presented Section 5.6. Each of these matrices provide a normalized minimum Euclidean distance of 2 with the smallest loop girth of 6. We choose the signature constellation with a guidelines presented as in Section 5.5, i.e.,

$$v_1 = \exp(i\theta_1), \quad v_2 = \exp(i\theta_2) \text{ and } v_3 = \exp(i\theta_3) \tag{5.68}$$

with $\theta_1 = 0$, $\theta_2 = \pi/3$ and $\theta_3 = 2\pi/3$.

We now compare the simulation results against the union bound, iterative decoding and an exhaustive method analytical curves.

5.7.1 $\mathbf{A}_{6,4}$

A binary matrix of size 6×4 is shown below, where $w_r = 2, w_c = 3, w_f = 1$.

$$\mathbf{A} = \begin{bmatrix} 1 & 1 & 0 & 0 \\ 0 & 0 & 1 & 1 \\ 0 & 1 & 1 & 0 \\ 1 & 0 & 0 & 1 \\ 1 & 0 & 1 & 0 \\ 0 & 1 & 0 & 1 \end{bmatrix} \tag{5.69}$$

Distributing the signature constellation points in a way to achieve a one to one mapping using the above described method, we obtain a spreading matrix shown below.

$$\mathbf{A} = \begin{bmatrix} v_3 & v_2 & 0 & 0 \\ 0 & 0 & v_2 & v_1 \\ 0 & v_3 & v_1 & 0 \\ v_2 & 0 & 0 & v_3 \\ v_1 & 0 & v_3 & 0 \\ 0 & v_1 & 0 & v_2 \end{bmatrix} \tag{5.70}$$

Figure 5.4 shows the bit error probability of a BPSK modulated LDS spreading system with an overloading factor of 150%. An iterative decoding performance is compared with union bound performance and exhaustive decoding. In addition, we find out the normalized minimum Euclidean distance for the considered spreading matrix $\mathbf{A}_{6,4}$ designed based on the procedure presented in Section 5.5. We find that the normalized minimum Euclidean distance to be 2 which is equal to the upper bound on the normalized euclidean distance that can be calculated using Proposition 8. The obtained result was very significant in achieving the best possible bit error rate for the overloading factor of 150%. Since the matrix are scalable by changing N and K keeping the ratio constant, by using the design principle presented in section 5.5, we can obtain a spreading matrix of any arbitrary size with minimum density of non-zero symbols with overloading factor 1.5 without changing the minimum Euclidean distance. Another example of the matrix is presented next.

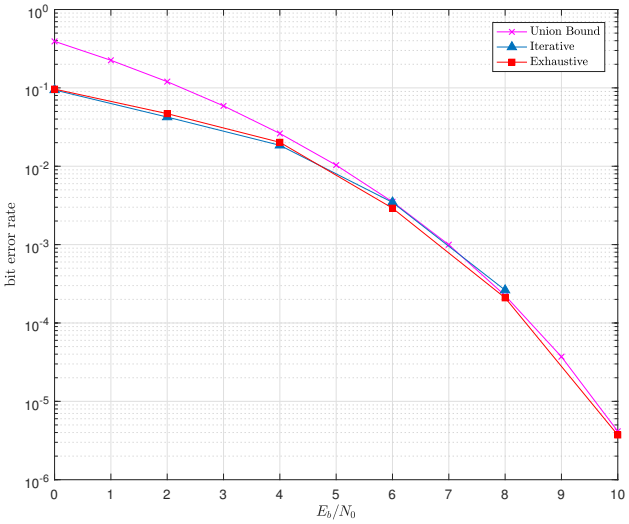

Fig. 5.4 Probability of a BPSK bit error for $\mathbf{A}_{6,4}$

5.7.2 $\mathbf{A}_{9,6}$

A binary matrix of size 9×6 is shown below, where $w_r = 2, w_c = 3, w_f = 1$.

$$\mathbf{A} = \begin{bmatrix} 1 & 1 & 0 & 0 & 0 & 0 \\ 0 & 0 & 1 & 1 & 0 & 0 \\ 0 & 0 & 0 & 0 & 1 & 1 \\ 1 & 0 & 0 & 1 & 0 & 0 \\ 0 & 0 & 1 & 0 & 1 & 0 \\ 0 & 1 & 0 & 0 & 0 & 1 \\ 0 & 0 & 1 & 0 & 0 & 1 \\ 1 & 0 & 0 & 0 & 1 & 0 \\ 0 & 1 & 0 & 1 & 0 & 0 \end{bmatrix} \tag{5.71}$$

Distributing the signature constellation points in a way to achieve one to one mapping using the above described method, we obtain a spreading matrix shown below.

$$\mathbf{A} = \begin{bmatrix} v1 & v2 & 0 & 0 & 0 & 0 \\ 0 & 0 & v1 & v3 & 0 & 0 \\ 0 & 0 & 0 & 0 & v1 & v2 \\ v2 & 0 & 0 & v1 & 0 & 0 \\ 0 & 0 & v2 & 0 & v3 & 0 \\ 0 & v1 & 0 & 0 & 0 & v3 \\ 0 & 0 & v3 & 0 & 0 & v2 \\ v3 & 0 & 0 & 0 & v2 & 0 \\ 0 & v3 & 0 & v2 & 0 & 0 \end{bmatrix} \tag{5.72}$$

In Figure 5.5 we present the bit error probability of a BPSK modulated LDS spreading system with an overloading factor of 150% with these parameters. Iterative decoding performance is compared with an union bound performance and exhaustive decoding. In addition, we find out the normalized minimum Euclidean distance for the considered spreading matrix $\mathbf{A}_{9,6}$ designed based on the procedure presented in Section 5.5. We find that the normalized minimum Euclidean distance to be 2 which is equal to the upper bound on the normalized Euclidean distance that can be calculated using Proposition 8. The obtained result is very significant in achieving the best possible bit error rate for the overloading factor of 150%. Since the matrices are scalable by changing N and K keeping the ratio constant, by using the design principle presented in section 5.5, we can obtain a spreading matrix of any arbitrary size with minimum density of non-zero symbols with overloading factor 1.5 without changing the minimum Euclidean distance. Another example of the matrix is presented next.

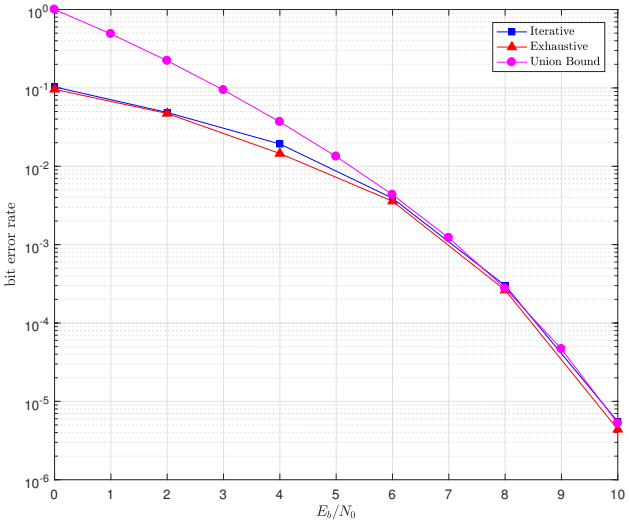

Fig. 5.5 Probability of a BPSK bit error for $A_{9,6}$

Chapter 6

Summary and Conclusions

In this thesis, we have presented various physical layer algorithms in context to 5G wireless communications. The focus has been on low latency and high reliability use cases, spectrum scarcity and spectrum efficiency problems and efficient Non-orthogonal Multiplexing Access. Different specific problems – reliability based decoding of Linear Block Codes, binary pattern synchronization, signal detection under practical imperfection and non-orthogonal multiplexing technique - have been formulated under a 5G physical layer framework.

In section 2, a simplified statistical approach has been investigated to analyse the properties of ordered vector components of Linear Block Codes. In this case, we have presented a novel statistic which computes the number of errors contained in the ordered received noisy codeword, which highlights and makes evidence to OSD property. This is a key parameter that can be applied to derive a further simplified error performance bound. Moreover, simplified expressions for the pdf and cdf of the proposed statistic have also been derived. The main application of these results is in highly efficient decoding of short-length algebraic Linear Block Codes which can be used for low latency use cases of 5G.

In section 3, Massey detector has been revisited in the context of efficient frame synchronization for low latency, high reliability use cases of 5G. We have presented a complete set of new analytical results for the pdfs and the false-alarm/miss-detection probabilities for both of these detectors. A new Extended Massey Detector has been introduced to eliminate a lower bound limitation on the P_{fa} for short pattern lengths. We have shown that the two Massey detectors achieve nearly-optimal performances

both at low and high SNR values. In comparison to optimal Likelihood Ratio test they have very limited penalty (small fraction of dB), but much less complexity. When compared to the classical soft and hard correlation tests, the Massey detectors achieve significant gains of several dBs. All the results have suggested that the Extended Massey detector (for small pattern length N) and the Massey detector (for large N) can be considered the best solution for many demanding applications requiring less complex and short binary pattern identification, like high bit rate, low latency and high reliability frame synchronization.

In section 4, examples of semi-blind signal detection algorithms under practical imperfections have been considered having in mind their possible application to Cognitive Radio - like spectrum sharingapproach for 5G. Both theoretical and numerical results have been presented, showing that a substantial performance loss (in terms of detection and false alarm probabilities) can be experienced under practical imperfections like noise uncertainty and unknown primary user traffic. By adopting approaches based on ML estimation of noise variances, the performance reduction under noise uncertainty can be improved. Also, specific expressions of signal detection performance have been derived for the considered scenarios, taking into account unknown noise variance and unknown primary user traffic.

In section 5, motivated by the the demand of efficient non-orthogonal multiplexing system for 5G networks, a structured approach to design low-density signatures providing 150% overloading for non-orthogonal LDS multiplexing system over the AWGN channel has been presented. Moreover, we have also provided a theoretical proof on the upper bound on the minimum Euclidean distance for the LDS multiplexing system with regular spreading matrix. On one hand, our sequences are of low density type a property which highly simplifies receiver operation. On the other hand, their minimum Euclidean distance properties ensure good performance on AWGN channel. Instead of relying on trial-and-error searches and on pseudo random design steps, we provided a a theoretical, structured approach towards the design of optimal spreading sequences. We have focused on their performance in the AWGN channel which is a good model for downlink multiple access systems operating in a flat, slowly fading radio environment. We evaluate the performance of our sequence constructions and we showed that they have beneficial properties in terms of their distance spectrum.

References

[1] Fp7 european project 317669 metis (mobile and wireless communications enablers for the twenty-twenty information society) 2012. URL https://www.metis2020.com.

[2] Etsi tr 101 557 v1.1.1 (2012-02). URL http://www.etsi.org/deliver/etsi_tr/101500_101599/101557/01.01.01_60/tr_101557v010101p.pdf.

[3] Ieee standard for information technology- local and metropolitan area networks- specific requirements- part 22: Cognitive wireless ran medium access control (mac) and physical layer (phy) specifications: Policies and procedures for operation in the tv bands. Ieee std 802.22-2011, July 2011.

[4] Fp7 european project 318555 5g now (5th generation nonorthogonal waveforms for asynchronous signalling), 2012. URL http://www.5gnow.eu.

[5] The tactile internet itu-t technology watch report august 2014. Technical report, August 2014. URL https://www.itu.int/dms_pub/itu-t/oth/23/01/T23010000230001PDFE.pdf.

[6] Ieee 802.19 wireless coexistence working group (wg). Technical report, July, 2013. URL http://ieee802.org/19/.

[7] Ieee 802.16 working group on broadband wireless access standards. Technical report, July, 2013. URL http://ieee802.org/16/.

[8] J. Adams. An introduction to ieee std 802.15.4. In *IEEE Aerospace Conference*, 2006.

[9] D. Agrawal and A. Vardy. Generalized minimum distance decoding in euclidean-space: Performance analysis. *IEEE Trans. Inform. Theory*, 46: 60–83, January 2000.

[10] G. Wunderet al. 5gnow: Challenging the lte design paradigms of orthogonality and synchronicity. In *Mobile and Wireless Communication Systems for 2020 and beyond, Workshop at 77th IEEE Vehicular Technology Spring Conference*, June 2013.

[11] M. Al-Imari, M. A. Imran, and R. Tafazolli. Low density spreading for next generation multicarrier cellular systems. In *International Conference on Future Communication Networks (ICFCN*, 2012.

[12] M. Al-Imari, M. A. Imran, R. Tafazolli, and D. Chen. Performance evaluation of low density spreading multiple access. In *International Wireless Communications and Mobile Computing Conference (IWCMC)*, 2012.

[13] M. AL-Imari, M. A. Imran, R. Tafazolli, and D. Chen. Performance evaluation of low density spreading multiple access. In *International Wireless Communications and Mobile Computing Conference (IWCMC) 2012, Limassol*, 2012.

[14] Saif E. A. Alnawayseh and P. Loskot. Complexity reduction of ordered statistic decoding using side information. *IEEE Comm. Letters*, 16(2):249–251, November 2012.

[15] 4G Americas. 5g spectrum recommendation. White paper, Aug. 2015. URL http://www.4gamericas.org/files/514/3930/9262/4G_Americas_5G_Spectrum_Recommendations_White_Paper.pdf.

[16] D. D. Ariananda, M. K. Lakshmanan, and H. Nikookar. A survey on spectrum sensing techniques for cognitive radio. In *Second International Workshop on Cognitive Radio and Advanced Spectrum Management, 2009. CogART 2009.*, May 2009. doi: 10.1109/COGART.2009.5167237.

[17] E. Arikan. Channel polarization: A method for constructing capacity achieving codes for symmetric binary-input memoryless channels. *IEEE Trans. Inf. Theory*, 55:3051–3073, July 2009.

[18] E. Axell, G. Leus, E. G. Larsson, and H. V.: Poor. Spectrum sensing for cognitive radio:state-of-the-art and recent advances. *IEEE Signal Process. Mag.*, 29(3):101–116, May 2012.

[19] S. Badrinath and V. U. Reddy. A hybrid energy detection approach to spectrum sensing. In *First UK-India International Workshop on Cognitive Wireless Systems (UKIWCWS), 2009*, volume 1, pages 10–12, December 2009. doi: 10.1109/UKIWCWS.2009.5749385.

[20] Z. D. Bai. Methodologies in spectral analysis of large-dimensional random matrices, a review. *Statistica Sinica*, 9:611–677, 1999.

[21] Jinho Baik and Jack W. Silverstein. Eigenvalues of large sample covariance matrices of spiked population models. *Journal of Multivariate Analysis*, 97.6: 1382–1408, 2006.

[22] M. Baldi, M. Bertinelli, F. Chiaraluce, P. Dhakal, R. Garello, N. Maturo, and E. Paolini. A study on state-of-the-art space mission telecommand receivers. *IEEE Aerospace and Electronic Systems Magazine*, 2017. In Press.

[23] R. H. Barker. Group synchronization of binary digital systems. *Communication Theory, London UK.*, 1953.

[24] A. Barron and A. Joseph. Toward fast reliable communication at rates near capacity with Gaussian noise. In *Proc. of IEEE ISIT 2010*, 2010.

[25] C. Berrou, A. Glavieux, and P. Thitimajshima. Near shannon limit error correcting coding and decoding: Turbo codes. In *in IEEE Proc. Int. Conf. Communications, Geneva, Switzerland.*, May 1993.

[26] P. Bianchi, M. Debbah, M. Maida, and J. Najim. Performance of statistical tests for single-source detection using random matrix theory. *Information Theory, IEEE Transactions on*, 57:2400–2419, April 2011. doi: 10.1109/TIT.2011.2111710.

[27] F. Boccardi, R. W. Heath, A. Lozano, T. L. Marzetta, and P. Popovski. Five disruptive technology directions for 5g. *in IEEE Communications Magazine*, 52(2):74–80, February 2014. doi: 10.1109/MCOM.2014.6736746.

[28] R. C. Bose and D. K. Ray-Chadhuri. On a class of error correcting binary group codes. *Inform. Control*, 3:68–79, March 1960.

[29] D. Cabric, A. Tkachenko, and R. W. Brodersen. Spectrum sensing measurements of pilot, energy, and collaborative detection. In *Military Communications Conference*, October 2006. doi: 10.1109/MILCOM.2006.301994.

[30] Danijela Cabric, Artem Tkachenko, and Robert W. Brodersen. Experimental study of spectrum sensing based on energy detection and network cooperation. In *First international workshop on Technology and policy for accessing spectrum (TAPAS '06).*, 2006.

[31] G. P. Calzolari, F. Chiaraluce, R. Garello, and E. Vassallo. Symbol synchronization properties of ccsds turbo codes. *Intl. Journal of Satellite Commun.*, 20:379–390, 2002.

[32] D. Chase. A class of algorithms for decoding block codes with channel measurement information. *IEEE Trans. Inform. Theory*, 8:170–182, January 1972.

[33] Jian Chen, A. Gibson, and J. Zafar. Cyclostationary spectrum detection in cognitive radios. In *IET Seminar on Cognitive Radio and Software Defined Radios: Technologies and Techniques, 2008*, September 2008.

[34] M. Chiani and M. G. Martini. Optimum synchronization of frames with unknown, variable lengths on Gaussian channels. In *Proc. IEEE Global Telecomm. Conf., Dallas, US.*, November 2004.

[35] M. Chiani and M. G. Martini. Practical frame synchronization for data with unknown distribution on awgn channels. *IEEE Commun. Lett*, 9(5):456–458, May 2005.

[36] M. Chiani and M. G. Martini. On sequential frame synchronization in awgn channels. *IEEE Trans. Commun*, 54(2), February 2006.

[37] M. Chiani and M. G. Martini. Analysis of optimum frame synchronization based on periodically embedded sync words. *IEEE Trans. Commun*, 55(11): 2056–2060, November 2007.

[38] J. Choi. Low density spreading for multicarrier systems. In *Proceedings of the Eighth International Symposium on Spread-Spectrum Techniques and Applications*, 2004.

[39] Cisco. Visual networking index. White paper at cisco.com, 2016.

[40] Federal Communication Commission. Notice of proposed rule making and order: Facilitating opportunities for flexible, efficient, and reliable spectrum use employing cognitive radio technology. Feb 2005.

[41] J. H. Conway and N. J. A. Sloane. Soft decoding techniques for codes and lattices, including the golay code and the leech lattice. *IEEE Trans. Inform. Theory*, 32:41–50, January 1986.

[42] E. Dahlman, G. Mildh, S. Parkvall, J. Peisa, J. Sachs, Y. Selén, and J. Sköld. 5g wireless access: requirements and realization. *IEEE Commun. Mag*, 52 (12):42–47, December 2014.

[43] Erik Dahlman, Stefan Parkvall, and Johan Skold. *4G: LTE/LTEAdvanced for Mobile Broadband, 2nd ed.* Elsevier, Waltham, MA, USA, 2014.

[44] P. Dhakal and D. Riviello. Multi-antenna energy detector under unknown primary user traffic. In *International Conference on Advances in Cognitive Radio (COCORA)*, Feb. 2016.

[45] P. Dhakal, D. Riviello, and R. Garello. Snr wall analysis of multi-sensor energy detection with noise variance estimation. In *IEEE ISWCS*, Aug. 2014.

[46] P. Dhakal, D. Riviello, F. Penna, and R. Garello. Impact of noise estimation on energy detection and eigenvalue based spectrum sensing algorithms. In *IEEE International Conference on Communications (ICC)*, June 2014.

[47] P. Dhakal, D. Riviello, F. Penna, and R. Garello. Hybrid approach analysis of energy detection and eigenvalue based spectrum sensing algorithms with noise power estimation. In *The Fourth Int. Conf. on Advances in Cognitive Radio*, 2014.

[48] P. Dhakal, R. garello, S. K. Sharma, S. Chatzinotas, and B. Otternsten. On the error performance bound of ordered statistics decoding of linear block codes. In *IEEE ICC 2016*, 2016.

[49] P. Dhakal, S. K. Sharma, S. Chatzinotas, B. Otternsten, and D. Riviello. Effect of largest eigenvalue based spectrum sensing technique. In *Springer International Publishing*, 2016.

[50] F. F. Digham, M.-s. Alouini, and Marvin K. Simon. On the energy detection of unknown signals over fading channels. In *IEEE International Conference on Communications, 2003.*, May 2003. doi: 10.1109/ICC.2003.1204119.

[51] F. F. Digham, M. S. Alouini, and Marvin K. Simon. On the energy detection of unknown signals over fading channels. *Communications, IEEE Transactions on*, 55:21–24, January 2007. doi: 10.1109/TCOMM.2006.887483.

[52] D. Divsalar and F. Pollara. One the design of turbo codes. Tda progress report 42-123, November 1995.

[53] D. Divslar and R. J. McEliece. Effective freee distance of turbo codes. *IEEE Electronic Letters*, 32(5):445–446, 1996.

[54] B. G. Dorsch. A decoding algorithm for binary block codes and j-ary output channels. *IEEE Trans. Inform. Theory*, 20:391–394, May 1974.

[55] C. Douillard and C. Berrou. Turbo codes with rate-m/(m+1) constituent convolutional codes. *IEEE Transactions On Communications*, 53:1630–1638, 2005.

[56] P. F. Driessen. Performance of frame synchronization in packet transmission using bit erasure information. *IEEE Trans. Commun.*, 39(4):567–573, April 1991.

[57] ECC. Spectrum allocation in europe. Technical report, 2013. URL http://www.erodocdb.dk/Docs/doc98/official/pdf/ercrep025.pdf.

[58] John D. Edell. Wideband, noncoherent, frequency-hopped waveforms and their hybrids in low-probability-of-intercept communications. *No. NRL-8025. NAVAL RESEARCH LAB WASHINGTON DC*, 1976.

[59] Ericsson. More than 50 billion connected devices. White paper, 2011.

[60] A. Osseiran et al. Scenarios for 5g mobile and wireless communications: the vision of the metis project. *in IEEE Communications Magazine*, 52(5):26–35, May 2014. doi: 10.1109/MCOM.2014.6815890.

[61] D. J. Costello et al. Spatially coupled sparse codes on graphs: Theory and practice. *IEEE Commun. Mag*, 52(7):168–179.

[62] J. G. Andrews et al. What will 5g be? *in IEEE Journal on Selected Areas in Communications*, 32(6):1065–1082, June 2014. doi: 10.1109/JSAC.2014.2328098.

[63] J. Thompson et al. 5g wireless communication systems: prospects and challenges. *IEEE Commun. Mag*, pages 62–64, February 2014.

[64] Jianfeng Wang et al. First cognitive radio networking standard for personal/portable devices in tv white spaces. April 2010. doi: 10.1109/DYSPAN.2010.5457855.

[65] Popovski P. et al. Deliverable d1.1 scenarios, requirements and kpis for 5g mobile and wireless system. Ict-317669-metis/d1.1, April 2013.

[66] Popovski P. et al. Deliverable d6.3 intermediate system evaluation results. Ict-317669-metis/d6.3, August 2014.

[67] R. Baldemair et al. Evolving wireless communications: addressing the challenges and expectations of the future. *IEEE Vehic. Tech. Mag*, 8(1):24–30, March 2013.

[68] R. Irmer et al. Coordinated multipoint: Concepts, performance, and field trial results. *IEEE Commun. Mag*, 49(2):102–111, February 2011.

[69] T. R. 102 889-2 Etsi. Part 2: Technical characteristics for srd equipment for wireless industrial applications using technologies different from ultra-wide band (uwb). Technical report, Aug 2011.

[70] FCC. Federal communication commission spectrum policy task force report. Technical report, Nov 2002.

[71] FCC. Spectrum allocation in us. Technical report, 2003. URL www.ntia.doc.gov/files/ntia/publications/2003-allochrt.pdf.

[72] F. Fettweis and S. Alamouti. 5g: personal mobile internet beyond what cellular did to telephony. *IEEE Commun. Mag*, 52(2):140–145, February 2014.

[73] Consultative Committee for Space Data Systems. Tc synchronization and channel coding. Ccsds 231.0-b-2 blue book, September 2010.

[74] M. Fossorier. Iterative reliability-based decoding of low density parity check codes. *IEEE Trans. Inf. Theory*, 19(5):908–916, May 2001.

[75] M. Fossorier. Reliability-based soft-decision decoding with iterative information set reduction. *IEEE Trans. Inf. Theory*, 48(12):3101–3106, December 2002.

[76] M. Fossorier and S. Lin. Soft-decision decoding of linear block codes based on ordered statistics. *IEEE Trans. Inform. Theory*, 41:1379–1396, September 1995.

[77] M. Fossorier and S. Lin. Computationally efficient soft decision decoding of linear block codes based on ordered statistics. *IEEE Trans. Inform. Theory*, 42:738–750, May 1996.

[78] M. Fossorier and S. Lin. First order approximation of the ordered binary symmetric channel. *IEEE Trans. Inform. Theory*, 42:1381–1387, September 1996.

[79] M. Fossorier and S. Lin. Error performance analysis for reliability based decoding algorithms. *IEEE Trans. Inform. Theory*, 48:287–293, January 2002.

[80] R. G. Gallager. Low-density parity-check codes. *IRE Trans. Inform. Theory*, 8:21–28, January 1962.

[81] D. Gazelle and J. Snyders. Reliability-based code search algorithms for maximum likelihood decoding of block codes. *IEEE Trans. Inform. Theory*, 43:239–249, January 1997.

[82] C. Georghiades and E. Serpedin. *Communication handbook*. CRC, Boca Raton, FL, 2002.

[83] A. Ghosh, J. Zhang, J. G. Andrews, and R. Muhamed. *Fundamentals of LTE*. Pearson Education, Upper Saddle River, NJ, 2010.

[84] A. Ghosh, R. Jana, V. Ramaswami, J. Rowland, and N. K. Shankaranarayanan. Modeling and characterization of large-scale wi-fi traffic in public hot-spots. In *IEEE INFOCOM*, April 2011.

[85] E. H. Gismalla and E. Alsusa. On the performance of energy detection using bartlett's estimate for spectrum sensing in cognitive radio systems. *Signal Processing, IEEE Transactions on*, 60:3394–3404, July 2012. doi: 10.1109/TSP.2012.2191544.

[86] Glenn L. Greig. On the shape of energy-detection roc curves. *Perception & Psychophysics*, 48(1):77–81, 1990. doi: 10.3758/BF03205013.

[87] Simon Haykin. Cognitive radio: brain-empowered wireless communications. *IEEE Journal on Selected Areas in Communications*, 23:201–220, February 2005. doi: 10.1109/JSAC.2004.839380.

[88] Simon Haykin, D. J. Thomson, and J. H. Reed. Spectrum sensing for cognitive radio. In *Proceedings of the IEEE*, May 2009.

[89] P. A. Hoeher and T. Wo. Superposition modulation: myths and facts. *IEEE Communications Magazine*, 49(12):110–116, December 2011.

[90] R. Hoshyar, F. P. Wathan, and R. Tafazolli. Novel low-density signature for synchronous cdma systems over awgn channel. *IEEE Trans. on Signal Processing*, 56(4):1616–1626, April 2008.

[91] R. Hoshyar, R. Razavi, and M. Al-Imari. Lds-ofdm an efficient multiple access technique. In *IEEE 71st Vehicular Technology Conference, Taipei*, 2010.

[92] Hwei P. Hsu. *Theory and Problems of Probability, Random Variables, and Random Processes*. SCHAUM'S OUTLINE SERIES McGRAW-HILL, 1996.

[93] T. Hwang, C. Yang, G. Wu, S. Li, and G. Ye Li. Ofdm and its wireless applications: A survey. *IEEE Trans. Veh. Technol.*, 58(4):1673–1694, May 2009.

[94] IEEE. 802.11 wireless local area networks. Technical report, 2013. URL http://ieee802.org/11/.

[95] European Telecommunications Standards Institute. Digital video broadcasting (dvb). framing structure, channel coding and modulation for digital terrestrial television. Etsi en 300 744, v1.6.1, January 2009.

[96] M. H. et al. Islam. Spectrum survey in singapore: Occupancy measurements and analyses. In *Cognitive Radio Oriented Wireless Networks and Communications (CROWNCOM), 2008*, May 2008. doi: 10.1109/CROWNCOM.2008.4562457.

[97] W. Jin and M. Fossorier. Reliability-based soft decision decoding with multiple biases. *IEEE Trans. Inf. Theory*, 53(1):105–120, January 2007.

[98] Iain M. Johnstone. On the distribution of the largest eigenvalue in principal components analysis. *The Annals of statistics*, 29.2:295–327, 2001.

[99] G. D. Forney Jr. Generalized minimum distance decoding. *IEEE Trans. Inform. Theory*, 12:125–131, April 1966.

[100] Iso/iec Jtc1/sc29/wg11. Mpeg-4 overview. (v.18 - singapore version), March 2001.

[101] A. Kabat, F. Guilloud, and R. Pyndiah. New approach to order statistics decoding of long linear block codes. In *Proc. Globecom*, pages 1467–1471, November 2007.

[102] A. Kopansky and M. Bystrom. Detection of aperiodically embedded syncronization patterns. In *Proc. IEEE International Symp. Inf. Theory (ISIT 2001)*, June 2001.

[103] A. Kopansky and M. Bystrom. Detection of aperiodically embedded syncronization patterns. *IEEE Trans. Wireless Commun*, 3(5):1386–1392, October 2004.

[104] A. Kortun, T. Ratnarajah, M. Sellathurai, Ying-Chang Liang, and Yonghong Zeng. Throughput analysis using eigenvalue based spectrum sensing under noise uncertainty. August 2012. doi: 10.1109/IWCMC.2012.6314237.

[105] V. I. Kostylev. Energy detection of a signal with random amplitude. In *IEEE International Conference on Communications, 2002.*, 2002. doi: 10.1109/ICC.2002.997120.

[106] A. Kothiyal, O. Y. Takeshita, W. Jin, and M. Fossorier. Iterative reliability-based decoding of linear block codes with adaptive belief propagation. *IEEE Commun. Lett*, 9(12):1067–1069, December 2005.

[107] Shira Kritchman and Boaz Nadler. Non-parametric detection of the number of signals: hypothesis testing and random matrix theory. *Signal Processing, IEEE Transactions on*, 57.10:3930–3941, 2009.

[108] M. Laner, P. Svoboda, N. Nikaein, and M. Rupp. Traffic models for machine type communications. In *Proc. Wireless Commun. Syst. (ISWCS'13)*, pages 1–5, August 2013.

[109] Wei Lin and Qinyu Zhang. A design of energy detector in cognitive radio under noise uncertainty. In *11th IEEE Singapore International Conference on Communication Systems, 2008. ICCS 2008.*, November 2008. doi: 10.1109/ICCS.2008.4737174.

[110] G. L. Lui and H. H. Tan. Frame synchronization for Gaussian channels. *IEEE Trans. Commun*, COM-35(8):818–829, August 1987.

[111] ITU-R M. Imt vision - framework and overall objectives of the future development of imt for 2020 and beyond. Itu working document 5d/temp/224-e, July 2013.

[112] X. Ma, J. Liu, and B. Bai. New techniques for upper-bounding the ml decoding performance of binary linear codes. *IEEE Trans. Commun*, 61(3):842–851, 2013.

[113] S. L. MacDonald and D. C. Popescu. Impact of primary user activity on the performance of energy-based spectrum sensing in cognitive radio systems. December 2013.

[114] D. J. MacKay. Good error-correcting codes based on very sparse matrices. *IEEE Trans. Inform. Theory*, 45(2):399–431, March 1999.

[115] F. J. MacWilliams and N. J. A. Sloane. *The Theory of Error-Correcting Codes: Part 2*. Elsevier, 1977.

[116] G. C. Madueno, C. Stefanovic, and P. Popovski. Reliable reporting for massive m2m communications with periodic resource pooling. *IEEE Wireless Communications Letters*, 3(4):429–432, August 2014.

[117] A. Mahram and M. C. Amirani. The complexity as a criterion for blind spectrum sensing in cognitive radio. *Developments in E-systems Engineering (DeSE)*, 444:6–8, December 2011. doi: 10.1109/DeSE.2011.62.

[118] A. Mariani, A. Giorgetti, and M. Chiani. Effects of noise power estimation on energy detection for cognitive radio applications. *IEEE Transactions on Communications,*, 59:3410–3420, December 2011. doi: 10.1109/TCOMM.2011.102011.100708.

[119] A. Mariani, A. Giorgetti, and M. Chiani. Snr wall for energy detection with noise power estimation. In *IEEE International Conference on Communications (ICC), 2011*, volume 1, pages 5–9, June 2011. doi: 10.1109/icc.2011.5963367.

[120] A. Mariani, A. Giorgetti, and M. Chiani. Effects of noise power estimation on energy detection for cognitive radio applications. *Communications, IEEE Transactions on*, 59:3410–3420, December 2011. doi: 10.1109/TCOMM.2011.102011.100708.

[121] George Marsaglia. Ratios of normal variables. *in Journal of Statistical Software*, 16(4), May 2006.

[122] J. L. Massey. Optimum frame synchronization. *IEEE Trans. Commun*, 20(2): 115–119, April 1972.

[123] J. Mitola and G. Q. Maguire, Jr. Cognitive radio: making software radios more personal. *Personal Communications, IEEE*, 6:13–18, 1999. doi: 10.1109/98.788210.

[124] Joseph Mitola. *Cognitive radio: An integrated agent architecture for software defined radio*. PhD thesis, Doctor of Technology, Royal Inst. Technol.(KTH), Stockholm, Sweden, 2000.

[125] F. Moghimi, R. Schober, and R. K. Mallik. Hybrid coherent/energy detection for cognitive radio networks. *Wireless Communications, IEEE Transactions on*, 10:1594–1605, May 2011. doi: 10.1109/TWC.2011.030411.100973.

[126] A. Montanari and D. Tse. Analysis of belief propagation for non-linear problems: The example of cdma (or: How to prove tanaka's formula). In *Proceedings of the 2006 IEEE Information Theory Workshop*, 2006.

[127] M. Morelli. Timing and frequency synchronization for the uplink of an ofdma system. *IEEE Trans. on Commun.*, 52(2):296–306, February 2004.

[128] Robb J. Muirhead. Latent roots and matrix variates: a review of some asymptotic results. *The Annals of Statistics*, pages 5–33, 1978.

[129] B. Nadler, F. Penna, and R. Garello. Performance of eigenvalue-based signal detectors with known and unknown noise level. June 2011. doi: 10.1109/icc.2011.5963473.

[130] J. Neyman and E. Pearson. On the problem of the most efficient tests of statistical hypotheses. *Philosophical Transactions of the Royal Society of London*, 231:289–337, 1933.

[131] J. Neyman and E. S. Pearson. On the problem of the most efficient tests of statistical hypotheses. *Philosophical Transactions of the Royal Society*, 231: 289–337, 1933.

[132] P. T. Nielsen. Some optimum and suboptimum frame synchronizers for binary data in Gaussian noise. *IEEE Trans. Commun*, 21(6):770–772, June 1973.

[133] P. T. Nielsen. On the expected duration of a search for a fixed pattern in random data. *IEEE Trans. Inf. Theory*, 19(6):702–704, September 1973.

[134] H. Nikopour and H. Baligh. Sparse code multiple access. In *2013 IEEE 24th Annual International Symposium on Personal, Indoor, and Mobile Radio Communications (PIMRC*, 2013.

[135] Nokia. 2020: Beyond 4g radio evolution for the gigabit experience. White paper, 2011. URL http://www.nokiasiemensnetworks.com.

[136] H. Ochiai and H. Imai. On the distribution of the peak-to-average power ratio in ofdm signals. *IEEE Trans. on Commun.*, 49(2):282–289, February 2001.

[137] R. Palit, K. Naik, and A. Singh. Anatomy of wifi access traffic of smartphones and implications for energy saving techniques. *International Journal of Energy, Information and Communication*, 3(1):1–16, February 2012.

[138] F. Penna and R. Garello. Detection of discontinuous signals for cognitive radio applications. *IET Communications*, 5(10):1453–1461, January 2011.

[139] F. Penna, R. Garello, and M. A. Spirito. Probability of missed detection in eigenvalue ratio spectrum sensing. In *IEEE conference on Wireless and Mobile Computing, Networking and Communications, 2009.*, October 2009. doi: 10.1109/WiMob.2009.29.

[140] H. Pradhan, A. S. Kalamkar, and A. Banerjee. Sensing-throughput tradeoff in cognitive radio with random arrivals and departures of multiple primary users. *IEEE Communications Letters*, 19(3):415–418, March 2015.

[141] J. G. Proakis. *Digital Communications*. McGraw-Hill, 4th edition, 2001.

[142] Qualcomm. 5g waveforms and multiple access techniques. Technical report. URL https://www.qualcomm.com/media/documents/files/5g-research-on-waveform-and-multiple-access-techniques.pdf.

[143] D. Ramirez, G. Vazquez-Vilar, R. Lopez-Valcarce, J. Via, and I. Santamaria. Multiantenna detection under noise uncertainty and primary user's spatial structure. May 2011. doi: 10.1109/ICASSP.2011.5946275.

[144] R. Razavi, M. AL-Imari, M. A. Imran, R. Hoshyar, and D. Chen. On receiver design for uplink low density signature ofdm (lds-ofdm). *in IEEE Transactions on Communications*, 60(11):3499–3508, November 2012.

[145] L. S. Reed and G. Solomon. Polynomial codes over certain finite fields. *SIAM J. Appli. Math*, 8:300–304, 1960.

[146] D. Riviello, P. Dhakal, and R. Garello. Performance analysis of multi-antenna hybrid energy detectors and optimization with noise variance estimation. In *International Conference on Advances in Cognitive Radio (COCORA)*, April 2015.

[147] D. Riviello, P. Dhakal, and R. Garello. On the use of eigen vectors in multi-antenna spectrum sensing with noise variance estimation. In *International Conference in Signal Processing and Integrated Networks*, Feb. 2015.

[148] S. N. Roy. On a heuristic method of test construction and its use in multivariate analysis. *The Annals of Mathematical Statistics*, 24:220–238, 1953.

[149] S. N. Roy. On a heuristic method of test construction and its use in multivariate analysis. *Ann. Math Stat.*, pages 220–238, 1953.

[150] Y. Saito, Y. Kishiyama, A. Benjebbour, T. Nakamura, A. Li, and K. Higuchi. Non-orthogonal multiple access (noma) for cellular future radio access. In *IEEE 77th Vehicular Technology Conference (VTC Spring), Dresden*, 2013.

[151] R. A. Scholtz. Frame synchronization techniques. *IEEE Trans. Commun*, COM-28:1204–1213, August 1980.

[152] S. Sequeira, R. R. Mahajan, and P. Spasojevic. On the noise power estimation in the presence of the signal for energy-based sensing. In *35th IEEE Sarnoff Symposium (SARNOFF), 2012*, May 2012. doi: 10.1109/SARNOF.2012.6222753.

[153] C. E. Shannon. A mathematical theory of communication. *Bell Sys. Tech.*, 27: 379–423, October 1948.

[154] S. K. Sharma, T. E. Bogale, S. Chatzinotas, B. Ottersten, L. B. Le, and X. Wang. Cognitive radio techniques under practical imperfections: A survey. *IEEE Commun. Surveys Tutorials*, 2015.

[155] B. Sklar and F. J. Harris. The abcs of linear block codes. *IEEE Signal Process. Mag*, 21:14–35, July 2004.

[156] DySPAN standards committe. Technical report. URL http://grouper.ieee.org/groups/dyspan/.

[157] J. J. Stiffler. *Theory of synchronous communications*. Prentice-Hall, Englewood Cliffs, NJ, 1971.

[158] R. Tandra and A. Sahai. Noise calibration, delay coherence and snr walls for signal detection. In *3rd IEEE Symposium on New Frontiers in Dynamic Spectrum Access Networks, 2008. DySPAN 2008.*, volume 1, pages 14–17, October 2008. doi: 10.1109/DYSPAN.2008.42.

[159] R. Tandra and A. Sahai. Snr walls for signal detection. *IEEE Journal of Selected Topics in Signal Processing,*, 2:4–17, February 2008. doi: 10.1109/JSTSP.2007.914879.

[160] L. Tang, Y. Chen, E. L. Hines, and M. S. Alouini. Effect of primary user traffic on sensing-throughput tradeoff for cognitive radios. *IEEE Transactions on Wireless Communications*, pages 1063–1068, Apr 2011.

[161] D. J. Torrieri. *Principles of Secure Communication Systems*. Artech House, Boston, US, 1992.

[162] J. K. Tugnait. On multiple antenna spectrum sensing under noise variance uncertainty and flat fading. *Signal Processing, IEEE Transactions on*, 60(4): 1823–1832, April 2012. doi: 10.1109/TSP.2011.2180721.

[163] R. Turyn. *Sequences with small correlation*. Wiley, New York, 1968.

[164] Harry Urkowitz. Energy detection of unknown deterministic signals. In *Proceedings of the IEEE*, April 1967.

[165] A. Valembois and M. Fossorier. Box and match techniques applied to soft decision decoding. *IEEE Trans. Inf. Theory*, 50(5):796–810, May 2004.

[166] V. Valenta, R. Marsalek, G. Baudoin, M. Villegas, M. Suarez, and F. Robert. Survey on spectrum utilization in europe: Measurements, analyses and observations. In *Cognitive Radio Oriented Wireless Networks and Communications (CROWNCOM), 2010*, June 2010.

[167] J. van de Beek and B. M. Popovic. Multiple access with low-density signatures. In *Proc. of the IEEE Global Telecommunications Conference GLOBECOM, Honolulu, HI*, 2009.

[168] H. G. Vu, H. H. Nguyen, and D. E. Dodds. Iterative ordered-statistic decoding for ldpc coded modulation systems. In *Proc. CCECE*, pages 196–199, May 2005.

[169] Rui Wang and Meixia Tao. Blind spectrum sensing by information theoretic criteria for cognitive radios. *Vehicular Technology, IEEE Transactions on*, 59: 3806–3817, October 2010. doi: 10.1109/TVT.2010.2065250.

[170] T. Wang, Y. Chen, E. Hines, and B. Zhao. Analysis of effect of primary user traffic on spectrum sensing performance. In *Fourth International Conference on Communications and Networking in China*. ChinaCOM, 2009.

[171] F. Wathan. *Low-density signature communications in overloaded CDMA systems*. 2007.

[172] A. R. Williamson, M. J. Marshall, and R. D. Wesel. Reliability-output decoding of tail-biting convolution codes. *IEEE Trans. Commun*, 62(6):1768–1778, April 2014.

[173] J. K. Wolf. Efficient maximum likelihood decoding of linear block codes using a trellis. *IEEE Trans. Inform. Theory*, 24:76–80, January 1978.

[174] J. Y. Wu, P. H. Huang, T. Y. Wang, and V. W. S. Wong. Energy detection based spectrum sensing with random arrival and departure of primary user's signal. December 2013.

[175] Y. Wu and C. Hadjicostis. Soft-decision decoding of linear block codes using efficient iterative g-space encodings. In *Proc. Globecom*, pages 921–925, November 2001.

[176] Y. Wu and C. N. Hadjicostis. Soft-decision decoding using ordered recodings on the most reliable basis. *IEEE Trans. Inf. Theory*, 53(2):829–836, February 2007.

[177] L. Xichun, A. Gani, R. Salleh, and O. Zakaria. The future of mobile wireless communication networks. In *Proc. Int. Conf. Commun. Softw. Netw*, February 2009.

[178] Zhuan Ye, G. Memik, and J. Grosspietsch. Energy detection using estimated noise variance for spectrum sensing in cognitive radio networks. March 2008. doi: 10.1109/WCNC.2008.131.

[179] Yonghong Zeng and Ying-Chang Liang. Maximum-minimum eigenvalue detection for cognitive radio. September 2007. doi: 10.1109/PIMRC.2007.4394211.

[180] Yonghong Zeng and Ying-Chang Liang. Spectrum-sensing algorithms for cognitive radio based on statistical covariances. *IEEE Transactions on Vehicular Technology,*, 58:1804–1815, May 2009. doi: 10.1109/TVT.2008.2005267.

[181] Yonghong Zeng and Ying-Chang Liang. Eigenvalue-based spectrum sensing algorithms for cognitive radio. *Communications, IEEE Transactions on*, 57:6, June 2009. doi: 10.1109/TCOMM.2009.06.070402.

[182] Yonghong Zeng, Ying-Chang Liang, Anh Tuan Hoang, and E.C.Y Peh. Reliability of spectrum sensing under noise and interference uncertainty. In *IEEE International Conference on Communications, Workshops, 2009. ICC Workshops 2009.*, June 2009. doi: 10.1109/ICCW.2009.5208033.

[183] Q. T. Zhang. Advanced detection techniques for cognitive radio. June 2009. doi: 10.1109/ICC.2009.5198712.

[184] Wei Zhao and Tobias Tynderfeldt. Contention-free random access procedure in wireless networks. *U.S. Patent US*, 9301(US9301323 B2), March 2016.

[185] D. Zijian, L. Fei, and S. Yaolian. Improved syndrome-based ordered statistic decoding algorithm for ldpc codes. In *Proc. ICSPS*, pages 295–297, Jul 2010.

[186] M. Zorzi, A. Gluhak, S. Lange, and A. Bassi. From today's intranet of things to a future internet of things: a wireless- and mobility-related view. *IEEE Wireless Communications*, 17(6):44–51, December 2010.